UNIVERSITY OF SOUTHAMPTON

The Long-Term X-ray, UV and Optical Variability of Active Galactic Nuclei

by

Samuel Dominic Connolly

Thesis for the degree of Doctor of Philosophy

in the
FACULTY OF PHYSICAL SCIENCES AND ENGINEERING
Department of Physics & Astronomy

June 2016

UNIVERSITY OF SOUTHAMPTON

ABSTRACT

FACULTY OF PHYSICAL SCIENCES AND ENGINEERING
Department of Physics & Astronomy

Doctor of Philosophy

THE LONG-TERM X-RAY, UV AND OPTICAL VARIABILITY OF ACTIVE GALACTIC NUCLEI

by Samuel Dominic Connolly

The variability of emission from active galactic nuclei (AGN), both intrinsic, due to changes in the emitting regions, and extrinsic, due to absorption and scattering from material near to the black hole, can reveal a wealth of information about their geometry and accretion behaviour. In this thesis, I use analysis of the spectral variability of the X-ray, UV/optical emission from AGN to probe the properties of the material surrounding supermassive black holes at their centres.

Firstly, I present constraints on the variability of the photon index of the X-ray spectrum of 24 *Swift* AGN from the Palomar sample of galaxies. The change in the behaviour of AGN from 'softer-brighter' to 'harder-when-brighter' at a critical accretion rate, seen previously in other samples of AGN, is found. 'Harder-when-brighter' behaviour is measured in several sources individually, achieved previously in only one AGN.

I present a study of the long-term (months-years) X-ray spectral variability of three Seyfert AGN known to exhibit strong absorption variations. Trends in the long-term behaviour of the absorbers, in particular a strong anti-correlation between the observed absorbing column and the intrinsic luminosity of NGC 1365, are explained using a variable wind model. In this model, the radius at which the wind arises is dependent on the luminosity of the central engine, leading to correlated long-time-scale changes in the observed absorption properties.

Finally, time lags between the X-ray and UV/optical variability of the Seyfert AGN NGC 4395 are measured, using cross-correlation techniques. The lags fit the $\lambda^{4/3}$ dependence expected from reprocessing of X-rays in the accretion disc. Modelling of the expected lags from a standard Shakura-Sunyaev thin disc with the previously-measured physical parameters of the system is then carried out. The results are consistent with the data, further supporting reprocessing as the principle source of UV/optical variability in NGC 4395.

Contents

List of Figures

List of Tables

Declaration of Authorship

I, Samuel Dominic Connolly, declare that this thesis titled, 'The Long-Term X-ray, UV and Optical Variability of Active Galactic Nuclei' and the work presented in it are my own. I confirm that:

- This work was done wholly or mainly while in candidature for a research degree at this University.
- Where any part of this thesis has previously been submitted for a degree or any other qualification at this University or any other institution, this has been clearly stated.
- Where I have consulted the published work of others, this is always clearly attributed.
- Where I have quoted from the work of others, the source is always given. With the exception of such quotations, this thesis is entirely my own work.
- I have acknowledged all main sources of help.
- Where the thesis is based on work done by myself jointly with others, I have made clear exactly what was done by others and what I have contributed myself.

Signed: ____

Date: ____

Acknowledgements

Many thanks to my supervisor, Ian McHardy, for his invaluable supervision, infectious enthusiasm, and limitless help and advice. Thanks to the lovely Keira, my wonderful family and my fantastic friends for their encouragement, support and company.

I would like to thank the Science and Technology Funding Council for financially supporting my research.

Finally, thanks to my colleagues and friends at the Southampton University Astronomy group, without whom this work would have been much harder and considerably less enjoyable.

Abbreviations

AGN	**A**ctive **G**alactic **N**ucleus
ACF	**A**uto **C**orrelation **F**unction
ACIS	**C**handra **A**dvanced **C**CD **I**maging **S**pectrometer
ACIS	**INTE**rnational **G**amma-**R**ay **A**strophysics **L**aboratory
ADAF	**A**dvection **D**ominated **A**ccretion **F**low
ARIES	**A**ryabhatta **R**esearch **I**nstitute of Observational Scienc**ES**
BALQSO	**B**road **A**bsorption **L**ine **Q**uasi-**S**tellar **O**bject
BBXRT	**B**road **B**and **X**-**R**ay **T**elescope
BEST	**B**lack Hole **E**volution in **S**pace-**T**ime Observatory
BHXRB	**B**lack **H**ole **X**-**R**ay **B**inary
BLR	**B**road **L**ine **R**egion
CCC	**C**ross-**C**orrelation **C**oefficient
CCCD	**C**ross- **C**orrelation **C**entroid **D**istribution
CCF	**C**ross-**C**orrelation **F**unction
DCF	**D**iscrete **C**ross-correlation **F**unction
EPIC	**E**uropean **P**hoton **I**maging **C**amera
EXOSAT	**E**uropean **X**-ray **O**bservatory **SAT**ellite
FR	**F**lux-**R**andomisation
FWHM	**F**ull **W**idth at **H**alf **M**aximum
HST	**H**ubble **S**pace **T**elescope
HXD	**H**ard **X**-ray **D**etector
ICF	**I**nterpolation **C**ross-correlation **F**unction
IRAF	**I**mage **R**eduction and **A**nalysis **F**acility
ISCO	**I**nnermost **S**table **C**ircular **O**rbit
JAVELIN	**J**ust **A**nother **V**ehicle for **E**stimating **L**ags **I**n **N**uclei)

LAXPC	**L**arge **A**rea **X**-ray **P**roportional **C**ounter
LCOGT	**L**as **C**umbres **O**bservatory **G**lobal **T**elescope
LINER	**L**ow-**I**onisation **N**uclear **E**mission-**L**ine **R**egion
LLAGN	**Low**-**L**uminosity **A**ctive **G**alactic **N**ucleus
MCMC	**M**arkov **C**hain **M**onte **C**arlo
NLR	**N**arrow **L**ine **R**egion
NT	**N**ovikov-**T**horne
NuSTAR	**Nu**clear **S**pectroscopic **T**elescope **AR**ray
OM	**O**ptical **M**onitor
PDF	**P**robability **D**ensity **F**unction
PSD	**P**ower **S**pectral **D**ensity
QSO	**Q**uasi-**S**tellar **O**bject
RGS	**R**eflection **G**rating **S**pectrometer
RIAF	**R**adiatively **I**nefficient **A**ccretion **F**low
RSS	**R**andom **S**ubset **S**election
RXTE	**R**ossi **X**-ray **T**iming **E**xplorer
SAS	**S**cientific **A**nalysis **S**ystem
SDSSS	**S**loan **D**igital **S**ky **S**urvey
SNR	**S**ignal-to-**N**oise **R**atio
SXT	**S**oft **X**-ray **T**elescope
UFO	**U**ltra-**F**ast **O**utflow
UVOT	**U**ltra **V**iolet and **O**ptical **T**elescope
WA	**W**arm **A**bsorber
XIPE	**X**-ray **I**maging **P**olarimetry **E**xplorer
XMM-Newton	**X**-rey **M**ulti-**M**irror **Mission Newton**
XRT	**X-R**ay **T**elescope

Physical Constants

Boltzmann Constant	k_B	$=$	$1.380\ 648\ 52 \times 10^{-23}$ m^2 kg s^{-2} K^{-1}
Gravitational Constant	G	$=$	$6.674\ 08 \times 10^{-18}$ m^3 kg^{-1} s^{-2}
Solar Mass	$M_\odot$	$=$	$1.988\ 55 \times 10^{30}$ kg
Thomson Cross-Section of an Electron	σ_T	$=$	$6.652\ 458\ 734 \times 10^{-29}$ m^2
Planck Constant	h	$=$	$6.626\ 070\ 04 \times 10^{-34}$ m^2 kg s^{-1}
Stefan Boltzmann Constant	σ_{SB}	$=$	$5.670\ 367 \times 10^{-8}$ W m^{-2} K^{-4}
Parsec	pc	$=$	$3.085\ 677\ 6 \times 10^{16}$ m
Megaparsec	Mpc	$=$	$3.085\ 677\ 6 \times 10^{22}$ m
e		$=$	$2.718\ 281\ 828$
Proton mass	m_p	$=$	$1.672\ 621\ 58 \times 10^{-27}$ kg
Electron volt	eV	$=$	$1.602\ 176\ 57 \times 10^{-19}$ J
pi	π	$=$	$3.141\ 592\ 65$

“And we came forth to contemplate the stars”

Dante Alighieri, *Inferno*

Chapter 1

Introduction

"In the beginning the Universe was created.
This has made a lot of people very angry and been widely regarded as a bad move."
Douglas Adams, The Restaurant at the End of the Universe

Black holes are a fascinating phenomenon, representing the most extreme gravitational objects in the universe. The importance of studying them cannot be overstated, their luminosities making them amongst the most luminous objects in existence, visible to the edge of the universe. The accretion of material onto the supermassive black holes can lead to the release of such an abundance of energy that the evolution of the entire galaxy is affected, the light emitted sometimes so bright as to outshine a billion stars.

This thesis aims to deepen our understanding of the process of accretion onto black holes through analysis of the spectral and temporal variability of the X-ray, UV and optical radiation which is emitted from the material close to accreting black holes, focussing on active galactic nuke (AGN)

In this chapter, I will give an overview of the variety of AGN observed and the components of the current state of the unified model of AGN. I will then briefly discuss the physics of accretion and the mechanisms resulting in both the emission and absorption of the radiation be observe from these systems. I then will discuss the similarities of the behaviour of AGN to that of the smaller black holes seen in X-ray binaries (BHXRBs), which point to universal accretion physics. Finally, I will give an outline of this thesis and its main aims.

1.1 Active Galactic Nuclei

The centre of almost every galaxy in the universe is thought harbour a supermassive black hole, most millions to billions of times the mass of the sun, accreting matter at a range of rates. The majority are in quiescence, their accretion rates very low and their emission usually too faint to observe, but a significant fraction ($\sim 43\%$ Ho et al., 1997a) accrete at higher rates; these are Active Galactic Nuclei (AGN). Emission lines from the nuclei of galaxies were first observed optically over a hundred years ago in NGC 1068 (Fath, 1909, Slipher, 1909). They were not found in other galaxies until a study by Seyfert (1943), however, who observed high-velocity emission lines in a small sample of galaxies including NGC 1068 (Shields, 1999). It was realised that a very large amount of mass was required to generate the widths of these lines from Doppler-broadening due to Keplerian motion, and that this mass had to be very compact, as the nuclei were unresolved (Woltjer, 1959).

Subsequently, the realisation that the broad emission lines in quasars, the 'quasi-stellar radio sources' found early radio surveys, were in fact a highly-redshifted Balmer series allowed them to be identified as very distant, and therefore extremely luminous (Schmidt, 1963), some with luminosities of up to 10^{47}ergs$^{-}1$ and above. Furthermore, the timescale of variability of their emission was found to be on the order of days, or even hours. As causality dictates that information cannot travel faster than the speed of light, the maximum size of an emission region cannot exceed $R = \Delta tc$, where Δt is the shortest timescale of the variability; any variability on shorter timescales is smoothed to Δt. The variability of AGN therefore implies an emitting region of $< 10^{-3}$ pc. The combination of the enormity of the power of their radiation, the rapidity of their variability and the broadness of their emission lines therefore lead these nuclei to be associated with supermassive black holes.

Nearby AGN are typically classified optically, though they radiate across the entire electromagnetic spectrum. The majority of AGN are though to be found in Low-Ionisation Nuclear Emission-line Regions (LINERs) ($\sim 50 - 75\%$ Ho et al., 1997a), the central regions of galaxies which possess optical emission lines from low-ionisation species. LINERs have relatively low accretion rates, their emission only able to partially ionise nearby gas and are often not directly observable. A large fraction of AGN are Seyfert galaxies ($\sim 25\%$ Ho et al., 1997a), which are brightly-emitting nuclei seen at the centres of resolved galaxies, with relatively higher accretion rates. Seyfert AGN possess strong optical emission lines and are further divided into two classes according to the width of these lines. Seyfert 1s have very broad emission lines, whilst Seyfert 2s have relatively narrow emission lines (Khachikian & Weedman, 1974). Narrow emission lines are also often seen within the broader lines observed in Seyfert 1s, and further intermediate classes also exist (e.g 1.2, 1.5, 1.8) based on the relative strength of the Hα and Hβ lines in the optical spectra (Osterbrock, 1977).

In the more distant universe, quasars/QSOs (Quasi-Stellar Objects) are commonly observed, visible due to their huge luminosities, greater than those seen in Seyfert galaxies, tending to greatly outshine their host galaxies. Quasars also often possess strong radio emission. Subclasses of quasar include blazars, which display particularly bright radio emission, and BAL QSOs (broad absorption line QSOs), whose optical spectra contain broad absorption lines.

In addition to the optical and radio emission, X-ray emission is observed from all classes of AGN. The luminosity of this X-ray emission is linked to the emission in other wavebands, but the relationship is not always simple. It is thought that the X-ray and radio luminosities of AGN (and BHXRBs) are linked, together with the mass of the system, on the 'fundamental plane of black hole activity' (e.g. Koerding et al., 2006, Merloni et al., 2003). The short-timescale (days-weeks) variability of UV/optical emission also appears to be strongly linked to the variability of X-ray emission in some systems (e.g. Breedt et al., 2009, Cameron et al., 2012, McHardy et al., 2014, Uttley et al., 2003).

1.1.1 The Unified Model of AGN

AGN are now commonly accepted to be supermassive black holes, their vast majority of their optical/UV and X-ray emission produced by, or very close to, the accretion disc of material falling towards the black hole and their radio emission produced by jets of material ejected perpendicular to the disc in some systems. Differences in the spectrum, variability and luminosity of this intrinsic radiation can be explained solely by the mass of the central black hole and the accretion rate of the system. A higher black hole mass will lead to a larger, cooler disc with variability on longer time scales, whilst a higher accretion rate in a given system will lead to a hotter disc. For these reasons, quasars are thought to contain the largest black holes on average, and possess high accretion rates.

AGN observed locally are generally thought to have lower black hole masses on average; Seyfert AGN are thought to have more intermediate accretion rates in comparison to quasars, whilst LINERs are thought to have very low accretion rates. Differences in the black hole mass and accretion rate cannot explain the many other differences in the characteristics of AGN, however, leading to the question of whether a single, unified model can explain the observed behaviour of all AGN.

The various observed properties of different AGN were first described in a single unified model by Antonucci & Miller (1985), who attributed the differences between AGN to differences in the viewing angle of the observer with respect to the system. In this model, broad emission lines are produced by orbiting gas which is ionised by the X-ray emission produced close to the central black hole, their width caused by their high Keplerian velocity. This broad emission line region (BLR) is surrounded by a torus of cool dust and gas which absorbs the majority of emission when viewing the AGN from high inclinations, hiding the BLR from view. The torus is also invoked to explain the large fraction of 'Compton-thick' AGN which experience very heavy absorption ($\mathrm{N_H} > 10^{24}\mathrm{cm}^{-2}$) (e.g. Brightman et al., 2015, Malizia et al., 2009). The narrow emission lines are produced by gas at greater distances from the black hole (in the 'narrow emission line region', NLR), their greater distance leading to lower Keplerian velocities and therefore narrower lines, as well as placing the emitting material outside the region obscured by the torus such that its emission is visible from any angle.

This picture was extended to include a wind of material blown from the accretion disc following the detection in some AGN of emission and absorption lines with high radial velocities (Elvis, 2000). This model attempts to explain both broad and narrow absorption lines, the large range of observed line velocities (from thousands to tens of thousands of kms^{-1}) and the large range of observed absorbing columns. A schematic of the components of the unified model is shown in Fig. 1.1.

Despite a great deal of work having been done on the unification of AGN, many of the details are still unclear - the size, shape and distance of the accretion disc, torus, NLR and BLR and accretion disc winds are not well known, nor are the causes of observational differences not due to inclination which are likely to be linked to the mass and accretion rate of the system. The work in this thesis aims to advance our understanding of

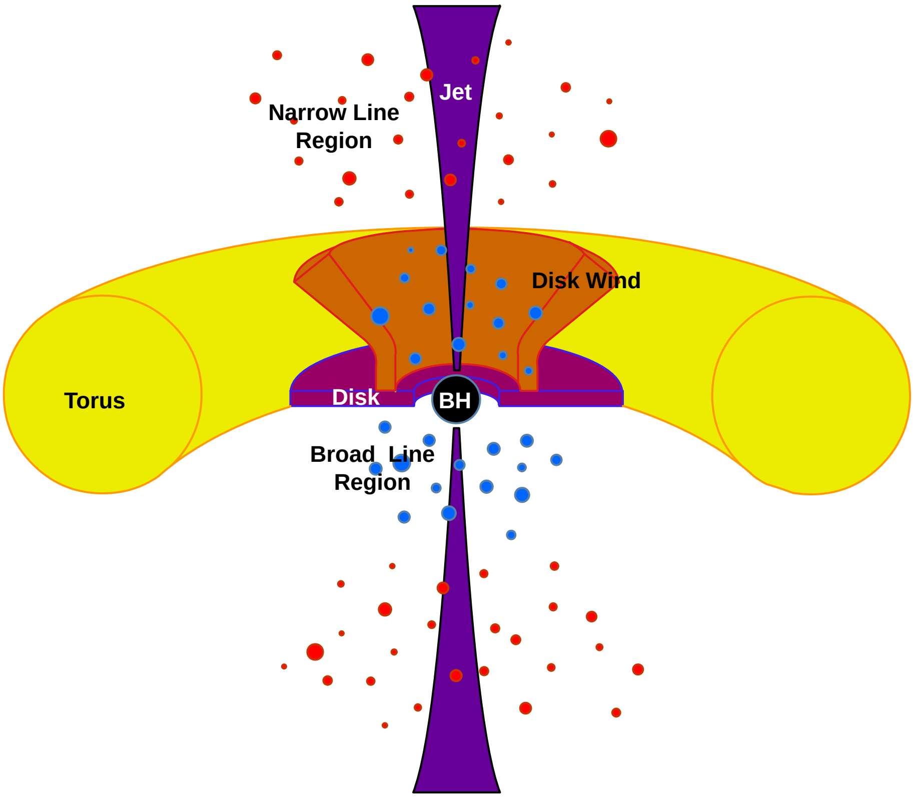

FIGURE 1.1: A diagram of the components of the unified model of AGN, based on figures from Urry et al. (1995) and Elvis (2000)

the geometry and accretion behaviour of AGN and in doing so take a step closer to a complete unified model of AGN.

1.2 Mass Accretion onto Black Holes

The only process known to be efficient enough to produce the huge luminosities of AGN is accretion, the process by which material is accumulated onto an object, in this case a black hole. The total energy (E) of a test particle of mass m in orbit around an object with mass M at distance r is the sum of its kinetic energy (K) and gravitational potential energy (P), given by:

$$E = K + P \tag{1.1}$$

where

$$K = \frac{1}{2}mv^2, P = -\frac{GMm}{r} \tag{1.2}$$

Assuming circular motion, the velocity of the orbiting particle is given by

$$v^2 = \frac{GM}{r} \tag{1.3}$$

which can be substituted into equation 1.2 to give:

$$K = \frac{GMm}{2r} \tag{1.4}$$

Differentiating with respect to r gives us the change in both quantities with changing radius

$$\frac{dK}{dr} = -\frac{GMm}{2r^2}, \frac{dP}{dr} = \frac{GMm}{r^2} \tag{1.5}$$

therefore

$$\frac{dK}{dr} = -\frac{1}{2}\frac{dP}{dr} \tag{1.6}$$

Half of the potential energy of the particle is therefore converted to kinetic energy in order to maintain the particle's orbit, whilst the remaining half must be lost through some either process, such as by emission of radiation.

As we are considering accretion on to a black hole, however, not all of this energy can be liberated, as any gravitational potential energy the particle still possesses when it reaches the innermost stable circular orbit (ISCO) of the black hole can effectively be considered lost. The energy that can be liberated is therefore given by:

$$\Delta V = \int_{R_{ISCO}}^{\infty} \frac{GMm}{r^2} dr = \left[\frac{GMm}{r}\right]_{R_{ISCO}}^{\infty} = \frac{GMm}{R_{ISCO}} \tag{1.7}$$

where R_{ISCO} is the radius of the ISCO. As the radius of the ISCO depends on the spin of the black hole, the amount of energy that can be liberated is also dependent on the spin. For a Schwarzschild black hole, i.e. with zero spin, the radius of the ISCO is given by

$$R_{ISCO} = \frac{6GM}{c^2} \tag{1.8}$$

thus

$$\Delta V = mc^2/6 \tag{1.9}$$

i.e. a sixth of the rest mass energy of the particle is converted from potential energy - as half of this becomes kinetic energy, this means that a twelfth of the rest mass energy is liberated, equivalent to an efficiency of $\eta = 0.083$, where the liberated energy is given by $E = \eta mc^2$. For a Kerr black hole, which is spinning, the ISCO is smaller, leading to efficiencies up to $\eta = 0.4$ for a maximally spinning black hole. This makes accretion a highly efficient mechanism for converting the gravitational potential energy of matter into other forms of energy, capable of producing the luminosities observed in AGN.

1.2.1 The Eddington Limit

As material needs to radiate in order to lose energy and fall towards the black hole, this radiation must also be able to escape the system. As radiation exerts a pressure on matter onto which it is incident, the very radiation which allows matter to be accreted can itself inhibit the process of accretion. The mode of accretion therefore has a huge effect on infalling matter's ability to radiate energy and make its way towards the black hole.

The momentum carried by a single photon (p_γ) is given by

$$p_\gamma = \frac{E_\gamma}{c} \tag{1.10}$$

where E_γ is the energy of the photon. If we assume that every emitted photon is absorbed by accreting matter, the force, F, exerted by radiation pressure on it is equivalent to the loss of the total momentum of the emitted photons, which is proportional to the total luminosity

$$F = \frac{d}{dt}\sum p_\gamma = \frac{1}{c}\frac{d}{dt}\sum E_\gamma = \frac{L_{bol}}{c} \tag{1.11}$$

If we assume radiation is emitted isotropically, the total radiation pressure, P_{rad} at distance d is given by

$$P_{rad} = \frac{L_{bol}}{4\pi d^2 c} \tag{1.12}$$

The force exerted on a particle is then given by

$$F_{rad} = P_{rad}\sigma_T = \frac{L_{bol}\sigma_T}{4\pi d^2 c} \tag{1.13}$$

where σ_T is the Thomson cross section of the particle. For a particle of mass m to be prevented from accreting, this force needs to be at least as large as the gravitational force exerted on it, given by

$$F_{grav} = \frac{GMm}{d^2} \tag{1.14}$$

where M is the mass of the black hole. As the mass and Thomson cross section depend on the type of particle, we assume that the accreting matter is composed of molecular hydrogen gas, i.e. an atom composed of an electron and a proton. In this case, we use the Thomson cross section of an electron, as this is far greater than that of a proton, but use the mass of the proton (m_p), which is much greater than that of an electron. Including this assumption and rearranging for L_{bol}, we find the maximum luminosity of an accreting system, known as the Eddington luminosity (L_{Edd}), is given by

$$L_{Edd} = \frac{4\pi GMm_p c}{\sigma_T} \tag{1.15}$$

and, equivalently, the maximum mass accretion rate, or Eddington accretion rate, is given by

$$\dot{M}_{Edd} = \frac{L_{Edd}}{\eta c^2} = \frac{4\pi G M m_p c}{\sigma_T \eta c^2} \tag{1.16}$$

Although the assumptions of spherically symmetrical accretion and purely neutral hydrogen are, in the vast majority of cases at least, not true, the ratio of the bolometric luminosity of a given system to the Eddington luminosity, referred to as the Eddington ratio, is still useful as an approximation of the relative accretion rate.

1.2.2 The Thin Disc Accretion Model

Spherically symmetrical accretion (also named Bondi accretion after it's original formulator (Bondi, 1952)) is the simplest form of accretion that can occur, however it requires that the accreting material has no initial angular momentum, such that it can fall directly towards the black hole. Furthermore, a spherical flow would have a very low radiative efficiency, making it unable to accrete at a high enough rate to explain the high bolometric luminosities of AGN and BHXRBs.

In the context of accreting binaries, Shakura & Sunyaev (1973) argued that matter accreting from a companion star would possess a large angular momentum which would need to be lost in order for the matter to be accreted. They proposed a model in which a steady-state disc of material in Keplerian orbits forms due to the outward transport of angular momentum, with a viscosity given by

$$v = \alpha c_s H \tag{1.17}$$

where c_s is the sound speed in the disc, H is the height of the disc and α is a parameter encompassing the unknown elements of the physics of this viscosity. This model is called the 'thin disc model' because of the small height (H) of the disc compared to the radius at a given point in the disc. Such an accretion disc is highly radiatively efficient, as required by the observed AGN luminosities.

If we assume the accretion disc to be optically thick, such that it emits as a blackbody, we can equate the total energy dissipated at a given radius, R, to the total energy emitted by blackbody (according to Planck's law), giving the temperature profile of the disc with radius

$$T(r) = \left(\frac{3}{8\pi\sigma_{SB}} \frac{GM\dot{m}}{R^3} \left(1 - \sqrt{\frac{R_0}{R}} \right) \right)^{1/4} \tag{1.18}$$

where R_0 is the radius of the inner edge of the accretion disc and $\dot{m}$ is the accretion rate of the system.

A relativistic generalisation of the Shakura & Sunyaev (1973) thin-disc accretion model called the Novikov-Thorne (NT) model also exists (Novikov & Thorne, 1973, Page & Thorne, 1974). The NT model allows the spin of the black hole to be taken into account, i.e. it uses a Kerr black hole in place of a zero-spin Schwarzschild black hole and also has the advantage of including material present in the 'plunging zone', i.e. material which has crossed the ISCO and is therefore in free-fall towards the black hole (Penna et al., 2011). For the purposes of the work in this thesis, the differences between the NT model and the standard Sharkura-Sunyaev model are negligible, however, so the NT model is not employed.

1.2.3 Radiatively Inefficient Accretion

At low accretion rates, the thin disc model is not thought to be applicable, as the accreting matter is thought to be optically thin and therefore inefficient at radiating. This mode of accretion is known as a radiatively inefficient accretion flow (RIAF). It is thought to consist of a geometrically-thick flow (i.e. a larger scale height in comparison to a thin disc) made up of a plasma of ions and electrons. The poor radiative ability of the ions leads to high temperatures, which is the cause of the large scale height. The electron population, being much better at radiating, is significantly cooler (e.g. Narayan, 1996). The best-known model of a RIAF is that of an advection-dominated accretion flow (ADAF), in which a fraction of the accretion energy is advected into the black hole, leading to the loss of the energy which went into heating the accreted matter but could not be radiated (Narayan, 1994).

1.3 AGN Emission

AGN emit significant radiation accross the entire electromagnetic spectrum, however in this thesis I will be concentrating on X-ray and UV/optical emission. The relevant emission mechanisms in these wavebands are described below.

1.3.1 The UV Spectra of AGN

If it is assumed that the accretion disc radiates as a blackbody, the total spectrum will consist of the sum of the blackbody emission components from each radius of the disc, with a temperature given by the profile shown in equation 1.18 and a luminosity scaled according the the area of the annulus forming the fraction of the disc at this radius. In AGN, this spectrum peaks in the UV waveband, thus the disc radiates strongly across the UV and optical wavebands. Significant optical emission is also produced by the BLR and NLR, most apparent by the emission lines from these regions present in optical spectra of AGN.

1.3.2 The X-ray Spectra of AGN

X-ray emission is observed in essentially all AGN and is thought to originate from very close to the black hole. It is widely thought that its source is a 'corona' of high-energy electrons above the centre of the accretion disc which produce X-ray emission via inverse Compton scattering of lower-energy UV/optical seed photons. This lead to a power law spectrum, with a photon number (N_α) distribution given by

$$N_\gamma(E) = nE^{-\Gamma} \tag{1.19}$$

where Γ is known as the photon index, E is the photon energy and n is the normalisation (typically the count rate at 1 keV). The photon energy (E_α distribution is then given by

$$E_\gamma(E) = nE^{1-\Gamma} = nE^{-\alpha} \tag{1.20}$$

where α is the spectral index. The value of Γ is dependant on the energy distribution of the electron population. In the model of Lightman & Zdziarski (1987) for the Comptonisation of thermal emission by a cloud of high-energy electrons, the value of Γ is given by

$$\Gamma = \sqrt{\frac{9}{4} + \frac{1}{\tau(k_B T/m_e c^2)(1+\tau/3)}} - \frac{5}{2} \tag{1.21}$$

where T is the temperate of the electron cloud and τ is the scattering depth. Thus, a hotter corona leads to a lower value of Γ, and a flatter spectrum with a greater proportion of higher-energy emission.

1.3.3 Synchtron emission

In addition to Comptonisation, non-thermal X-rays can be produced in AGN through Synchrotron emission. This is thought to be the emission mechanism in AGN jets, due to strong magnetic fields they are thought to possess; X-ray emission from jets has been observed in a number of AGN by Chandra. Sychrotron is also thought to be the main emission mechanism of RIAFs. Synchrotron emission could therefore be contributing to the measured X-ray spectra of AGN which show evidence of jets or RIAFs (Harris & Krawczynski, 2006). As synchrotron emission tends to produce power law spectra, synchrotron components can be hard to disentangle from Comptonisation. Synchrotron photons are highly-polarised and therefore distinguishable from Compton emission in this way, but the lack of existing X-ray polarimeters has prevented this difference from being utilised.

1.3.4 X-ray Hardness Ratios

As measuring the photon index requires spectral fitting, which is model dependent, calculating the hardness ratio of an X-ray spectrum is commonly used as a model-independent method of estimating changes in the photon index, by comparing the count rates in two independent X-ray bands. In this thesis, the hardness ratio is defined as

$$HR = \frac{R_{hard} - R_{soft}}{R_{hard} + R_{soft}} \tag{1.22}$$

where R_{hard} is the count rate in the harder (higher-energy) of the two bands and R_{soft} is the count rate in the softer (lower-energy) band. A hardness ratio of 1 therefore indicates a spectrum in which all of the flux is in the hard band, a hardness ratio of -1 indicates all of the flux is in the soft band, and a hardness ratio of 0 indicates an equal count rate in both bands. A higher hardness ratio therefore implies a low photon index and vice versa, though this relies on the assumption that there are no additional spectral components which could be affecting the hardness of the spectrum. A power law with constant Γ but variable luminosity in combination with a constant soft component, for example, can also lead to hardness changes.

1.4 Variability in AGN

There are many sources of variability in AGN, both intrinsic and due to absorption and scattering. The main sources of variability relevant to this thesis are described below.

1.4.1 Propogating Accretion Fluctuations

The main source of variability in the intrinsic emission of AGN, i.e. from the accretion disc and X-ray corona, is fluctuations in the accretion rate throughout the accretion disc. These fluctuations are thought to occur at all radii in the disc and be on a timescale similar to the Keplerian angular velocity (Ω_K) at the radius at which they occur. These are thought to propagate inwards on the viscous timescale, t_{visc}, given by

$$t_{visc} = \left[\alpha \left(\frac{H}{R} \right)^2 \Omega_K \right]^{-1} \tag{1.23}$$

where α is the viscosity parameter from the Shakura & Sunyaev (1973) thin disc model, H is the height of the disc and R is the radius from which the accretion time is being calculated (Lyubarskii, 1997). As the characteristic timescale of these variations decreases with decreasing radius, higher frequency variability is introduced as the variations propogate inwards, on top of the lower frequency variability from further out. A higher accretion rate at a given radius leads to a higher temperature and therefore increased blackbody radiation. When these variations reach the inner accretion disc, from which the seed photons for X-ray emission originate, the extra thermal emission then causes an increase in X-ray emission, on timescales of months to years.

1.4.1.1 X-Ray Reprocessing

If we assume that the X-ray-emitting corona is either above the accretion disc or has a larger scale height than the accretion disc, the disc will be illuminated by a fraction of the X-ray radiation produced. As some of this radiation will be absorbed by the disc, this irradiation will cause an increase in the temperature at a given point on the disc which is proportional to the intensity of the X-ray radiation incident at that point. This in turn will lead to an increase in the thermal emission of the disc at lower wavelengths, determined by the increase in temperature. As the X-ray emission from the corona is variable, the degree of irradiation of the disc will also be variable, causing variability in the luminosity of the thermal emission which is correlated with the X-ray variability. This variability of emission at a given point on the disc will be lagged in time according to the light travel time from the corona to that point. Additionally, the inclination of the system will affect the distance from a given point to the disc to the observer, changing the time lag of emission from that point with respect to the X-ray emission. Any reprocessing timescale will also add to any existing lag, however this is thought to be likely to be negligibly small. The combination of the time lags to each point on the disc, the temperature profile of the disc, produces a transfer function describing the thermal flux produced over time after an X-ray impulse. For typical AGN black hole masses of $10^6 - 10^8\ M_\odot$, the light travel times are of the order of minutes to days, the lags lengthening with increasing mass, but are also likely to be dependent on the accretion rate of the system (e.g. Breedt et al., 2009, 2010). The flux from the X-ray source at a given radius is $\sim R^{-2}$ and, assuming $R >> H_X$, the foreshortening of the disc with respect to the X-ray source is $\sim H_X/R$, the irradiation of the disc decreases as $\sim L_X H_X R^{-3}$. Consequently, the temperature of the disc decreases as $T(R) \sim L_X^{1/4} H_X^{1/4} R^{-3/4}$. As the time delay to a given radius goes as $\sim R/c$ and the peak wavelength goes as $\sim T^{-1}$, the time lags therefore are expected to lengthen with increasing wavelength (Cackett et al., 2007, Frank et al., 2002, Lira et al., 2011), with the lag given by

$$\tau(\lambda) = A\lambda^{4/3} \tag{1.24}$$

Where τ is the time lag, λ is the wavelength and A is a normalisation factor. It is important to note, however, that in order for reprocessed emission to be observed, it must be comparable to the intrinsic emission due to accretion variations in the disc.

The energy per unit area of the disc from absorbed X-rays is dependent on both the luminosity of the X-ray source and the solid angle subtended by the disc at a given radius. The flux at a given radius from the X-ray source is given by

$$F(R) = \frac{L_X}{A_{sphere}(R)}, \text{ where } A_{sphere}(R) = 4\pi(H^2 + R^2) \tag{1.25}$$

where $A_{sphere}(R)$ is the area of the sphere centred on the X-ray source extending to the disc radius R and H is the height of the X-ray source. The area of an annulus at radius R is given by

$$A_{annulus}(R) = 2\pi R dR \tag{1.26}$$

however this area is foreshortened according to the height of the X-ray source above the disc. The projected area of the ring is given by

$$A_{projected}(R) = 2\pi R dR cos\theta \tag{1.27}$$

where

$$cos\theta = \frac{H}{\sqrt{H^2 + R^2}} \tag{1.28}$$

giving a projected area with respect to H and R of

$$A_{projected}(R) = \frac{2\pi R dR H}{\sqrt{H^2 + R^2}} \tag{1.29}$$

The total energy absorbed by a ring at radius R is therefore given by

$$E(r) = \frac{L_X(1 - A)H}{4\pi(H^2 + R^2)^{3/2}} \tag{1.30}$$

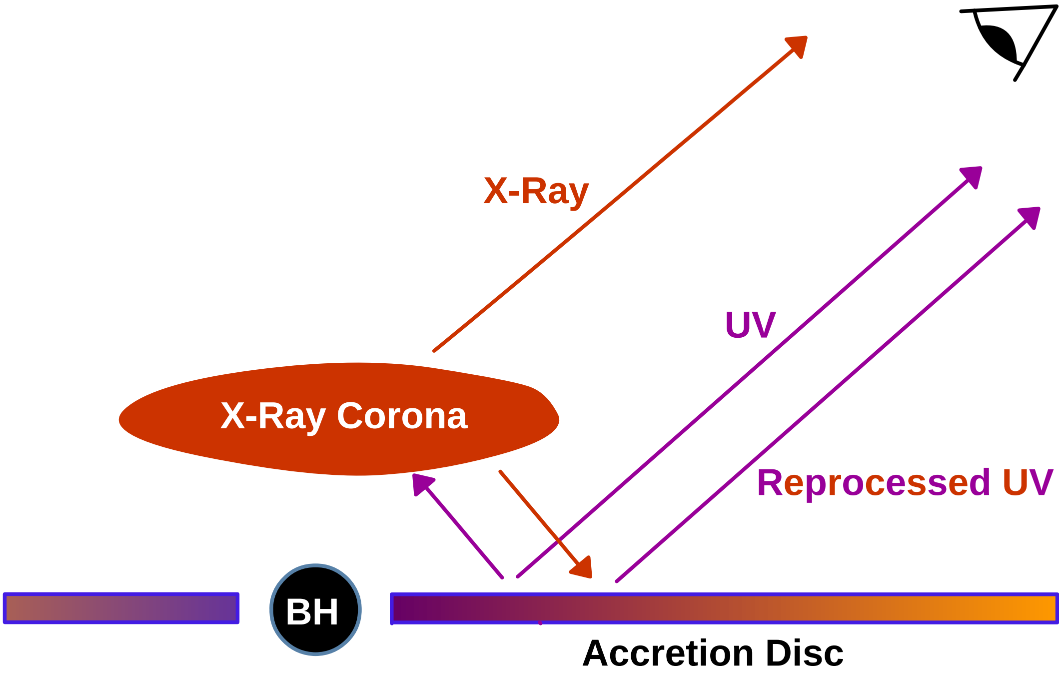

Figure 1.2: Diagram of the reprocessing of X-rays in the accretion disc vs. Comptonisation of UV in the X-ray corona as sources of variability in AGN.

where L_X is the total X-ray luminosity and A is the albedo of the disc. Using a height h and radius r in units of gravitational radii, $R_G = GM/c^2$, this is

$$E(r) = \frac{L_X(1-A)hc^4}{4\pi(GM)^2(h^2+r^2)^{3/2}} \tag{1.31}$$

This extra energy modifies the temperature profile of the disc, given by Eqn. 1.18, such that it has an extra term to include the X-ray irradiation

$$T(r) = \left(\frac{1}{\sigma_{SB}}\right)^{1/4}\left(\frac{3}{2\pi}\frac{m_p c^5 \dot{m}}{G\eta\sigma_T R^3}\left(1-\sqrt{\frac{R_0}{r}}\right)+\frac{L_X(1-A)hc^4}{4\pi(GM)^2(h^2+r^2)^{3/2}}\right)^{1/4} \tag{1.32}$$

1.4.1.2 X-Ray Emission through Comptonisation of Accretion Disc Seed Photons

As the X-ray emission from AGN is thought to be produced by Compton-upscattering of thermal seed photons which originate from the disc, it follows that variability in the UV emission will affect the supply of seed photons to the corona. This would lead to correlated variability between the X-ray emission and the UV emission, with the X-ray

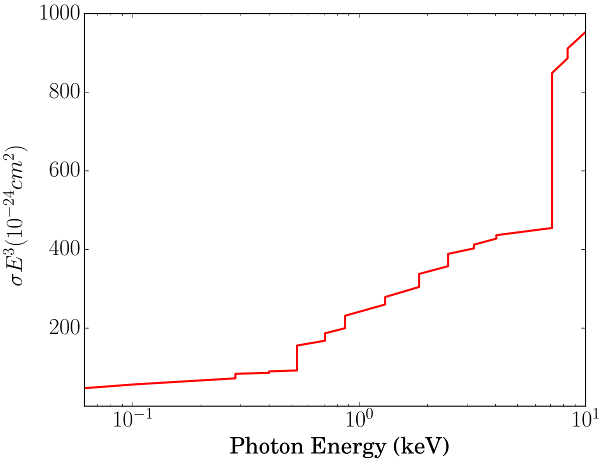

FIGURE 1.3: The photoelectric cross-section per hydrogen atom as a function of energy, assuming Solar abundance, multiplied by the energy cubed for clarity. Based on Fig. 1 from Morrison & McCammon (1983).

variability lagging the UV variability by the extra light travel time due to travelling via the corona, plus any scattering time. As well involving an X-ray lag instead of a UV lag, these lags would also be shorter than those due to reprocessing and not be wavelength-dependent.

1.4.2 X-Ray Absorption in AGN

The main form of absorption present in the X-ray spectra of AGN is photoelectric absorption, whereby an X-ray photon is absorbed by an atomic electron, transferring all of its energy to the electron and thereby ionising the atom. The degree of absorption depends on the photoelectric cross-section of an electron, $\sigma(E)$, and the column density, i.e. the number of atoms of different elements per unit area along the line of sight. The column density is normally expressed as the number of hydrogen atoms along the line of sight, n_H, and Solar abundance is assumed relative to this value in calculating the total absorption. In this case, the fraction of flux ($F(E)$) which is absorbed at a given photon energy is given by

$$F(E) = 1 - exp[-n_H \sigma(E)] \tag{1.33}$$

In this thesis, the photoelectric cross-section, $\sigma(E)$, used is that given in Morrison & McCammon (1983), using Solar abundances (see Fig. 1.3).

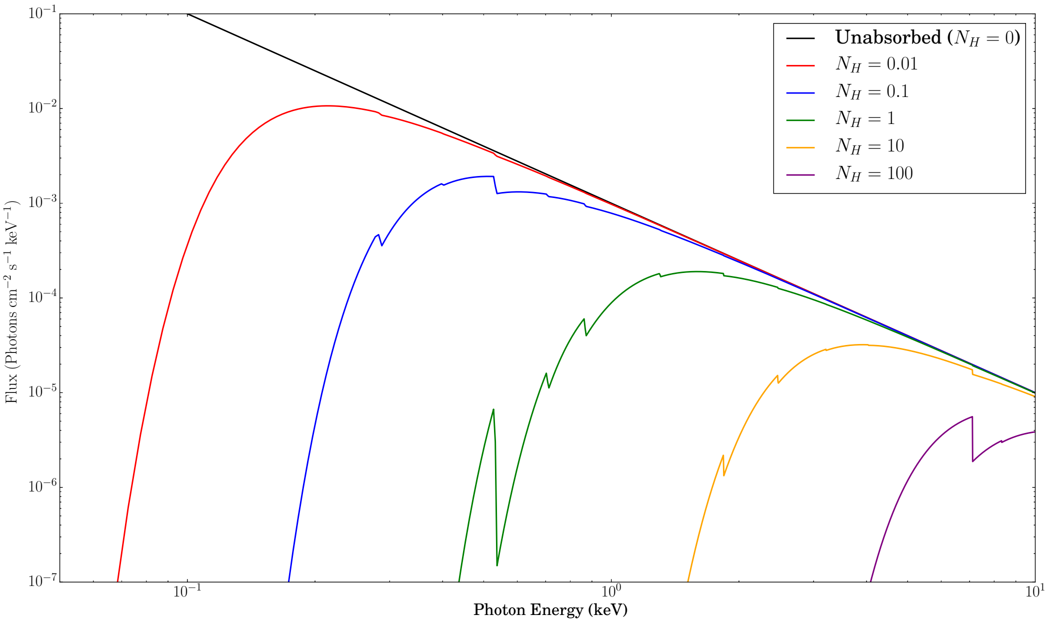

Figure 1.4: A power law with photoelectric absorption (colours) for five different values of the absorbing column (in 10^{22}cm^{-2}), and an unabsorbed power law (black).

The effect of photoelectric absorption is modified if the absorber is ionised. In this case, there are fewer electrons per ion with increasing ionisation state, and the remaining electrons are in lower orbits requiring more energy to escape from the ion. These effects combine to reduce the absorption cross-section of absorbing matter as the ionisation state increases; highly ionised material is therefore very poor at absorbing radiation. Fig. 1.5 shows the effect of different ionisation states on the photoelectric absorption of an X-ray power law. The ionisation state, η, of absorbing matter is here defined using the ratio of the number density of ions of a given ionisation state to that of the next ionisation state up, given by

$$\xi = \frac{L}{N_e R^2} \tag{1.34}$$

where

$$\frac{N(X^{i+1})}{N(X^i)} = \frac{1}{\alpha(X^{i+1})} \xi \int_{\nu_{min}}^{\nu_{max}} \frac{f_\nu}{4\pi h\nu} \sigma_\nu(X^i) d\nu \tag{1.35}$$

where $N(X^i)$ is the number density of the ith ionisation state of a given element X, N_e is the electron number density, Lf_ν is the luminosity in ergs s^{-1} Hz^{-1} at frequency ν, σ_ν is the photoelectric cross-section, α is the recombination rate of the reaction

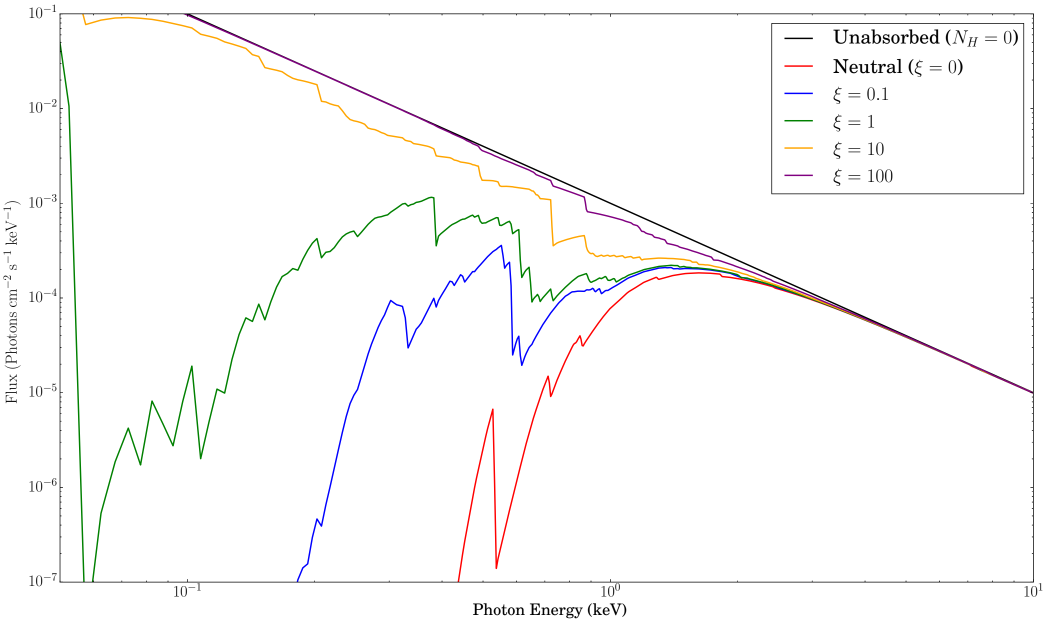

FIGURE 1.5: A power law with photoelectric absorption by an ionised absorber with an absorbing column of 10^{22} cm^{-2} (colours) for five different values of the ionisation parameter (see Equation 1.35), and an unabsorbed power law (black).

$X^i + \gamma \rightarrow X^{i+1} + e^-$, and R is the distance from the source of the ionising radiation to the ionised material (see Done et al., 1992). The relative abundances of each ionisation state are then described by this single parameter (combined with a chemical abundance parameter and a recombination rate based on the absorber temperature). Combined with the photoelectric cross-sections of each ion, in this case taken from Reilman & Manson (1979), this ionisation state can then be used with Eqn. 1.33 to calculate the total absorption from an ionised absorber.

As well as broad-band absorption, absorption lines are also seen in the spectra of AGN, at photon energies close the transition energies for electrons to change to a higher-energy orbit. The availability of specific absorption lines is dependent on the ionisation state of the absorbing material, as this determines the electron transitions available. The energy of these lines is Doppler-shifted by the velocity of the absorbing material, allowing measurement of in-flow and out-flow velocities. The same effect causes broadening of the lines due to both bulk motions, e.g. from the Keplerian velocity of orbiting absorbing material, and to thermal motions of individual particles, dependent on the temperature of the absorbing material. Depending on the ionisation state of the absorbing matter, line absorption can be very significant compared to photoelectric absorption, so it is important to include both effects when modelling an ionised absorber. Fig. 1.6 shows

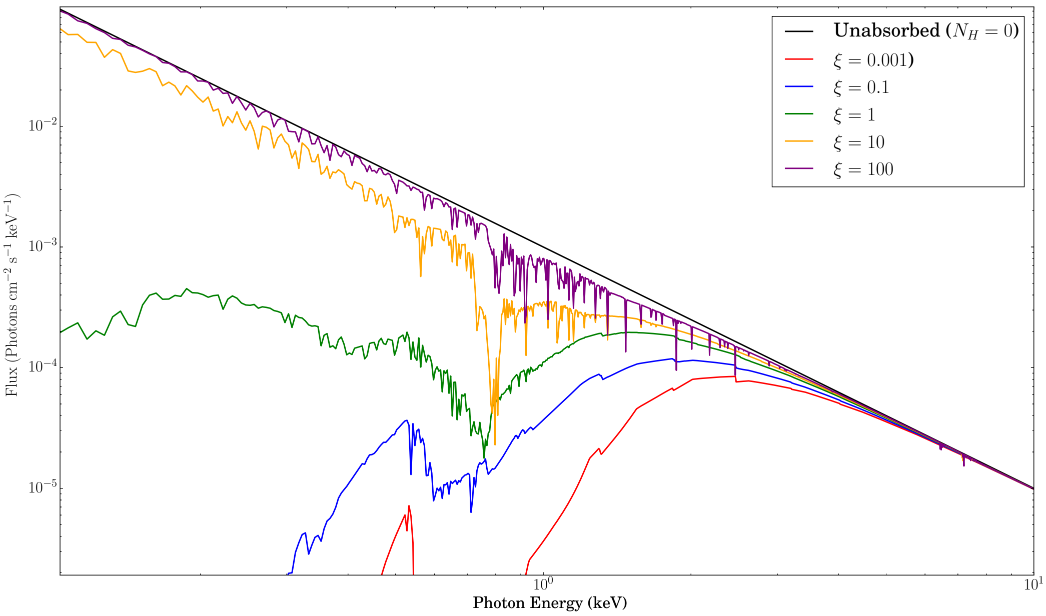

FIGURE 1.6: A power law with photoelectric and line absorption by an ionised absorber with an absorbing column of 10^{22} cm^{-2} (colours) for five different values of the ionisation parameter (see Equation 1.35), and an unabsorbed power law (black).

the combined effect of photoelectric and line absorption of a power law by material with different ionisation states.

Finally, in addition to absorption, if the column is very high ($n_H \gtrsim 10^{22}$ cm^{-2}), Compton scattering can cause emission to be scattered out of the line of sight. In this case, the fraction of emission scattered out of the line of sight is given by

$$F(E) = 1 - exp[-n_H \sigma_T] \tag{1.36}$$

where σ_T is the Thomson cross-section; Fig. 1.7 shows the effect of Compton scattering on X-ray emission for different columns.

1.4.2.1 Absorbing Components in the Unified Model of AGN

There are three principle components of the unified model of AGN thought to cause absorption which can be seen in their X-ray spectra: the surrounding torus, composed of cool gas and dust, ‘warm’ (low-ionisation state) gas in the BLR, and disc winds, which are thought to have a range of ionisation states and outflow velocities.

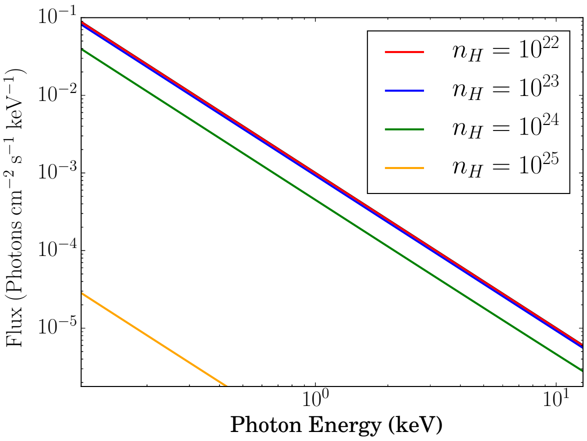

FIGURE 1.7: A power law with Compton scattering (colours) for five different columns (n_H), and an unscattered power law (black).

The torus, being thick and dense, causes both strong photoelectric absorption and Compton scattering, almost entirely blocking the soft X-ray band ($\lesssim$ 10keV) from lines of sight which pass through it. AGN for which this is the case are referred to as ‘Compton-thick’, as the absorbing column along the line of sight is large enough for Compton scattering to be significant (see e.g. Brightman et al., 2015, Risaliti et al., 1999).

Both the BLR and disc winds cause broad-band photoelectric absorption and line-absorption. The exact nature of neither of these components is not well-known. A range of outflow velocities have been observed, including observations of ‘ultra-fast outflows’ (UFOs) which can be $> 10,000$ kms^{-1}, which are highly-ionised (e.g. Fig. 1.8 Risaliti et al., 2005a), ‘non-ultra-fast outflows’ (non-UFOs) at 1000 kms^{-1} and intermediate ionisation states, and ‘warm absorbers’ (WAs) at $100 - 1000$ kms^{-1}, which have lower ionisation states. A study of measurements of absorbers in a sample of AGN by Tombesi et al. (2013) showed the ionisation state and absorbing column to be correlated with the outflow velocity (see Fig. 1.9), implying a structured wind combining WAs, UFOs and non-UFOs (Fig. 1.10). This structure may even continue outward to also encompass the BLR. In the AGN model proposed by Elvis (2000), based on the body of existing research on quasars, absorbing material arises from a narrow range of accretion disc radii in a biconical ‘wind’ the opening angle of which is dependent on the radiation pressure from the central engine.

On short timescales (days-months), variations in the observed absorbing column are seen in a significant fraction of AGN (Risaliti et al., 2002). This is largely attributed to ‘occultations’ by ‘clouds’ or clumps of gas in the BLR passing along the line of sight

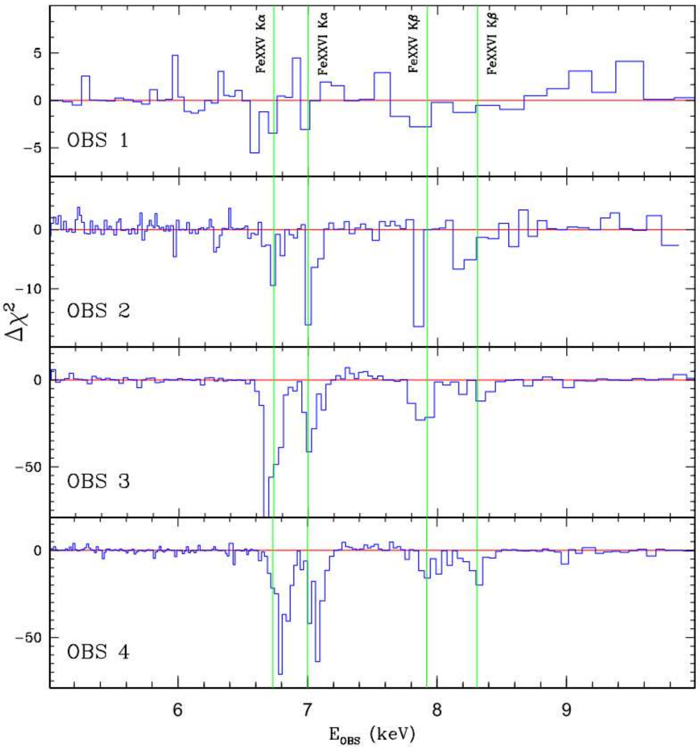

Figure 1.8: Contributions to χ^2 in the $5-10$keV range for four *XMM-Newton MOS* observations of the Seyfert AGN NGC 1365, from Risaliti et al. (2005a). The four vertical lines show the rest-frame energy of four absorption lines, Fe XXV Kα, Fe XXVI Kα, Fe XXV Kβ, and Fe XXVI Kβ. The spectra show these highly-ionised absorption lines to be shifted by several thousand kms^{-1}.

(e.g. Risaliti et al., 2007a). The existence of absorption variability from disc winds is not known, as it is not clear whether the wind is dynamic as a whole, or whether the outflows are relatively smooth or clumpy, though there is evidence from both hydrodynamic and radiative-transfer modelling that a clumpy wind is necessary to explain observations (e.g. Matthews et al., 2016, Proga et al., 2000). The torus is thought to be largely static, though there is some evidence for changes in the radius of the inner edge of the torus with increasing luminosity from IR observations on timescales of several years (e.g. Kishimoto et al., 2013).

1.4.2.2 Driving Disc Winds in AGN

Disc winds, i.e. material blown off the disc and escaping the system entirely, are seen in accreting systems of all types (cataclysmic variables, neutron stars, BHXRBs, AGN). They are thought to be driven by a variety of mechanisms dependent on the characteristics of the system, all of which may be present in different AGN.

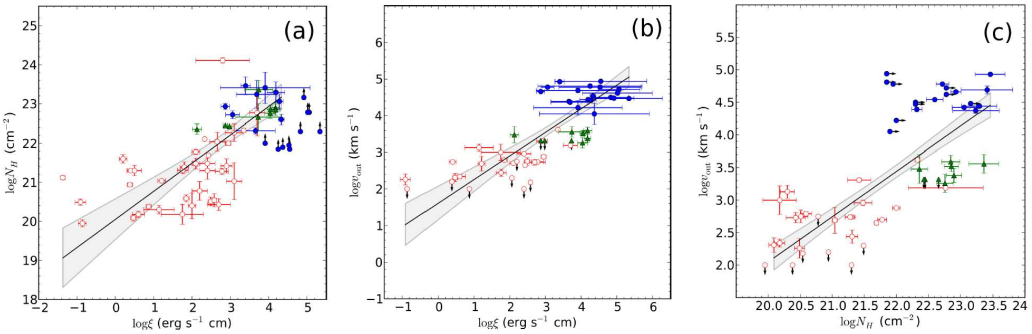

FIGURE 1.9: A comparisons of three of the parameters of X-ray absorbers (absorbing column, n_H, ionisation state, ξ, and outflow velocity, v_{out}) from Tombesi et al. (2013), showing strong correlations in each case. WAs are shown in red, non-UFOs in green and UFOs in blue. Arrows indicate lower or upper limits. solid lines represent the best-fit linear correlations and the gray areas show the 2σ confidence range of the fits.

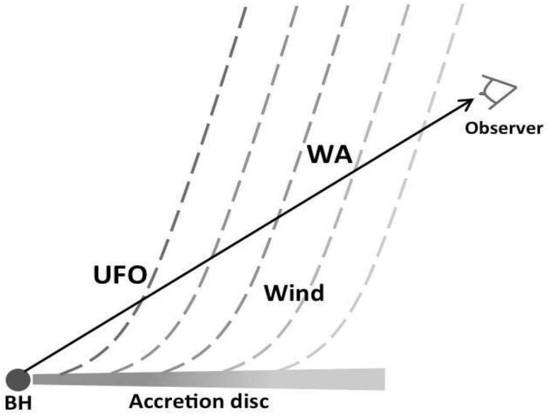

FIGURE 1.10: Diagram of a possible structure for outflows in AGN, with decreasing ionisation and outflow velocity for increasing radii, from Tombesi et al. (2013).

If the disc reaches very high temperatures ($> 10^5$ K), for example through strong irradiation, this can lead to thermal driving of a wind. In this case, the thermal velocity of the wind can exceed the local escape velocity. As the escape velocity decreases with increasing radius, thermal driving is more effective at larger radii and is likely to be responsible for driving low-velocity X-ray-absorbing outflows in AGN (i.e. WAs) (e.g. Chelouche & Netzer, 2005).

Radiation pressure can also drive winds, dependent on the ionisation state of the outflowing gas. If the gas is fully ionised, radiation pressure is due only to scattering of photons off electrons, meaning a wind can only be driven at very high luminosities ($\mathrm{L} > \mathrm{L}_{\mathrm{Edd}}$). If the gas is only partially ionised, however, there is an additional force due to the absorption of photons via photoionisation and electron transitions. This additional force is known as ‘line-driving’ and can be a very significant effect as long as the ionisation state of the gas is low enough to allow the UV continuum from the accretion disc to interact via the UV line transitions, as there are a large number of transitions in this energy range (Castor et al., 1975). A wind driven by this mechanism would be launched at radii at which the radiation is mostly in the UV band, and could therefore be responsible for driving winds in AGN, as long as the ionisation state of the outflowing matter is not too high.

Finally, magnetic effects are also likely to play a role in driving outflows in AGN. If the magnetic field of the accretion disc is strong and ordered, and the poloidal component of the field is at an angle of $< 60°$ with respect the plane of the disc, a 'magneto-centrifugal' wind can be driven, in which the material is accelerated by the centrifugal force (e.g. Cannizzo & Pudritz, 1988). As this mechanism does not require radiation pressure, it may be important in both low-luminosity systems and in systems in which the gas is very highly-ionised, both of which can apply to AGN. For an overview of disc wind driving mechanisms in AGN, see Proga (2007).

1.5 AGN as an Analogie of BHXRB Spectral States

Black holes are thought to behave in the same way, physically, regardless of their size, as their lack of a surface allows them to be defined purely by their mass, spin and charge, the last of which is thought to be negligible in Astronomical black holes. For this reason, it is hypothesised that the accretion physics of black holes of all scales should be universal, meaning AGN should behave in essentially the same way to BHXRBs, but on significantly longer timescales. Testing this hypothesis is essential to reinforcing our understanding of the nature of black holes in general.

BHXRBs go through a number of different X-ray spectral states on timescales of years to decades, thought to be linked to the mode of accretion occurring. The most common of these states are the so-called 'low-hard' state and 'high-soft' state, characterised by the hardness and luminosity of the X-ray spectrum. As with AGN, the main components of the spectrum of a BHXRB are an X-ray power law, due to Comptonised emission from a corona, and a blackbody component which, in the case of BHXRBs, is at a high enough temperature to make a significant contribution of the soft end of the X-ray spectrum. The spectral states of BHXRBs are determined by the relative dominance of these components and the overall luminosity of the system.

In the low-hard state, the X-ray spectrum is dominated by the power law component, whose spectral index is low. This is thought to be due to a low accretion rate leading to truncation of the inner edge of the accretion disc, reducing the contribution of the thermal component and the seed photon flux to the corona, which in turn leads to a harder power law. Within the truncation radius, the disc is thought to be replaced by a hot accretion flow, i.e. an ADAF. This state is also associated with jet launching.

The high-soft state is thought to occur at higher accretion rates ($\gtrsim 1\%\dot{M}_{Edd}$) and is characterised by a much stronger blackbody component and a softer power law, thought to be due to the accretion disc extending closer to the black hole and increasing in temperature, increasing the energy and luminosity of the thermal emission and increasing the seed flux to the corona, which cools the electron population of the corona and softens the power law emission. When BHXRBs transition from the hard state to the soft state, jets are observed to be quenched immediately, until the system returns to the hard state.

As the timescales on which AGN evolve will be orders of magnitude longer, and significantly greater than the human lifetime, they are unlikely to be observed changing state. A given type of AGN is therefore associated with a single state equivalent to those of a BHXRB. High-luminosity AGN, i.e. quasars and blazars, are thought to be equivalent to a BHXRB in the soft state, whilst the low-luminosity AGN (LLAGN) observed in the local universe, i.e. Seyferts and LINERs, are thought to be equivalent to the hard state.

1.6 Thesis Summary

This thesis is composed of three separate but, closely linked, studies of the X-ray and UV/optical variability of nearby AGN, all of which have the aim of revealing more about the geometry of the material close to the central black hole, and physics of the origin and variability of the radiation they emit or absorb.

In Chapter 2 of this thesis, I will discuss a study of the variability of the intrinsic X-ray spectra of a sample of AGN drawn from the Palomar sample of nearby galaxies, particularly in relation to the variability of the photon index in relation to the luminosity of the system. In Chapter 3, I will discuss a study of the X-ray spectral variability of three Seyfert galaxies known to possess variable absorption and the implications of the results on the nature of the absorbers found in the vicinity of the black hole. In Chapter 4, I will discuss a study on the reprocessing of X-rays into UV/optical emission due to X-ray illumination in the disc of the Seyfert galaxy NGC 4395. The results of an XMM-Newton and ground-based optical campaign will be compared to the results of a physical model of accretion in this system and the results discussed. Finally, in Chapter 5, I will summarise the results of this thesis, and discuss the implications of the combined results on our understanding of the geometry of the components of AGN, and the possibilities for future work which will allow these findings to be built upon.

Chapter 2

Intrinsic X-Ray Spectral Variability in AGN

"This was no fruit of such worlds and suns as shine
on the telescopes and photographic plates of our observatories.
This was no breath from the skies whose motions and dimensions
our Astronomers measure or deem too vast to measure.
It was just a colour out of space"
H P Lovecraft, *The Colour out of Space*

2.1 Introduction

The main component of the intrinsic X-ray spectrum of both AGN and BHXRBs is the power law component thought to originate from the Comptonisation of UV/optical photons from the accretion disc by a corona of hot electrons, whose steepness is defined by the photon index Γ (see section 1.3.2).

This photon index has been found to vary over time in both AGN and BHXRBs. In many studies of black holes with relatively high accretion rates, including both single-epoch observations of samples of objects and multi-epoch observations of individual objects, the X-ray spectrum becomes softer as the luminosity increases (see section 1.3.4). This 'softer-when-brighter' behaviour is seen in both BHXRBs (e.g. Gu & Cao, 2009) and in

AGN (e.g. McHardy et al., 1998, Shemmer et al., 2006, Sobolewska & Papadakis, 2009). This behaviour is usually attributed to a real increase in the photon index, Γ.

The increase in Γ in these systems is attributed to an increase in seed photons cooling the X-ray corona, thereby softening the spectrum. This increase in seed photons is thought to be due to an increased accretion rate in the accretion disc close to the black hole, leading to higher temperatures and increased UV/optical emission from this region. As the number of X-ray photons emitted is directly equivalent to the number of seed photons, this also leads to an increase in X-ray brightness, and the observed softer-when-brighter correlation (e.g. Beloborodov, 1999a, Coppi, 1999, Zdziarski et al., 1999). The X-ray spectra of AGN have been observed to respond to UV/optical variations in exactly the way one would expect for Comptonisation (e.g. Nandra & Papadakis, 2001) and correlations between X-ray and UV variability have been seen in many AGN (Arévalo et al., 2009, Breedt et al., 2009, Edelson et al., 1996, McHardy et al., 2014, Uttley et al., 2003, see Chapter 4, e.g.)). Other possible explanations for softer-when-brighter behaviour include a constant soft component, due to e.g. reflection in combination with a variable power law component with constant spectral index (e.g. Ponti et al., 2006, Taylor et al., 2003) and complex absorption variability with a constant power law component (e.g. Turner & Miller, 2009). Whilst intrinsic variability of the X-ray slope due to Comptonisation appears to be the main cause of softer-when-brighter behaviour in many AGN, these possibilities must also be considered.

This 'softer-when-brighter' correlation has not been found to hold for lower accretion rate systems. In a sample of single-epoch observations of low-luminosity AGN (LLAGN, i.e. LINERs and low-luminosity Seyferts), Gu & Cao (2009) found Γ to be *anticorrelated* with the accretion rate, i.e. '*harder*-when-brighter'. A similar conclusion was reached by both Younes et al. (2011) and Hernández-García et al. (2014) in samples of LINERs. Harder-when-brighter behaviour has also been observed in multi-epoch data of individual BHXRBs by e.g. Kalemci et al. (2004) and Yuan et al. (2007). This behaviour has, however, only been observed once in multi-epoch observations of in an individual AGN, the LLAGN NGC 7213, by Emmanoulopoulos et al. (2012), and was once again thought to be caused by an anticorrelation between Γ and the accretion rate.

In the case of harder-when-brighter behaviour, the seed photons for Comptonisation are likely to originate from synchrotron or cyclo-synchrotron emission from the X-ray emitting corona itself, or from a hot inner flow/advection dominated accretion flow (ADAF) within a truncated disc. In ADAF models, an increase in the accretion rate as a fraction of the Eddington rate ($\dot{m}_{\rm Edd}$) leads to an increasing optical depth and hence to a higher Compton parameter in the hot accretion flow, 'hardening' the X-ray spectrum and producing an anticorrelation between Γ and $\dot{m}_{\rm Edd}$, and therefore harder-when-brighter behaviour (Narayan, 2005, Sobolewska et al., 2011).

The harder-when-brighter spectral relationship is also commonly observed in blazars (e.g. Gliozzi et al., 2006, Krawczynski et al., 2004, Zhang et al., 2006), due to the fact that synchrotron self-Compton emission dominates blazar jet emission, with luminosity-increases associated with an injection of hard-spectrum electrons, e.g. from a shock (e.g. Ghisellini et al., 2009). There is no evidence yet for highly relativistic outflows in LLAGN, such as are seen in blazars, but weak jets are detected (e.g Martí-Vidal et al., 2011) and models for such jets (e.g. Markoff et al., 2008) can explain the observed X-ray spectral variability (Emmanoulopoulos et al., 2012).

Further possible explanations for harder-when-brighter behaviour which do not require a jet or a truncated disc also exist, for example by invoking a outflowing hot thermal corona - for details see Sobolewska et al. (2011) and references therein.

At extremely low accretion rate ($<\sim 10^{-6}$ $\dot{m}_{\rm Edd}$), the behaviour has been found to change once again, with the spectral hardness no longer changing, thought to be due to Γ saturating at a relatively constant, and high, level as the accretion rate decreases (Yang et al., 2015). This change is once again observed in observations of both AGN and BHXRBs, using a small number of observations from large samples of sources (Gu & Cao, 2009, Yang et al., 2015).

In a study of a sample of BHXRBs by Wu & Gu (2008), harder-when-brighter behaviour was observed below a 'critical' accretion rate ($\dot{m}_{\rm crit}$) of ~ 0.01 in units of Eddington rate ($\dot{m}_{\rm Edd}$), above which softer-when-brighter behaviour was seen. The same change in behaviour above a certain critical accretion rate has also been seen into multi-epoch observations of the XRB Cyg X-1 (Axelsson et al., 2008, Skipper et al., 2013). Single-epoch observations of large samples of AGN have shown that they follow the same change in behaviour (Constantin et al., 2009, Gu & Cao, 2009, Younes et al., 2011), supporting the idea that AGN behave in a similar way to BHXRBs. Note that the change from harder-when-brighter to softer-when-brighter at $\dot{m}_{\rm crit}$ occurs within the hard state and is not considered to be a state transition. The accretion rate below which BHXRBs are never seen in the soft state (Maccarone et al., 2003, 2% $\dot{m}_{\rm Edd}$) occurs factors of 2-3 above $\dot{m}_{\rm crit}$.

The change in the relationship between the Γ and $\dot{m}_{\rm Edd}$ in these systems at a particular critical $\dot{m}_{\rm Edd}$ from a negative correlation to a positive correlation as $\dot{m}_{\rm Edd}$ increases implies that the seed photon source to the X-ray corona is changing (e.g. Emmanoulopoulos et al., 2012, Skipper et al., 2013). It has been suggested that the reason for this change may be that the accretion disc is transitioning from an ADAF to a standard thin disc as $\dot{m}_{\rm Edd}$ increases (Constantin et al., 2009, Esin et al., 1997, Narayan, 1994, Wu & Gu, 2008).

The 'hard state', with which ADAFs are associated in BHXRBs, is usually also associated with the presence of a jet (Russell et al., 2010). The X-ray emission mechanism in BHXRBs is not known unambiguously, but self-Comptonisation of synchrotron emission from the corona, or possibly from a jet at higher energies, is a possibility.

As described in Section 1.5, LINERs and Seyferts are thought to be analogues of hard state BHXRBs, meaning we expect to see both harder-when-brighter and softer-when-brighter behaviour individually in these systems, with a transition at a similar Eddington fraction. Finding further evidence of harder-when-brighter behaviour in individual LLAGN in addition to NGC 7213 is therefore significant in confirming the validity of the hypothesis that AGN are analogues of BHXRBs.

In this chapter, I present results on changes in hardness with luminosity of a sample of 24 AGN from the Palomar sample (Ho et al., 1997a) which have been observed by *Swift*. For those sources for which there is enough data for spectral analysis, spectral fitting is performed with a variety of models, and changes in Γ with luminosity are measured, in order to confirm whether hardness changes are as a result of of photon index changes or are due to other factors.

2.2 Observations & Data Reduction

2.2.1 The AGN Sample

The sample used in this study consists of all known AGN in the Palomar sample of galaxies for which there is sufficient data for meaningful analysis. The Palomar sample contains 163 such objects (Seyfert galaxies and LINERs), 70 of which have been observed by *Swift*. So that sufficient data exist for at least a rudimentary spectral analysis, only objects for which there are a total of > 350 total photon counts and 4 or more separate observations were included in the analysis, leaving a final sample of 24 AGN. Table 2.1 gives a summary of the *Swift* observations of each of the selected AGN. The Palomar sample contains almost every galaxy in the northern sky with a magnitude of $\mathrm{B_T} > 12.5$; the AGN within this sample are therefore all relatively nearby and a large fraction of them are low-luminosity - 85% lie below $\mathrm{L(H\alpha)} = 10^{40}$ergs $\mathrm{s^{-1}}$ (Ho et al., 1997a,b). As my sample contains only a relatively small subset of the Palomar AGN sample it is not statistically complete. However, whilst some galaxies were observed because they contained known AGN, others were observed for different reasons, e.g. because they contained a supernova, thus the subset is not particularly biased.

Object	Observations	GTIs	Start & end date	Total exposure (s)	Total counts	No. summer spectra
NGC 315	5	42	2007-05-31 - 2009-03-03	26054	644	1
NGC 1052	21	126	2007-01-19 - 2011-03-06	81041	3043	3
NGC 1068 (M77)	13	44	2007-06-19 - 2015-02-05	32681	15819	5
NGC 2655	33	120	2011-01-11 - 2014-12-31	60351	1056	1
NGC 3031 (M81)	605	1033	2005-04-21 - 2014-06-22	771530	205159	28
NGC 3147	28	63	2009-01-11 - 2014-07-13	52929	2417	3
NGC 3226	26	63	2008-10-28 - 2015-07-06	52841	699	1
NGC 3227	26	63	2008-10-28 - 2015-05-23	19269	38816	10
NGC 3628	6	32	2006-11-12 - 2014-07-21	26518	379	1
NGC 3998	2	20	2007-04-20 - 2007-04-29	27285	6362	4
NGC 3998†	376	376	2010-12-31 - 2011-12-26	287568	7628314	25
NGC 4051	55	100	2009-02-14 - 2013-10-10	58002	30821	10
NGC 4151	5	33	2005-12-26 - 2012-11-12	27387	17808	7
NGC 4258 (M106)	12	8	2008-03-01 - 2014-06-22	32238	1270	1
NGC 4321 (M100)	26	88	2005-11-06 - 2011-04-15	27426	282	1
NGC 4388	4	34	2005-12-27 - 2008-05-09	10594	1219	4
NGC 4395	225	412	2005-12-31 - 2013-05-10	302125	34277	22
NGC 4486 (M87)	19	46	2006-12-23 - 2015-05-18	29601	4264	4
NGC 4472 (M49)	6	19	2007-11-13 - 2010-03-30	14298	1268	1
NGC 4579 (M58)	27	41	2007-05-15 - 2007-05-18	20463	3555	3
NGC 4736 (M94)	18	39	2013-04-15 - 2015-05-12	23700	104	1
NGC 5194 (M51)	112	261	2005-06-30 - 2014-09-24	233095	5599	1
NGC 5548	656	878	2005-04-08 - 2014-06-21	574670	206387	42
NGC 5806	49	147	2012-01-14 - 2014-09-17	141994	381	1
NGC 7331	34	90	2007-02-12 - 2015-05-19	77403	616	1

TABLE 2.1: Details of the observations of the 24 AGN considered in this study. All data are from *Swift* except for the observations of NGC 3998 denoted by †, from *RXTE*. The number of summed spectra is also given, denoting the number of flux bins into which the observations for each source were divided. Where the number is one, all the observations for that source were summed into a single spectrum (i.e. not flux-binned).

The data for all Palomar AGN except NGC 3998 were obtained by *Swift* and, in almost all cases, are composed of observations from a number of different programmes covering a number of years. The data for NGC 3998 are from a single campaign by the *Rossi X-ray Timing Explorer* (*RXTE*), a preliminary analysis of which is described in Skipper (2013); whilst there are some *Swift* data available for NGC 3998, the *RXTE* data are of better quality.

In all *Swift* pointings, the observations were performed using the *Swift* XRT in 'photon counting mode'. Exposure times of individual good time interval (GTI) observations ranged from less than 10 seconds to over 10^4 seconds. In each case, GTIs were excluded if they had a low signal-to-noise ratio (S/N < 3), very short exposure time ($T_{\rm exp} < 50$ s) or the source was in close proximity to bad pixels. The raw data for all *Swift XRT* observations were downloaded from the HEASARC archive[1].

In addition to the data from this work, I also include data from NGC 7213 (Emmanoulopoulos et al., 2012) in the discussion, to allow comparison with what was, until now, the only confirmed detection of harder-when-brighter behaviour in an individual AGN. NGC 7213 is not part of the Palomar sample, and has not been observed extensively by *Swift*. However, it has been observed extensively (882 times) by *RXTE* and is known to possess a relatively simple power law spectrum (Emmanoulopoulos et al., 2013). I therefore do not include NGC 7213 within my discussion of *Swift* spectral fitting (Section 2.5) or of the properties of the Palomar sample, but take the results of the *RXTE* spectral fitting from Emmanoulopoulos et al. (2012).

2.2.2 Data Reduction

The XRT data were reduced using my automatic pipeline, described in e.g Cameron et al. (2012), Connolly et al. (2014). The most recent version of the standard *Swift* XRTPIPELINE software (versions 0.12.4 - 0.12.6) was used in each case. Spectra and light curves were extracted using the XSELECT tool, using flux-dependent source and background extraction regions chosen such that background contamination at faint fluxes was minimised, and to account for the effects of pile-up at high fluxes. The effects of vignetting and the presence of bad pixels and columns on the CCD were removed by using the *Swift* XRTEXPOMAP and XRTMKARF tools to create an exposure map and

---

[1] http://heasarc.gsfc.nasa.gov/cgi-bin/W3Browse/swift.pl

an ancillary response file (ARF) for each visit. The relevant redistribution matrix file (RMF) from the *Swift* calibration database was also used in each case. The local X-ray background was estimated and subtracted from the instrumental count rates, using the area-scaled count rate measured in a background annulus region. The observed XRT count rates were corrected to take into account the fraction of counts lost due to bad pixels and columns, vignetting effects, and the finite extraction aperture (including regions excised in order to mitigate pileup effects).

RXTE observed NGC 3998 376 times under my own proposal 96398, from 2010 Dec 31 until 2011 Dec 26, and with exposure times of between 542 seconds and 6,770 seconds. The earlier observations were each separated by a period of roughly two days, but after approximately 2011 Oct 25 the frequency of observations increased to roughly once every six hours. All the data reduction was performed only upon the standard-2 data, with a time-resolution of 16 s.

For each observation a GTI was generated based upon the spacecraft elevation angle being greater than 10 degrees, the pointing offset being less than 0.02 degrees, and the time since the last south Atlantic anomaly (SAA) being at least 30 minutes. Synthetic background data were generated using the script RUNPCABACKEST with the faint background model (pca_bkgd_cmfaintl7_eMv20051128.mdl), and suitable response files were created using PCARSP.

Spectra were extracted from the standard-2 data and the background data for all layers of PCU 2 using SAEXTRACT, and subsequently rebinned using RBNPHA into 14 channels. All the analysis described in this chapter uses channels 2-13, which roughly corresponds to the energy range

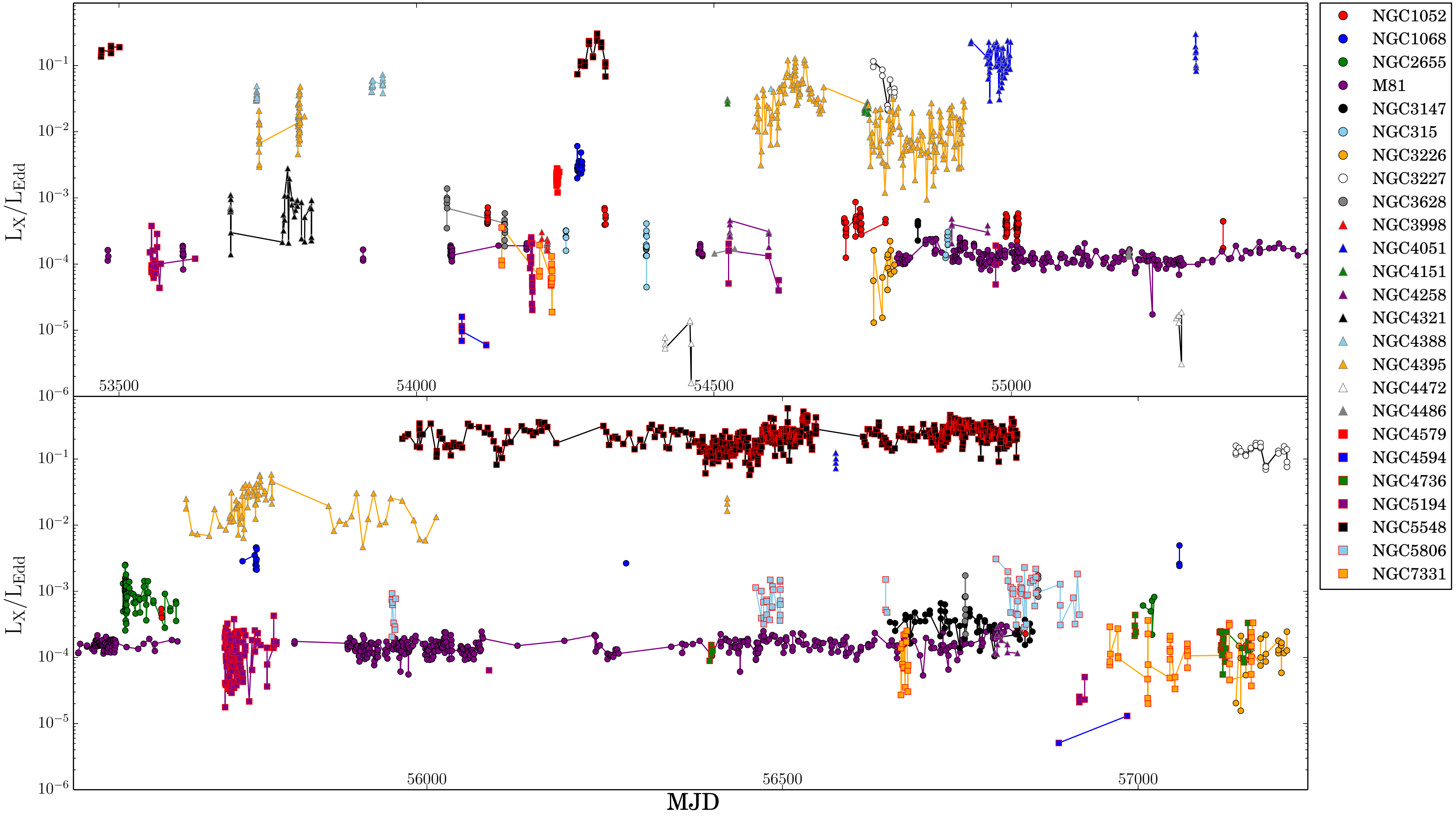

FIGURE 2.1: Light curve showing the ratio of the X-ray Luminosity to the Eddington Luminosity of each of the sources over time, showing the large range of Eddington rates present in the sample. The light curve is split into two sections for clarity.

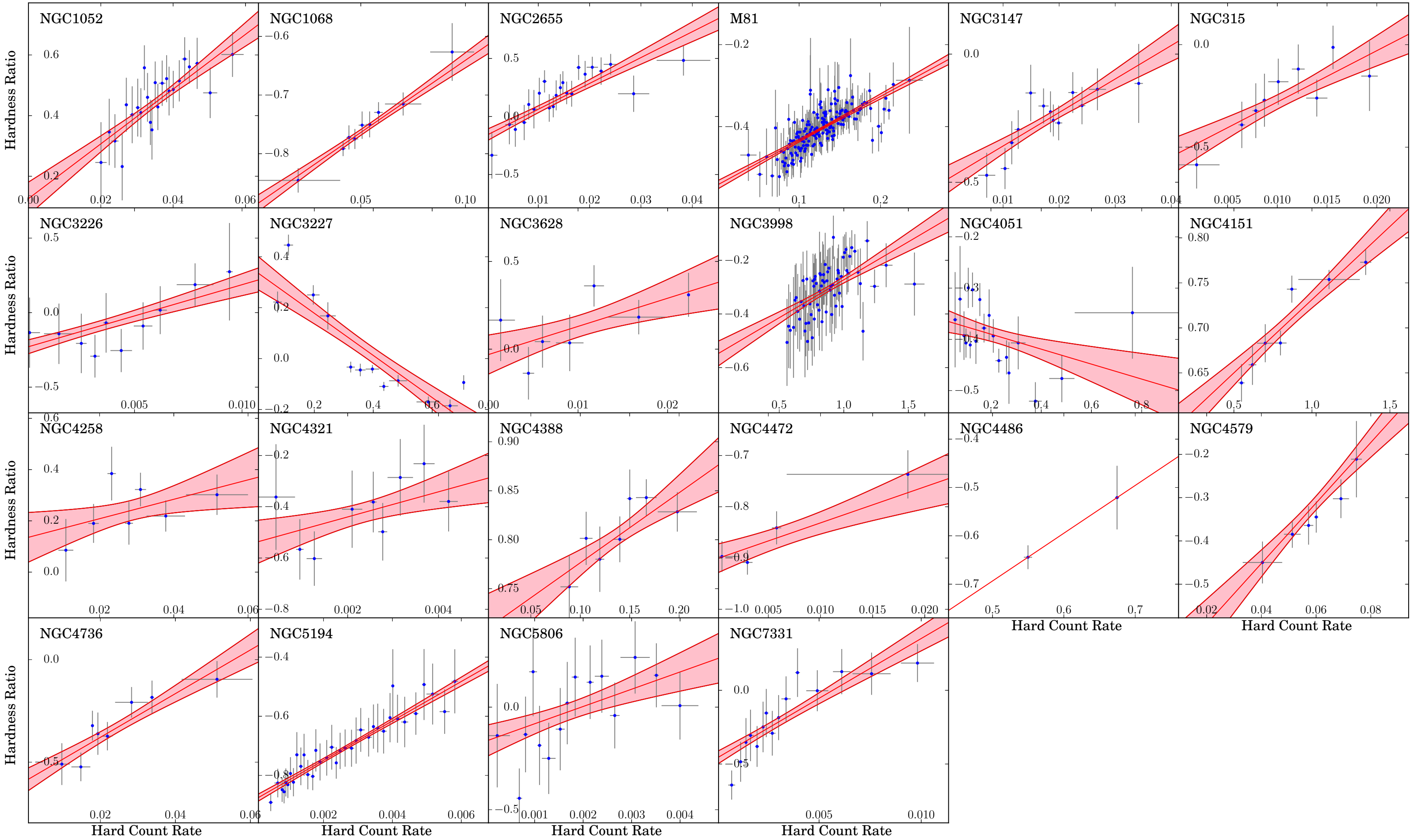

FIGURE 2.2: The hardness ratio of the spectrum of each *Swift* object using the 0.5-2 and 2-10 keV bands, plotted against its 2-10 keV count rate, and the hardness ratio of NGC 3998 using the 3.3-7 and 7-20 keV bands, plotted against its 7-20 keV count rate. The data are binned into bins of 10 data points. Error bars show the one-sigma confidence levels. In each case, the red line shows the best-fitting linear model and the pink region bounded by red indicates the one-sigma error region of the model parameters. A clear correlation between the two parameters, either positive or negative, is present in all objects except NGC 4321 and NGC 4468. NGC 4486 possessed too little data for meaningful binning with more than ten bins, so errors are not given.

3.3 to 20 keV. The observations covered a large range of exposure times, with many being too short for useful spectral analysis. In many cases, time-binning would not have produced spectra of sufficient quality for meaningful spectral analysis without using broad time bins, which would itself have lead to spectra consisting of data taken across a large range of fluxes. Whilst there is some scatter in the hardness of a given source at a given flux, the scatter is not large (see Section 2.3), indicating that spectral shape is a function mainly of luminosity rather than of time. Thus, flux-binning is legitimate. To improve the S/N, the data were therefore binned in flux.

Where there were sufficient data, the *Swift* spectra were binned such that each resultant summed spectrum had a minimum of 1000 total counts and a maximum width in count rate of 5×10^{-3}counts s^{-1}, with the exception of NGC 1052, NGC 3147 and NGC4579 which, due to fewer data, were binned with a minimum of 900, 600 and 900 total counts per spectrum, respectively. For objects for which there were insufficient data to obtain at least 3 flux-binned spectra with a minimum of 350 total counts, a total summed spectrum was produced. The *RXTE* spectra, having a considerably higher count rate but lower signal-to-noise ratio, were binned such that each resultant summed spectrum had a minimum of 8000 total counts per spectrum. The number of summed spectra produced for each source is shown in Table 2.1.

The spectra were combined using the *HEADAS* tool ‘addspec’. As the amount of data varied between sources, the number of spectra produced in each case also varied. The energy channels of each of the summed spectra were then grouped, using the *HEADAS* tool ‘grppha’, such that each group contained a minimum of 15 counts.

The light curves of the ratio of the X-ray luminosity to the Eddington luminosity of each of the 24 AGN are shown in Fig. 2.1.

2.3 Spectral Hardness

Plots of the hardness ratio against the hard count rate of each object are shown in Figs. 2.3 and 2.2. These plots show, in a model-independent way, the way in which the spectrum of a given source is changing with increasing luminosity; if the spectral hardness increases with increasing luminosity, the source is harder-when-brighter, if the opposite is true the source is softer-when-brighter. For the objects observed by *Swift*, hard emission is defined as $2.0 - 10.0$ keV and soft emission as $0.5 - 2.0$ keV; for NGC 3998 (observed by *RXTE*), hard emission is defined as $7.0 - 20.0$ keV and soft emission as $3.3 - 7.0$ keV (see Section 1.3.4.

For 22 of the 24 AGN, the hardness ratio changed with luminosity in an approximately linear way. The hardness ratios vs. luminosity of these objects were fitted with a linear model in order to determine numerically whether they were harder- or softer-when-brighter. In each case, errors on the best-fitting parameters of the linear fits were calculated using 10000 Monte Carlo simulations in which the data were randomly varied within their error distributions (assuming Gaussian errors) and refitted. The standard deviations of the resulting distributions of parameters were then taken as the one-sigma errors on these parameters. As the two parameters (gradient and intercept) are strongly dependent, the error regions delineated by the combined one-sigma errors of the parameters are parabolic.

The reduced χ^2 ($\chi^2_R = \chi^2/DoF$) and best-fitting parameters from these fits are shown in Table 2.2; the best-fitting lines and the error regions are also shown in the hardness ratio vs. luminosity plots in Fig. 2.2.

NGC 4395 and NGC 5548 showed more complex variations in hardness ratio with increasing luminosity and were not well fit by a linear model. Both objects show evidence of being very soft at low luminosity and hardening rapidly with increasing luminosity, then changing to becoming softer-when-brighter at higher luminosity (see Fig. 2.3). This behaviour is also very similar to that observed in the Seyfert galaxies NGC 1365 and Mkn 335 (see Chapter 3, Connolly (2015a), Connolly et al. (2014)).

The linear fits to the hardness ratio vs. count rate data showed that 18 of the AGN possess harder-when-brighter behaviour. In addition to NGC 4395 and NGC 5548, two other sources showed softer-when-brighter behaviour. Two of the sources (NGC 4486 and NGC 4321) could not be constrained as being either harder- or softer-when-brighter, as errors in the gradients of the linear fits to their hardness ratio vs. count rate data do not constrain the gradients to be positive or negative. A high fraction (72%) of the sample therefore show harder-when-brighter behaviour.

Object	χ^2/DoF	Gradient	Intercept	Behaviour when brighter
NGC 315	0.70	$26.26^{+11.76}_{-9.39}$	$-0.53^{+0.11}_{-0.11}$	harder
NGC 1052	0.54	$8.95^{+2.33}_{-1.90}$	$0.14^{+0.07}_{-0.10}$	harder
NGC 1068	0.40	$2.44^{+0.96}_{-0.56}$	$-0.88^{+0.03}_{-0.06}$	harder
NGC 2655	1.04	$21.82^{+4.45}_{-4.67}$	$-0.15^{+0.07}_{-0.07}$	harder
NGC 3031	0.80	$1.10^{+0.13}_{-0.10}$	$-0.54^{+0.01}_{-0.01}$	harder
NGC 3147	0.54	$13.11^{+3.21}_{-3.56}$	$-0.49^{+0.07}_{-0.06}$	harder
NGC 3226	0.49	$40.52^{+17.39}_{-14.40}$	$-0.24^{+0.08}_{-0.07}$	harder
NGC 3227	13.44	$-0.83^{+0.06}_{-0.05}$	$0.34^{+0.03}_{-0.03}$	softer
NGC 3628	1.11	$14.32^{+9.07}_{-7.97}$	$-0.01^{+0.13}_{-0.14}$	harder
NGC 3998†	2.43	$1.74^{+1.50}_{-0.67}$	$-0.53^{+0.07}_{-0.11}$	harder
NGC 4051	2.22	$-0.19^{+0.16}_{-0.18}$	$-0.34^{+0.04}_{-0.05}$	softer
NGC 4151	1.64	$0.16^{+0.03}_{-0.03}$	$0.57^{+0.02}_{-0.02}$	harder
NGC 4258	1.13	$3.69^{+3.70}_{-2.67}$	$0.12^{+0.11}_{-0.10}$	harder
NGC 4321	2.69	$25.69^{+30.60}_{-25.80}$	$-0.46^{+0.05}_{-0.05}$	undetermined
NGC 4388	0.76	$0.73^{+0.27}_{-0.27}$	$0.71^{+0.03}_{-0.04}$	harder
NGC 4395	14.27	$-1.75^{+0.18}_{-0.17}$	$0.40^{+0.02}_{-0.02}$	softer
NGC 4472	1.78	$7.81^{+7.95}_{-5.17}$	$-0.91^{+0.05}_{-0.05}$	harder
NGC 4486	0.68	0.04	−0.68	undetermined
NGC 4579	0.19	$6.38^{+3.12}_{-2.05}$	$-0.71^{+0.12}_{-0.18}$	harder
NGC 4736	0.80	$10.39^{+4.99}_{-2.88}$	$-0.57^{+0.08}_{-0.11}$	harder
NGC 5194	1.28	$35.59^{+11.66}_{-9.96}$	$-0.80^{+0.04}_{-0.03}$	harder
NGC 5548	5.03	$-0.32^{+0.03}_{-0.02}$	$0.32^{+0.01}_{-0.01}$	softer
NGC 5806	0.58	$105.89^{+25.23}_{-30.11}$	$-0.22^{+0.06}_{-0.04}$	harder
NGC 7331	0.86	$80.45^{+15.10}_{-15.01}$	$-0.46^{+0.06}_{-0.06}$	harder

Table 2.2: The reduced χ^2 and best-fit parameters (with one-sigma errors) for linear fits to the hardness ratio vs. $2-10$keV count rate plots of each object (see Fig. 2.2). The behaviour of each source with increasing count rate is always shown, determined by whether the slope of the linear fit is positive (softer-when-brighter) or negative (harder-when-brighter). The behaviour of objects with increasing luminosity is 'undetermined' if the errors on the gradient of the fit cross zero. NGC 4486 possessed too little data for meaningful binning with more than ten bins, so errors are not given.

2.4 Resolving a Constant Spectral Component

Whilst the hardness ratio vs. flux plots indicate that there is a division in the behaviour of spectral variation in the AGN sample, the causes of the spectral variation cannot be discerned from hardness ratio changes alone. If the spectrum is a simple absorbed power law, with no or constant absorption, correlated hardness changes imply changes in the photon index which are correlated with luminosity. However, a hardness ratio correlated with luminosity would also be seen if an additional constant soft component is present in the spectrum, or could be produced by variable absorption. In both of these cases, the photon index of the underlying power law would not be required to vary.

A constant soft spectral component can be produced by background contamination from hot gas due to circumnuclear star formation, which is seen in some AGN spectra (Nemmen et al., 2006, Perez-Olea & Colina, 1996, Wang et al., 2009). As the source brightens, the contribution of such a component would become smaller, increasing the

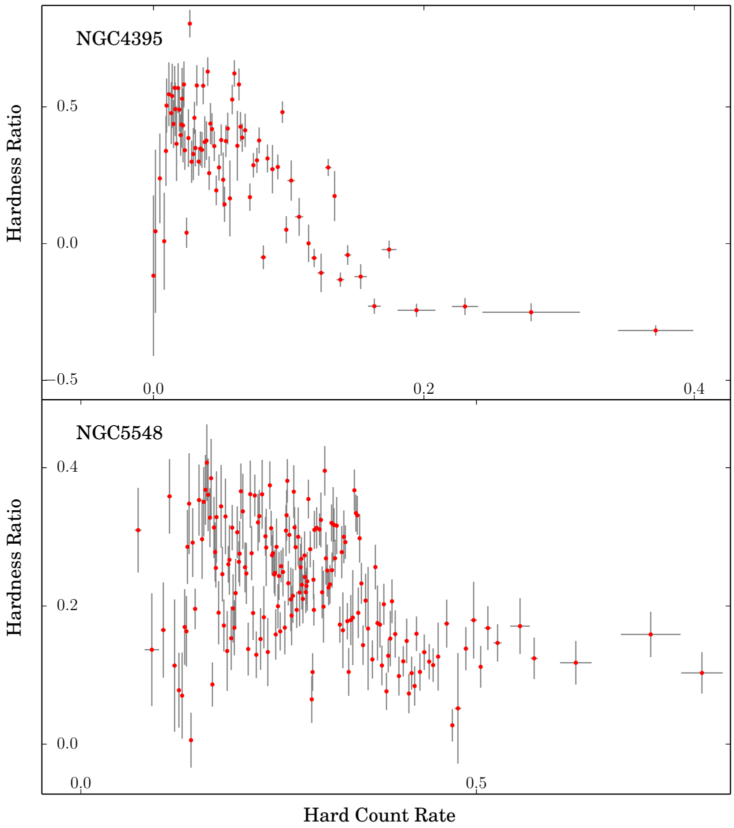

Figure 2.3: The hardness ratio of the spectra of NGC 4395 and NGC 5548 using the 0.5-2 and 2-10 keV bands, plotted against the 2-10 keV count rate. The data are binned into bins of 10 data points. Error bars show the one-sigma confidence levels. Both objects show more complex behaviour in their hardness ratios with increasing count rate when compared to the other objects. Both also show a general softer-when-brighter trend at intermediate count rates.

hardness of the overall spectrum without the need for any change in the photon index. This soft component must, however, be luminous enough to produce the observed hardness changes.

A model-independent method to determine whether a constant spectral component is present, and if so what form it takes, is to plot the flux in different X-ray bands against one another (see e.g. Taylor et al., 2003). If one assumes a linear relationship between two bands, a linear model can be fitted to the data and extrapolated to estimate the flux in one band when the other is at zero flux (see Fig. 2.4). If it is assumed that any constant component present becomes negligibly small at high energies, as is reasonable for models of e.g. emission from hot plasma due to star formation, a high-energy reference band can be used to find the flux of the lower-energy bands when the variable component is zero. In this way, the shape of the underlying constant spectral component can be estimated. If the spectral shape of any constant component is known, it is then possible to determine in a model-independent way whether this component is the sole cause of hardness changes with luminosity, or whether intrinsic variations in the spectrum are required.

The only harder-when-brighter source for which this method could produce reasonably well-constrained results was M81. The X-ray count rates in 7 soft energy bands (0.3-0.5, 0.5-1.0, 1.0-1.5, 1.5-2.0, 2-3, 3.-4 and 4-5 keV) were plotted against the 5-10 keV hard energy band. These data were then fitted with a linear model in the same manner as were the hardness ratio vs. flux plots in Section 2.3. By assuming that there is no underlying component in the 5-10 keV band, the intercepts of these linear fits can be taken as the count rates of any soft component in each band. The bands all showed a weak positive correlation, with an average Pearson correlation coefficient of 0.32. Fig. 2.4 shows an example of a plot of the count rate in two bands in the spectrum of M81, the best-fitting linear model and the errors in its parameters.

The constant spectral component is measured in count space from the instrumental data and must therefore be deconvolved using the instrumental response for *Swift* in the same way as for any other X-ray spectrum. A typical instrumental response matrix for *Swift* was therefore applied to the derived constant spectrum during spectral modelling. A significant excess was only found in 3 of the 7 bands, two of these were in the $0.5 - 1.5$ keV range; Fig. 2.5 shows the extrapolated count rate in each band.

This spectrum was fitted with three models - a power law, a hot gas model (mekal) and combination of the two. None of the models fitted the spectrum well (χ^2_{R} of 3.31, 3.67 and 4.04, for 6, 6 and 4 degrees of freedom, respectively), however the power law was the best-fitting model. Whilst this model may not be a perfect physical approximation of the constant component, it may still be used to test the possibility that such a component is causing the observed spectral variability. The lack of a good spectral fit, combined with the lack of a significant excess rate in 4 of the 7 bands may indicate that a constant component is not present at all, or extremely weak; despite this, the model fitted to the extrapolated spectrum was used in subsequent spectral modelling of M81 in order to test whether its contribution would be large enough to cause the observed hardness changes, under the assumption that it may be real.

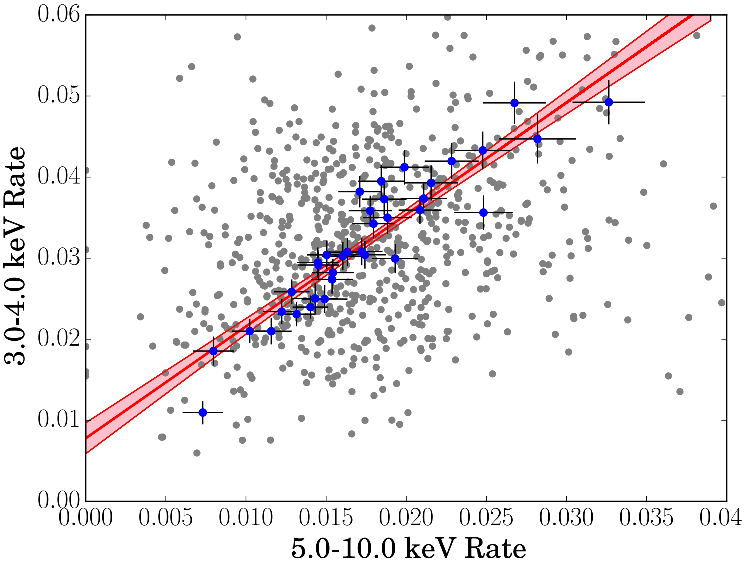

FIGURE 2.4: An example of a flux-flux diagram for M81, of the 3-4 v. 5-10 keV bands (binned). Blue points are binned data, with a minimum of 20 points per bin. Grey points shown behind are unbinned data. Error bars show the one-sigma confidence levels. The red line shows the best-fitting model, assuming a linear trend, and the pink region bounded by red indicates the one-sigma error region of the model parameters.

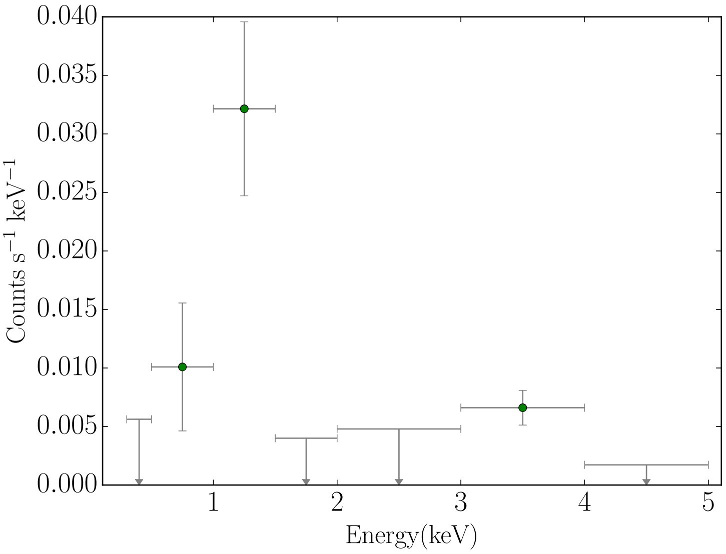

FIGURE 2.5: The constant, soft component of the spectrum of M81, assuming a linear relationship between the flux in different bands and zero flux in the 5-10 keV band. The data are folded through a typical response for *Swift*.

2.5 Spectral Modelling

Enough data existed for spectral fitting of 14 of the 24 AGN at multiple flux levels. A set of models, in increasing degrees of complexity from a simple power law to a partially covered power law (see Table 2.3), were successively fitted to the spectra of each source until a good fit was found, using the XSPEC 12.7 analysis package (Arnaud, 1996). Models were fitted to data in the $0.5 - 10$keV energy range in all cases except that of the NGC 3998 *RXTE* data, for which the $3 - 20$keV energy range was used. In all models, a neutral absorber whose column was fixed at the Galactic column in the direction of the source was included.

Table 2.3 contains descriptions of all of the spectral models fitted to the spectra. In all cases, the model was fitted simultaneously to all of the flux-binned spectra for a given object - for some models, some parameters were 'tied', meaning they were allow to vary, but constrained to be the same value for all spectra. In each case, F-tests were used to determine whether the addition of complexity to a model improved the fit sufficiently to better describe the spectra.

The only models for which only the power law normalisation was allowed to vary were the two-component models, i.e. those containing a power law plus a constant (hot gas) component or the partial covering model. Only for these models can simple changes in the normalisation of the power law change the hardness ratio.

The simplest model fitted was a power law with the photon index and normalisation allowed to vary with luminosity (model 1 in Table 2.3). The next simplest set of models consisted of an absorbed power law, including models in which the absorbing column or the photon index were tied between spectra (models 2-4). The next were a pair of models consisting of an absorbed power law plus a hot gas model, for which the normalisation of the power law was free to vary and the photon index was either free to vary or tied between spectra; all parameters of the hot gas model (i.e. temperature and normalisation) were tied, as it was assumed to be constant (models 56). Also fitted was a set of models consisting of a power law absorbed by an ionised absorber (absori), in which the normalisation of the power law and either the photon index, ionisation state, absorbing column or all three were free to vary between spectra, with the remaining parameters tied (models 8-11). These spectral models were fitted to all 14 objects with flux-binned spectra; the results of these fits are in Tables 2.4 and Table 2.5.

Objects whose spectra were not well fitted by any of these models were also fitted with a set of models consisting of a power law and a partially-covering absorber (pcfabs) in which, in addition to the normalisation of the power law, either the photon index, absorbing column or covering fraction, the absorbing column *and* the covering fraction, or all three were free to vary (models 12-17). These objects were also fitted with a set of similar models with the addition of a hot gas component, whose parameters were tied between spectra (models 18-23). The results of these fits are in Tables 2.6 and Table 2.7.

In addition, NGC 1068 was fitted with a model consisting of a power law with a neutral absorber plus a Gaussian, to account for excess emission at ~ 6.7keV which is likely to be due to an iron fluorescence line (model 7) (see Section A). The results of these fits are also in Table 2.7.

The data from the remaining 11 AGN, for which there were not enough data to fit multiple flux-binned spectra, were instead combined to produce a single, total spectrum for each object. These total spectra were fitted in the same fashion as the flux-binned spectra. As only one spectrum was fitted in each case, all parameters were free to vary in all models (except the galactic absorbing column and redshift). Table 2.9 shows the results of these fits.

Table 2.8 summarises the best-fitting spectral model for each of the objects for which flux-binned spectra could be produced.

N	Description	Xspec Description	Free Parameters
1	Simple power law	pow	Γ
2	Power law with neutral absorber	wabs*pow	Γ
3	Power law with neutral absorber	wabs*pow	N_H
4	Power law with neutral absorber	wabs*pow	N_H, Γ
5	Power law with neutral absorber and hot gas	mekal + (wabs*pow)	-
6	Power law with neutral absorber and hot gas	mekal + (wabs*pow)	Γ
7	Power law with neutral absorber, Gaussian and hot gas	mekal + (wabs*(pow + gauss))	Γ
8	Power law with ionised absorber	absori*pow	Γ
9	Power law with ionised absorber	absori*pow	N_H
10	Power law with ionised absorber	absori*pow	ξ
11	Power law with ionised absorber	absori*pow	N_H, ξ, Γ
12	Partially covered power law	pcfabs*pow	-
13	Partially covered power law	pcfabs*pow	Γ
14	Partially covered power law	pcfabs*pow	N_H
15	Partially covered power law	pcfabs*pow	CF
16	Partially covered power law	pcfabs*pow	N_H, CF
17	Partially covered power law	pcfabs*pow	N_H, CF, Γ
18	Partially covered power law and hot gas	mekal + pcfabs*pow	-
19	Partially covered power law and hot gas	mekal + pcfabs*pow	Γ
20	Partially covered power law and hot gas	mekal + pcfabs*pow	N_H
21	Partially covered power law and hot gas	mekal + pcfabs*pow	CF
22	Partially covered power law and hot gas	mekal + pcfabs*pow	N_H, CF
23	Partially covered power law and hot gas	mekal + pcfabs*pow	N_H, CF, Γ

TABLE 2.3: A description of the series of models applied successively to the spectra of each AGN. All models also included the 'wabs' model of neutral absorption set to the Galactic absorption column in the direction of each AGN. The free parameters, which can vary between spectra, are shown as symbols: Γ (photon index), N_H (absorbing column), ξ (ionisation parameter) and CF (covering fraction). In all cases the normalisations of the power law was free to vary. In models involving a mekal component, its normalisation was always tied to be the same value in all spectra of a given source.

Xspec Model	pow		wabs*pow						wabs*pow +mekal				wabs*(pow + gauss) + mekal	
Model No.	1		2		3		4		5		6		7	
Free Parameters	Γ		Γ		$\mathrm{N_H}$		$\Gamma, \mathrm{N_H}$		–		Γ		Γ	
	χ^2_R	DoF	χ^2_R	DoF	χ^2_R	DoF	χ^2_R	DoF	χ^2_R	DoF	χ^2_R	DoF	χ^2_R	DoF
NGC 1052	2.09	162	2.11	161	2.17	161	2.13	159	1.42	161	1.41	159		
NGC 1068	2.69	436	2.58	435	2.58	435	2.59	431	1.62	437	1.61	433	**1.0743**	**430**
NGC 3031	1.01	5902	1.01	5901	1.03	5901	1.01	5874	1.01	5927	**0.98**	**5899**		
NGC 3147	0.73	125	**0.70**	**124**	0.72	124	0.70	122	0.73	124	0.71	122		
NGC 3227	1.17	1094	1.10	1093	1.57	1093	1.09	1082	1.52	1102	1.08	1091		
NGC 3998	**1.40**	**225**	1.39	224	1.69	224	1.42	200	1.63	271	1.42	247		
NGC 4051	2.04	784	2.05	783	2.07	783	2.11	774	1.25	790	**1.10**	**781**		
NGC 4151	2.11	703	2.11	702	2.62	702	2.13	696	1.29	707	1.31	695		
NGC 4388	1.92	260	1.93	259	1.92	259	1.94	256	**1.17**	**261**	1.17	258		
NGC 4395	1.15	1373	1.15	1372	1.30	1372	1.17	1351	1.31	1392	1.15	1371		
NGC 4486	3.01	261	1.83	260	1.82	260	1.83	257	**1.02**	**261**	1.02	258		
NGC 4579	1.09	201	1.10	200	1.09	200	1.11	198	**1.00**	**200**	1.00	198		
NGC 5548	1.66	8659	1.46	8658	1.43	8658	1.43	8617	1.15	8697	1.11	8656		

Table 2.4: The reduced χ^2 values, χ^2_R, and number of degrees of freedom (DoF) of the best fit with models 1-7 to each of the sources. In each case, the free parameters are indicated by Γ (photon index) and $\mathrm{N_H}$ (absorbing column). The best fitting model for each source is highlighted in bold.

Xspec Model	absori*pow							
Model No.	8		9		10		11	
Free Parameters	Γ		ξ		N_H		Γ, ξ, N_H	
	χ^2_R	DoF	χ^2_R	DoF	χ^2_R	DoF	χ^2_R	DoF
NGC 1052	1.42	159	1.51	159	1.85	159	1.48	155
NGC 1068	2.37	433	2.59	433	2.59	433	2.56	425
NGC 3147	0.71	122	0.72	122	0.73	122	0.72	118
NGC 3031	1.01	5900	1.03	5900	1.03	5900	1.02	5846
NGC 3227	**1.05**	**1091**	1.27	1091	1.31	1091	1.17	1069
NGC 3998	1.47	247	1.64	247	1.82	247	1.78	199
NGC 4051	1.15	781	1.14	781	1.13	781	1.11	763
NGC 4151	2.02	701	1.78	701	1.96	701	1.16	689
NGC 4388	2.38	258	1.92	258	1.93	258	1.66	252
NGC 4395	**1.03**	**1370**	1.08	1370	1.06	1370	1.01	1328
NGC 4486	1.82	259	1.81	259	1.84	259	1.86	253
NGC 4579	1.09	198	1.18	198	1.08	198	1.08	194
NGC 5548	0.96	8656	0.95	8656	0.96	8656	**0.94**	**8574**

TABLE 2.5: The reduced χ^2 values, χ^2_R, and number of degrees of freedom (DoF) of the best fit with models 8-11 to each of the sources. In each case, the free parameters are indicated by Γ (photon index), N_H (absorbing column) and ξ (ionisation state). The best fitting model for each source is highlighted in bold.

Xspec Model	pcfabs*pow											
Model No.	12		13		14		15		16		17	
Free Parameters	–		Γ		N_H		CF		N_H, CF		Γ, N_H, CF	
	χ^2_R	DoF	χ^2_R	DoF	χ^2_R	DoF	χ^2_R	DoF	χ^2_R	DoF	χ^2_R	DoF
NGC 1052	1.11	162	**1.01**	**160**	1.08	160	1.03	160	1.00	158	0.99	156
NGC 1068	2.24	438	2.24	434	2.25	434	2.26	434	2.27	430	2.28	426
NGC 4151	1.23	708	1.20	702	1.22	702	1.16	702	1.15	696	1.13	690

TABLE 2.6: The reduced χ^2 values, χ^2_R, and number of degrees of freedom (DoF) of the best fit with models 12-17 to the sources not well fit by models 1-11. In each case, the free parameters are indicated by Γ (photon index), N_H (absorbing column) and CF (covering fraction). The best fitting model for each source is highlighted in bold.

Xspec Model	pcfabs*pow + mekal											
Model No.	18		19		20		21		22		23	
Free Parameters	–		Γ		$\mathrm{N_H}$		CF		$\mathrm{N_H}$, CF		$\Gamma, \mathrm{N_H}$, CF	
	χ^2_R	DoF	χ^2_R	DoF	χ^2_R	DoF	χ^2_R	DoF	χ^2_R	DoF	χ^2_R	DoF
NGC 1068	1.12	436	1.10	432	1.11	432	1.12	432	1.12	428	1.12	424
NGC 4151	1.11	706	1.11	700	1.12	700	1.07	700	1.06	694	**1.03**	**688**

TABLE 2.7: The reduced χ^2 values, χ^2_R, and number of degrees of freedom (DoF) of the best fit with models 18-23 to the sources not well fit by models 1-17. In each case, the free parameters are indicated by Γ (photon index), $\mathrm{N_H}$ (absorbing column) and CF (covering fraction). The best fitting model for each source is highlighted in bold.

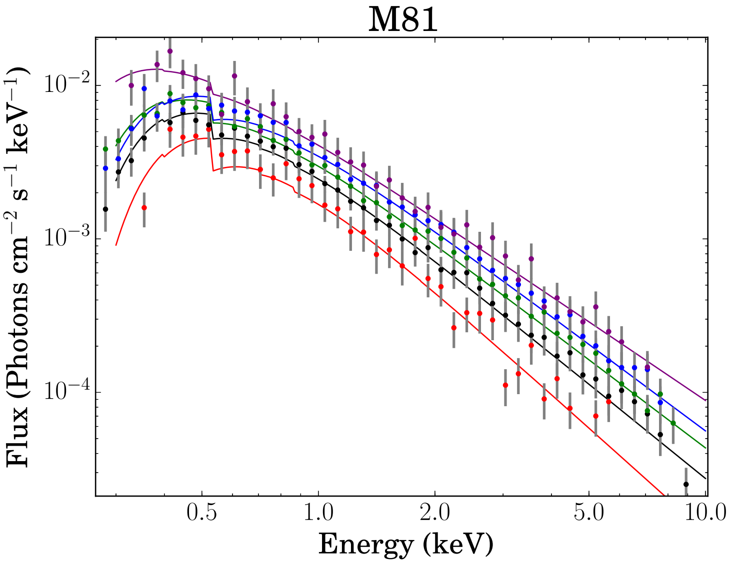

Figure 2.6: A sample of the flux-binned spectra of M81, fitted with the best-fitting spectral model (see Table 2.4). Error bars show the one-sigma confidence levels.

2.5.1 M81 (NGC 3031)

As the most extensively observed object to show harder-when-brighter behaviour, the spectra of M81 were studied in the greatest detail. The soft component of M81 in particular, extrapolated from its colour-colour plots (see section 2.4), was derived in order to be able to draw conclusions about similar sources in the sample. Fig. 2.6 shows a sample of the spectra from M81, covering the full observed flux range.

The X-ray spectrum of M81 is well described by a simple power law absorbed by the Galactic absorbing column of 7.2×10^{21}cm^{-2}. This is consistent with the many previous shorter-term X-ray studies of M81 (e.g. Elvis & Van Speybroeck, 1982, Markoff et al., 2008, Swartz et al., 2003); past studies discovered narrow features attributed to high-ionisation emission lines including Fe lines (e.g. Ishisaki et al., 1996, Page et al., 2003, 2004, Pellegrini et al., 2000), but these are not detectable in the *Swift* data.

The variability in the spectral data is well described by changes in Γ alone; no extra spectral components other than the Galactic absorption in the direction of M81 are required. If the spectrum is assumed to be absorbed by an additional neutral absorber, the variability in the spectral data is equally well described by changes in Γ with the absorbing column fixed or by changes in the absorbing column with a fixed Γ. As these models require an extra component and do not provide a better fit, it is, however, unlikely to be a better description of the data.

If Γ is held constant, I require that the absorbing column decreases as the luminosity rises. In the case of NGC 1365 (Connolly et al., 2014), which has complex luminosity-dependent absorption, greatly in excess of the Galactic column in its direction, such a model is readily explained in terms of a luminosity-dependent wind. However, for M81 there is no evidence in the total summed spectrum for any absorption in excess of the Galactic column. No previous spectral studies have found evidence for such an excess column. As the model with variable absorption requires an additional variable absorbing column in addition to the fixed Galactic column, I consider it less likely than the model of variable Γ, which has one parameter fewer.

Spectral models including the constant component extrapolated from the colour-colour plots (see section 2.4) were also tested; the component was found not to make a significant enough contribution to the spectrum to account for the variability. The inclusion of this constant component in a model consisting of a power law and a neutral absorber, with a fixed photon index, gave significantly worse fit ($\chi^2_{\mathrm{R}} = 1.15$).

In addition to the constant component extrapolated from the colour-colour plots, I also separately test a model consisting of a constant hot gas (mekal) component together with a power law with varying normalisation but fixed photon index and fixed absorption. In this model, the parameters of the hot gas component are tied to be the same between spectra, but allowed to vary, in order to test whether any significant constant soft component can be found in this way. This model fits the data approximately as well as the model of an absorbed power law with varying photon index. As the photon index is free to vary between flux-binned spectra in the model without the hot gas component, it has more free parameters (i.e. is more complex). However an F-test shows that the simple power law with variable Γ is preferred to the constant-Γ model with a hot component (f = 2.26, p = 3.30×10^{-4}). Similarly, if the model with a hot gas component in which the photon index is constant is compared to the same model but with the photon index allowed to vary between flux-binned spectra, an f-test shows that the model in which Γ is variable is preferred (f = 7.78, p = 1.27×10^{-29}) and the varying-photon index model is therefore overwhelmingly preferred; this model is also statistically preferable to the simple absorbed power law, despite its higher level of complexity (f = 76.0, p = 2.48×10^{-33}). The integrated flux of the extrapolated constant component is within a factor of 2 of that of the hot gas component in the best-fitting model of the full spectrum, and therefore likely to be the same component, though perhaps not well recovered. The data therefore require a constant hot gas component, but it does not contribute to the spectrum enough to explain the overall spectral variability. It is therefore most likely that the observed spectral variability is driven by changes to Γ.

The top-left panel in Fig. 2.7 shows how Γ changes with increasing flux for the best-fitting model to M81 (model 6). Γ shows a clear anticorrelation with the luminosity of the source, well fitted by a linear model (see Table 2.10). Significantly, the same anticorrelation is seen in all models in which Γ is free to vary, regardless of the presence of a hot gas component and whether or not the absorbing column was also left free to vary, strengthening still more the evidence that intrinsic variability of the photon index is required to explain the spectral variability of M81. This anticorrelation between Γ and luminosity is therefore found to be the cause of the observed harder-when-brighter behaviour in M81.

2.5.2 The Palomar Swift Sample of AGN

Details on the spectral fitting of individual AGN in the sample are given in Appendix A, along with examples of the spectra (Figs. A.2, A.1).

2.5.2.1 Flux-Binned Spectral Modelling

A simple power law, either not absorbed, absorbed by a neutral absorber, or absorbed by an ionised absorber, fitted the spectra of 4 of the 13 flux-binned sources well; in all 4 cases, a varying photon index was required to account for spectral variability. Two of the sources were, however, better fit when the absorbing column and ionisation state of the absorber were also allowed to vary.

The addition of a constant hot gas component to the absorbed power law was required in 6 of the 13 flux-binned sources (including M81). The spectral variability of only 1 of these 6 sourced can only be explained by variability in the normalisation of a power law with constant Γ together with this constant hot gas component. The other 5 sources required Γ to also be free to vary. Allowing the absorber to vary (i.e. absorbing column and ionisation state where the absorber was ionised) did not improve the fit in any of these sources.

A more complex model was required for a good fit to the remaining 3 of the 13 flux-binned objects - NGC 1052, NGC 4151 and NGC 4388. NGC 1052 and NGC 4151 both required a partial covering absorber; Allowing the photon index to vary did not improve the fit in this model for NGC 1052, whilst in NGC 4151 a varying photon index was required, but a varying absorbing column and covering fraction were also needed. NGC 4388 required a two-component model consisting of two power laws, one of which is absorbed by a neutral absorber. The normalisations of the two power laws were correlated in this model, implying both originate from the central source. In this model, allowing the photon index to vary did not improve the fit.

The results of the fits to the spectra of NGC 1068, NGC 4151, NGC 4388 were not included in subsequent analysis, as they were deemed unphysical (see Appendix A).

Fig. 2.7 shows plots of the value of Γ as a function of flux of the 9 objects observed by *Swift* whose best-fitting models required variations in Γ (including M81), plus NGC 7213 for comparison. The data are fitted with linear models in the same manner as were the hardness data described in Section 2.3. The results of these fits are shown in Table 2.10. Of these 10 objects, 9 show a clear trend of changing Γ with luminosity. 6 of the objects showed a negative correlation, 3 showed a positive correlation and 1 shows no clear correlation. The best linear fits to NGC 3998 and NGC 5548 (harder-when-brighter), NGC 3227, NGC 4051 and NGC 4395 (softer-when-brighter) all have high χ^2_{R} values, due to the larger degree of scatter in the measured values of Γ for these systems. The Pearson correlation coefficients for these systems still show them to be fairly strongly correlated, however. All of the objects' behaviours are consistent with that implied by their hardness ratio vs. flux plots, except for NGC 5548; however the behaviour of its hardness ratio with changing flux is not as simple as the others (as described above) and spectral modelling shows that it possesses complex, variable absorption (Kaastra et al., 2014).

The data therefore imply that a significant fraction of objects which displayed harder-when-brighter behaviour do show hardening of their intrinsic spectra, i.e. a decrease in photon index, Γ, with increasing luminosity. All of the objects showing softer-when brighter showed softening of their intrinsic spectra (i.e. an increase in Γ) with increasing luminosity. One can therefore conclude that the behaviour of the hardness ratio with changing luminosity is a reasonable predictor of the behaviour of the spectral slope of the underlying power law, and that it is likely that a similar fraction of the remaining objects which showed harder-when-brighter behaviour in their hardness ratio vs. count rate plots,, whose data did not allow spectral fitting, would also possess intrinsic hardening.

2.5.2.2 Total Spectral Modelling

Spectral fitting was also carried out on the total spectra of the 11 objects for which there was sufficient data to produce plots of hardness ratio vs. luminosity, but not sufficient data for flux-binned spectral fitting. All of the available good-quality data on each of these objects was summed and fitted in the same manner as for the flux-binned spectra. The results of this spectral analysis are presented in Table 2.9. Of these 11 objects, 7 possessed evidence for either complex absorption, i.e. variable partial-covering absorbers, or strong contamination, e.g. from hot gas. The remaining 4 objects possessed spectra which can be described by simple power laws, with evidence of absorption in 3 of the objects. These four objects also show harder-when-brighter behaviour in the plots of hardness ratio vs. luminosity (Fig. 2.2). The spectral modelling therefore shows the harder-when-brighter behaviour of these objects due to changes in their photon indices and/or absorbing columns which are correlated with luminosity.

The harder-when-brighter behaviour seen in 6 of the 7 objects with more complex spectra could be caused by variations in parameters other than γ, i.e. the absorption, ionisation state and/or covering fraction. NGC 4321, whose hardness ratio behaviour with increasing luminosity did not follow any simple pattern, has a complex spectrum which could not be well fitted by any of the models. As I have limited spectral data in all of these cases, I cannot be sure of the cause of their behaviour without further data to allow multi-epoch or flux-binned spectral modelling.

Source	Best-Fitting	Best-Fitting Parameters				
	Spectral Model	$N_H(10^{22}cm^{-2})$	Γ	kT (keV)	CF	Ξ
NGC 315	1	0.78	1.94	0.56	-	-
NGC 1052	13	8.60	$1.37 - 1.70$	-	0.91	-
NGC 1068	7	55.7	$2.90 - 3.06$	0.67	0.95	-
NGC 2655	23	20.5	1.35	0.57	0.95	-
NGC 3031	6	0	1.69-2.05	0.55	-	-
NGC 3147	2	-	$1.35 - 1.58$	-	-	-
NGC 3226	4	0.54	2.57	-	-	-
NGC 3227	8	0.13	$1.43 - 1.65$	-	-	0.045
NGC 3628	4	0.35	1.36	-	-	-
NGC 3998	1	-	$1.87 - 2.50$	-	-	-
NGC 4051	6	0	$1.35 - 1.97$	0.20	-	-
NGC 4151	23	$3.01 - 5.07$	$0.76 - 1.20$	0.23	$0.76 - 0.95$	-
NGC 4258	23	9.89	1.66	0.60	0.95	-
NGC 4321	6	1.51	4.46	0.43	-	-
NGC 4388	5	26.3	$1.05 - 1.24$	0.62	-	-
NGC 4395	8	2.17	$0.91 - 1.60$	-	-	215.16
NGC 4472	6	0.81	3.83	0.74	-	-
NGC 4486	5	0.45	2.68	1.52	-	-
NGC 4579	5	0.01	1.67	0.52	-	-
NGC 4736	6	0.055	1.48	0.35	-	-
NGC 5194	7	0	0.7	0.60	-	-
NGC 5806	4	0.057	1.65	-	-	-
NGC 5548	11	$0.64 - 1.43$	$1.09 - 1.40$	-	-	$7.46 - 35.88$
NGC 7331	6	0.075	1.37	0.37	-	-

Table 2.8: The best-fitting spectral model for each of the sources, and the values of the parameters which were free to vary (excluding normalisations, which were always free but are not included). See Table 2.3 for a description of each model.

Xspec Model	pow		wabs*pow		absori*pow		wabs*pow + mekal		pcfabs*pow		pcfabs*pow + mekal		wabs*(pow+gauss) + mekal	
	χ^2_R	DoF	χ^2_R	DoF	χ^2_R	DoF	χ^2_R	DoF	χ^2_R	DoF	χ^2_R	DoF	χ^2_R	DoF
NGC 315	3.80	26	3.28	26	4.92	24	**1.02**	**24**						
NGC 2655	10.37	47	9.76	46	4.65	44	2.51	44	3.36	45	**1.15**	**43**		
NGC 3226	2.64	31	**0.90**	**30**	0.97	28								
NGC 3628	2.66	16	**0.88**	**15**	1.02	13								
NGC 4258	6.77	56	6.90	55	3.27	52	2.70	53	2.91	54	**1.03**	**52**		
NGC 4321	3.71	11	2.56	10	5.04	8	**1.62**	**7**						
NGC 4472	13.36	46	4.84	45	6.37	45	**1.03**	**43**						
NGC 4736	1.69	82	1.55	81	1.75	79	**0.97**	**79**						
NGC 5194	12.25	134	7.13	133	12.27	131	1.80	131	9.75	132	1.46	131	**1.18**	**127**
NGC 5806	1.27	16	**1.16**	**15**	1.45	13								
NGC 7331	2.63	26	2.69	25	2.79	23	**0.83**	**23**						

TABLE 2.9: Results of spectral fitting to the total spectra of those objects with too little data for flux binning. All models included a neutral absorber fixed at Galactic absorbing column in that direction.

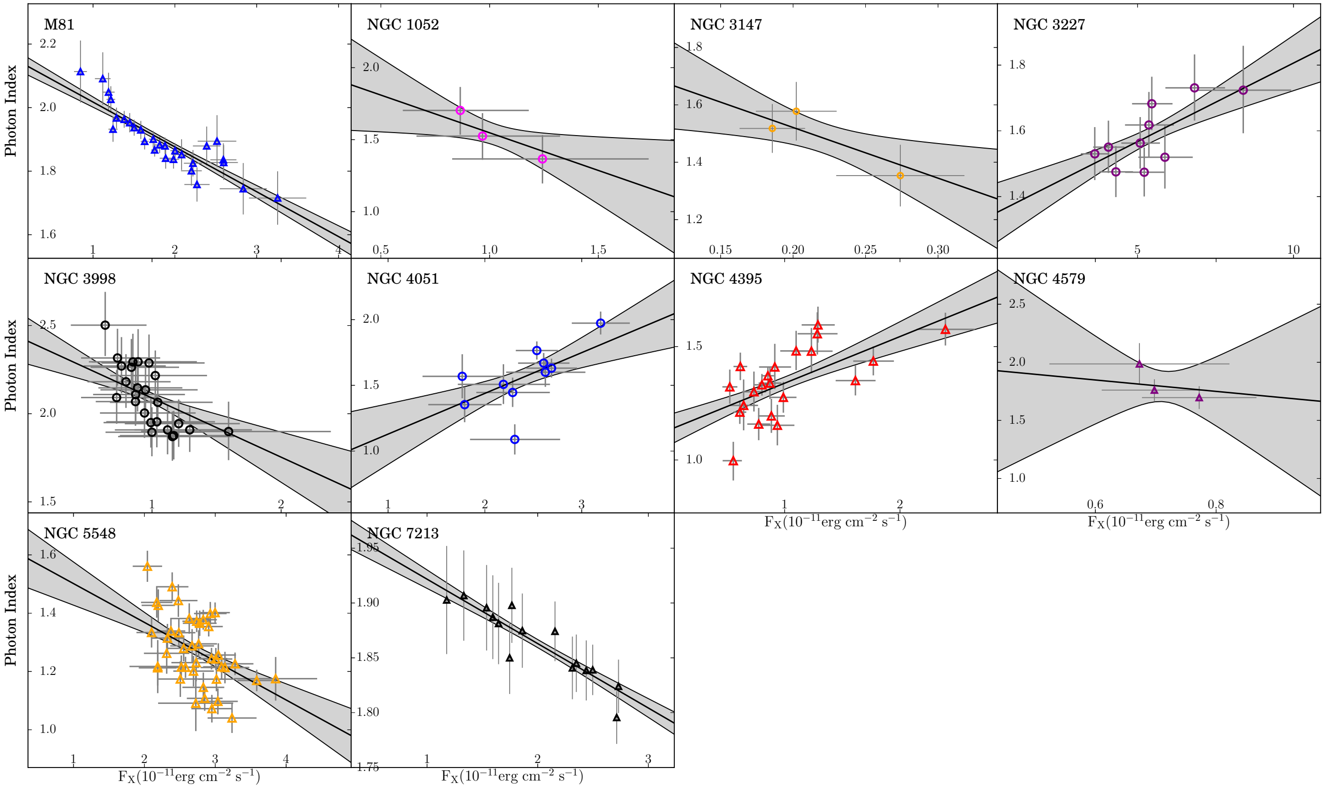

FIGURE 2.7: Plots of the photon index Γ against the X-ray flux of each of the sources for which flux-binned spectral fitting was carried out, using the best-fitting model in each case. The $0.5 - 10$keV flux is used in all cases except for NGC 3998, for which the $3 - 20$keV *RXTE* flux is used. Error bars show the one-sigma confidence levels. The data are fitted with linear models; the best-fitting model is shown in black and the one-sigma error regions of each fit are shown in grey.

Object	χ^2/DoF	Gradient	Intercept	Pearson coefficient	Behaviour when brighter
M81	0.95	$-0.14^{+0.02}_{-0.024}$	$2.16^{+0.04}_{-0.05}$	-0.89	harder
NGC 1052	1.70	$-0.52^{+0.36}_{-0.53}$	$2.07^{+0.52}_{-0.37}$	-0.96	harder
NGC 3147	0.58	$-1.77^{+1.46}_{-1.94}$	$1.87^{+0.44}_{-0.31}$	-0.91	harder
NGC 3227	2.81	$0.048^{+0.02}_{-0.01}$	$1.33^{+0.07}_{-0.08}$	0.73	softer
NGC 3998	3.11	$-0.34^{+0.10}_{-0.11}$	$2.42^{+0.10}_{-0.09}$	-0.74	harder
NGC 4051	13.22	$0.31^{+0.09}_{-0.09}$	$0.82^{+0.21}_{-0.22}$	0.65	softer
NGC 4395	10.21	$0.21^{+0.02}_{-0.02}$	$1.13^{+0.02}_{-0.02}$	0.63	softer
NGC 4579	1.59	$-0.49^{+1.52}_{-1.48}$	$2.14^{+1.07}_{-1.16}$	-0.83	undetermined
NGC 5548	19.46	$-0.13^{+0.02}_{-0.02}$	$1.63^{+0.06}_{-0.05}$	-0.50	harder
NGC 7213	0.23	$-0.06^{+0.02}_{-0.02}$	$1.98^{+0.04}_{-0.04}$	-0.91	harder

Table 2.10: The reduced χ^2 and best-fit parameters (with one-sigma errors) for linear fits to the photon index vs. flux plots of each object (see Fig. 2.7). The Pearson correlation coefficient for each object is also shown.

2.6 Summary & Discussion

I have analysed the long-term observations with *Swift* of a sample of 24 nearby AGN from the Palomar sample in order to determine the reason for their variability, to determine long-term systematic trends rather than investigating short-term fluctuations which may not be representative of the overall underlying behaviour. The main results of this chapter are:

- From examination of simple hardness ratios, I find that 18 of the AGN show hardening of their X-ray spectra with increasing luminosity, 2 showed softening of their X-ray spectra with increasing luminosity, 2 showed more complex behaviour although generally softening with increasing luminosity and the remaining 2 did not show any correlation between their spectral hardness and luminosity.
- There are 13 AGN for which there were sufficient data for flux-binned spectral fits to be made. Of these, NGC 1068, NGC 4395, NGC 4151 and NGC 5548 show complex absorption, i.e. variable partial-covering absorbers, in their spectra, both in my Swift observations and in previous observations (see notes on individual sources), which makes it difficult to determine the true cause of the hardness variability. The other 8 are fit by relatively simple power law plus absorption models, making interpretation of the hardness variations simpler. Of these 8, NGC 3227 and NGC 4051 show increasing Γ with increasing luminosity. Of the other 6, NGC 3031 (M81) and NGC 3998, for which there are a large number of observations, all show a decrease of Γ with increasing luminosity. NGC 1052, NGC 3147 and NGC 4579, for which there are fewer observations, show the same

behaviour. All of the AGN which show decreasing Γ with increasing luminosity have values of $\mathrm{L_x/L_{Edd}}$ of $< 2 \times 10^{-4}$. The 2 AGN which show increasing Γ with increasing luminosity have values of $\mathrm{L_x/L_{Edd}}$ of $> 10^{-3}$.

- For the 11 objects for which spectral analysis could only be carried out on a summed spectrum of all their data, 3 were found to have spectra which could be described by a simple absorbed power law - NGC 3226, NGC 3628 and NGC 5806. The spectral modelling therefore implies that the harder-when-brighter behaviour of these 3 objects can only be due either to changes in their photon indices which are negatively correlated with luminosity, or due to changes in absorption which are negatively correlated with luminosity. As with the harder-when-brighter objects whose spectra were flux-binned, the value of $\mathrm{L_x/L_{Edd}}$ is $< 2 \times 10^{-4}$ for NGC 3226. The masses of NGC 3628 and NGC 5806 have not been determined, so their Eddington luminosities could not be calculated, but their low X-ray luminosities imply that they are very likely to have values of $\mathrm{L_x/L_{Edd}}$ which are $< 2 \times 10^{-4}$; They would have to have very low masses of $< 6.3 \times 10^5$ $M_\odot$ and $< 3.2 \times 10^5$ $M_\odot$ respectively in order to have values of $\mathrm{L_x/L_{Edd}}$ which are $> 2 \times 10^{-4}$.

2.6.1 Correlations between Photon Index and Luminosity

I find that below $\mathrm{L_x/L_{Edd}}$ of 2×10^{-4}, all AGN with well measured spectral variability show a decrease in Γ with increasing luminosity (i.e. hardening of the underlying spectral slope). Above that value of $\mathrm{L_x/L_{Edd}}$, Γ increases with $\mathrm{L_X}$. For an assumed bolometric correction factor of $\mathrm{L_{bol}/L_x} = 16$ (Constantin et al., 2009, Ho, 2008), this value would correspond to $\mathrm{L_Bol/L_{Edd}}$ (i.e. $\dot{\mathrm{m}}_{\mathrm{Edd}}$) of 3.2×10^{-3}. NGC 5548 and NGC 4395 both show complex behaviour in their hardness ratios (see Fig. 2.3), with the largest scatter in my sample and are both known to possess complex variable absorption (see Kaastra et al. (2014), Nardini & Risaliti (2011), Chapter 3) which is likely to complicate the interpretation of their observed behaviour. Previous studies (e.g. Sobolewska & Papadakis, 2009) have shown an increase in Γ with increasing Luminosity within individual AGN at high accretion rates, with the exception of NGC 5548.

In Fig. 2.8 I show all of the measurements of Γ for the sample, excluding those for which I had reason to distrust the measured values of Γ (see Appendix A). I also plot the fits to Γ from previous samples of LLAGN by Constantin et al. (2009) and, at higher accretion rates, from Shemmer et al. (2008), using assumed constant bolometric corrections of 16 and 83 respectively (for LLAGN and quasars).

The variations of Γ in M81 and NGC 7213, which are relatively bright sources with well measured spectra, follow the trend of Constantin et al. (2009) fairly well. However, the individual observations of some objects show a steeper variation with luminosity. This difference might be real or it might be due to an unknown systematic effect, e.g. over-subtraction of the hard background spectrum. If the steeper gradients are not a systematic effect, they could be explained in a number of ways. A weak constant soft component which is not resolved in the spectrum would artificially enhance the flattening of the photon index with increasing luminosity, as its relative contribution to the soft end of the spectrum decreases. Absorption variability could also enhance the change in the photon index, but the amount of absorption would be required to increase with increasing luminosity, which is hard to explain physically; it is perhaps possible if a higher luminosity leads to an increase in the wind-driving ability of the system, due to e.g. a hotter disk or more ionised matter available for line-driving, but the timescales for this mechanism to lead to an increase in absorption are likely to be too long to explain the observed spectral changes (see e.g. Proga, 2007). Finally, the difference in the rate of change of Γ with luminosity between individual AGN and sample averages could be real. I note that the spread of data points around the best fit relationship for both Constantin et al. (2009) and Shemmer et al. (2008) is very large. Thus although the change in Γ within any individual AGN is determined only by the change in accretion rate and any subsequent related changes, e.g. change in absorption, the spread of Γ within samples can also be affected by changes related to the black hole mass. For example mass-related changes in disc temperature at a given Eddington ratio could lead to differences in the relative importance of disc seed photons and coronal synchrotron seed photons (McHardy et al., 2014, Shakura & Sunyaev, 1973).

All of the AGN with $\mathrm{L_x/L_{Edd}} < 2 \times 10^{-4}$ are seen to broadly lie on a similar track, indicating that a similar physical process is responsible for the behaviour of all of the objects in the sample. The rate of change in Γ with luminosity in these lower accretion rate objects is relatively similar in all harder-when-brighter sources, implying similarities between all of the objects in the physical causes of this anticorrelation. Some of the sources show similar gradients to that of the Constantin et al. (2009) relationship, but several show slightly steeper gradients. The accuracy of the measurement of the distances and black hole masses of the AGN is limited in some cases and consequently the values of L_X/L_{Edd} may be offset for some objects. It should be noted that, in addition to the aforementioned caveats, the bolometric correction could also vary between objects, meaning that their position on this plot is not precisely correct.

For the softer-when-brighter sources, NGC 4051 and NGC 3227 are broadly consistent with the trend shown by Shemmer et al. (2008) and can be explained by the standard model of cooling of the corona with increasing accretion rate and disc seed photon flux. As discussed above, the behaviour of NGC 4395 and NGC 5548 is more complex.

Fig. 2.9 shows the photon index plotted against the Eddington ratio (L_{Bol}/L_{Edd}) of the same AGN as Fig. 2.8 (excluding the objects for which flux-binning was not possible). Bolometric corrections ($\kappa_{2-10keV} = L_{Bol}/L_{2-10keV}$) were taken from the literature (Eracleous et al., 2010, Vasudevan & Fabian, 2007, 2009). Values were not available for NGC 3147 or NGC 1052, so a typical correction of $\kappa_{2-10keV} = 16$ was used. The agreement with the fits to samples by Constantin et al. (2009) and Shemmer et al. (2006) are similar, the slopes not being changed, however the shift does bring four of the AGN (NGC 1052, NGC 3998, NGC 4486 and NGC 4579) into a closer, steep trend, whilst M81 and NGC 3147 appear to lie on a seperate, less steep track together. NGC 7213 remains very close to the Constantin et al. (2009) fit, seperate from the rest of the lower-accretion-rate AGN. The higher-accretion remain together along the Shemmer et al. (2008) fit.

The shift from a negative to a positive correlation between Γ and $\dot{m}_{Edd}$, and therefore from harder-when-brighter to softer-when-brighter behaviour, is probably due to a transition of the dominant seed photon population for X-ray production, from synchrotron or cyclo-synchrotron emission from the X-ray emitting corona itself, or from a hot inner flow/ADAF, to black body photons from a surrounding accretion disc (e.g. Skipper et al., 2013, Sobolewska et al., 2011).

The same synchrotron self-Compton emission process which dominates the X-ray emission from coronae at low accretion rates could also come from a jet; harder-when-brighter behaviour due to a Γ-$\dot{m}_{Edd}$ anticorrelation is common in blazars (e.g. Gliozzi et al., 2006, Krawczynski et al., 2004, Zhang et al., 2006), e.g. due to shock acceleration of electrons in a jet producing both higher energy synchrotron seed photons and higher energy (inverse) Compton scattering. This mechanism has been proposed to explain e.g. the spectral evolution of the BHXRB XTEJ1550-564 as it transitions from the 'soft state' towards the 'hard state' (Emmanoulopoulos et al., 2012, Russell et al., 2010). There is no evidence yet for highly relativistic outflows in LLAGN, such as are seen in blazars, but weak jets are detected (e.g Martí-Vidal et al., 2011) and models for such jets (e.g. Markoff et al., 2008) can explain the observed X-ray spectral variability.

One further explanation for harder-when-brighter behaviour is a hot outflowing corona above an X-ray illuminated untruncated disc (Sobolewska et al., 2011), in which the seed photons are from the disc. In this model, the seed photon flux is limited by relativistic beaming of the outflowing corona. At higher luminosities, a higher outflow velocity decreases the illumination of the disc and therefore the seed photon population, softening the spectrum. However, this model predicts that at the lowest luminosities there should be a strong reflection component from an untruncated disk, whilst many of the low-luminosity sources in this study, including M81, show little evidence for reflection, but good evidence for an ADAF flow and a truncated disc from the x-ray spectrum and the presence of radio emission (Brenneman et al., 2009, Markoff et al., 2008, Nowak et al., 2010, Ptak, 2004, Young & Nowak, 2007).

2.6.2 AGN and BHXRB State Analogues

Both the harder-when-brighter relation and the softer-when-brighter relation are also well established in black hole X-ray binaries (BHXRBs) and have been observed both in samples of single-epoch observations and in multi-epoch observations of individual objects (e.g. Kalemci et al., 2004, Yamaoka et al., 2005, Yuan et al., 2007). As in samples of AGN, they are seen to switch from a positive correlation to a negative correlation between Γ and $\dot{m}$, and therefore from harder-when-brighter to softer-when-brighter behaviour, when $\dot{m}_{\rm Edd}$ increases above a critical value, $\dot{m}_{\rm crit}$. This value is identified as $\sim 10^{-2}$ $\dot{m}_{\rm Edd}$ from samples of AGN (Wu & Gu, 2008), and directly observed in the BHXRB Cyg X-1, (Axelsson et al., 2008, Skipper & McHardy, 2016, Skipper et al., 2013).

Previous studies have looked for changes in the photon index with luminosity of individual LLAGN before (Hernández-García et al., 2013, 2014, Younes et al., 2011, e.g.), but been unsuccessful; my ability to detect changes in the photon index more easily is likely due to the larger flux-ranges covered by my data. As the amplitude of the change in Γ is proportional to the change in the luminosity of the system, a large flux range is essential. A large amplitude of variability is therefore also important, as changes in Γ will be hard to find in systems with very low variability regardless of the timescales covered. Methodological differences, such as the use of flux-binning, may also contribute, but I believe these effects to be less significant.

For BHXRBs, the transition from harder-when-brighter to softer-when-brighter takes place entirely within the hard state Skipper & McHardy (2016), Wu & Gu (2008) and softer-when-brighter behaviour continues throughout the hard-intermediate state, at accretion rates below that of the change to the soft state. Thus all of the AGN in my sample are probably analogues to either hard state or hard-intermediate state BHXRBs. Thus LINERS, with accretion rates $<\sim 10^{-2}$ $\dot{\mathrm{m}}_{\mathrm{Edd}}$ are analogues to hard state BHXRBs whilst Seyferts may be analogues to either higher accretion rate hard state, or to hard-intermediate state BHXRBs.

A so-called ‘fundamental plane’ relationship between X-ray luminosity, radio luminosity and black hole mass has previously been shown for samples of AGN and BHXRBs (e.g. Koerding et al., 2006, Merloni et al., 2003). In Table 2.11 I give the X-ray luminosities for my sample from my observations together with radio luminosities and black hole masses from the literature. I do not show the ’fundamental plane’ derived from the data in Table 2.11, but note that there is no obvious distinction between Seyferts and LINERs, indicating again that they are parts of a continuous distribution. The X-ray luminosities are from my present data and the radio are from the literature.

The discovery that the individual variations in Γ in the *Swift* AGN sample are consistent with previous fits to samples of AGN as well as similar studies showing the variability in Γ of individual BHXRBs therefore adds strong evidence the idea that AGN are scaled-up analogues of the BHXRBs. Based on the present data, which are the best data in which a harder-when-brighter correlation may be found in individual AGN, I suggest that this behaviour is very common amongst LLAGN.

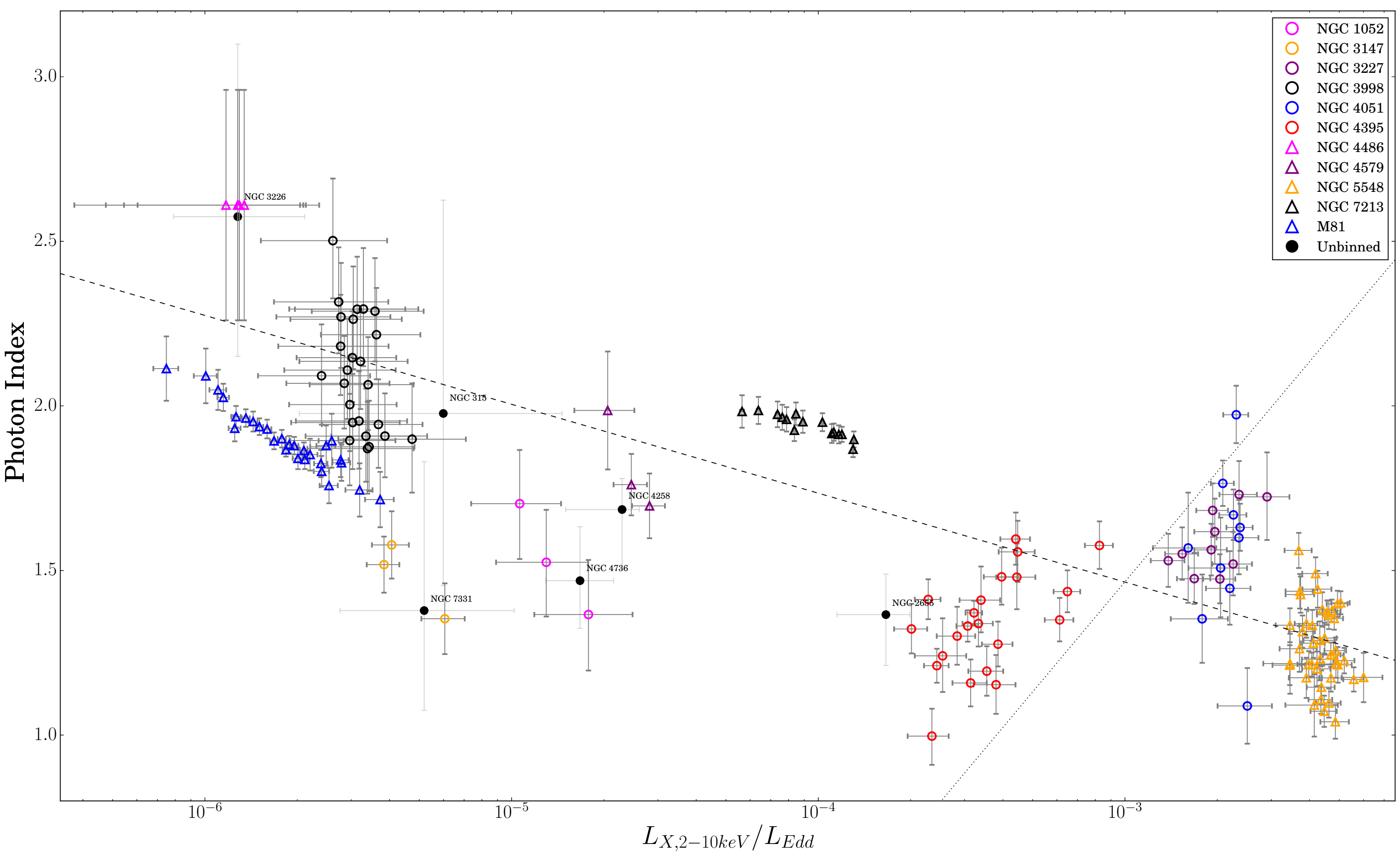

FIGURE 2.8: Plot of Γ against $L_{X,2-10keV}/L_{Edd}$ (as a proxy for $\dot{m}_{Edd}$), for all of the Palomar *Swift* AGN for which values of the photon index could be constrained, and NGC 7213 (data from Emmanoulopoulos et al. (2012)). In the cases of NGC 3998 and NGC 7213, the flux was scaled from the 3.3-20 keV flux according to the best-fitting model. Objects which did not have enough data to be flux-binned are plotted individually in grey and labelled. The dashed line is the fit to a sample of LLAGN from (Constantin et al., 2009), the dotted line is the fit to a sample of higher Eddington rate radio-quiet AGN from (Shemmer et al., 2006), using assumed constant bolometric corrections of 16 and 83 respectively (for LLAGN and quasars). Error bars show the one-sigma confidence levels. The black hole masses and distances used to calculate the Eddington luminosities and the X-ray luminosities are shown in Table 2.11.

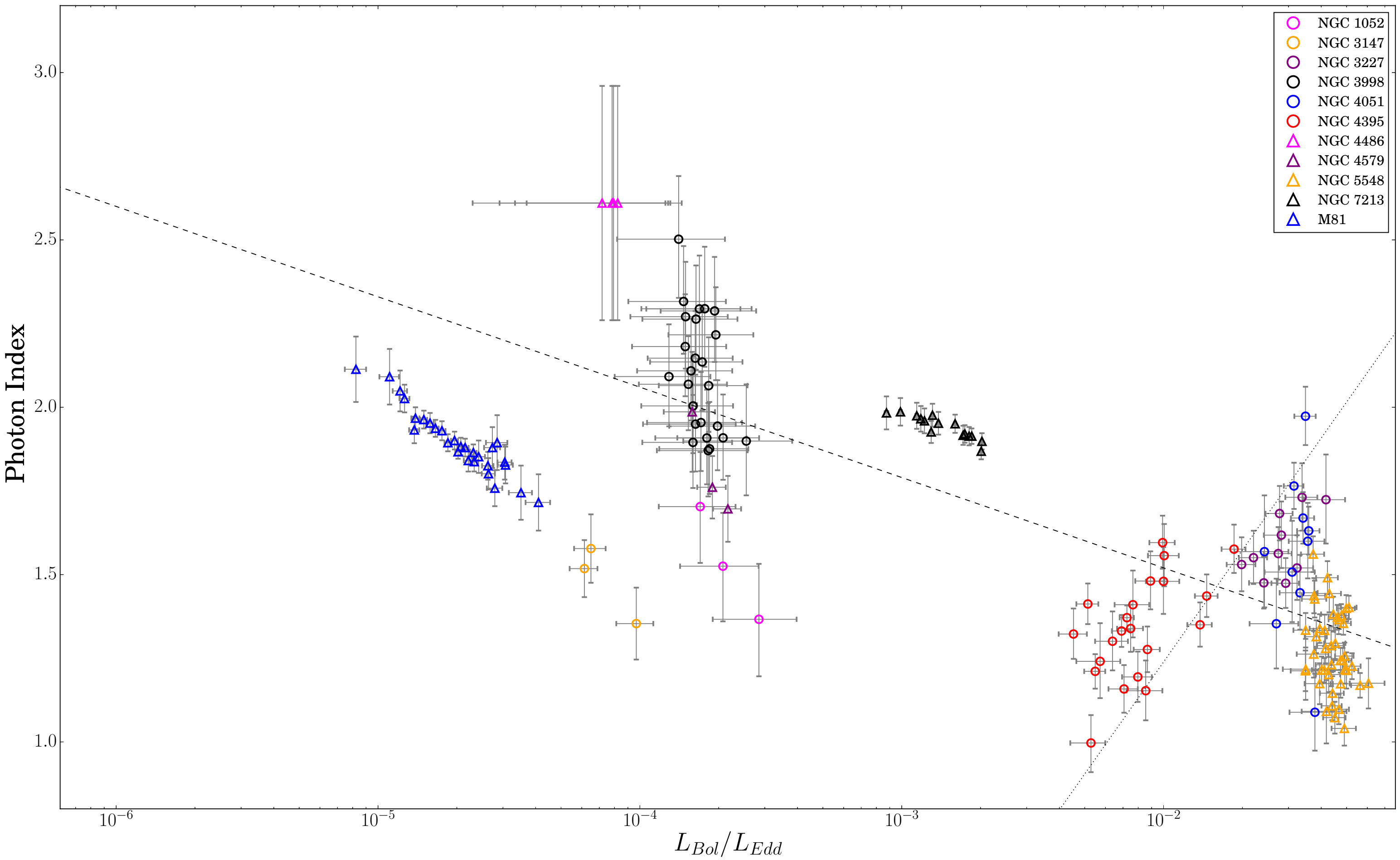

FIGURE 2.9: Plot of Γ against $\mathrm{L_{Bol}/L_{Edd}}$ (as a proxy for $\dot{m}_{\mathrm{Edd}}$), for all of the Palomar *Swift* AGN for which flux-binned spectra could be produced and values of the photon index could be constrained, and NGC 7213 (data from Emmanoulopoulos et al. (2012)). In the cases of NGC 3998 and NGC 7213, the flux was scaled from the 3.3-20 keV flux according to the best-fitting model. Objects which did not have enough data to be flux-binned are plotted individually in grey and labelled. The dashed line is the fit to a sample of LLAGN from (Constantin et al., 2009), the dotted line is the fit to a sample of higher Eddington rate radio-quiet AGN from (Shemmer et al., 2006). Error bars show the one-sigma confidence levels. The black hole masses and distances used to calculate the Eddington luminosities and the X-ray luminosities are shown in Table 2.11.

Object	Log(L_{R}, 5GHz) (ergs s^{-1})	Log($L_{X,2-10keV}$) (ergs s^{-1})	Log(L_x/L_R)	L_{bol} (ergs s^{-s})	Eddington Ratio (L_{bol}/L_{Edd})	Log(Mass) ($M_{\odot}$)	Dist (Mpc)
NGC 1052	35.4^a	39.8	4.40	42.2^p	7.3×10^{-5}	8.3^r	19.0
NGC 1068	36.9^b	39.8	2.90	45.0^r	5.0×10^{-1}	7.2^r	12.25
NGC 2655	36.3^d	41.2	4.91	42.2*	3.6×10^{-4}	7.8^{ee}	24.4
NGC 3031	36.8^c	41.9	5.10	41.5^m	3.5×10^{-5}	7.9^t	3.63
NGC 3147	38.0^d	40.4	2.40	41.4*	5.3×10^{-6}	8.8^bb	43.7
NGC 315	39.7^d	41.6	1.87	42.6*	6.1×10^{-5}	8.9^r	51.3
NGC 3226	37.3^d	40.4	3.10	41.4*	2.0×10^{-5}	8.2^{bb}	26.35
NGC 3227	36.3^d	41.0	4.70	43.1^s	1.3×10^{-2}	7.6^x	20.85
NGC 3628	39.2^e	40.2	1.00	41.2*	-	-	11.25
NGC 3998	38.2^d	41.4	3.20	43.5^r	3.2×10^{-4}	9.0^r	18.65
NGC 4051	37.0^b	41.8	4.80	42.6^s	1.9×10^{-2}	6.2^x	15.5
NGC 4151	39.8^f	44.1	4.30	44.0^s	1.8×10^{-2}	7.7^y	16.2
NGC 4258	35.8^d	40.4	4.57	43.5^r	6.1×10^{-3}	7.6^z	7.56
NGC 4321	35.7^g	39.7	4.01	43.5^n	3.6×10^{-2}	6.8^{bb}	16.0
NGC 4388	39.0^b	43.1	4.10	43.7^s	6.5×10^{-2}	6.8^{bb}	18.55
NGC 4395	34.8^d	40.0	7.20	40.7^aa	3.9×10^{-2}	5.6^{aa}	4.3
NGC 4472	36.5^d	40.3	3.80	41.5*	1.5×10^{-6}	8.8^{ff}	15.9
NGC 4486	38.9^d	42.6	3.70	43.8*	1.6×10^{-4}	9.5^{bb}	16.5
NGC 4579	37.7^d	42.2	4.50	42.0^o	1.1×10^{-4}	7.9^{bb}	20.5
NGC 4736	37.6^f	39.9	2.3	41.1*	5.6×10^{-5}	7.0^{cc}	4.86
NGC 5194	36.7^f	39.2	2.46	43.8^r	5.7×10^{-2}	7.0^{bb}	7.94
NGC 5548	36.1^b	40.8	4.70	44.1^s	1.6×10^{-2}	7.8^y	92.50
NGC 5806	-	39.9	-	40.9*	-	-	26.1
NGC 7331	37.2^e	39.8	2.61	40.8*	2.3×10^{-5}	7.6^{dd}	14.55
NGC 7213	38.7^i	42.1^k	3.40	43.0^n	7.4×10^{-4}	8.0^r	22.00
Sag A*	32.6^j	33.4^l	0.80	41.0^o	1.0×10^{-5}	6.6^v	8.33×10^{-3}

Table 2.11: Radio luminosities at 5Ghz and 2-10 keV X-ray luminosities, Eddington ratios, masses and distances for all 24 AGN, plus NGC 7213 and Saggitarius A* for comparison. The ratios between the luminosities of each object are also given. Data taken from: (a) Horiuchi et al. (2004), (b) Gallimore et al. (2004), (c) Perez-Olea & Colina (1996), (d) Nagar et al. (2005), (e) Sramek (1975), (f) Laurent-Muehleisen et al. (2008), (g) Filho et al. (2006), (h) Irwin et al. (2015), (i) Bell et al. (2011),(j) Zhao et al. (2001), (k) Emmanoulopoulos et al. (2012), (l) Baganoff et al. (2003), (m) Ho et al. (1996), (n) Ptak (2004), (o) Lewis & Eracleous (2006), (p) Skipper (2013), (q) Starling et al. (2005), (r) Woo & Urry (2002), (s) Vasudevan & Fabian (2009), (t) Devereux et al. (2003), (u) Walsh et al. (2012), (v) Gillessen et al. (2009), (w) McHardy et al. (2014), (x) Denney et al. (2010), (y) Bentz et al. (2006), (z) Herrnstein et al. (2005), (aa) Peterson et al. (2005), (bb) Merloni et al. (2003) (cc) Hernández-García et al. (2014) (dd) Filho et al. (2004), (ee) Gu & Cao (2009), (ee) Panessa & Giroletti (2013), (ff) Ho (1999), * - using bolometric corretion, x16. Dashes indicate that no measurement known to the authors exists.

Chapter 3

Long-term Absorption Variability in the X-Ray Spectra of AGN

"This wild Abyss
The womb of Nature, and perhaps her grave
Of neither sea, nor shore, nor air, nor fire,
But all these in their pregnant causes mixed
Confusedly, and which thus must ever fight"
John Milton, *Paradise Lost*

3.1 Introduction

X-ray spectral observations have shown that variability in the column of absorbing material between the X-ray source and the observer is present in many Seyfert galaxies (Risaliti et al., 2002), as described in section 1.4.2. The detection of variable absorption on a timescales of hours has indicated that the absorbing material must be close to the nucleus, at a distance similar to that of the Broad Emission Line Region (e.g. Elvis et al., 2004, Lamer et al., 2003, Puccetti et al., 2007). Claims also exist that complete occultations by Broad Line Region 'clouds' have been observed on timescales of days (Risaliti, 2007). It is also known that X-ray-absorbing disc winds are present in many of these systems and contribute to absorption - the existence of absorbing outflows in

Seyferts is well established observationally (Tombesi et al., 2013). The nature of these winds is not well known, however, including the timescales of any variability in their obscuration of the X-ray source, if such variability exists.

The long time-scale (months-years) variability of X-ray absorbers in AGN has not previously been studied in detail, most studies having concentrated on short-term variations. A study by Markowitz et al. (2014) showed the long-term absorption variability of a sample of Seyfert AGN, however they used *RXTE* data which, which an energy range of 3-20 keV, is sensitive only to high absorbing columns (10^{22-25} cm^{-2}) and focused on ‘eclipse events’, caused by clumps of material crossing the line of sight, thought to exist in the BLR or torus. The changes in absorption at lower absorbing columns known to be common in Seyfert AGN have not been studied on long time scales. Long-term changes which are not necessarily part of ‘eclipse events’ in which the absorbing column increases then returns to its previous level, but are increases or decreases due to other changes in the absorbers, have also not been studied previously.

In this chapter, I discuss the study of the absorption variability of three Seyfert galaxies on these long timescales, using the wealth of data available in the *Swift XRT* data archive. The *Swift XRT* has an energy range of 0.3-10 keV, allowing it to probe absorbing columns in the 10^{19-22} cm^{-2} range. Whilst *Swift* does not provide spectral resolution as high as that used in many previous short-time X-ray spectral studies, e.g. with *XMM-Newton* or *Suzaku*, the *Swift* data cover a longer time period and a greater flux range for the three sources. The *Swift* data therefore allow proper investigation of flux-related spectral variability and of long term spectral variations, over a much larger dynamic range than in previous studies. Here, I use several hundred individual *Swift* spectra of the three AGN taken over a period of 6-9 years, which cover the entire flux range of these systems.

3.2 Three Absorption-Variable Seyfert AGN

Three Seyfert AGN known to exhibit spectral variability due to absorption variability, and for which there was a large quantity of *Swift* data, were selected for study. All three AGN are relatively nearby and cover a range of physical parameters; the physical attributes of the three Seyfert AGN are shown in Table 3.1. Details of previous spectral studies of each object are given below.

3.2.1 NGC 1365

NGC 1365 is a nearby Seyfert 1.8 galaxy (Maiolino & Rieke, 1995) of mass $\sim 2.9 \times 10^7\ M_{\odot}$ citep[][]Risaliti2009 which displays a large amount of X-ray spectral variability (Risaliti et al., 2009) on timescales of hours to years (Brenneman et al., 2012). These variations have been interpreted as the spectrum changing from being 'transmission dominated' to 'reflection dominated'. When the spectrum is 'transmission dominated' (e.g. Risaliti et al., 2000) the absorbing material is Compton thin and the transmitted component dominates the spectrum; when the spectrum is 'reflection dominated' (e.g. Iyomoto et al., 1997) the absorbing material is Compton thick, meaning the majority of direct emission is absorbed and reflected emission dominates the spectrum (Matt et al., 2003, Risaliti et al., 2007b).

A number of absorption and emission lines have been seen in the spectrum. A strong Fe fluorescence emission line is present at 6.4 keV, together with a group of Fe absorption lines between 6.7 and 8.3 keV, attributed to FeXXV and FeXXVI Kα and Kβ transitions. The measured velocities of these lines has lead to speculation that they originate from a highly-ionised, high-velocity outflow from NGC 1365 (Risaliti et al., 2005b).

The spectrum of NGC 1365, as with most AGN, has previously been modelled using a power law component, with an intrinsic spectral index, Γ. It is not known whether Γ varies or not during changes in X-ray luminosity. Many groups (e.g. Fabian et al., 2005, Miller et al., 2008, Pounds et al., 2004, Turner et al., 2007) assume that there is no change. Observations in the $2-10$ keV band generally do show some variation, although the changes with luminosity are not large (e.g. Sobolewska & Papadakis, 2009, Zdziarski et al., 1999). Sobolewska & Papadakis (2009), for example, who simply fit a power law to the 2-10 keV spectra, find that the observed Γ varies as 2.7these measurements of Γ are, of course, depend on other parameters which were not included in the fits, such as the reflection component and any absorption. If the variation in the observed spectral index is interpreted in terms of the sum of a variable, steep spectrum component and a relatively constant reflection component with a hard spectrum, the intrinsic spectral index can remain constant; in this case, when the flux of the variable steep spectrum component is low, the hard spectrum component dominates, causing the observed spectral index to change (e.g. Fabian & Vaughan, 2003, Guainazzi & Antonelli, 1999, Ponti et al., 2006, Uttley et al., 1999). Furthermore, where observations with a large spectral range have been made, allowing good definition of the primary continuum slope, the observed variation of Γ with luminosity has not been large (e.g. 0.1 in NGC 4151, Lubiński et al. 2010), 0.2 in NGC 4507, Braito et al. 2013).

Theoretical Comptonisation modelling (e.g. Beloborodov, 1999b, Coppi, 1992) shows that the photon index can depend on the ratio of L_{diss} to L_s (where L_{diss} is the power dissipated in the corona during variations and L_s is the input soft photon luminosity) to a low power (-0.1 for AGN). Unless there are very large variations in these parameters, the intrinsic spectral index should therefore not change by more than a few tenths. Thus, although it is possible that a small change in spectral index may occur over the flux range sampled by my observations, the large changes in Γ required by the pivoting power law models are assumed to be unlikely. In many of my models, including the model I deem most accurate, I therefore assume Γ to be constant, as this is likely to be a reasonable approximation.

The variability of the spectrum of NGC 1365 has previously been modelled using a partial covering model, in which a varying fraction of the X-ray source is obscured by absorbing material (e.g. Risaliti et al., 2009). This model has been found to fit the data for individual, short-timescale events and is therefore also tested here.

Although there have been many previous X-ray spectral studies of NGC 1365, these studies have all concentrated either on detailed analysis of a single epoch spectrum or on analysis of a small number of spectra taken over a relatively short timescale (hours or days).

3.2.2 Mkn 335

Mkn 335 is an X-ray bright Seyfert 1 galaxy, with a well-measured mass of 1.4×10^7 $M_\odot$ measured with reverberation mapping (Peterson et al., 2004). Large-amplitude X-ray variability on timescales of days to years have been observed in this system (Grupe et al., 2012). Many previous spectral studies of individual epochs have been carried out on Mkn 335. A strong soft X-ray excess was found by Pounds et al. (1986) and Turner et al. (1993), using the it European X-ray Observatory Satellite (EXOSAT) and the *Broad Band X-ray Telescope (BBXRT)* respectively. The shape of the spectrum has been variously attributed to both a warm absorber (e.g Leighly, 1999, Nandra &

Pounds, 1994) and X-ray reflection from the accretion disc (e.g. Ballantyne et al., 2001, Larsson et al., 2008, Longinotti et al., 2007), though in most cases neither model could be completely ruled out. The majority of these studies have used data from periods when Mkn 335 was in a high-flux state; the only two studies to have modelled the spectrum during a low X-ray flux state are Pounds et al. (1986), who found a two-component model consisting of two power laws, one of which is absorbed by a column of 10^{20-21}cm^{-1}, and Grupe et al. (2008), who found both blurred reflection and partial covering models to be statistically well-fitting.

Photon indices of $\Gamma_{hard} = 1.7 - 2.2$ are measured in most cases for the hard component of the spectrum, however the soft component is generally measured to be significantly softer, with values of $\Gamma_{soft} = 2.2 - 2.8$. Recent studies using *NuStar*, which has a large energy range extending to very hard X-ray energies (3-79 keV), at which very little absorption occurs, have found reflection models to fit the spectrum well, with photon indices of $\Gamma = 1.9 - 2.5$ (Parker et al., 2014, Wilkins et al., 2015).

A number of emission lines have been found in the spectrum of Mkn 335, including a strong Fe fluorescence line at 6.4 keV and highly-ionised lines including Fe XXIII-XXVIII, O VII, Ne IX, and Mg XI (Grupe et al., 2008). The highly-ionised state of the emitting gas implies that it is very close to the X-ray source (Longinotti et al., 2008). The velocities of the X-ray emission lines are not well constrained, however, though an optical study by van Groningen (1987) did suggest that evidence of a low-density high-ionisation outflow is present in the optical spectrum of Mkn 335. As with NGC 1365, despite the large number of spectral studies of individual epochs, there are no existing studies of the long-term spectral variability of Mkn 335.

3.2.3 NGC 5548

NGC 5548 is an X-ray bright Seyfert 1 galaxy, with a mass of $4 - 6 \times 10^7\ M_\odot$ measured with reverberation mapping (Bentz et al., 2007, Pancoast et al., 2014b). It shows large-amplitude X-ray variability on timescales of days to years (McHardy et al., 2014). Many previous spectral studies of individual epochs have been carried out on NGC 5548, generally concluding that the X-ray spectrum consists of a power law absorbed by a moderately-ionised absorber, and a contribution from distant cold reflection (e.g Branduardi-Raymont, 2005, Brenneman et al., 2012, Pounds et al., 2003). Many of these papers also suggest the presence a soft excess below 0.7 keV (Done et al., 1995, Pounds et al., 2003, e.g.), however a study by Nicastro et al. (2000) suggested that a soft excess is not required, and that the spectral variability can be explained by changes in the slope of the power law alone. A long-term study of the spectral index in the 2-10 keV band using *RXTE* found little to no variation in Γ (Sobolewska & Papadakis, 2009) on average, though with a large scatter.

Ebrero et al. (2014) carried out a study of the long-term variability of the long-term absorption variability of NGC 5548, concluding that it possess a multi-phase warm absorber, the absorption from which varies solely due to changes in ionisation state due to changes in the ionising continuum. However, this study used only grating spectra to estimate ionisation states and outflow velocities and did not look at the broadband variability due to absorption. Furthermore, although the study by Ebrero et al. (2014) does cover a long time-period ($\sim$ 8 years) it utilises only 12 observations; our data covers a slightly longer period ($\sim$ 9 years) and has a significantly larger number of individual observations (over five hundred).

A great deal of spectral evidence exists for an outflow from NGC 5548 in the form of a fast, highly-ionised wind in addition to lower-ionisation, lower-velocity outflowing material thought to lie further from the black hole; Doppler-shifted absorption lines are seen in both the X-ray and UV spectrum (Cappi et al., 2016, Ebrero et al., 2014, Kaastra et al., 2014).

	Black Hole Mass [1,2,3] ($M_\odot$)	Eddington Ratio [4,5,6] (L_{Bol}/L_{Edd})	Viewing angle [7] (°)
NGC 1365	2.0×10^6	0.02	$36 - 60$
NGC 5548	6.5×10^7	0.04	$22 - 40$
Mkn 335	2.5×10^7	0.38	$38 - 49$

Table 3.1: Physical parameters of each of the three Seyfert galaxy nuclei, taken from [1] Risaliti et al. (2013), [2] Bentz et al. (2006), [3] Grier et al. (2012), [4] Risaliti et al. (2005a), [5] Uttley et al. (2008), [6] Vasudevan & Fabian (2007), [5] Emmanoulopoulos et al. (2014).

3.3 Observations & Data Reduction

Observations of NGC 1365, NGC 5548 and Mkn 335 were all made using *Swift* and have been carried out as part of a number of different programmes, the combined data from which have been used in this study. The observations were performed using the

Swift XRT in 'photon counting mode', between April 2005 and August 2015. Individual exposure times ranged from $<$ 10 seconds to $>$ 5000 seconds. Table 3.2 gives details of all observations used in this study. The raw data for all *Swift XRT* observations were downloaded from the HEASARC archive[1].

The XRT data were reduced using an automatic pipeline, previously used in e.g. Cameron et al. (2012), Connolly et al. (2014, 2016a). In each case, the reduction used the most recent version of the standard *Swift* XRTPIPELINE software (versions 0.12.4 - 0.12.6). The XSELECT tool was used to extract spectra and light curves, using flux-dependent source and background extraction regions which were chosen such as to reduce the background contamination at faint fluxes, and to mitigate the effects of pile-up at high fluxes. The sensitivity of the XRT is not uniform over the field of view, due to vignetting and the presence of bad pixels and columns on the CCD; the *Swift* XRTEXPOMAP and XRTMKARF tools were therefore used to generate an exposure map (including vignetting and bad pixels) and an ancillary response file (ARF) for each visit, in order to correct for these effects. The relevant redistribution matrix file (RMF) from the *Swift* calibration database was also supplied in each case. The local X-ray background was estimated and subtracted from the instrumental count rates, using the area-scaled count rate measured in a background annulus region. The observed XRT count rates were carefully corrected for the fraction of counts lost due to bad pixels and columns, vignetting effects, and the finite extraction aperture (including regions excised in order to mitigate pileup effects).

Fig. 3.1 shows a $0.5 - 10.0$ keV light curve of all of the *Swift* data over the six-year period of observation. The large flux range is readily apparent on a range of timescales.

3.3.1 NGC 1365

A total of 293 spectra from individual *Swift* 'visits', or exposures, were used, with a total of more than 220 kiloseconds of exposure time. More intensive monitoring took place between MJD 56220 - 56330, due to Supernova 2012fr, which went off in NGC 1365 during this period (but which was neither bright enough nor close enough to the nucleus to affect the data used in this study (e.g. Childress et al., 2013, Klotz et al., 2012)). Of the 293 spectra, 103 were rejected due to either very low signal to noise or

---

[1] http://heasarc.gsfc.nasa.gov/cgi-bin/W3Browse/swift.pl

artifacts near the source, leaving 190 usable spectra, consisting of ∼ 165 kiloseconds of exposure time and over 25000 photon counts.

Chandra images show that the nucleus of NGC 1365 is embedded within a region of extended low surface brightness emission, of radius approximately 15 arcsec (see Wang et al. 2009). The region used to determine the *Swift* background contribution lies outside this small region of extended emission. Thus, a contribution from the constant extended emission within the *Swift* PSF will remain in my *Swift* spectra. To determine what that contribution is, I examined *Chandra* spectra of the extended emission region. The *Chandra* data used were taken in December 2002, using the ACIS-S instrument (OBSID 3554). Four spectra were extracted from circular regions, of size similar to the *Swift* PSF, lying close to the nucleus. The spectra were extracted from the the event files in the primary (reduced) data set, using the CIAO 4.6 tool ‘specextract’. Extraction regions of radius 2 arcsecs were used in each case.

3.3.2 NGC 5548

Observations of NGC 5548 consisted of a total of 878 spectra from individual *Swift* visits’, and more than 518 kiloseconds of exposure time. Of the 878 spectra, 155 were rejected due to either very low signal to noise or artifacts near the source, leaving 723 usable spectra, with a total of ∼ 472 kiloseconds of exposure time and over 170000 photon counts. The majority of the data is from MJD 56020 - 56830, during which time a long-term monitoring campaign took place; the latter portion of this period (from ∼MJD 56380 onwards) is particularly intensive, with approximately two observations made per day.

3.3.3 Mkn 335

The Mkn 335 observations were total of 551 spectra from individual *Swift* visits, consisting of more than 386 kiloseconds of exposure time. Of the 551 spectra, 82 were rejected due to either very low signal to noise or artifacts near the source, leaving 469 usable spectra, with a total of ∼ 1455 kiloseconds of exposure time and over 82000 photon counts. The Mkn 335 data cover the ∼ 7 year period for which there are data fairly evenly, with no significant gaps or particularly intensely monitored periods.

Object	Obs IDs	MJD range	N_{obs}	N_{visits}	T_{tot} (s)	$Cnts_{tot}$
NGC 1365	00035458001-002	53937.0-53940.8	2	20	14714	433
	00090101001-009	54964.0-55117.5	8	56	44576	8795
	00035458003, 00080317001, 00032614001-071	56134.1-56368.5	41	114	105515	16227
	Total	53937.0-56368.5	51	190	164805	25455
NGC 5548	00030022004-237	53468.4-56743.9	129	166	113438	43044
	00033204001-255	56739.1-56828.8	161	163	93552	40550
	00080131001	56647	1	2	19523	485
	00091404001-069	56021.9-56356.7	60	63	58881	21715
	00091711001-140	56383.7-56547.1	105	207	122016	38233
	00091737001-014	56387.6-56399.7	14	23	867	159
	00091739001-014	56401.7-56413.3	13	27	14896	3524
	00091744001-052	56509.0-56431.2	46	66	62960	22086
	00091964001-004	56827.4-56829.9	4	6	3474	1368
	Total	53468.4-56829.9	533	723	472037	171164
Mkn 335	00035755001-027	54237.0-54474.9	16	119	69400	17107
	00090006001-076	55233.2-54618.6	61	175	1233356	41497
	00035755029-222	55337.1-56677.9	144	175	146022	23750
	Total	54237.0-56677.9	221	469	1448778	82354

TABLE 3.2: Summary of *Swift* observations of NGC 1365 used in this Chapter. N_{obs}, N_{visits} and T_{tot} are the values remaining after unusable data has been excluded.

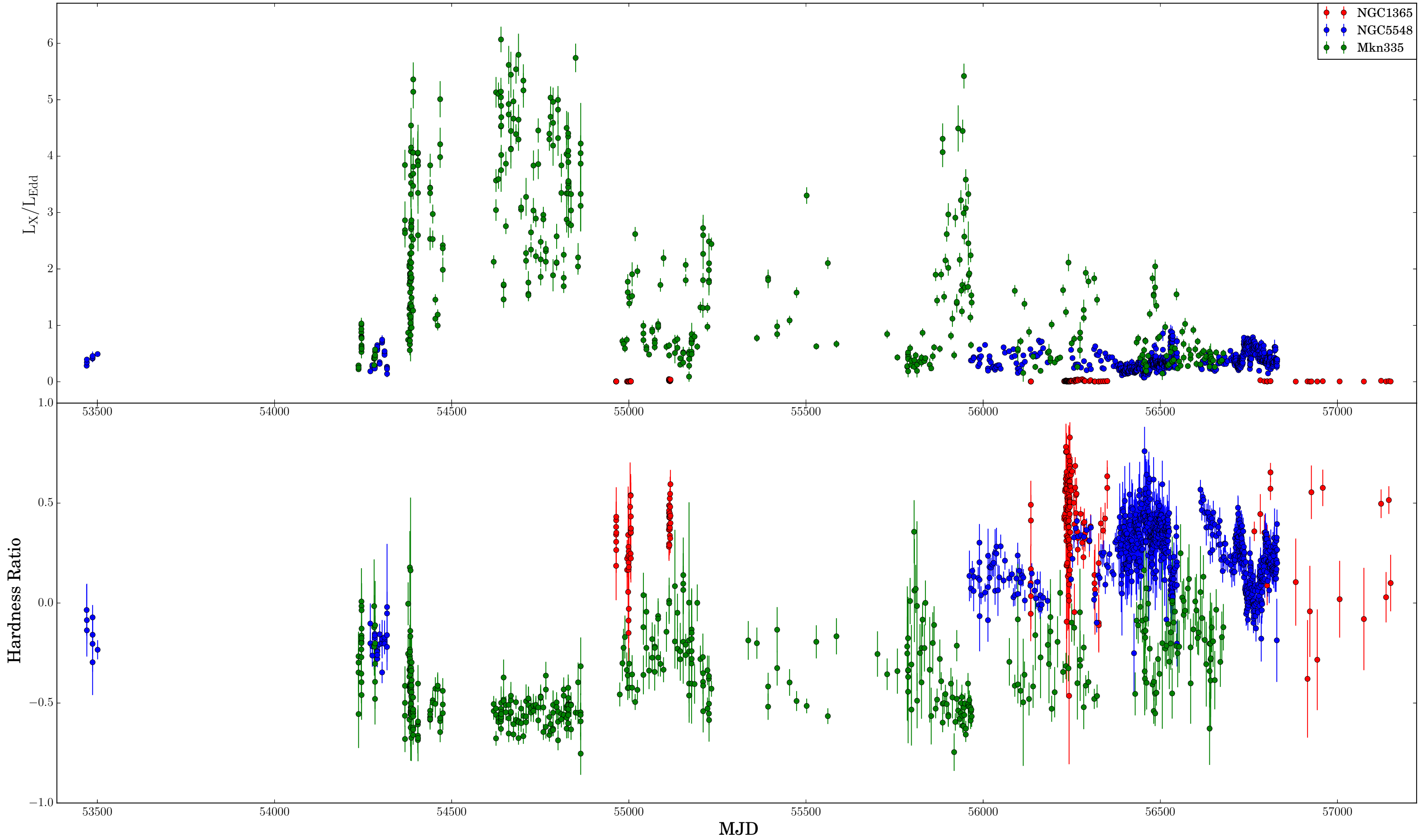

FIGURE 3.1: The ratio of 0.5-10 keV X-ray luminosity to Eddington luminosity of each source over time, as a proxy for the Eddington ratio.

3.4 Spectral Hardness

Plots of the hardness ratio against the hard count rate, and the hard count rate against the soft count rate are shown in Figs. 3.2 and 3.3, respectively. Whereas most previous measurements of the photon index, Γ, concentrate on the $2.0 - 10.0$ keV energy band, here I look at spectral shape across a broader range of $0.5 - 10.0$ keV. As lower energies are more sensitive to absorption, this energy range allows a more complete look at spectral changes due to absorbing material. In each case, hard emission is defined as $2.0 - 10.0$ keV and soft emission as $0.5 - 2.0$ keV (see Section 1.3.4).

The hardness ratios show similarities in the spectral variation of all three AGN. The hardness ratio of NGC 1365 shows the clearest behaviour; its spectrum starts extremely soft at very low fluxes, but becomes hard very rapidly with with increasing flux. Beyond this sharp rise, still at a relatively low flux, the hardness decreases again more gradually with increasing flux, as often seen in Seyfert galaxies within the $2.0-10.0$ keV band (e.g. Lamer et al., 2003, Sobolewska & Papadakis, 2009). The data display a relatively small amount of scatter about this general trend; for this reason, the shape of the spectrum can be assumed to be approximately similar at a given flux level, independent of time. This implies that the system is behaving in approximately the same manner at each flux level, irrespective of what state the system was in at an earlier time.

The hardness ratio of Mkn 335 appears to follow a similar pattern to NGC 1365, starting soft at the lowest fluxes, hardening with increasing flux to a certain flux then softening again with increasing flux, in the manner normally observed in Seyfert AGN. Unlike NGC 1365, however, the hardness ratio shows a relatively large amount of scatter, though the scatter becomes relatively small at higher counts. The hardness ratio of Mkn 335 also does not soften to, or below, the level it reaches at the highest count rates, unlike NGC 1365. This may be due to the fact that Mkn 335 is observed at a higher luminosity as a fraction of the Eddington luminosity on average and has not been seen at luminosities as low as those seen in NGC 1365.

The hardness ratio of NGC 5548 appears to shows the softening with increasing count rate normally observed in Seyfert AGN, but does not the show hardening with increasing count rate seen in the other two objects as clearly, though the binned data due show hints of it. The NGC 5548 hardness ratios also display a reasonably high level of scatter, as well as a significant number of very soft data points at lower fluxes beyond the main scatter of the data.

As NGC 1365 shows a very small amount of scatter in hardness at a given flux compared to the other two AGN, the spectra could be binned by flux, giving a high signal-to-noise ratio spectrum at each flux level. As Mkn 335 and NGC 5548 show much greater variation in hardness at a given flux, this assumption is not valid for these objects. Their spectra were therefore binned in both flux and time intervals and the results of spectral fitting to both taken into account.

3.5 Spectral Modelling

As the majority of the *Swift XRT* spectra from all three sources were too short to have high-enough signal-to-noise ratios (SNRs) for meaningful spectral analysis, the spectra were binned in flux and, in the case of NGC 5548 and Mkn 335, in time. This produced spectra with high enough SNRs for spectral fitting. In the case of flux-binning, the bins were chosen such that each binned spectrum had both a minimum of 1500 total counts and a minimum width of 0.025 counts s^{-1} across the total range of hard count rates (2-10 keV). The time-binned spectra of Mkn 335 and NGC 5548 were binned such that the resultant spectra covered the smallest time period possible whilst having a minimum of 1500 and 3500 counts in total, respectively. The bins also had a maximum width of 50 days - a small number of the time-binned spectra had fewer than 1500 counts even with this bin-width - these spectra were excluded for this reason. In both cases, the binning methods were chosen to ensure that each summed spectrum would possess a sufficient SNR for accurate spectral fitting, but that the bins width (in time or flux) would be as small as possible to give the highest attainable time/flux resolution the data would allow. The time bins into which the spectra of Mkn 335 and NGC 5548 were binned are shown together with their light curves and hardness ratios, and the average flux and hardness of each time bin, in Figs. 3.4 and 3.5. The spectra in a given time/flux bin were combined using the *HEADAS* tool 'addspec'. The energy channels of each of these summed spectra were then grouped, using the *HEADAS* tool 'grppha', such that each group contained a minimum of 15 counts.

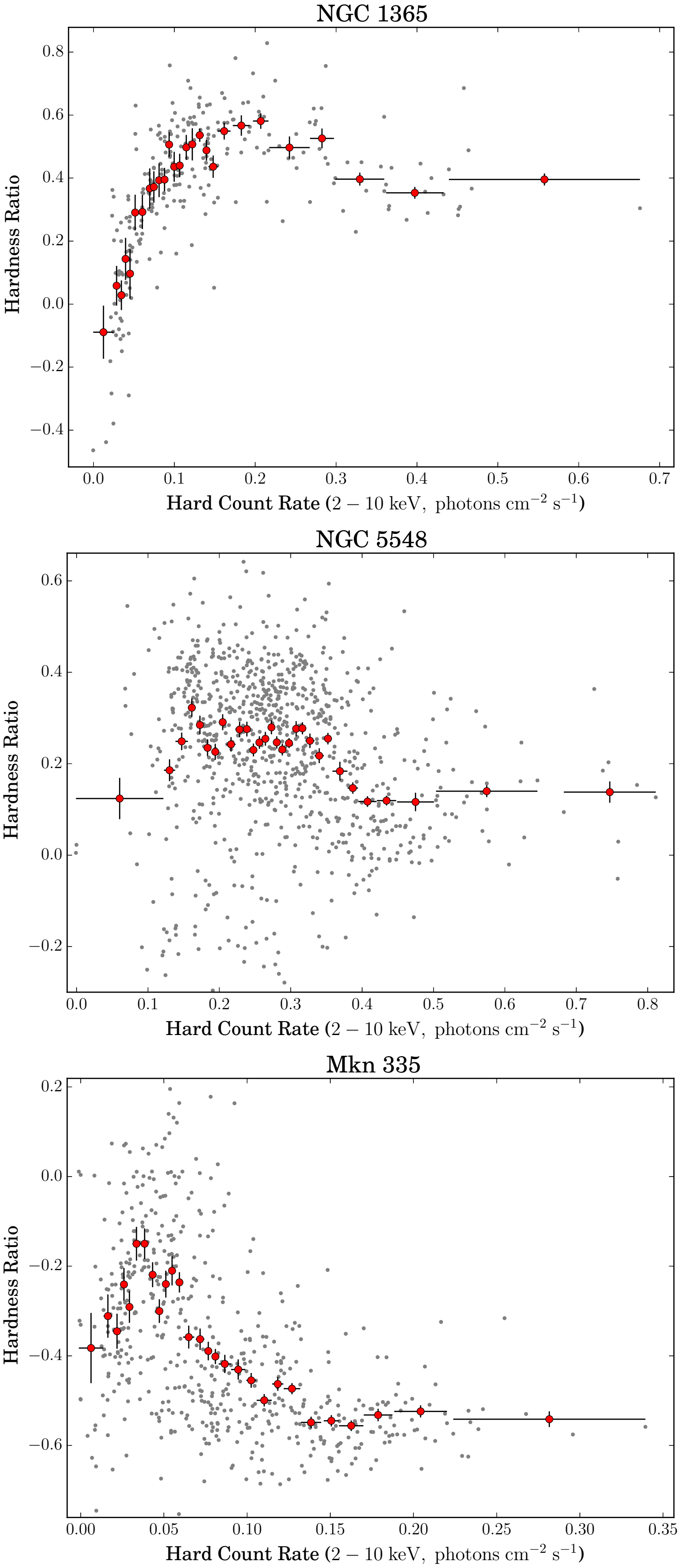

FIGURE 3.2: Plots of the hard count rate against hardness ratio of the three Seyfert AGN. The data are binned such that each bin contains 10, 30 and 20 data points for NGC 1365, NGC 5548 and Mkn 335, respectively. The unbinned data are shown in grey behind the binned data.

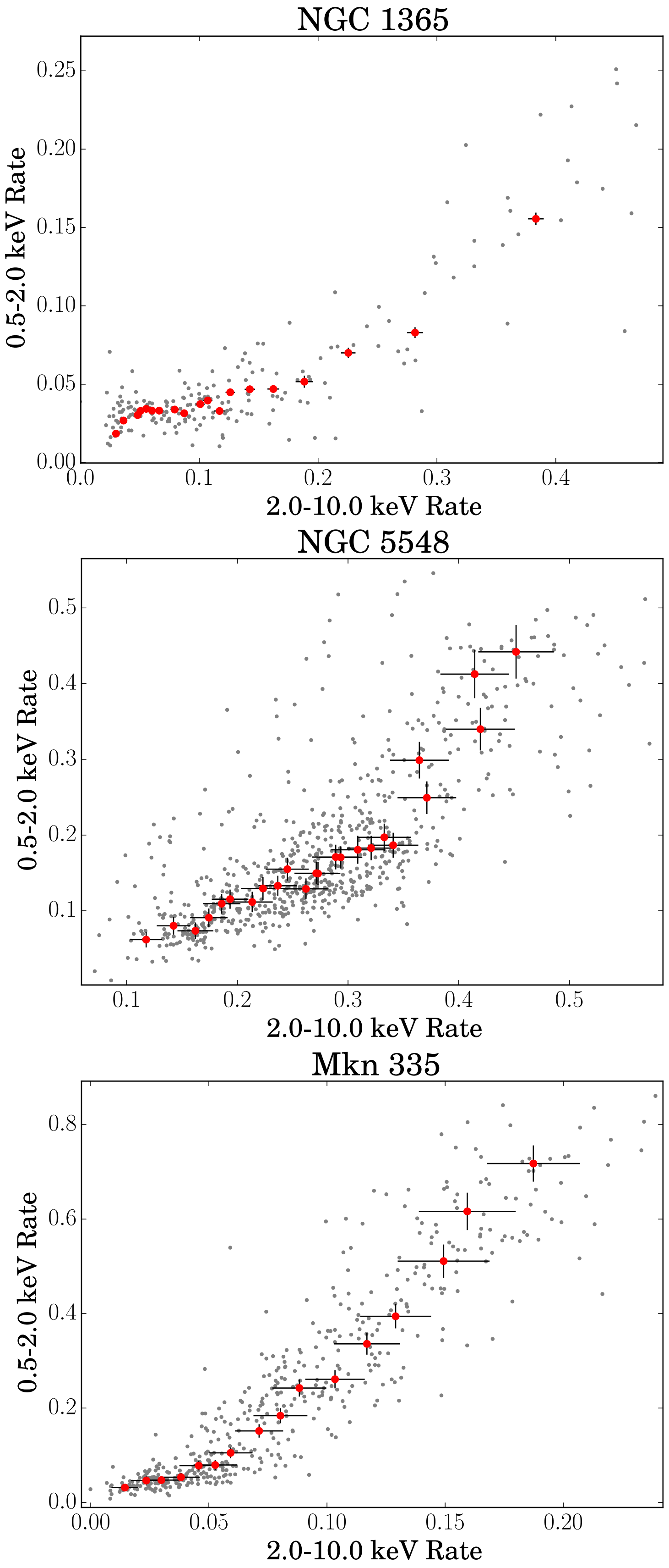

FIGURE 3.3: Plots of the hard count rate against soft count rate of the three Seyfert AGN. The data are binned such that each bin contains 10, 30 and 20 data points for NGC 1365, NGC 5548 and Mkn 335, respectively The unbinned data are shown in grey behind the binned data.

In each case, all of the flux- or time-binned spectra of a given object were fitted simultaneously with a given model, in which parameters were either fixed at a given value, allowed to vary but tied to be same for each spectrum, or free to vary between spectra. Three main sets of models were applied to each spectrum - a single power law absorbed by an ionised absorber, a single power law absorbed by a partially-covering neutral absorber and a two-component model consisting of two power laws with the same photon index, one of which is absorbed by an ionised absorber. Variations of each of these models, in which different combinations of parameters were fixed, tied or free to vary were tested, forming a total of 21 models. Table 3.3 lists these models, their components and whether key parameters were free, tied or fixed. Models 1-4 and 12-15, in which the photon index is fixed, were not applied to the spectra of Mkn 335, as the photon index is not well constrained. The remaining models (5-11, 16-21) were all applied to the spectra of all three AGN. All models also contained a 'wabs' neutral absorption component, with an absorbing column fixed at the the galactic absorbing column in the direction of the source. In all cases, the models were fitted to the data using the *XSPEC* 12.7 analysis package (Arnaud, 1996). The results of the fits of these models to the data are shown in Tables 3.4, 3.5 and 3.6. Details of the fitting for each source individually are given below.

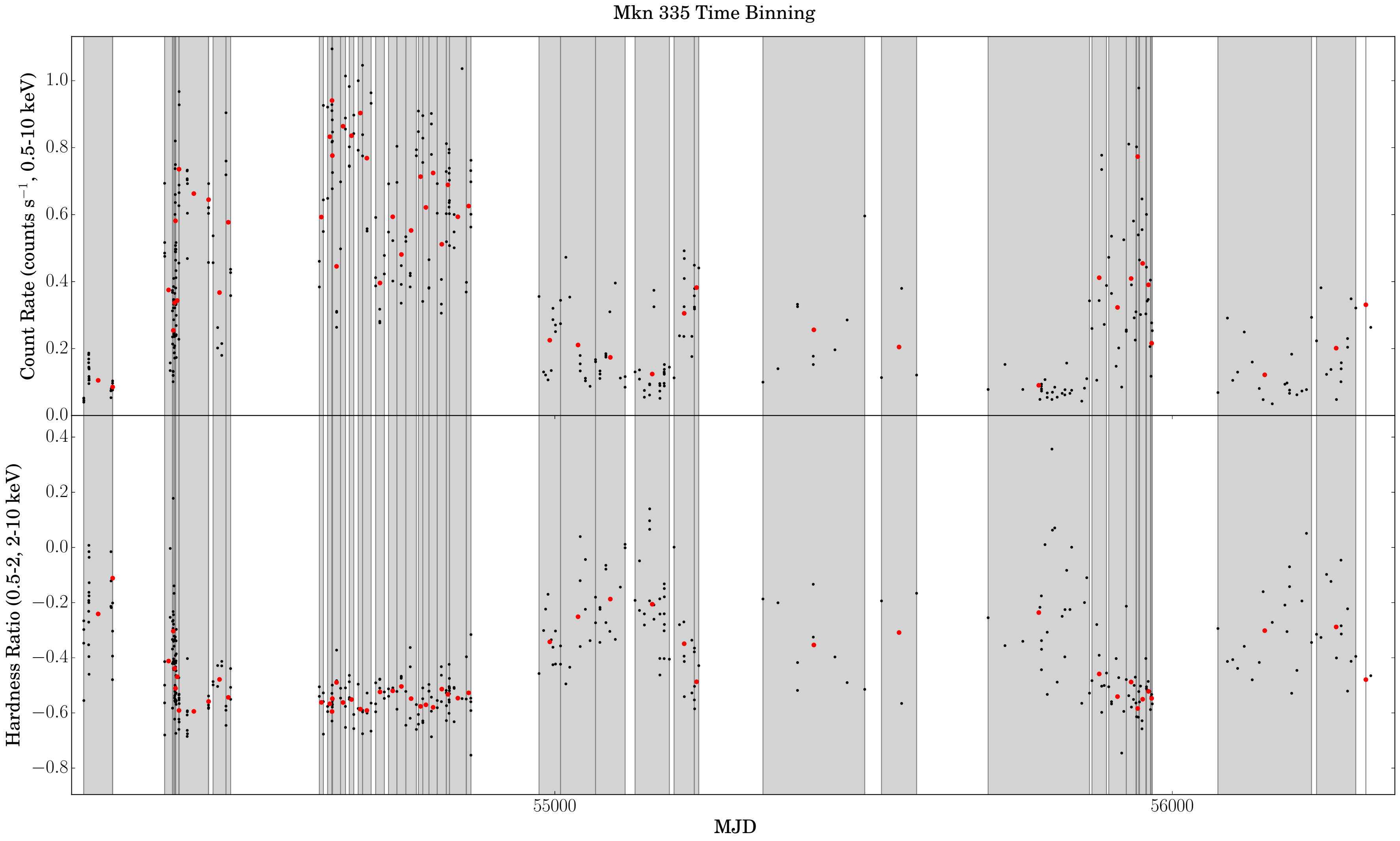

FIGURE 3.4: The light curve (top) and hardness ratio over time (bottom) of the GTI spectra of Mkn 335 (black points), the edges of the time bins into which the GTI spectra were binned (grey boxes) and the average flux of each summed spectrum (red points).

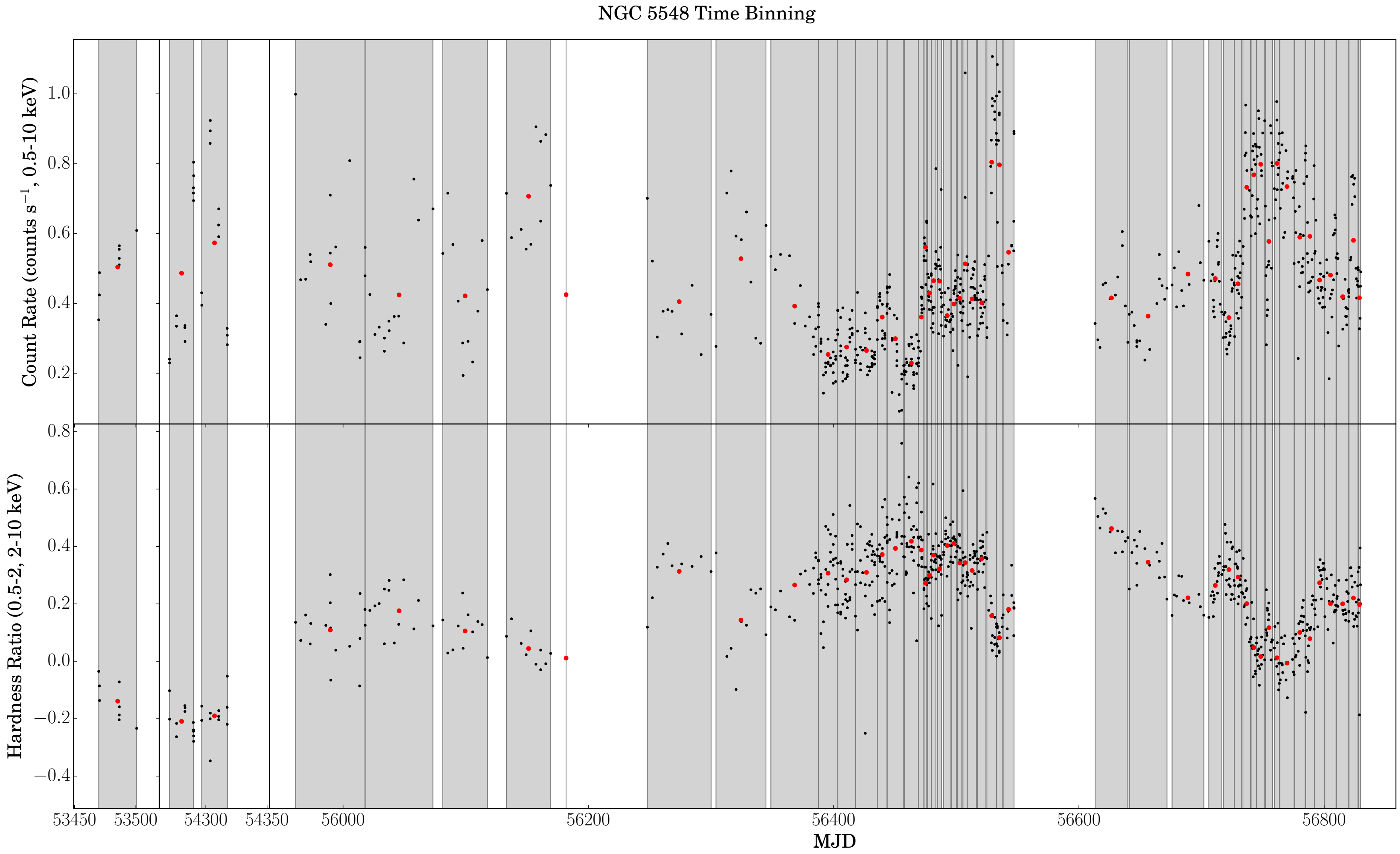

Figure 3.5: The light curve (top) and hardness ratio over time (bottom) of the GTI spectra of NGC 5548 (black points), the edges of the time bins into which the GTI spectra were binned (grey boxes) and the average flux of each summed spectrum (red points).

3.5.1 NGC 1365

To account for the diffuse emission surrounding the nucleus of NGC 1365 (see Section 3.3), four *Chandra* spectra of this emission were fitted. These spectra were composed of a minimum of 1300 total counts. The spectral energy channels were grouped in the same way as the *Swift* spectra, such that each group contained a minimum of 15 counts. The best fitting model is the *apec* model for collisionally-ionised diffuse gas combined with the *tbabs* model for absorption by gas and dust; this is consistent with the best-fit found previously by Wang et al. (2009). A simultaneous fit to 4 regions, allowing N_H to vary, but with all other parameters tied, gave a reduced χ^2 of 0.96, with 197 degrees of freedom. The absorbing column varied a little between regions. However, as a single value is required to fit the average contribution to the *Swift* nuclear spectrum, we fitted all regions with the same N_H, giving a reduced χ^2 of 1.46, with 200 degrees of freedom. In this model, the best fitting parameters were: an absorbing column of $6.97^{-0.02}_{+0.02} \times 10^{20}$ cm^{-2} in addition to galactic absorption, a gas temperature of $0.77^{-0.03}_{+0.03}$ keV, a normalisation of the *apec* model of $5.51^{-0.63}_{+0.73} \times 10^{-4}$, and a metal abundance of $0.069^{-0.010}_{+0.012}$. The unphisically-low value of the abundance implies that the gas is actually a multi-temperature gas, however as the data are well-fitted by the single-temperature model and the parameters of the gas are not of importance here, this model is still used. The components of this model, with each of the parameters fixed at the best fit values, were included in all of the subsequent fits of the *Swift XRT* data.

The 190 separate time-resolved spectra of NGC 1365 were summed into 11 flux bins for fitting. When modelling the resultant XRT background-subtracted nucleus, it was discovered that a single, unabsorbed power law of photon index ~ 1.92 (as found by Risaliti et al. 2013), fitted the lowest flux observations very well, except for a small excess at higher energies ($>\sim 4.0$ keV). With increasing total flux, this excess was seen both to increase in flux relative to the lower energy component and to expand to lower energies, such that the single power law model become increasingly inadequate. At the highest fluxes, it was found that a single power law would fit the data very well if absorbed by a partially ionised absorbing column. This model was, however, still insufficient to give a good fit at intermediate fluxes, as these spectra had a comparable flux at both the low- and high-energy ends of the spectra.

Motivated by the steep unabsorbed spectrum, with its high energy excess, found at low fluxes, and the absorbed component found at the higher fluxes, a set of two-component and partial covering models were fitted to the data (see models 1-10 and 16-26 in Table 3.3). These models were found to fit the data well in simultaneous fits of the spectra from all flux ranges. This was then the motivation for testing the same set of models to NGC 5548 and Mkn 335.

In the two-component models in which the photon index was fixed to be the same at all flux-levels (1-4), it was set to $\Gamma = 1.92$, the value found by Risaliti et al. (2013) using the very wide spectral range allowed by *NuStar*. It was possible to obtain equally good fits at all fluxes using a single absorbed pivoting power law (models 11-14) and better fits using two pivoting power laws of the same spectral index (models 8-10). However, the best fitting models of this kind required a very large range of Γ (from ~ 0.6 to $>\sim 1.8$), and, very unusually, an extremely low value of Γ at high fluxes. As described in Section 3.2, this is considered to be unphysical over the observed luminosity range.

In all models, the absorbed power law was modelled using the *absori* model for an ionised photoelectric absorber. The absorber temperature was tied in all fits. A redshift of 5.569×10^{-3} (Lavaux & Hudson, 2011) and an iron abundance of 2.8 times solar abundance, as found by Risaliti et al. (2009), were used in all fits. Galactic absorption of 1.39×10^{20} cm^{-2} was also included in each model, using the *wabs* model for electromagnetic absorption (Dickey & Lockman, 1990).

As the absorbing column approaches a value at which Compton scattering starts to become important ($\gtrsim 10^{22} cm^{-2}$), the effects of Compton Scattering on the fits were tested by adding the *cabs* model in *XSPEC* (see model 12 in Table 3.3). The inclusion of this model was found to have very little effect on the best fit parameters, or the goodness of fit. This result is not unexpected, as the highest measured absorbing column is 1.0×10^{24}cm^{-2}, which is below the column required to be Compton thick (1.5×10^{24} cm^{-2}, see Malizia et al. 2009).

In model 3 of Table 3.3 the absorbing column is neutral, i.e. the ionisation state is fixed at zero. The best fit in this model is almost the same as those in which the ionisation is free (models 1 and 2). Thus, although the value of the absorbing column has a large effect on my fits, the ionisation state is not well constrained.

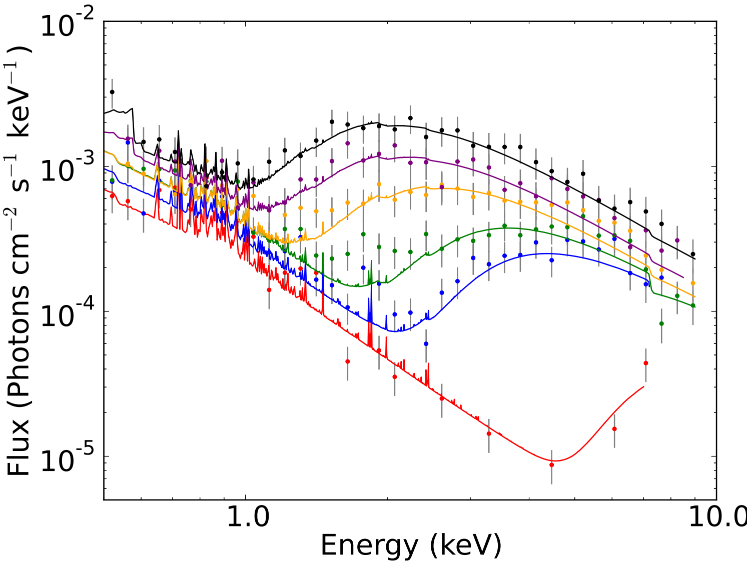

FIGURE 3.6: A sample of the set of unfolded, summed spectra of NGC 1365 produced by combining spectra in the same flux range. Alternate spectra are excluded, to prevent the plot being crowded. The spectra are simultaneously fitted with the best fitting model, consisting of two power laws, one of which is absorbed by a partially ionised absorbing column (using the 'absori' model) and one of which is not. This model gives best-fit parameters of $\xi = 0.40$, $N_H = 1.70 - 100.0$ and effective covering fractions (assuming the unabsorbed power law is the uncovered component of a partially absorbed power law) of 0.963-0.973.The parameter values for the equivalent 'zxipcf' model were very similar, though the column of the most obsorbed spectrum was higher ($\xi = 0.61$, $N_H = 1.70 - 340.0$, covering fraction 0.964-0.976). The photon index was fixed at 1.92 in both cases (see text).

Finally, a set of partial covering models were fitted to the data, as this type of model has previously been found to be successful in modelling changes over short timescales (e.g. Risaliti et al., 2009) (see models 16-24 in Table 3.3). The model (*pcfabs* in *XSPEC*) consists of a neutral absorber which covers a fraction of the X-ray source, resulting in a spectrum composed of an absorbed and an unabsorbed component. I found that the data could not be well fit by a model in which the absorbing column is constant between spectral fits, with only the covering fraction changing (model 13). If I allow the absorbing column to vary, we obtain the same quality of fit whether I allow the covering fraction to vary or not, as, when the fraction is allowed to vary, the same value is derived at each flux level. Once again, models in which Γ was free to vary, whilst better fitting, produced a range of values of Γ which was both broader and lower than expected physically.

The two-component model in which Γ is fixed is therefore taken as the best-fitting model. Fig. 3.6 shows a sample of the flux-binned spectra fitted with the best fitting model.

3.5.2 Mkn 335

The 469 time-resolved spectra of Mkn 335 were separately summed into 23 flux bins and 51 time bins. Both sets of summed spectra were fitted with models 5-14 and 19-26; models in which Γ is fixed were not applied as its value is not well known for Mkn 335.

The flux-binned spectra were best-fit by the two-component models (models 5-10 χ^2_R of 1.00 - 1.02). The single-component models also fit reasonably well (models 11-14 χ^2_R of 1.13 - 1.20), but are statistically not as well-fitting (f = 378, p=10^{-80} from an f-test between models 11 and 5). The partial covering models provide significantly worse fits than the two-component models in all cases (models 5-10 χ^2_R of 1.22 - 1.39). Two models including a reflection component were also fitted, as some previous work has claimed a reflection component to be responsible for the variability of Mkn 335 (see Section 3.2.2), however, I find that reflection from both a neutral (pexrav model in xspec) and ionised reflector (pexriv model in xspec) do not fit the spectra well (χ^2_R of 1.70 and 1.69 respectively).

The χ^2_R values for the two-component models are very similar, however statistically, models in which Γ is not required to vary are superior (f = 1.8, p=0.13 from an f-test between models 8 and 5). Variation in both N_H and ξ are, however required by the data (f = 3.8, p=10^{-9} and f = 5.1, p=10^{-13} from f-tests between models 5 and 6, 7 respectively). Model 5 is therefore taken as the best-fitting model. In this model, a photon index of $\Gamma = 2.39$ is found, similar to previously-measured values (see Section 3.2.2).

The time-binned spectra were also best-fit by the two-component models (models 5-10, χ^2_R of 1.01 - 1.05). The χ^2_R values for all of the models were very similar to those of the flux-binning; the single absorbed power models gave a slightly worse fit (models 11-14 χ^2_R of 1.10 - 1.47, f = 338 and p = 10^{-72} for an f-test between models 5 and 11). The partial covering models and reflection models also gave worse fits to the data (models 19-24 and 25-26, χ^2_R of 1.19 - 1.47 and 1.68-1.70 respectively), as did the reflection models (models 25 and 26, χ^2_R of 1.69 and 1.68, respectively).

The time-binned spectra were also found to be best-fit by two-component models in which Γ is tied between spectra (f = 1.10, p=0.30 from an f-test between models 8 and 5). Similarly, the model in which both N_H and ξ were allowed to vary was found to be

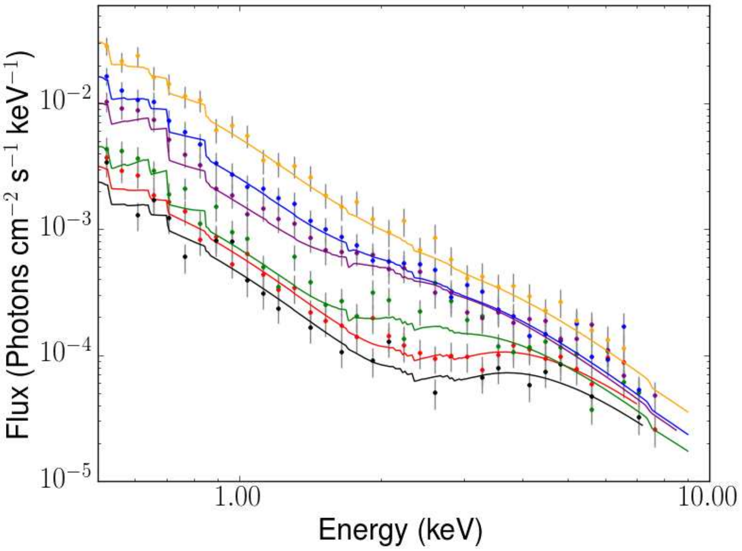

FIGURE 3.7: A sample of the time-binned spectra from Mkn 335, fitted with the best-fitting model, consisting of two power laws, one of which is absorbed by a partially ionised absorbing column (using the 'absori' model) and one of which is not (model 5). This model gives best-fit parameters of $\Gamma = 2.41$, $\xi = 91.9 - 821.8$, $N_H = 1.09 - 41.2$ and effective covering fractions (assuming the unabsorbed power law is the uncovered component of a partially absorbed power law) of 0.40-1.0. The parameter values for the equivalent 'zxipcf' model were slightly different ($\Gamma = 2.76$, $\xi = 0.01 - 108$, $N_H = 2.08 - 18.6$, covering fraction 0.60-0.96).

the best description of the data (f = 3.7, p=10^{-16} and f = 3.6, p=10^{-15} from f-tests between models 5 and 6, 7 respectively). In this model, a photon index of $\Gamma = 2.41$ is found, very similar to that found with the same model for the flux-binned spectra and therefore also similar to previously-measured values. Figure 3.7 shows a sample of the time-binned spectra of Mkn 335 fitted with the best-fitting model.

3.5.3 NGC 5548

The 723 time-resolved spectra of NGC 5548 were summed into 45 flux bins and 50 time bins, respectively. Models 1-14 and 16-24 were fitted to both the time-binned and flux-binned spectra (i.e. only the reflection models and the Compton scattering model were excluded). For models 1-4 and 16-18, in which Γ was fixed, its value was set to $\Gamma = 1.735$, as found by long-term (several years) monitoring by $\widehat{\mathrm{R}}$XTE (Sobolewska & Papadakis, 2009).

The flux-binned spectra of NGC 5548 were found to be well-fitted by both single-power law models absorbed by an ionised absorber and two-component models in which one of two power laws is absorbed by an ionised absorber (models 11-14, χ^2_R of 0.96 - 1.00 and models 1-10, χ^2_R of 0.97 - 1.11). The single power law models, being simpler for similar χ^2_R values, were found to be statistically better in describing the data (f = 3.0, p=10^{-18} from an f-test between models 11 and 5).

Partial covering models were also found to fit the spectrum well, however the fits with the single-power law model produced lower χ^2_R values and were confirmed to be a better representation of the model by f-tests (f = 19.8 and p = 10^{-148}, f = 670.6 and p= 10^{-142} for f-tests between model 11 and 19, 22 respectively).

The data are well fit by all of the single absorbed power law models (11-14), however the data are statistically best-described by the model in which N_H, ξ and Γ were all allowed to vary (f = 8.5, p=10^{-52}, f = 7.2, p=10^{-42} and f = 2.4, p=10^{-7} from f-tests between models 11 and 12, 13, 14 respectively). In this model, Γ varies between approximately 1.0-1.6, as described in Chapter 2. Model 11 is therefore taken as the best-fitting model to the flux-binned spectra of NGC 5548.

It should be noted that a known absorption event, during which the observed absorption in NGC 5548 increased dramatically for several weeks during June 2013 (Kaastra et al., 2014). As this was likely to be an 'occultation' by a clump of absorbing material, and the only such occurance recorded over $\sim$ 9 years of data, it is likely to change the results of the flux-bin in which the data taken during this time lies.

Contrary to the flux-resolved spectra, the time-resolved spectra of NGC 5548 were best-fitted by the two-component models (1-10). As with the flux-binned data, both the two-component models and the single absorbed power law models fitted the data well, but statistically the two-component model was superior (f = 5.9, p=10^{-36} for an f-test between models 8 and 11). Worse fits are obtained with all partial covering models with the time-binned data.

All fitted variations of the two-component models (models 5-10) provided good fits (χ^2_R = 0.99-1.10), however f-tests show that, as with the flux-binned data, models in which Γ is allowed to vary are a better description of the data (f = 4.7, p = 10^{-25}). As also found for the flux-binned data, albeit with a one-component model, allowing N_H and ξ to vary were also required by the data statistically (f = 3.1 and p= 10^{-12}, f = 3.4 and p = 10^{-14} for f-tests between models 8 and 9, 10 respectively). Once again, the photon indices were consistent with those stated in Chapter 2 ($\Gamma \simeq 1.0 - 1.6$).

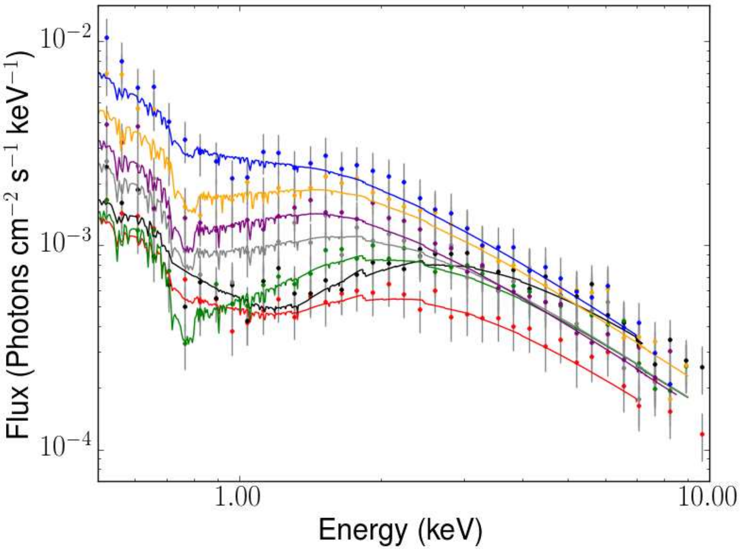

FIGURE 3.8: A sample of the time-binned spectra from NGC 5548.

Model 8 was therefore taken as the best-fitting model in this case. Fig. 3.8 shows a sample of the time-binned spectra of NGC 5548 fitted with the best-fitting model. The effects of the absorption event described above are apparent in the green spectrum.

	Model	Xspec description	Spectral index (Γ)	Absorbing column (N_H)	Ionisation (ξ)	Covering Fraction (CF)
1	Absorbed & unabsorbed power laws	powerlaw + absori × powerlaw	Fixed	Free	Free	-
2	Absorbed & unabsorbed power laws	powerlaw + absori × powerlaw	Fixed	Free	Tied	-
3	Absorbed & unabsorbed power laws	powerlaw + absori × powerlaw	Fixed	Free	0	-
4	Absorbed & unabsorbed power laws	powerlaw + absori × powerlaw	Fixed	Tied	Free	-
5	Absorbed & unabsorbed power laws	powerlaw + absori × powerlaw	Tied	Free	Free	-
6	Absorbed & unabsorbed power laws	powerlaw + absori × powerlaw	Tied	Free	Tied	-
7	Absorbed & unabsorbed power laws	powerlaw + absori × powerlaw	Tied	Tied	Free	-
8	Absorbed & unabsorbed power laws	powerlaw + absori × powerlaw	Free	Free	Free	-
9	Absorbed & unabsorbed power laws	powerlaw + absori × powerlaw	Free	Free	Tied	-
10	Absorbed & unabsorbed power laws	powerlaw + absori × powerlaw	Free	Tied	Free	-
11	Single, absorbed power law	absori × powerlaw	Free	Free	Free	-
12	Single, absorbed power law	absori × powerlaw	Tied	Free	Free	-
13	Single, absorbed power law	absori × powerlaw	Free	Free	Tied	-
14	Single, absorbed power law	absori × powerlaw	Free	Tied	Free	-
15	Compton scattering	(powerlaw + absori × powerlaw) × cabs	Fixed	Free	Tied	-
16	Partial covering, fraction free	pcfabs × powerlaw	Fixed	Free	-	Free
17	Partial covering, fraction tied	pcfabs × powerlaw	Fixed	Free	-	Tied
18	Partial covering, fraction tied	pcfabs × powerlaw	Fixed	Tied	-	Free
19	Partial covering, fraction free	pcfabs × powerlaw	Tied	Free	-	Free
20	Partial covering, fraction tied	pcfabs × powerlaw	Tied	Free	-	Tied
21	Partial covering, fraction tied	pcfabs × powerlaw	Tied	Tied	-	Free
22	Partial covering, fraction free	pcfabs × powerlaw	Free	Free	-	Free
23	Partial covering, fraction tied	pcfabs × powerlaw	Free	Free	-	Tied
24	Partial covering, fraction tied	pcfabs × powerlaw	Free	Tied	-	Free
25	Reflection from neutral matter	pexrav × powerlaw	Free	-	-	-
26	Reflection from ionised matter	pexriv × powerlaw	Free	-	Tied	-

TABLE 3.3: Summary of the main components of each model fitted to the average spectra, showing the parameters which were fixed, tied or left free in each case, and the value or range of values for the spectral index, Γ, which was fixed or best fitting. The reduced χ^2 value and number of degrees of freedom (DoF) of the best fit with each model is also shown. Each model also contains the fixed components of the best fit model to the diffuse gas around the nucleus (tbabs $*$ apec) and the entire model is multiplied by the wabs model set to the galactic absorbing column.

Xspec Model	pow + absori*pow																			
Model No.	1		2		3		4		5		6		7		8		9		10	
Free Parameters	$\mathrm{N_H}$, ξ		$\mathrm{N_H}$		$\mathrm{N_H}$		ξ		$\mathrm{N_H}$, ξ		$\mathrm{N_H}$		ξ		Γ, $\mathrm{N_H}$, ξ		Γ, $\mathrm{N_H}$		Γ, ξ	
Tied Parameters	-		ξ		-		$\mathrm{N_H}$		Γ		Γ, ξ		Γ, $\mathrm{N_H}$		–		ξ		$\mathrm{N_H}$	
	χ^2_R	DoF	χ^2_R	DoF	χ^2_R	DoF	χ^2_R	DoF	χ^2_R	DoF	χ^2_R	DoF	χ^2_R	DoF	χ^2_R	DoF	χ^2_R	DoF	χ^2_R	DoF
NGC 1365	1.39	1329	**1.42**	**1339**	1.44	1339	2.28	1339	1.21	1306	1.25	1316	1.94	1316	1.17	1318	1.20	1328	1.86	1328
NGC 5548	1.05	8276	1.05	8320	1.11	8321	1.10	8320	0.98	8275	0.98	8319	0.98	8319	0.96	8231	0.97	8275	0.97	8275
Mkn 335	-	-	-	-	-	-	-	-	**1.01**	**3343**	1.02	3365	1.03	3365	1.00	3321	1.02	3343	1.02	3343

Table 3.4: **Flux-binned spectra:** The reduced χ^2 values, χ^2_R, and number of degrees of freedom (DoF) of the best fit with models 1-10 to each of the sources. In each case, the free and tied parameters are indicated by Γ (photon index), $\mathrm{N_H}$ (absorbing column) and ξ (ionisation parameter). The best fitting model for each source is highlighted in bold.

Xspec Model	absori*pow								pow + absori*cabs*pow		pcfabs*pow					
Model No.	11		12		13		14		15		16		17		18	
Free Parameters	Γ, $\mathrm{N_H}$, ξ		$\mathrm{N_H}$, ξ		Γ, $\mathrm{N_H}$		Γ, ξ		$\mathrm{N_H}$		–		$\mathrm{N_H}$		$\mathrm{N_H}$, CF	
Tied Parameters	–		Γ		ξ		$\mathrm{N_H}$		ξ		$\mathrm{N_H}$, CF		CF		–	
	χ^2_R	DoF	χ^2_R	DoF	χ^2_R	DoF	χ^2_R	DoF	χ^2_R	DoF	χ^2_R	DoF	χ^2_R	DoF	χ^2_R	DoF
NGC 1365	1.80	1307	1.94	1317	1.90	1317	2.05	1317	1.42	1339	1.65	1341	1.64	1351	2.57	1351
NGC 5548	**0.96**	**8276**	1.00	8320	1.00	8320	0.97	8320	-	-	1.11	8322	1.19	8366	1.15	8366
Mkn 335	1.12	3344	1.20	3366	1.13	3366	1.17	3366	-	-	-	-	-	-	-	-

Table 3.5: **Flux-binned spectra:** The reduced χ^2 values, χ^2_R, and number of degrees of freedom (DoF) of the best fit with models 11-18 to each of the sources. In each case, the free parameters are indicated by Γ (photon index), $\mathrm{N_H}$ (absorbing column), ξ (ionisation parameter) and CF (covering fraction). The best fitting model for each source is highlighted in bold.

Xspec Model	pcfabs*pow											
Model No.	19		20		21		22		23		24	
Free Parameters	N_H, CF		N_H		CF		Γ, N_H, CF		Γ, N_H		Γ, CF	
Tied Parameters	Γ		Γ, CF		Γ, N_H		–		CF		N_H	
	χ^2_R	DoF	χ^2_R	DoF	χ^2_R	DoF	χ^2_R	DoF	χ^2_R	DoF	χ^2_R	DoF
NGC 1365	1.26	1340	1.28	1350	2.70	1350	1.25	1308	1.28	1318	1.73	1318
NGC 5548	1.06	8321	1.13	8365	1.10	8365	1.04	8277	1.06	8321	1.05	8321
Mkn 335	1.22	3367	1.39	3389	1.29	3389	1.23	3345	1.28	3367	1.29	3367

TABLE 3.6: **Flux-binned spectra:** The reduced χ^2 values, χ^2_R, and number of degrees of freedom (DoF) of the best fit with models 19-24 to each of the sources. In each case, the free parameters are indicated by Γ (photon index), N_H (absorbing column) and CF (covering fraction). The best fitting model for each source is highlighted in bold.

Xspec Model	pow + absori*pow												absori*pow							
Model No.	5		6		7		8		9		10		11		12		13		14	
Free Parameters	N_H, ξ		N_H		ξ		Γ, N_H, ξ		Γ, N_H		Γ, ξ		Γ, N_H, ξ		N_H, ξ		Γ, N_H		Γ, ξ	
Tied Parameters	Γ		Γ, ξ		Γ, N_H		–		ξ		N_H		–		Γ		ξ		N_H	
	χ^2_R	DoF	χ^2_R	DoF	χ^2_R	DoF	χ^2_R	DoF	χ^2_R	DoF	χ^2_R	DoF	χ^2_R	DoF	χ^2_R	DoF	χ^2_R	DoF	χ^2_R	DoF
NGC 5548	1.01	9238	1.03	9287	1.10	9287	**0.99**	**9189**	1.00	9238	1.00	9238	1.01	9239	1.13	9288	1.04	9288	1.01	9288
Mkn 335	**1.01**	**4004**	1.05	4053	1.04	4053	1.01	3954	1.02	4004	1.02	4004	1.10	4005	1.19	4055	1.12	4055	1.47	4055

TABLE 3.7: **Time-binned spectra:** The reduced χ^2 values, χ^2_R, and number of degrees of freedom (DoF) of the best fit with models 5-14 to NGC 5548 and Mkn 335. In each case, the free parameters are indicated by Γ (photon index), N_H (absorbing column) and ξ (ionisation parameter). The best fitting model for each source is highlighted in bold.

Xspec Model	pcfabs*pow											
Model No.	19		20		21		22		23		24	
Free Parameters	N_H, CF		Γ, N_H		CF		Γ, N_H, CF		Γ, N_H		Γ, CF	
Tied Parameters	Γ		Γ, CF		Γ, N_H		–		CF		N_H	
	χ^2_R	DoF	χ^2_R	DoF	χ^2_R	DoF	χ^2_R	DoF	χ^2_R	DoF	χ^2_R	DoF
NGC 5548	1.21	9289	1.29	9338	1.16	9338	1.09	9240	1.11	9289	1.07	9289
Mkn 335	1.27	4106	1.47	4106	1.23	4056	1.19	4006	1.27	4056	1.234	4056

TABLE 3.8: **Time-binned spectra:** The reduced χ^2 values, χ^2_R, and number of degrees of freedom (DoF) of the best fit with models 19-24 to NGC 5548 and Mkn 335. In each case, the free parameters are indicated by Γ (photon index), N_H (absorbing column) and CF (covering fraction). The best fitting model for each source is highlighted in bold.

Xspec Model	pow + absori*pow								pcfabs*pow					
Model No.	1		2		3		4		16		17		18	
Free Parameters	$\mathrm{N_H}$, ξ		$\mathrm{N_H}$		$\mathrm{N_H}$		ξ		$\mathrm{N_H}$, CF		$\mathrm{N_H}$		CF	
Tied Parameters	–		ξ		–		$\mathrm{N_H}$		–		CF		$\mathrm{N_H}$	
	χ^2_R	DoF	χ^2_R	DoF	χ^2_R	DoF	χ^2_R	DoF	χ^2_R	DoF	χ^2_R	DoF	χ^2_R	DoF
NGC 5548	1.06	9239	1.08	9288	1.13	9289	1.13	9288	1.13	9289	1.28	9338	1.21	9338

TABLE 3.9: **Time-binned spectra:** The reduced χ^2 values, χ^2_R, and number of degrees of freedom (DoF) of the best fit with models 1-4 and 16-18 to NGC 5548. In each case, the free parameters are indicated by Γ (photon index), $\mathrm{N_H}$ (absorbing column), ξ (ionisation parameter) and CF (covering fraction). The best fitting model for each source is highlighted in bold.

Xspec Model	pexrav*pow		pexriv*pow	
Model No.	26		27	
Free Parameters	Γ		Γ	
Tied Parameters	–		ξ	
	χ^2_R	DoF	χ^2_R	DoF
Mkn 335 (flux-binned)	1.70	3367	1.69	3366
Mkn 335 (time-binned)	1.69	4056	1.68	4055

TABLE 3.10: The reduced χ^2 values, χ^2_R, and number of degrees of freedom (DoF) of the best fit with models 26 and 27 to both the time- and flux-binned spectra of Mkn 335. In each case, the free parameters are indicated by Γ (photon index) and ξ (ionisation parameter).

3.6 Two-Component Spectral Variability

A two-component model consisting of two power laws, in which one is absorbed by an ionised absorber, has been found to be best-fitting to the long-term X-ray spectral variability of the flux-binned spectra of NGC 1365, both the flux-binned and time-binned spectra of Mkn 335, and the time-binned spectra of NGC 5548. This model has previously been used to describe AGN spectra in many cases, e.g. the two-component models has been used by Done et al. (1996) and Braito et al. (2013) to describe the spectra of NGC 4945 and NGC 4507 and in samples of AGN by e.g. Hernández-García et al. (2014).

Variations in hardness ratio versus count rate similar to those seen in the the three AGN, in Fig. 3.2, have also been seen in the spectra of BHXRBs (Fig. 1 in Kuulkers et al. 1998) from RXTE data (2-13 keV). Although Kuulkers et al. (1998) do not discuss flux-binned spectra as seen in my Fig. 3.6, they also favour a similar two-component model of the X-ray spectra of these BHXRBs with strong absorption variability.

The physical implications of this model are dependent on the presence (or lack thereof) of correlations between the best-fit parameters. The relationship between the parameters of the best-fitting model to each system are therefore discussed below.

3.6.1 Relationships between Absorber Parameters

3.6.1.1 NGC 1365

The best-fitting model to NGC 1365 (model 2 in Table 3.3), required a large range of absorbing columns, from 1.69×10^{22} to 10^{24} cm^{-2}. The temperature of the absorber was 9.5×10^{5} K and the ionisation state of the absorber was 0.11. The normalisations of the two power laws varied by a factor of 3, giving a range of intrinsic luminosities of approximately 1.1 to 3.5 $\times 10^{-11}$ ergs s^{-1} for the 0.5-10.0 keV band.

Fig. 3.6 shows a sample of the flux-binned spectra fitted with this model. Fig. 3.12 shows how the two power law components vary as the flux changes. It is clear from the spectra that the degree of absorption is decreasing as the normalisation of the power law (i.e. the flux before absorption) of the system increases (see Fig. 3.9). As the ionisation state is constant in the best fitting model, it follows that that the absorbing column of

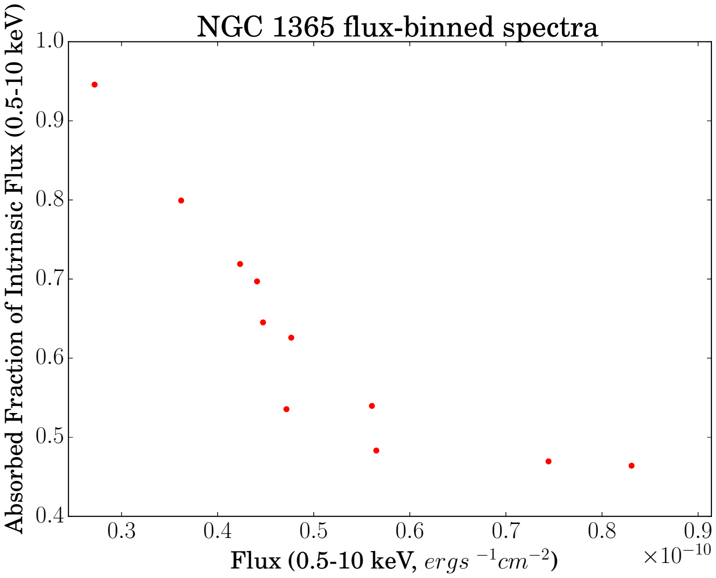

FIGURE 3.9: **Flux-binned spectra of NGC 1365:** The ratio between the intrinsic flux of the absorbed component of the best-fit model to the flux of the same component with absorption (for the 0.5-10 keV energy range).

the absorbed power law decreases as the intrinsic flux increases. These two parameters are plotted in Fig. 3.11. There is a strong decrease in the absorbing column as the normalisation increases (Spearman ranked correlation coefficient $\rho = 0.98^{+0.02}_{-0.20}$), but the data are not of sufficient quality to precisely determine the form of the relationship between these parameters.

In Fig. 3.11 the normalisation of the unabsorbed power law is plotted against that of the absorbed power law. The normalisations can be fitted well with a linear model, showing them to be correlated (r = 0.91). These observations confirm that there is a real change in the underlying luminosity of the source and that the observed flux changes are not just due to changes in absorption. The $15-150$ keV *BAT* light curve of NGC 1365, which undergoes far less absorption than the 0.5-10 keV band, confirms this intrinsic variability, showing variation of approximately a factor of 4.

As a consistency check, the hard count rate and hardness ratio from each model fitted to the summed data are plotted over the original data as in Fig. 3.2 (Fig. 3.10). These plots show that the summed spectra also follow the trends shown by the individual spectra, reinforcing the assumption that the spectrum is similar at a given flux level, independent of time.

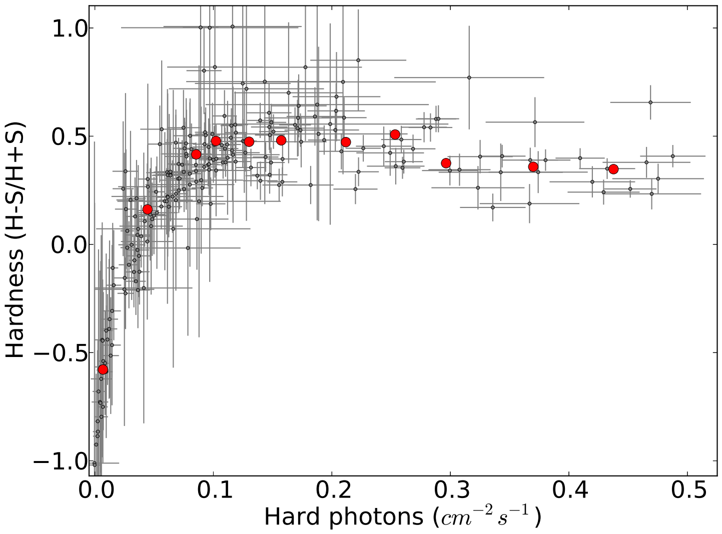

FIGURE 3.10: Plot of the hardness against the hard count rate of each of the 190 observed spectra (*small circles*), together with that of the model spectra described above (model 2 in Table 3.3) when fitted to each of the 11 summed, flux binned spectra (*large circles*).

The data therefore show, for the best-fitting two-component model, the column of absorbing material to be inversely related to the normalisation parameter of the absorbed power law, i.e. to the flux prior to absorption. As this component dominates the unabsorbed luminosity of the source, the absorbing column is inversely proportional to the source luminosity. Whilst one might initially assume any reduction in absorption with increasing flux to be due to increased ionisation, I have shown that models involving varying ionisation alone do not fit the data; models allowing variation of ionisation and absorbing column simultaneously also require an inverse relationship between the absorbing column and the unabsorbed luminosity and do not require the ionisation to vary significantly. Fits to spectra of NGC 4151 by Lubiński et al. (2010) at different flux levels show a similar reduction in the absorbing column with increasing flux, implying that this relationship is not unique to NGC 1365. A physical mechanism is required to explain this relationship and a possible solution lies in an X-ray wind of absorbing material rising from the accretion disc (see Section 3.7).

3.6.1.2 Mkn 335

The best-fitting model to Mkn 335 (model 5 in Table 3.3), required a large range of absorbing columns for both the flux- and time-binned spectra (2.4-45.5 and 1.1-41.2

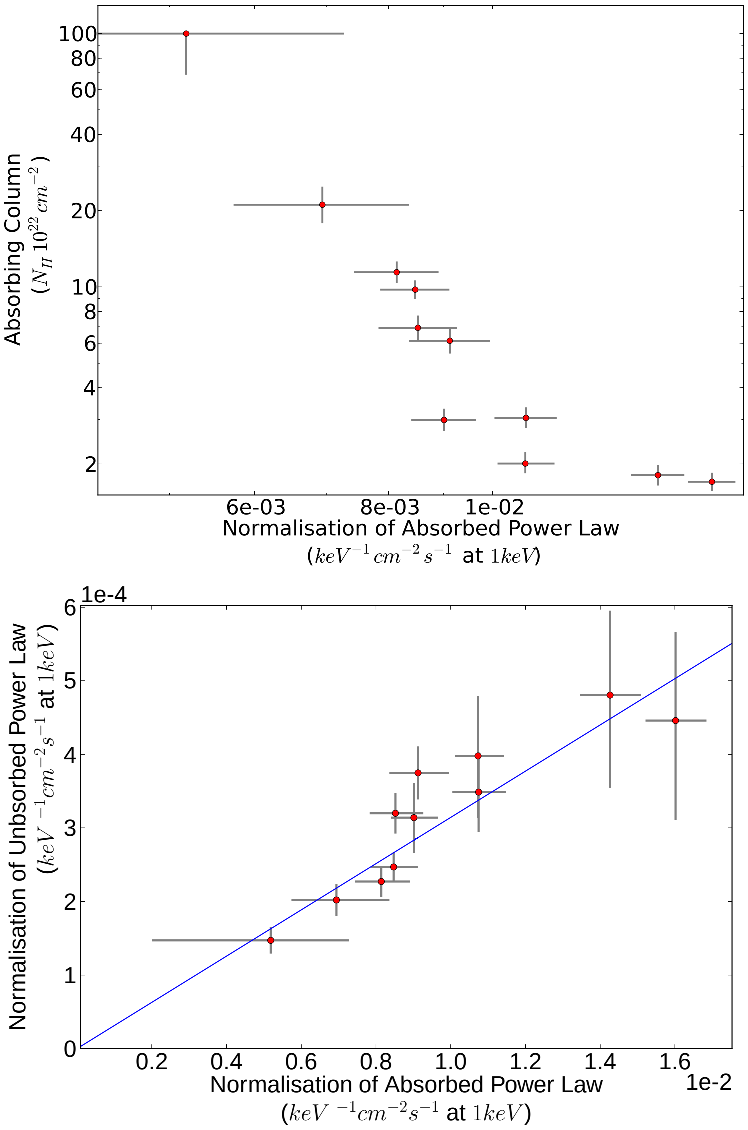

FIGURE 3.11: (Top) Log plot of the normalisation parameter of the absorbed power law against the column of the absorbing material in the model described above. The normalisation of the power law is equivalent to the flux of this component before absorption, and therefore the X-ray luminosity of the source. (Bottom) Plot of the normalisation parameter of the absorbed power law against the normalisation parameter of the unabsorbed power law in the model described above. The correlation between them implies the two components originate from the same source.

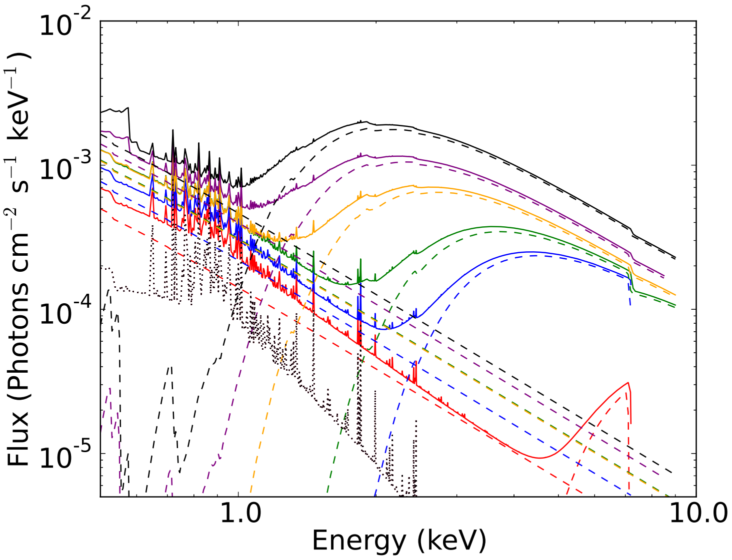

FIGURE 3.12: The sample of best fitting models shown in Fig. 3.6 (*solid lines*), together with the components of each model - the unabsorbed power law and absorbed power law (*dashed lines*), and the spectrum of the underlying diffuse emission (*dotted line*).

$\times 10^{22}$ cm^{-2} respectively). The range of ionisation parameters required in each case was also similar, showing a range of intermediate ionisation states (ξ = 185-722 and 92-822 for flux- and time-binned spectra, respectively). The temperatures of the absorbers were consistent in both cases (1.22 and 1.29 $\times 10^5$ K for the flux- and time-binned spectra, respectively). The normalisations of the two power laws varied by a factor of ~ 5 in each case, covering very similar ranges, giving intrinsic luminosity ranges of approximately 1.0-4.6 $\times 10^{-11}$ ergs s^{-1} for the 0.5-10.0 keV band in both cases.

Fig. 3.7 shows a sample of the flux-binned spectra fitted with this model. The spectra show that the degree of absorption of the absorbed power law decreases as the normalisation of the absorbed power law (i.e. the flux before absorption) decreases with increasing flux up to a certain flux, above which the absorption is no longer significant and the effects are therefore no longer seen. This is very clear in Fig. 3.14, which shows the fraction of the intrinsic flux of the absorbed component of the spectrum which is absorbed at a given intrinsic flux, for the flux-binned spectra; the degree of absorption follows a very clear trend until the flux reaches $\sim 3.0 \times 10^{-11}$ergss^{-1}, beyond which it remains roughly constant, with some scatter. Fig. 3.13 shows the same parameters for the time-binned spectra; there is a great deal more scatter at a given flux compared to the flux-binned spectra, however a very weak downward trend can still be seen. As these plots combine the effects of changes in ionisation and the absorbing column of the absorber, they do not show whether changes in one or both of these are responsible. Plots of the absorbing column and ionisation state are therefore plotted against the normalisation of the absorbed power law in Figs. 3.15 and 3.16 respectively. There are indications of a weak anticorrelation between the normalisation and absorbing column with the flux-binned data, however this is not the case for the time-binned data. Conversely, the when the ionisation parameter is plotted against the normalisation of the unabsorbed power law, the time-binned data show a positive correlation between the two parameters; the flux-binned data hint at a similar correlation, however the errors and scatter are large.

Fig. 3.17 shows the normalisations of the unabsorbed power law plotted against that of the absorbed power law for both binning regimes. Both plots show a correlation between the two parameters, though there is significantly more scatter in the time-binned data. This does seem to imply, however, that the two components are linked. Fig. 3.18 shows how the absorbing column and ionisation parameter change over time, showing variability in both components at all epochs.

It is therefore unclear whether the main driver of the variations in absorption in Mkn 335 is changes in the absorption column or changes in the ionisation state of the absorbing material, or both, as there is a degeneracy between the two parameters when fitting the Mkn 335 data. As the flux-binned data will show the average behaviour at a given flux regardless of the time of observation, whilst the time-binned data will show changes on short timescales at the average flux of a given time-bin, comparison of the two can give information about the relative importance of parameter variability in these two regimes. The flux-data imply that there may be a decrease in the absorbing column with increasing luminosity on long timescales, as seen in NGC 1365, whilst changes in the ionisation state are not well constrained. The time-binned data show huge scatter and no clear trends in the absorbing column with changing luminosity, but show a reasonable clear trend of increasing ionisation state with increasing luminosity. It could therefore be that correlated changes in the ionisation state of the absorbing matter alone are the cause of the observed decrease in the degree of absorption with increasing luminosity; in this case it could either be that the absorbing column does not in fact vary much at all (which is not unsupported by the goodness of fit with a model in which it does not vary, e.g. model 10), or that the variations are uncorrelated and therefore likely due purely to relatively small variations in the density of the absorber, i.e. BLR clumps or 'clouds'.

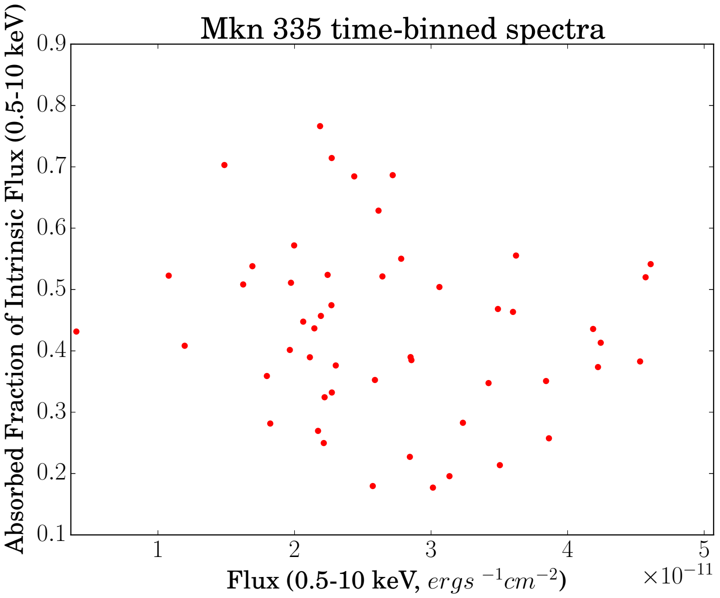

FIGURE 3.13: **Time-binned spectra of Mkn 335:** The ratio between the intrinsic flux of the absorbed component of the best-fit model to the flux of the same component with absorption (for the 0.5-10 keV energy range).

The X-ray spectral variability of Mkn 335 appears to have some similarities to that of NGC 1365, in that a large fraction of the observed variation is likely to be driven by changes in absorbing material between the X-ray source and the observer. In the case of Mkn 335 it is, however, much less clear whether the changes are primarily in ionisation state or in absorbing column, or an approximately even combination of the two. As Mkn 335 posses a much larger Eddington ratio than that of NGC 1365 (see Fig. 3.1), it would not be unexpected to find a difference in the way in which absorbing material reacts to changes in the X-ray luminosity of the system.

3.6.1.3 NGC 5548

As described above, the flux- and time-binned spectra of NGC 5548 were best-fitted by different models, the flux-binned data with a single absorbed power law (model 11 in Table 3.3) and the time-binned data with the addition of an unabsorbed power law (model 8). In both cases, Γ, N_H and ξ were all left free to vary between spectra. Both data sets required only a small range of relatively low absorbing columns ($0.42 - 1.77$ and $0.73 - 3.5 \times 10^{22}$ cm^{-2} for the flux- and time-binned spectra, respectively). The temperature of the absorber was relatively low and very similar in both cases (6.13 and 6.27×10^{4}K for the flux- and time-binned spectra, respectively). In both

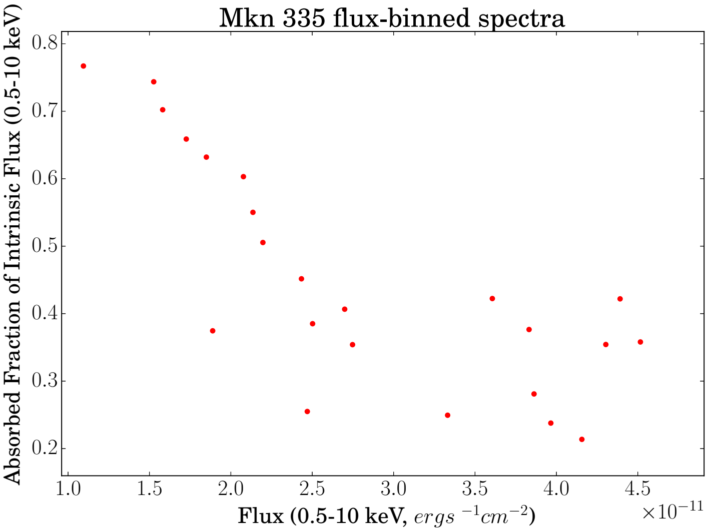

FIGURE 3.14: **Flux-binned spectra of Mkn 335:** The ratio between the intrinsic flux of the absorbed component of the best-fit model to the flux of the same component with absorption (for the 0.5-10 keV energy range).

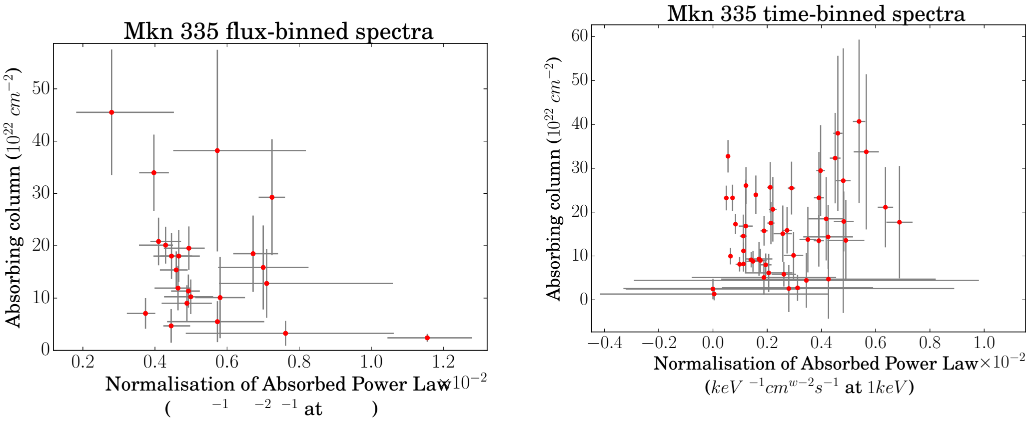

FIGURE 3.15: The absorbing column against the unabsorbed flux of the system in the best-fitting spectral model to the flux-binned spectra (top) and time-binned spectra (bottom) of Mkn 335.

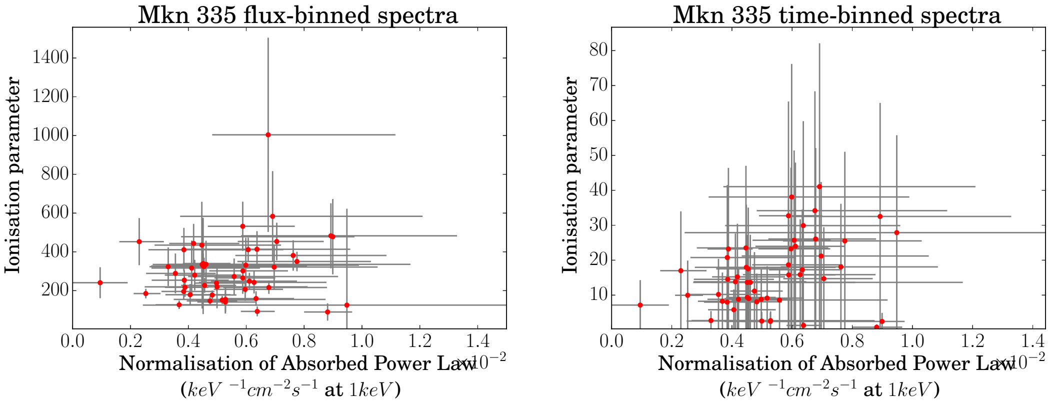

FIGURE 3.16: The ionisation parameter against the unabsorbed flux of the system in the best-fitting spectral model to the flux-binned spectra (top) and time-binned spectra (bottom) of Mkn 335.

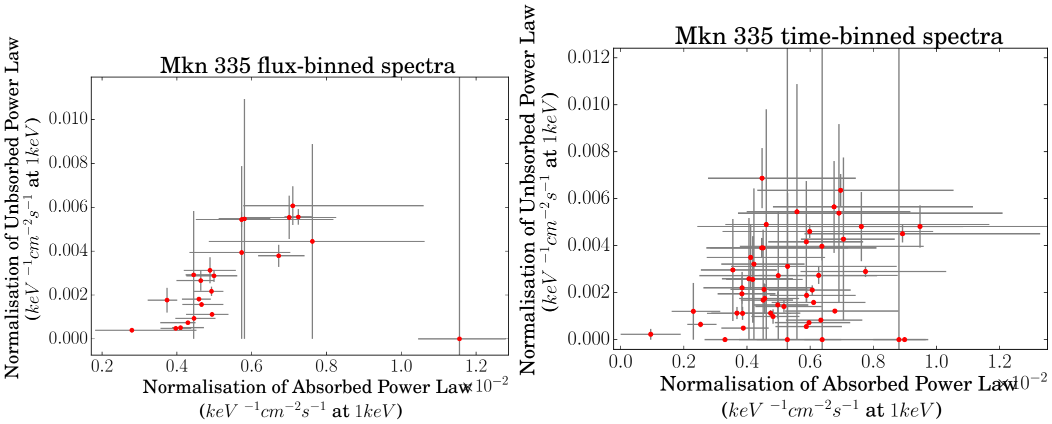

FIGURE 3.17: The intrinsic flux of the absorbed power law component against the intrinsic flux of the absorbed power law component in the best-fitting spectral model to the flux-binned spectra (top) and time-binned spectra (bottom) of Mkn 335.

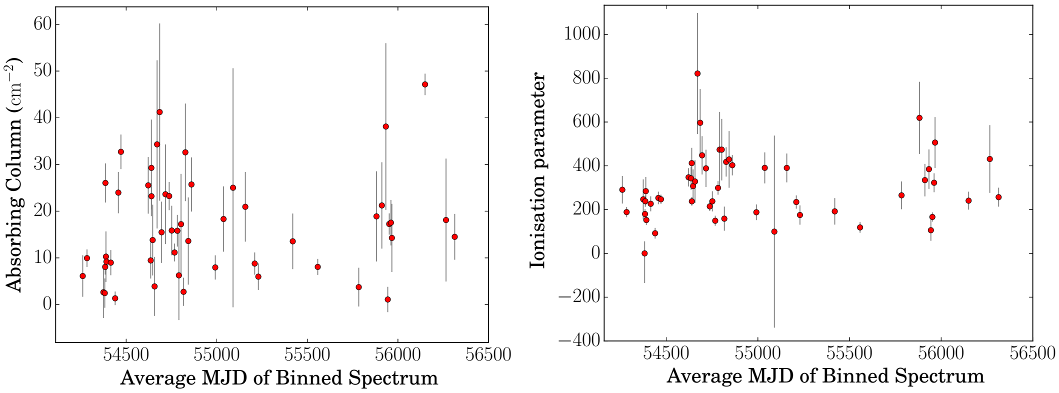

FIGURE 3.18: The absorbing column (top) and ionisation parameter (bottom) in the best-fitting spectral model to the time-binned spectra of Mkn 335 against time.

models, the absorber also required a fairly large range of ionisation states from very low to intermediate states, though the flux-binned data required slightly higher values ($\xi =$ 3.7-82.0 and 0-39.1 for the flux- and time-binned spectra, respectively).

The normalisations of the two power laws varied by factor of $\sim 10 - 15$ in each case, covering similar ranges, giving intrinsic luminosity ranges of approximately 1.4-7.5 and 0.5-5.5 $\times 10^{-11}$ ergs s^{-1} in the 0.5-10.0 keV band for the flux- and time-binned data, respectively.

Fig. 3.8 shows a sample of the flux-binned spectra fitted with this model. Unlike the spectra of NGC 1365 and Mkn 335, the degree of absorption does not appear, by eye, to change systematically in any way with increasing or decreasing flux. It is, however, clear that there are large changes in the amount of absorption. Figs. 3.19 and 3.20 show the fraction of the intrinsic flux of the absorbed component of the spectrum which is absorbed at a given intrinsic flux for both the flux- and time-binned spectra. Interestingly, both plots show a clear trend of *increasing* absorption with increasing flux, converse to the behaviour seen in both NGC 1365 and Mkn 335. The change in the absorption fraction is also smaller than observed in the other two systems.

The absorbing column and is plotted against the normalisation of the absorbed power law for both binning regimes in Fig. 3.21. Neither plot shows any trend with increasing flux, both are inconsistent with being approximately constant at 1-2 $\times 10^{22} cm^{-2}$ with a scatter of $0.5 - 1.0 \times 10^{22} cm^{-2}$. The plots of the ionisation parameter against the normalisation of the absorbed power law (Fi.g 3.22), however, both show a decrease in ionisation with increasing flux. This is particularly clear in the flux-binned data. The data therefore imply that it is this decrease in ionisation, rather than any change in the absorbing column, which leads to an increased degree of absorption with increasing flux.

Fig. 3.23 shows the normalisations of the unabsorbed power law plotted against that of the absorbed power law for the time-binned data of NGC 5548 (for which, unlike the flux-binned data) the two-component model was the best fit). The plot shows no correlation between the two parameters, showing the unabsorbed component to be approximately constant with some scatter. The lack of variability in this component implies that this component is not intrinsic emission, but is either distant reflected emission, with a lower degree of variability to the intrinsic emission, or a residual background component. In either scenario, this component can be excluded in analysis of the variability of the absorption in the system. Fig. 3.24 shows how the absorbing column and ionisation parameter change over time, chowing variability in all three parameters at all epochs.

The data therefore imply that changes in the absorber are due mostly to variability in the its ionisation state, consistent with the results of the long-term study of X-ray grating data by Ebrero et al. (2014). The absorbing column is not seen to change significantly, though a small amount of variability is observed, which can be explained by short-term (days-weeks) variability due to inhomogeneities in the absorbing material moving across the line of sight. The anticorrelation between the ionisation state and the luminosity of the system is less simply explained, as the natural response of material to an increase in flux is an increase in ionisation, not a decrease. It is, however, potentially possible to explain by a change in the distance of the absorbing material through which we are observing the X-ray source which is correlated with the luminosity of the system, such that the ionising flux incident on the absorbing material actually decreases despite an increase in the luminosity of the central source. The absorbing columns are not high, however, implying we are unlikely to be looking at the system through a dense part of the wind. As the goodness-of-fit was very similar for a number of models in the case of the NGC 5548 data, it is also possible that there are degeneracies between the model parameters leading to an apparent correlation which is not real, particularly as the changes in absorption are smaller than NGC 1365 and Mkn 335. A degeneracy between the ionisation state and the absorbing column could lead to an apprent decrease in ionisation with increasing flux when the actual of absorption variability is changes in the absorbing column. In this scenario, however, an increase in the absorbing column would be required. As the absorbing columns are relatively low here, the viewing angle is likely to be relatively high and therefore not through the main part of the disc wind. Absorption here may therefore be caused by material close to the black hole, for example a failed wind. In this case a greater luminosity could lead to stronger thermal driving of the absorbing material from the disc, leading to increased absorption. Alternatively, as the best-fitting model to the spectra of NGC 5548 required a variable photon index, it may be that there is a degeneracy between Γ and the degree of absorption. In this case, 'harder-when-brighter' behaviour, i.e. an anticorellation between the photon index and the luminosity, would be required to explain the observed spectral variations. Whilst both previous studies (e.g. Sobolewska & Papadakis, 2009) find little variation in Γ on long time scales using the 2-10 keV energy range, my own spectral fitting does imply that such an anticorrelation may be present (see Chapter 2).

3.7 The AGN Wind Model

X-ray absorption is often attributed to outflows, in particular to a disc wind (see e.g. Kaastra et al. 2000, Blustin et al. 2005, Tombesi et al. 2013). In the AGN model proposed by Elvis (2000), absorbing material arises from a narrow range of accretion disc radii in a rotating biconical 'wind'. Nicastro (2000) shows that an X-ray absorbing wind could originate from a narrow boundary region between the radiation-pressure-dominated and gas-pressure-dominated regions of the accretion disc. In these models, a rise in accretion rate, which will give rise to an increase in X-ray luminosity, naturally leads to an increase in the radii from which the wind arises through at least two mechanisms. Firstly, a higher accretion rate leads to an increase in disc temperature and hence an increase in the radii

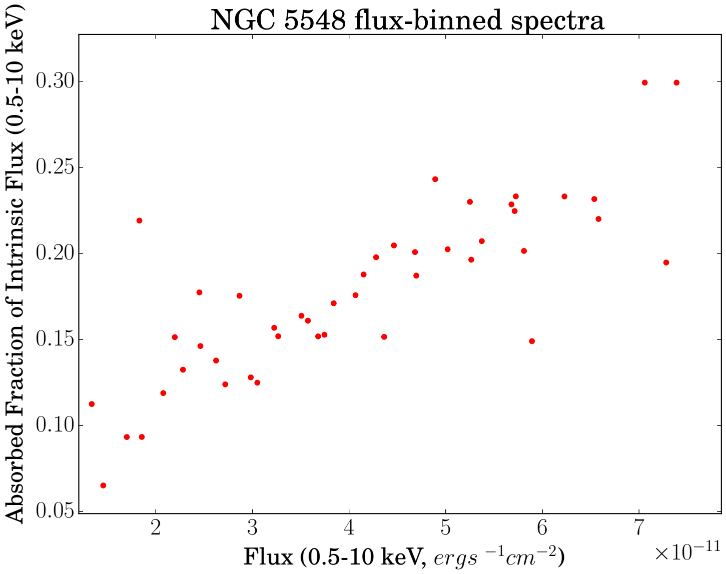

FIGURE 3.19: **Flux-binned spectra of NGC 5548:** The ratio between the intrinsic flux of the absorbed component of the best-fit model to the flux of the same component with absorption (for the 0.5-10 keV energy range).

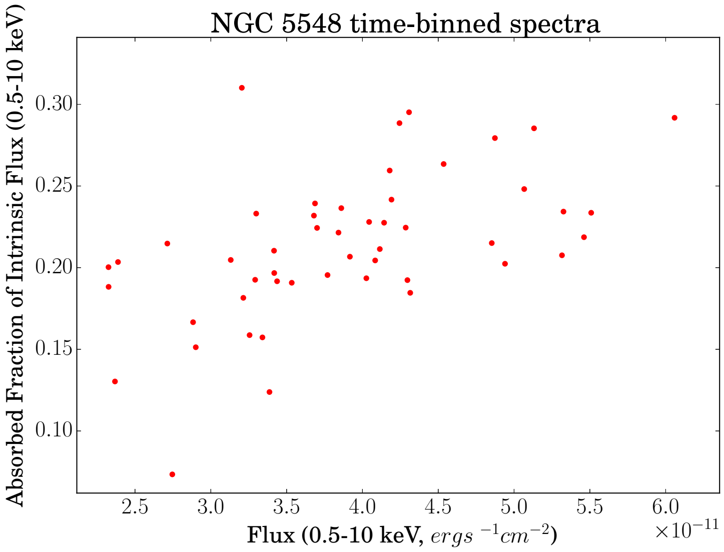

FIGURE 3.20: **Time-binned spectra of NGC 5548:** The ratio between the intrinsic flux of the absorbed component of the best-fit model to the flux of the same component with absorption (for the 0.5-10 keV energy range).

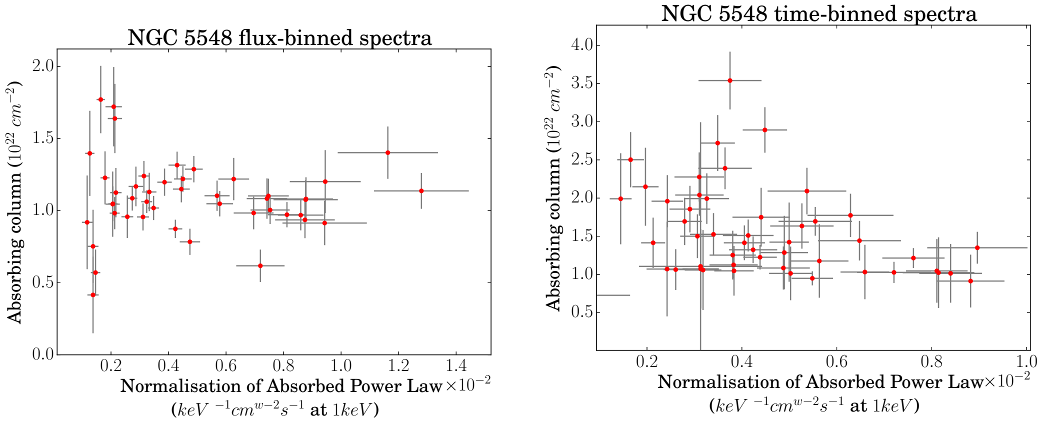

FIGURE 3.21: The absorbing column against the unabsorbed flux of the system in the best-fitting spectral model to the flux-binned spectra (top) and time-binned spectra (bottom) of NGC 5548.

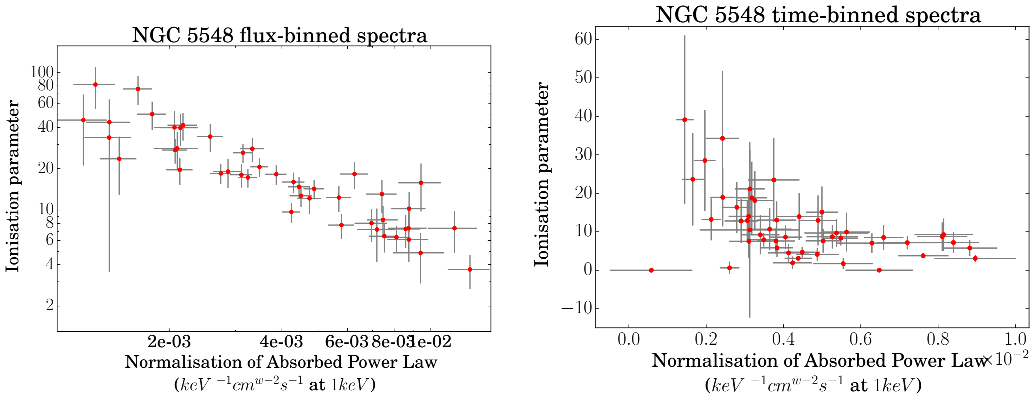

FIGURE 3.22: The absorbing column against the unabsorbed flux of the system in the best-fitting spectral model to the flux-binned spectra (top) and time-binned spectra (bottom) of NGC 5548.

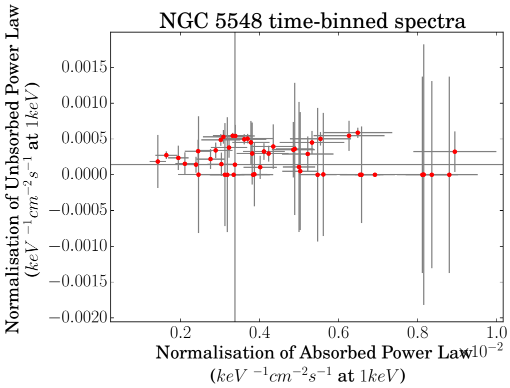

FIGURE 3.23: The intrinsic flux of the absorbed power law component against the intrinsic flux of the absorbed power law component in the best-fitting spectral model to the time-binned spectra of NGC 5548.

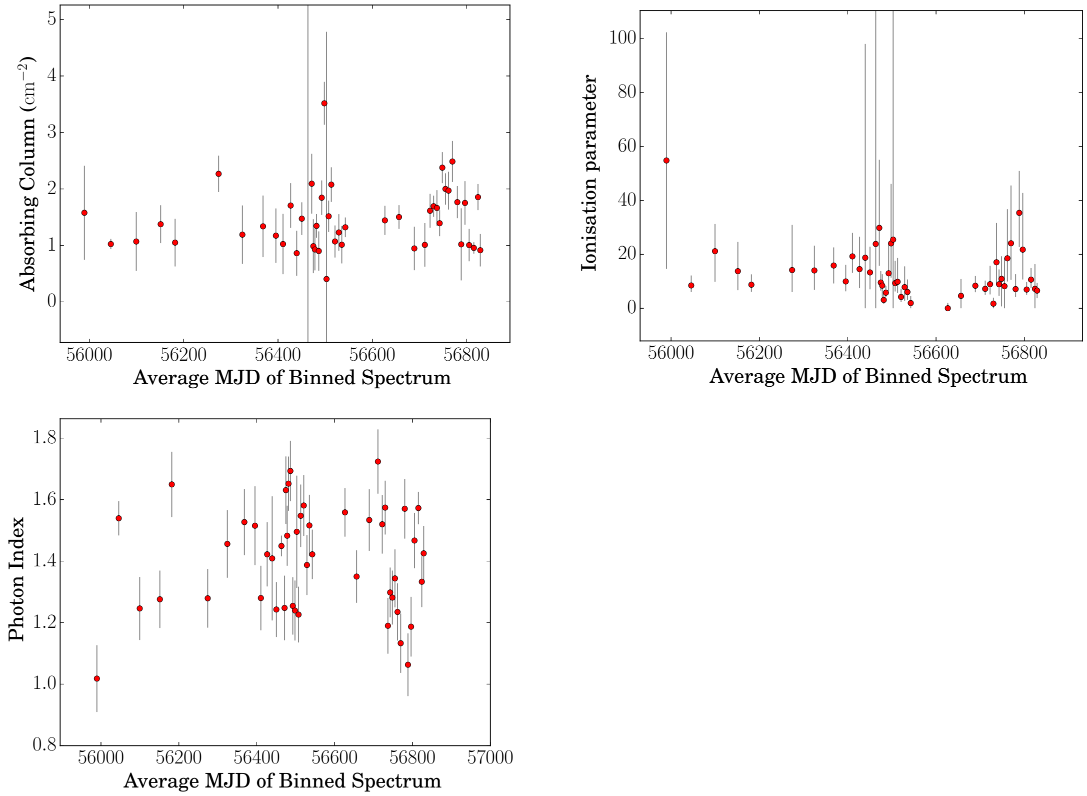

Figure 3.24: The absorbing column (top), ionisation parameter (middle) and photon index (bottom) in the best-fitting spectral model to the time-binned spectra of NGC 5548 against time. The jump in the absorbing column, and accompanying change in the ionisation state, due to the absorbing event in June 2013 (MJD $\sim$ 56460) is apparent.

from which the wind arises. Secondly, a higher accretion rate leads to an increased ionising UV flux from the inner disc. When potential wind material at the disc surface is fully ionised, it is only subject to Compton scattering; the much more powerful line-driving force (Proga et al., 1999) is no longer applicable, hence this material would never be driven off as a wind. Thus, if the inclination is such that the observer views the X-ray source through the inner edge of the wind, an increase in accretion rate would move the wind outwards such that the observer would now be viewing the source through a lower absorbing column, as observed in the spectra of NGC 1365. If it is the case that the absorbing column of Mkn 335 is also decreasing with increasing flux, as implied by the fits to the flux-binned spectra, it is likely to be observed from a similar inclination with respect to the edge of the disc wind. An additional geometric factor which would reduce absorbing column is that, in the Elvis (2000) model, an increase in X-ray luminosity causes the opening angle of the wind to increase due to the increased radiation pressure. The above affects will thus naturally lead to the inverse relationship between absorbing column and luminosity which I see in NGC 1365. Moving the absorbing wind to larger radii also means that the line of sight would go through the less dense, more highly ionised front part of the wind, as I see in my fits to both NGC 1365 and Mkn 335.

The low ionisation states found in the best-fitting models to the spectra of NGC 1365 suggest that the material involved is not associated with the highly-ionised, high-velocity outflows suggested by Risaliti et al. (2005b), which is too ionised to cause the observed broadband X-ray absorption. We therefore suggest that the absorbing material lies in a region which is further out than this highly ionised material, as part of a stratified wind (Tombesi et al. 2013, Elvis 2000). As the ionisation states observed in Mkn 335 are much higher, it is likely that I are looking through a part of the wind which is closer in relative to my view of the wind of NGC 1365. Furthermore, the large variation in ionisation states seen in Mkn 335 in comparison to NGC 1365 is likely to be linked to its relatively high luminosity with respect to the Eddington ratio, meaning variability in the luminosity causes relatively larger changes in the ionising flux in the system. The lack of significant absorption at the highest luminosities in Mkn 335 in this case could be due to the absorbing wind being pushed out to a point where the absorbing column is low enough, and the ionisation state high enough, that absorption from the wind is negligible. The remaining absorption in the spectrum of Mkn 335 would then be due solely to absorption from BLR ‘clouds’, leading the approximately constant absorption with scatter seen at the highest fluxes; this would also explain the large degree of scatter in the absorption of the time-binned spectra in comparison to the flux-binned spectra, in which the variation due to ‘occultations‘ by BLR gas is averaged out.

Depending on which mechanism dominates in pushing the wind to larger radii with increasing accretion rate, we expect different lags between the change in absorbing column and the change in luminosity which could lead to hysteresis and scatter in the X-ray luminosity / hardness relationships.

If the outward movement of the wind launch radii is caused by a change in disc temperature due to inwardly propagating accretion rate fluctuations, then the X-ray luminosity will lag by the viscous travel time of those fluctuations to either the inner edge of the disc where the seed photons are mainly produced and/or to the X-ray emitting corona itself. For typical wind launch radii of a few hundred $\mathrm{R_g}$ (Higginbottom et al., 2013), this timescale would be of order weeks to months.

If the outward movement of the wind is dominated by an increase in ionising UV photons from the inner edge of the disc, which also dominate the X-ray seed photon flux, then variations in the X-ray luminosity will lead changes in the absorbing column slightly, by the difference between the light travel time from the UV region to the wind and to the corona respectively. This difference is likely to be small (hours). Alternatively, if the wind moves outwards in response to increased UV flux, but the X-ray luminosity rises in response to increased accretion rate rather than increased seed photon flux, then the X-ray luminosity will lag by the difference between the viscous propagation time from the UV to X-ray emitting regions and the light travel time from the UV emitting to wind launch radii. This difference is also likely to be small (1-2 days).

The observations of NGC 1365 do not show a great deal of scatter in the hardness-count rate diagram, indicating that any lags are short. I therefore favour a mechanism by which the wind launch radii are pushed outwards mainly by a rise in ionising UV flux, rather than by a rise in local disc temperature. Regardless of mechanism by which these outflows are driven, it is clear from my data that a geometrical response to changes in luminosity is necessary in the absorber in order to explain the variability in the spectra.

As described above in Section 3.6.1.3, the causes of the spectral variability of NGC 5548 are not clear. The best-fitting model to the spectra of NGC 5548 requires a decrease in absorption with increasing flux, due to an increase in ionisation, entirely unlike the behaviour seen in NGC 1365 and Mkn 335, however degeneracies in the model parameters may exist. If the variability is, in fact, caused by an increase in the column density, or by changes in the photon index of the intrinsic spectrum, the system is likely to be viewed from a higher angle and therefore not obscured by the main body of the wind. This possibility is supported by the relatively low column densities and higher ionsation parameters in comparison to NGC 1365 and Mkn 335 However, if the spectral variability is caused by ionisation changes, the differences may still be explained in terms of a moving disc wind viewed from a lower angle that its opening angle, such changes in the absorbing column would not be observed as it moved further from or closer to the X-ray source, but would stay relatively constant except for changes due to inhomogeneities in the wind crossing the line of sight as it rotates or by orbiting BLR clouds beyond the wind, as observed in the spectra of NGC 5548. As the wind moves out, a change in the average ionisation state of the wind would be observed, except in the situation in which the radius at which the wind is launched is not dependent on luminosity in the same way as the degree of ionisation. If the outward movement of the wind is more strongly dependent on the luminosity than the ionisation state, a decrease in the ionisation state of the wind, could therefore be observed, despite the overall increase in ionising flux, as observed in the NGC 5548 data.

Fig. 3.25 shows a schematic of the possible orientations of the three systems with respect to an absorbing disc wind which best fit my spectral fitting results.

Finally, I note that, in all models, the wind is expected to be clumpy, meaning short timescale variations of the absorbing column, independent of the unabsorbed luminosity, should also occur, which would also add scatter to the relationship between X-ray luminosity and absorbing column. The spectral variations reported previously on short timescales are probably mainly the result of fitting variations induced as clumps pass over the line of sight.

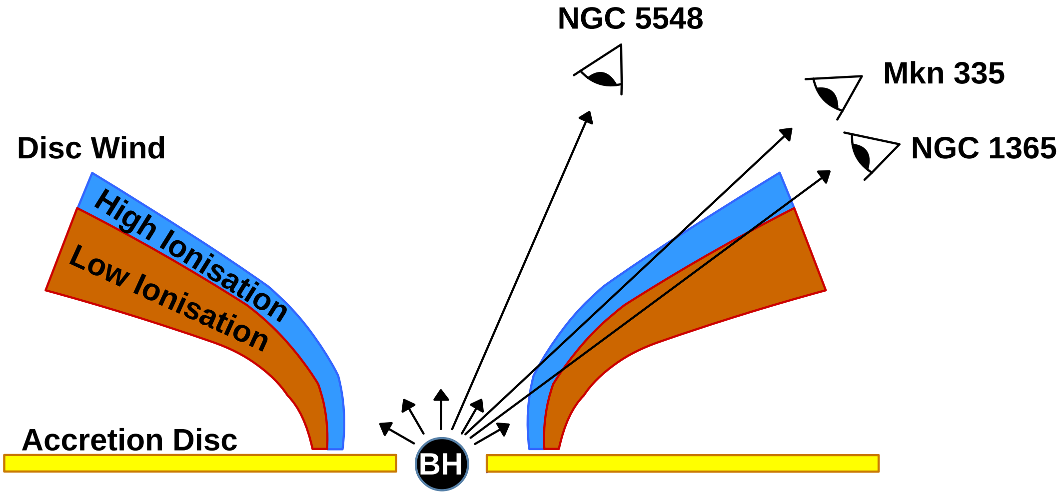

FIGURE 3.25: The possible orientations of each AGN with respect to a disc wind indicated by the *Swift* data. As in the Elvis (2000) wind model.

Chapter 4

Inter-Waveband Lags in AGN

"The heavens are lit by the stars
Where years of secrets of universal forces lay hid"
Emperor, *Cosmic Keys to My Creations and Times*

4.1 Introduction

The emission of UV/optical and X-ray radiation in AGN can be linked, as described in section 1.4.1.1. Testing whether or not these two bands are correlated, and what the direction and magnitude of any time lags between their variability are can provide a great deal of information on the main drivers of variability in both bands, and the geometry of the regions from which each is emitted. If the bands are correlated, the variability of the waveband which lags can be assumed to be driven by the variability of the other, and the time lag between them indicates the distance between the main emission regions of the two bands according to the timescale relevant to their connection (i.e. the light travel time or viscous timescale).

Despite a large number of studies looking at the relationship between UV/optical variability and X-ray variability in AGN, and the origin of the UV/optical variability, it is still not clear how the two are linked. Strong correlations between the X-ray and the UV, and between the X-ray and the optical, have been observed in a number of systems on short timescales (weeks - months), with lags constrained to be less than a day (e.g.

Arévalo et al., 2009, Breedt et al., 2009, Cameron et al., 2012, Lira et al., 2011, Shappee et al., 2014, Uttley et al., 2003). In all cases, the UV/optical was found to be lagging the variability of the X-rays. This can explained physically by both X-ray irradiation of the disc driving UV variability and by variability in the UV/optical seed photon flux which is upscattered to produce the X-ray emission. The relative shortness of the optical lags supports reprocessing of X-rays into the UV/optical emission by the nearby accretion disc as the main source of variability, as this would lead to UV/optical variations which lag the X-rays by the short light travel time between the X-ray source and the disc.

On longer timescales (months - years), however, poorer correlations are seen, usually due to long-term UV/optical trends that are not present in the X-ray variability. This suggests that UV/optical variability is dominated by different processes on these longer timescales, e.g. due to variations in the accretion rate within the disc.

Until recently, these lags had not been measured well enough to completely rule out an optical lead. Measurements of the Seyfert 1 AGN NGC 5548, however, used long-term high-intensity monitoring by the *Swift* observatory to unambiguously determine that the UV/optical variability lags the X-ray variability in this system (Edelson et al., 2015, McHardy et al., 2014).

If we assume that these lags are produced by the reprocessing of X-rays by a point-source above the centre of a Shakura-Sunyaev accretion disc (Shakura & Sunyaev, 1973), the measured lags will be proportional to the wavelength to the power of 4/3 (see Sections 1.2.2, 1.4.1.1). Accurate measurement of these lags can therefore allow this, and other, models of accretion to be tested and the geometry of the accretion disc directly probed.

Several studies testing the wavelength dependence of time lags have been carried out, e.g. Cackett et al. (2007), Sergeev et al. (2005) measured the lags between the UV/optical bands (without the X-rays) in samples of AGN and found that the $\lambda^{4/3}$ model fit the data well. A study by Shappee et al. (2014) including the X-rays, however, found the lags to be proportional to $\lambda^{0.37}$; without the X-ray lag, they found the UV/optical lags to be proportional to $\lambda^{1.18}$ (i.e. close to 4/3), but extrapolation to X-ray wavelengths predicted a lag 2.4 days from the measured X-ray lag.

The long-term *Swift* monitoring of NGC 5548 found that the $\lambda^{4/3}$ relation fits both the X-ray lag and the UV/optical lags (Edelson et al., 2015, McHardy et al., 2014). Despite fitting this relation, however, the data showed longer lags than would be expected from a Shakura-Sunyaev disc with the measured characteristics of NGC 5548. This implies the disc may appear larger in a given wavelength than expected. This agrees with the results from microlensing studies of AGN accretion discs, which come to a similar conclusion (Morgan et al., 2010). This could be explained by a low radiative efficiency in the disc, or alternatively by an inhomogeneous disc, in which the outer regions are 'clumpy', leading to enhanced emission at larger radii (Dexter & Agol, 2011, Morgan et al., 2010). Additionally, it is possible that the assertion that the UV/optical variability originates from an irradiated disc is incorrect and is produced elsewhere, e.g. at the inner edge of the BLR irradiated by the inner accretion disc, as suggested by Gardner & Done (2016).

In this chapter, I will discuss the use of cross-correlation analysis and the modelling of reprocessing in measuring time lags and the geometry of the accretion discs of AGN (see Sections 4.2 and 4.3 respectively). In Section 4.4, this will be discussed in particular relation to the AGN NGC 4395, and a set of quasi-simultaneous UV/optical and X-ray data of NGC 4395 from *XMM-Newton* and several ground-based observatories. The implications of the results for the geometry and accretion physics of AGN will be discussed in Section 4.6.

4.2 Cross-Correlation

Cross-correlation is a method of determining the strength of the linear correlation between two data sets. The cross-correlation coefficient (CCC), of two data sets is given by

$$CCC = \frac{1}{N} \sum_{i=1}^{N} \frac{x_i y_i}{\sigma_x \sigma_y} \tag{4.1}$$

where x_i and y_i are the corresponding data from the two data sets and σ_x and σ_y are the standard deviations of the two data sets. If the data sets are mean-subtracted, the CCC is normalised such that a value of 1 is a perfect positive correlation, a value of -1 is a perfect negative correlation and a value of 0 is no correlation.

For time series, cross-correlation is a powerful tool in determining not only whether two time series are correlated, but also whether there is a lag between the variability in these two time series. This lag can be determined by calculating the CCCs of the time series for a range of time lags introduced to one of the two data sets. The resultant set of CCCs for each time lag is the cross-correlation function (CCF), which will peak at the time lag at which the two data sets are most strongly correlated. The normalised CCF of two data sets is given by:

$$CCF(\tau) = \frac{1}{N} \sum_{t=0} \frac{(x(t) - \bar{x})(y(t - \tau) - \bar{y})}{\sigma_x \sigma_y} \tag{4.2}$$

This equation will only work for evenly spaced data with the same time-sampling, however. As real Astronomical data is often unevenly sampled, a different method is required to calculate the CCF of such data. There are two main methods for this purpose, which are detailed below.

4.2.1 Interpolation Cross-Correlation Function

The interpolation cross-correlation function (ICF, see Gaskell & Sparke, 1986) of a data set is calculated by interpolating between the data points of one set of data, which has been shifted by a time delay τ, in order to obtain an estimated value of that data set at the times at which the second data set were taken (see Fig. 4.1). This produced simultaneous data, to which equation 4.2 can be applied. Simple linear interpolation is normally used for this method. As this is unlikely to be a good approximation to the real value at the time for which the data is interpolated, systematic errors can be introduced and the resultant CCFs must be interpreted accordingly.

4.2.2 Discrete Cross-Correlation Function

The discrete cross-correlation function (DCF), developed by Edelson & Krolik (1988), has the advantage of not requiring any form of interpolation or evenly-spaced data, though in the case that the number of data points is low it has been found to be less sensitive than ICFs (White, 1994). In this method, CCCs are worked out for every combination of pairs of data points in the two data sets. The equivalent time lag for each CCC is then simply the time difference between the times at which the two data points were taken, i.e.

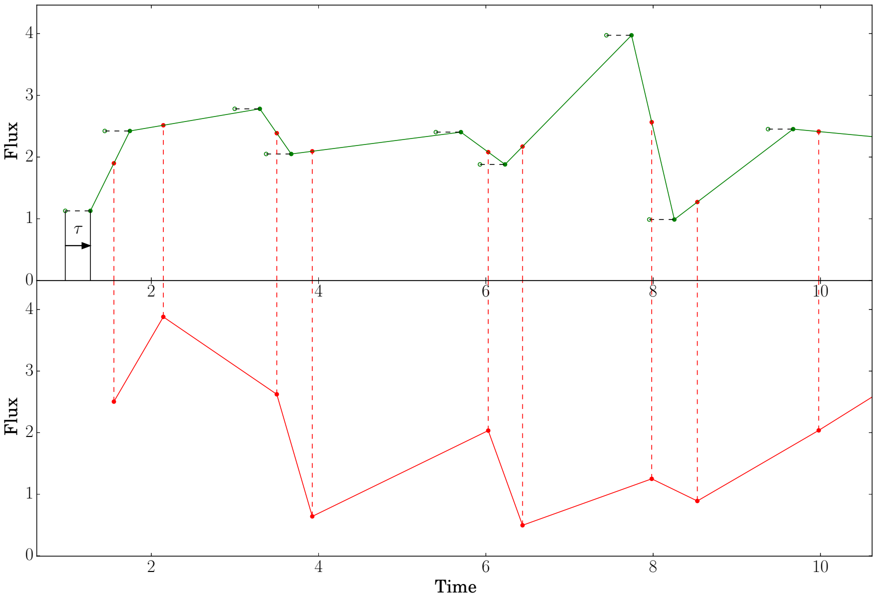

Figure 4.1: The use of linear interpolation in calculating estimated values in one data set at the measurement times of the other, for an interpolation cross-correlation function

$$CCC(\tau) = \frac{(x_i - \bar{x})(y_j - \bar{y})}{\sigma_x \sigma_y}, \text{where } \tau = t_i - t_j \tag{4.3}$$

For unevenly-spaced data, each CCC will have a different time lag, however. In order to obtain a CCF, the CCCs are therefore binned in equal time lag intervals, such that the average degree of correlation is found for a given time lag bin.

4.2.3 Auto-Correlation Function

The Auto-Correlation Function (ACF) refers to the CCF that results from cross-correlating a data set with itself. The ACF is therefore always symmetrical about zero, peaking at a value of one at zero lag. The width of the ACF of a data indicates the timescale on which the strongest variability is occurring, with a narrower ACF indicating that most of the variability is on shorter timescales. An ACF which is, or is close to being, a Dirac delta function, i.e. zero everywhere except at zero lag, at which it is one, is therefore indicative of either white noise data or variability which is occuring on timescales shorter than the sampling of the data.

4.2.4 Confidence Curves

The size of a peak in a CCF is an indication of how significant any time lag shown by that peak is, however, in order to have a numerical estimate of the significance of a given peak, confidence curves must be calculated. Confidence curves indicate the value of the CCF for a given time lag at which there is a given chance of a peak being real, i.e. the confidence in the peak not having been produced by chance. Peaks which are above this level therefore have a confidence at least as high as that of the confidence curve above which it lies.

In order to calculate confidence curves, it is necessary to simulate light curves which have the same statistical properties as that of one of the two data sets which are being cross-correlated. The standard method for simulating such light curves is the Timmer & Konig (1995) method. This method produces a light curve with a given power spectral density (PSD), by adding Gaussian noise to a given PSD model to produce a simulated periodogram, then taking the inverse Fourier transform of this periodogram.

Whilst the Timmer & Konig (1995) method is a reasonable method for producing simulated light curves, it can only produce data whose probability density function (PDF) is Gaussian. This is not the case in most real Astronomical data sets, including the light curves of AGN, which are 'bursty', as well as always being positive, both traits which a Gaussian PDF cannot reproduce. In this thesis I therefore use a more recent method, developed by Emmanoupolous et al. (2013), which can also reproduce a given PDF in the simulated light curves, in addition to a given PSD. This is achieved by using a loop to vary the phases and amplitudes of a periodogram produced using the Timmer & Koenig method with the desired PSD until its PDF also matches the input. In each step, the Fourier amplitudes of the simulated periodogram are adjusted such that they match that of the desired PSD whilst the phases are left unaltered, this will change the PDF of the light curve, however. The values of the inverse Fourier transform of the adjusted periodogram are then replaced with values from a white-noise set of random numbers generated from the desired PDF, by matching the ranked values from both sets of data (i.e. the highest point in the simulated light curve is replaced by the highest point in the data set generated from the PDF, then the second highest from both etc.). This will produce a light curve with the same PDF, but a PSD different from the desired one. By iterating over the light curve with the same steps, however, the PSD

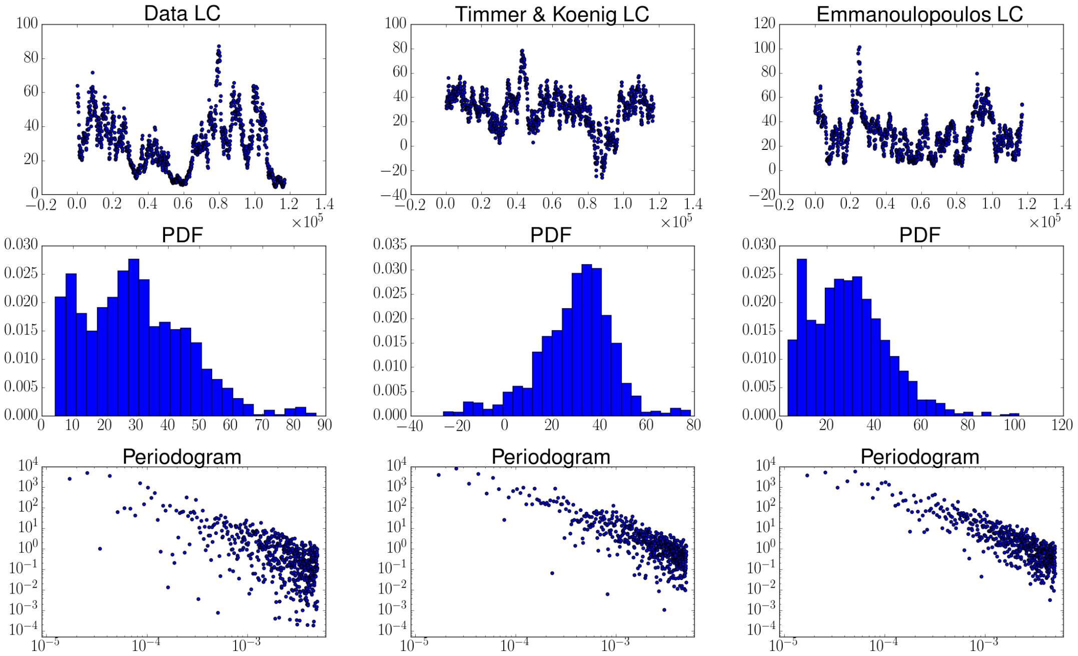

FIGURE 4.2: Comparison to the data of light curves and the corresponding PDFs and PSDs produced using the Timmer & Konig (1995) method and the Emmanoupolous et al. (2013) method.

and PDF will eventually converge on the desired distributions. Fig. 4.2 shows examples of the PDF, PSD and light curve of simulated data compared to real data, produced with my Python implementation of the algorithm[1] (Connolly, 2015b), previously used in e.g. Chidiac et al. (2016). The periodogram of the light curve produced using the Emmanoupolous et al. (2013) method (bottom right in Fig. 4.2) shows less scatter than the periodogram of the original data, as it is produced from an analytical function fitted to the histogram of the data (a Gamma distribution plus a log-normal distribution) and therefore does not include the Poisson noise present in the data.

To determine the confidence curves of a cross-correlation, a large number (e.g. $N = 100,000$) light curves are simulated from the statistical properties of one of the two data light curves, then cross-correlated with the second data light curve. The resultant CCCs are then ordered in each time lag value. The n probability confidence curve is then determined by taking the $(N * n)$th value at each time lag. These significances correspond to a single test, however, i.e. a test looking for a single, known lag. As in this case we are looking for a number of different lags, this is equivalent to multiple tests, meaning the actual random chance of obtaining a peak at a given lag is higher than

---

[1] Available at https://github.com/samconnolly/DELightcurveSimulation

these values. In order to account for this, the full widths at half maximum (FWHMs) of the ACFs of both data light curves are measured and added in quadrature, in order to obtain a combined characteristic timescale of variability. By dividing the range of time lags calculated for the CCF by this characteristic timescale, the number of independent peaks forming the CCF is obtained, equivalent to the number of independent tests. The significance of the confidence curve formed by the $(N * n)$th value at each time lag is then given by n^t, where t is the number of independent tests.

4.2.5 Estimating the Power Spectral Density

The PSD of a light curve is the degree of variability present in the data at a given temporal frequency. The PSD can be estimated from the periodogram, obtained by calculating the Fourier transform of the light curve. Direct fitting of the periodogram is problematic, however, as the standard deviation at a given frequency is equal to the value of the periodogram at that frequency. This problem can be addressed either through binning, as proposed by Papadakis & Lawrence (1993), or by using a maximum-likelihood method. Accurate fitting of the PSD to a binned periodogram requires normally distributed data in each bin, however, meaning relatively large data sets are required. I therefore employ a maximum-likelihood method for PSD estimation in this thesis.

For a given underlying PSD model, $\mathscr{P}(f_j;\vec{\gamma})$, in which $\vec{\gamma} = \gamma_1, \gamma_2, ..., \gamma_n$ is a vector consisting of the parameters of this model (e.g. normalisation, frequency slopes etc.), the probability of obtaining a single periodogram data point $P(f_j)$, given the PSD model $\mathscr{P}(f_j;\vec{\gamma})$, is given by

$$\lambda_j[P(f_j)|\mathscr{P}(f_j;\vec{\gamma})] = \begin{cases} \frac{e^{-P(f_j)/\mathscr{P}(f_j;\vec{\gamma})}}{\mathscr{P}(f_j;\vec{\gamma})} & j = 1, 2, ... \begin{cases} N/2 - 1 \text{ (even N)} \\ (N-1)/2 \text{ (odd N)} \end{cases} \\ \frac{e^{-P(f_{Nyq})/\mathscr{P}(f_{Nyq};\vec{\gamma})}}{[\pi P(f_{Nyq})\mathscr{P}(f_{Nyq};\vec{\gamma})]^{1/2}} & j = N/2 \text{ (even N)} \end{cases} \tag{4.4}$$

where f_j is a given frequency and f_{Nyq} is the Nyquist frequency. The total probability of the entire periodogram for the PSD model $\mathscr{P}(f_j;\vec{\gamma})$ is the given by the product of the individual estimates, i.e.

$$\mathscr{L} = \prod_{i=1}^{N/2(evenN)(N-1)/2(oddN)} \lambda[P(f_j)|\mathscr{P}(f_j;\vec{\gamma})] \tag{4.5}$$

The maximum-likelihood estimate of the PSD model parameters, $\vec{\gamma}$, are obtained by maximising $\mathscr{L}$. As $\mathscr{L}$ is given by a product of the individual values from Eqn. 4.4, the maximum-likelihood parameters are equivalently obtained by minimising the log-likelihood function $\mathscr{C} = -2\ln\mathscr{L}$, i.e.

$$\mathscr{C} = \begin{cases} \left[2\sum_{j=1}^{j=N/2-1}\left(\ln[\mathscr{P}(f_j;\vec{\gamma})] + \frac{P(f_j)}{\mathscr{P}(f_j;\vec{\gamma})}\right)\right] + \ln\left(\pi P(f_{Nyq})\mathscr{P}(f_j;\vec{\gamma}) + 2\frac{P(f_{Nyq})}{\mathscr{P}(f_{Nyq};\vec{\gamma})}\right) & \text{(even N)} \\ 2\sum_{j=1}^{j=(N-1)/2}\left(\ln[\mathscr{P}(f_j;\vec{\gamma})] + \frac{P(f_j)}{\mathscr{P}(f_j;\vec{\gamma})}\right) & \text{(odd N)} \end{cases} \tag{4.6}$$

This is achieved using a Basin-Hopping algorithm to find the global minimum (Wales & Doye, 1997). Further details of this method can be found in e.g. (Barret & Vaughan, 2012, Vaughan, 2005).

As AGN light curves are not white noise, but rather are red noise, periodogram estimates can suffer from 'red noise leak', by which variability power is shifted from low to higher frequencies due to the finite length of observations (Deeter, 1984). This effect can be avoided by randomly selecting a small section of an initially much longer (e.g. 100 times longer) simulated light-curve which is of the desired length (see e.g. Uttley et al., 2002).

In addition, aliasing due to a finite sampling rate can cause distortions in the measured PSD, pushing power from high to lower frequencies (Kirchner, 2005). In order to avoid this problem, the time resolution used for simulations is increased, e.g. to 10 times that of the data light curve.

4.2.6 Estimating the Probability Density Function

The PDF of a light curve is the probability distribution of fluxes in the light curve. The underlying PDF can be estimated by binning the fluxes in the light curve and fitting the resultant histogram. The PDFs of 'bursty' sources, such as AGN, are often best-fitted by a log-normal distribution (likely arising due to a non-linear, multiplicative process, see Uttley et al., 2005)), sometimes in conjunction with a gamma function at higher energies (Chidiac et al., 2016). As the histogram of the light curve has to be fitted, it is important that the correct number of bins are used to properly represent the underlying PDF and thereby obtain the correct model parameters when fitting the data. Here I use the method of Knuth (2006), by which the optimum number of equal-width bins is obtained by maximising the the likelihood that a given data set $\vec{d} = \{d_1, d_2, ..., d_N\}$ of length N is represented by a probability density consisting of M box-functions of equal width, i.e.

$$\mathscr{H}(x) = \sum_{k=1}^{M} \frac{N_k}{Nw} \Pi(\eta_{k-1}, x, \eta_k) \tag{4.7}$$

where N_k is the number of data points in the k^{th} bin, w is the bin width, η_{k-1} and η_k are the edges of the box functions and $\Pi(\eta_{k-1}, x, \eta_k)$ is a box function equal to 1 where $\eta_{k-1} <= x < \eta_k$ and zero otherwise. In this chapter, I use a python implementation of the 'optBINS' algorithm based on this method from (Knuth, 2006).

4.3 Modelling Reprocessing

As the ultimate aim of calculating the cross-correlation function is determine the geometry and physics of the accretion disc, the next step is to model the reprocessing of the X-ray flux in order to predict the resultant UV flux. This is achieved by calculating the response of the disc to an impulse of X-ray illumination.

4.3.1 JAVELIN

A simplified version of this method not based on a physical model is implemented in the JAVELIN code (Just Another Vehicle for Estimating Lags In Nuclei) for determining inter-band lags (Zu et al., 2011, 2013). In this implementation, the driving light curve (i.e. the data light curve to which the second data light curve responds), is assumed to vary as a damped random oscillator, which is thought to be a reasonable estimation for AGN (Kelly et al., 2009). The value of the flux between data points is estimated using simulated light curves generated from the covariance between the amplitude at times t_i and t_j, given by

$$\langle s_c(t_i) s_c(t_j) \rangle = \sigma^2 exp\left(\frac{-|t_i - t_j|}{\tau_d}\right) \tag{4.8}$$

where σ is the amplitude of the variability and τ_d is the damping timescale. These parameters are obtained by fitting the covariance matrix of the data.

The response function is assumed to be a 'top hat function', i.e. zero everywhere except between times given by the time lag and the width of the 'top hat', at which it is a constant normalisation value, such that the response of an impulse is given by

$$\Psi(t) = \begin{cases} A & \tau \leq t \leq \tau + \omega \\ 0 & \text{o/w} \end{cases} \tag{4.9}$$

where A is the normalisation, i.e. the height, of the top hat function, ω is its width and τ is the time lag (see Fig. 4.3). The parameters of the top hat response function are obtained by convolving the response with the driving light curve and varying the parameters to fit the reprocessed light curve data. The maximum-likelihood parameters are obtained using Markov chain Monte Carlo (MCMC). Despite the assumption of a damped random walk and a top hat response function, JAVELIN has been shown to give reliable results in determining the time lag in AGN data sets (Pancoast et al., 2014a, Shappee et al., 2014). JAVELIN is therefore used in this chapter for estimating time lags.

4.3.2 Physical Modelling

Whilst conclusions can be drawn from time lag measurements alone with regard to physical models of reprocessing, the ideal way to test physical models is to model the actual response of the disc for a given physical model and test whether the observed parameters of the system predict the observed lags within this model.

As described in Section 1.4.1.1, the temperature of an accretion disc is dependent on the intensity of X-ray illumination incident on it, in addition to the basic physical parameters of the system (i.e. the black hole mass and spin, and the accretion rate). As the X-ray illumination will vary as the luminosity of the X-ray source varies, the temperature of

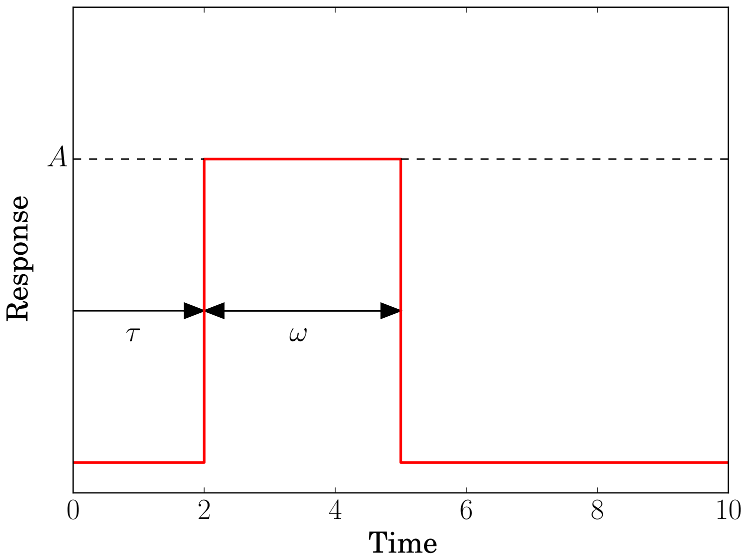

FIGURE 4.3: A top hat function of width ω, height A and lag τ.

the disc will also vary over time, and subsequently the black body emission it produces at a given radius.

The thermal spectrum of the accretion disc (at optical/UV wavelengths), consists of the sum of the black body spectra emitted by the annuli at each radius, given by Planck's law

$$L(\lambda) = 4\pi B(\lambda) A_{annulus}(R) = \sum_{i=1}^{N} \frac{8\pi hc^2}{\lambda^4} \frac{1}{e^{\frac{hc}{\lambda k_B T(R_i)}} - 1} \times \pi (R_{i+1} - R_i)^2 \tag{4.10}$$

where $L(\lambda)$ is the luminosity at wavelength λ, $B(\lambda)$ is the spectral radiance in W sr^{-1} m^{-2} Hz^{-1}, $A_{annulus}(R)$, and N is the number of annuli into which the disc is divided, with the inner radius if the innermost annulus given by $R_1 = R_{in}$, the ISCO of the black hole, and the outer radius of the outermost annulus given by $R_{N+1} = R_{out}$, the sublimation radius.

The X-ray illumination at a given radius of an impulse is also dependent on the light travel time from the X-ray source to that radius, meaning the radial temperature profile is dependent on the luminosity history of the X-ray source. The response function of an illuminated disc has been calculated analytically by e.g. (Berkley et al., 2000, Cackett et al., 2007), however this method is not used in this thesis, as it is not computationally preferred when variable X-ray illumination is included. Instead, I use the analytical function for the response of an annulus of the disc at a given radius and inclination, and

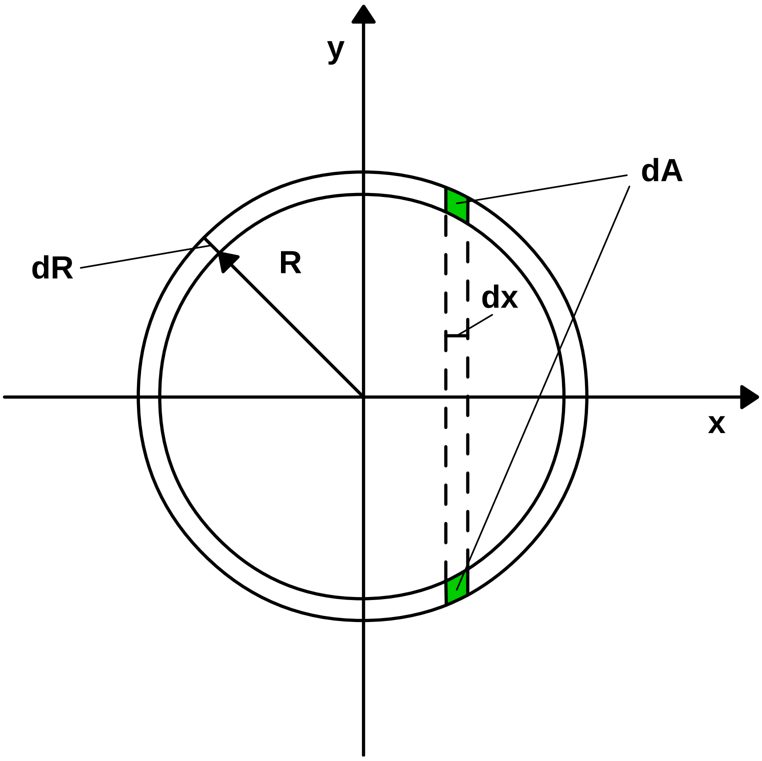

FIGURE 4.4: An infinitesimal slice of an annulus of area dA and width dx in the axis through the disc parallel to the plane through the centre of the disc which is perpendicular to the disc and parallel to the direction of the observer.

an impulse of a given luminosity. This allows the response function for each radius to be calculated only once, then applied repeated to the calculated spectrum of each radius for a given X-ray illumination as it changes over time.

The response of an inclined annulus can be obtained by calculating the area of the infinitesimal slice moving across the annulus in the direction parallel to the plane perpendicular to the disc and parallel to the direction of the observer, whose emission is visible after time t. The area of such a slice, dA, is the area of the annulus of radius R and width dR which is between x and $x + dx$, where x is the axis through the centre of the disc which lies in the plane parallel to the to the direction of the observer and perpendicular to the surface of the disc (see Fig. 4.4), given by

$$x = \frac{tc}{sin(i)} \tag{4.11}$$

where i is the inclination and t is the time difference before or after emission from the slice level with the centre of the annulus, defined as x = 0, reaches the observer (i.e. the time lag/lead of the emission). In this case, the emitting area with respect to x is given by

$$A(x, R, dR) = \int_{x_1}^{x_2} dA(x)dx \tag{4.12}$$

where

$$dA(x, R, dR) = \begin{cases} \sqrt{(R+dR)^2 - x^2} - \sqrt{R^2 - x^2} & -R <= x <= R \\ \sqrt{(R+dR)^2 - x^2} & -(R+dR) <= x < -R \\ \sqrt{(R+dR)^2 - x^2} & R < x =< R+dR \\ 0 & \text{o/w} \end{cases} \tag{4.13}$$

The response of such an an annulus is shown in the top panel of Fig. 4.6 The emission response for such an annulus at radius R is then given by

$$L(\lambda, x, R) = \frac{8\pi hc^2}{\lambda^4} \frac{1}{e^{\frac{hc}{\lambda k_B T(R)}} - 1} A(x) \tag{4.14}$$

The total response of the disc is formed by the sum of the responses of each annulus, however each response also needs to be delayed by the difference between the lags associated with the direct (X-ray) and the reprocessed (optical/UV) emission. The lag experienced by the reprocessed (optical/UV) emission (τ_R) originating at the annulus at a given radius, R, is constant and is equal to the sum of the light travel time from the X-ray source at height H to the radius R at which the annulus lies ($\tau_{X,R}$), given by

$$\tau_{X,R} = \frac{\sqrt{H^2 + R^2}}{c} \tag{4.15}$$

and the extra light travel time from radius R to the observer ($\tau_{X,obs}$), i.e. the light travel time from radius R to the plane perpendicular to the direction of the observer at the distance of the point on the disc closest to the observer (the observer-plane), given by

$$\tau_{R,Obs} = \tau_{max} - \tau_i \tag{4.16}$$

where t_{max} is the light travel time from the centre of the disc to the observer-plane, and t_i is the distance from the plane perpendicular to the direction of the observer at the distance of the centre of the disc (the centre-plane), given by

$$\tau_i = \frac{Rsin(i)}{c} \tag{4.17}$$

The lag experience by the direct (X-ray) emission (τ_X) is the distance from the X-ray source to the observer-plane, given by

$$\tau_{R,obs} = \tau_{max} - \tau_{X,i} \tag{4.18}$$

where $\tau_{X,i}$ is the light travel time between the centre of the disc and the plane perpendicular to the observer at the distance of the X-ray source, given by

$$\tau_{X,i} = \frac{Hcos(i)}{c} \tag{4.19}$$

The observed lag between the reprocessed and direct emission is therefore given by

$$\Delta\tau = \tau_R - \tau_X = (\tau_{max} - t_i + \tau_{X,R}) - (\tau_{max} - \tau_{X,i}) = \tau_{X,R} - \tau_i + \tau_{X,i} \tag{4.20}$$

however, τ_i is included in the inclined annulus response and does not need to be added. The lag of each annulus response is therefore

$$\Delta\tau = \tau_{X,R} + \tau_{X,i} = \frac{\sqrt{H^2 + R^2} + Hcos(i)}{c} \tag{4.21}$$

This lag is applied to each annulus in order to build the total response of the inclined disc.

A further addition to the response function is the inclusion of the radial response of the annulus due to the light travel time between the inner and outer edges. At most

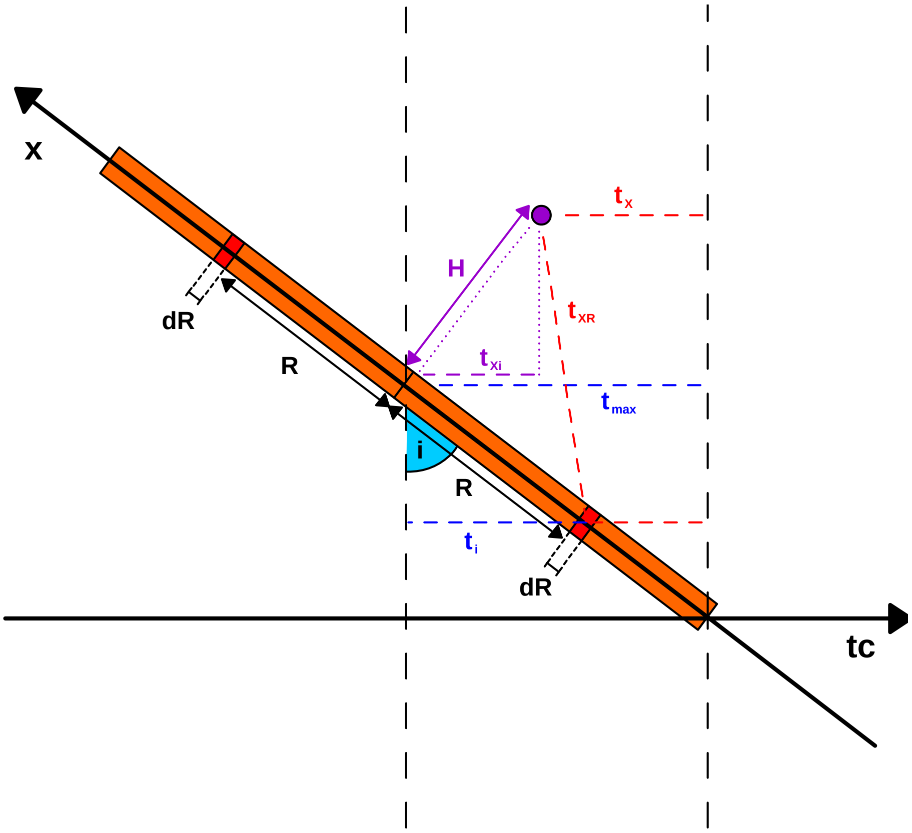

FIGURE 4.5: The lags associated with the emission from an annulus of the disc

inclinations this response is unimportant, as its timescale is small compared to the timescale of the response due to inclination. At low inclinations, however, the difference in the travel time from either end of the annulus to the observer is small and can therefor be comparable to the width of the radial response. The radial response of a given slice can be approximated to a box function of width dR/c. The total response is the convolution of this with the response due to inclination. Fig. 4.6 shows the effect of the inclusion of the radial response on the total response of an annulus inclined at 0.1^0.

As the data to which these functions will be compared are from optical/UV data taken through filters, the final step is to apply the response of each filter to the spectrum at each time, such that the flux in a given band at a given time is obtained. The responses of the optical/UV filters of the *XMM-Newton Optical Monitor* (*OM*) and ground-based instruments used in this chapter are shown in Fig. 4.8. Examples of the resultant response functions and how they change with inclination, mass and accretion rate are shown in Fig. 4.7.

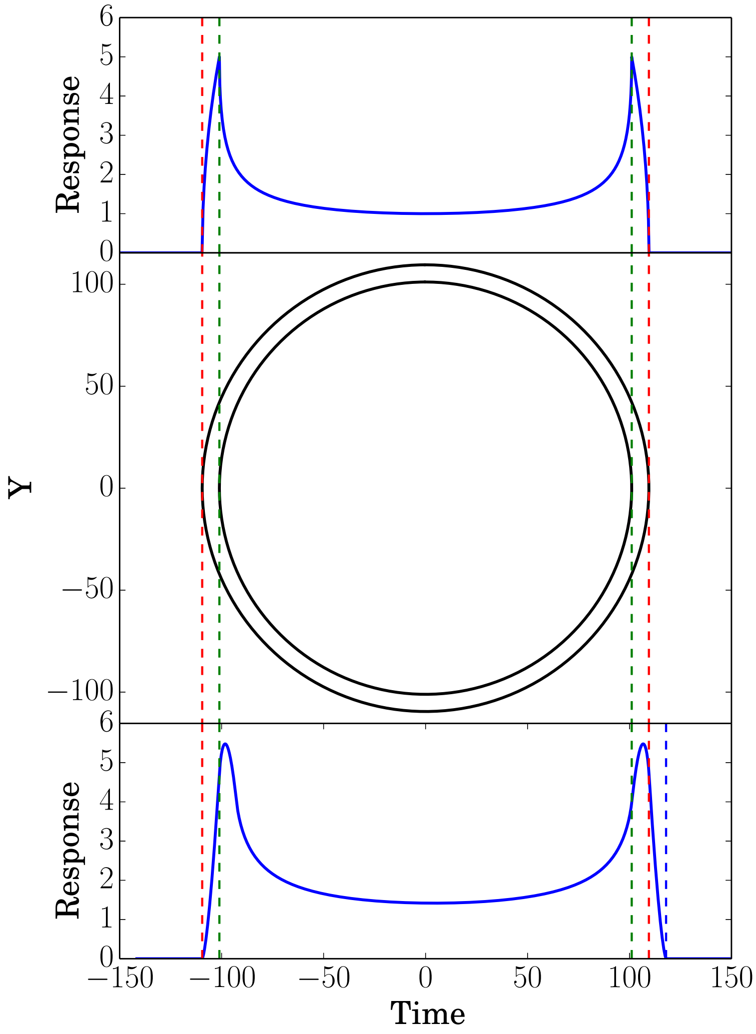

FIGURE 4.6: Response function of an annulus inclined at 0.1^0 before (top) and after (bottom) convolution with the radial response.

4.4 NGC 4395

NGC 4395 is a nearby (~ 4.3 Mpc, Thim et al., 2004) Seyfert 1.8/1.9 AGN (Filippenko & Sargent, 1989) with a relatively small mass of $(3.6 \pm 1.1) \times 10^5\ M_\odot$, measured using reverberation mapping (Peterson et al., 2005). However, the lack of a significant galactic bulge and the very short characteristic time-scale of the X-ray variability of NGC 4395 imply its mass may be still smaller (Vaughan, 2005). In either case, this makes NGC 4395 one of the lowest-mass Seyfert AGN known. The luminosity of NGC 4395 is relatively low ($L_{Bol} \sim 5 \times 10^{40}$ erg s^{-1} Lira et al., 1999, Peterson et al., 2005)), likely due in part to its mass, however its proximity makes its flux high enough to be observable. It is known to be highly variable in X-rays (Iwasawa et al., 2000, Vaughan, 2005) and moderately variable at optical and UV wavelengths (Lira et al., 1999).

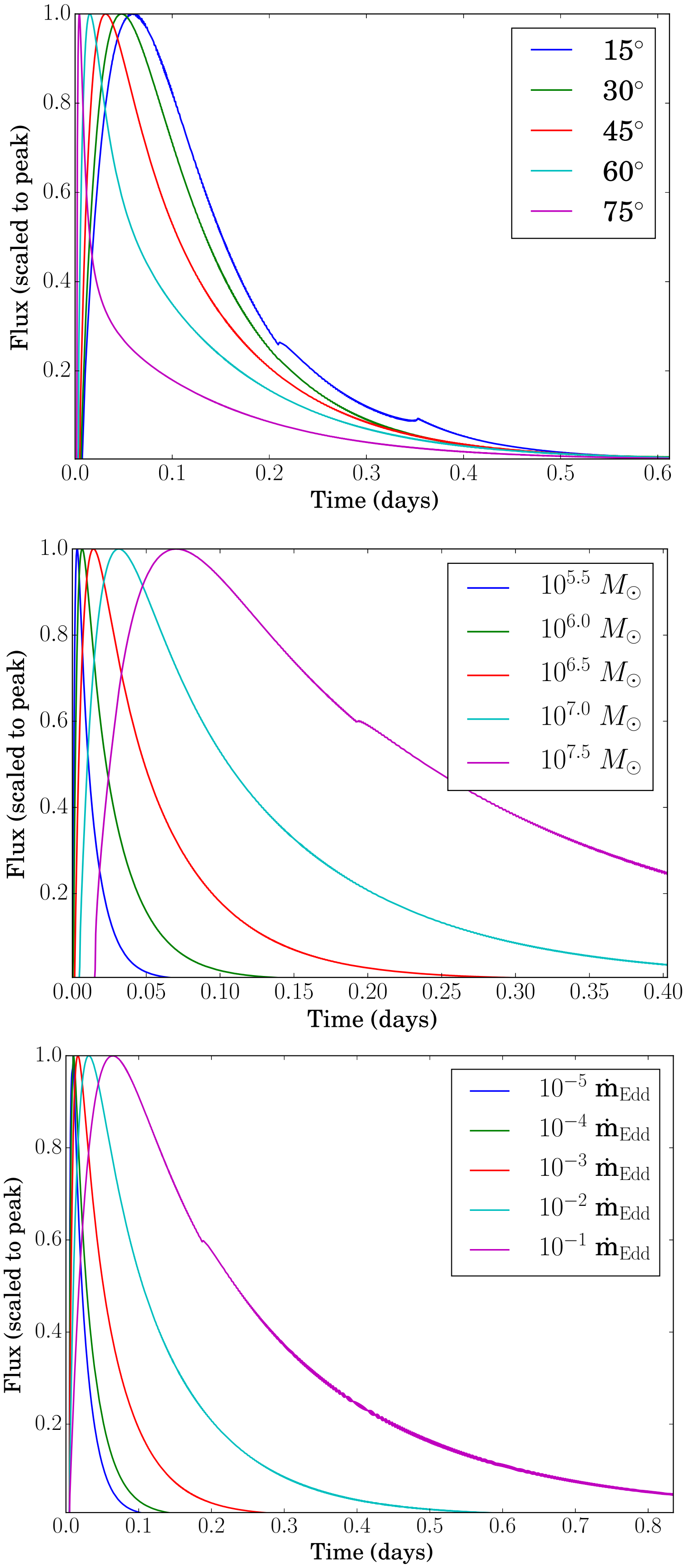

FIGURE 4.7: UVW1 response functions of the model accretion disc from an X-ray impulse: *Top:* a 10^7 $M_\odot$ black hole, accreting at 10^{-2} $\dot{\mathrm{m}}_{\mathrm{Edd}}$, for a range of inclinations. *Middle:* a black hole at an inclination of 45°, accreting at 10^{-2} $\dot{\mathrm{m}}_{\mathrm{Edd}}$, for a range of masses. *Bottom:* a 10^7 $M_\odot$ black hole at an inclination of 45°, for a range of accretion rates as a fraction of the Eddington rate.

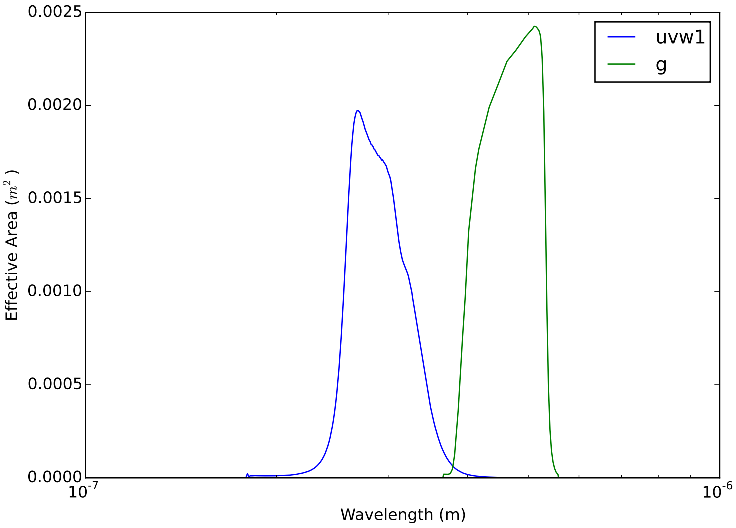

FIGURE 4.8: The filter responses of the XMM-Newton OM UVW1 band and the SDSS G band.

Short-timescale quasi-simultaneous X-ray and optical/UV data of NGC 4395 were first obtained using *Chandra* and the *Hubble Space Telescope (HST)* by O'Neill et al. (2006). They found a correlation between the 1350 Å UV and the 0.4-8.0 keV X-ray light curves, with a lag of -300 ± 1400 s. Ground-based B-band observations taken during the same *Chandra* observations found a moderate correlation between the X-ray and optical light curve in this band, with a lag of 2640 ± 780 s.

A year-long observation campaign made using *Swift* by Cameron et al. (2012) found strong correlations between the 2-10 keV X-ray light curve and the UV/optical light curve in the UVW2, U, B and V bands, all with lags close to zero. A weak correlation with a lag of around 400 s was found between the X-ray and the UVW2 light curves by splitting up the *Swift* X-ray observations into 200 s bins, however the errors on this measurement were too large for this result to be reliable.

4.4.1 XMM Observations

As the lags from smaller-mass AGN such as NGC 4395 are expected to be relatively short (hundreds-thousands of seconds), the long-term data (weeks-months) data required to accurately measure lags in more massive AGN are not necessary. Rather, a relatively high time resolution is needed. This is possible using long single observations with XMM-Newton, using EPIC-PN for X-ray observations in combination with the OM in fast readout mode for the UV/optical observations. The fast readout mode has not been widely used for AGN observations, as optical variability is typically on longer time scales, however in this case the expected time lags were short enough for its use to be beneficial. Timing mode allows continuous readout of the OM CCD with sub-second time resolution, in comparison to ~ 1100 s time resolution with standard OM imaging observations, which would make measuring lags expected to be only a few hundred seconds extremely difficult.

Observations using *XMM-Newton* were therefore made on 28 and 30 December 2014, using fast readout mode on the OM. Both observations were ~ 53 ks in length. All OM observations were made in the UVW1 band. The UVW1 band has the highest sensitivity at UV wavelengths and suffers less from host galaxy contamination than optical bands. Furthermore, the UVW1 band lies at a wavelength too short to be observed by ground-based instruments.

The data were reduced using the *XMM-Newton* Scientific Analysis System (SAS v13.5.0) (Gabriel et al., 2004). The EPIC-PN and fast-mode OM data were reduced using the *omfchain* and *epchain* tools respectively. EPIC-PN light curves were extracted with the tool *epclccorr*, using circular extraction regions of radius 22 arcsec. This tool automatically corrects for systematic effects due to vignetting, bad pixels, PSF variation, quantum efficiency and dead time. The data were binned into 100s time bins. The OM light curves were produced automatically by the *omfchain* tool; the nucleus of NGC 4395 was the only point source in the fast-mode window and could be therefore reliably extracted automatically.

4.4.2 Ground-Based Optical Observations

In addition to the *XMM-Newton* observations, continuous ground-based coverage was arranged. During the XMM-Newton observations, NGC 4395 was observable from a given location on the ground for only ~ 4 hours. Observations were therefore made from 6 different ground based observatories: the Las Cumbres Observatory Global Telescope (LCOGT) Network Telescope, McDonald Observatory, Texas; the Whipple Observatory, Arizona; the LCOGT Faulkes telescope, Haleakala Maui, Hawaii; the Kanata Observatory, Japan; The ARIES (Aryabhatta Research Institute of observational sciencES) observatory, India and the Wise Observatory, Israel. CCD imaging observations were

Instrument/Observatory	Observation Times (UTC)		Filter	Central Wavelength (nm)
	2014-12-28 - 2014-12-29	2014-12-30 - 2014-12-31		
XMM-Newton EPIC	10:31-00:57	11:08-00:33	X-Ray	0.62
XMM-Newton OM	10:30-00:57	10:25-00:40	UVW1	291.0
LCOGT Network Telescope, Texas (1m)	10:10-12:56	10:00-12:56	G	477.0
LCOGT Faulkes telescope, Hawaii (2m)	12:40-16:08	12:40-16:09	G	477.0
Whipple Observatory, Arizona (1.2m)		09:05-13:25	G	477.0
Kanata Telescope, Japan (1.5)		15:09-20:35	V	477.0
ARIES observatory, India (1.3m)	08:31-12:42	08:16-12:24	G	477.0
Wise Observatory, Israel (1m)	22:03-07:00	22:00-03:46	G	477.0

TABLE 4.1: Details of the observations of the NGC 4395.

taken at each telescope with either 100 or 200 s integrations, depending on telescope size. All observations were taken in the optical G-band except data taken at the Kanata observatory, which were taken in the V-band. Unfortunately, planned observations were not taken during a long period on the first night of observations (28 December 2014), due to a scheduling error. However, almost full coverage was obtained for the second night of observations (30 December 2014). Full details of the the telescopes and observing times are given in Table 4.1.

The optical data was reduced using the Image Reduction and Analysis Facility (IRAF) software, using the *phot* tool for aperture photometry. This tool automatically tracks the position of the sources to be extracted across images and uses PSF-fitting to find the optimum extraction region sizes and positions. Seven standard stars of known, constant magnitude were used to cross-calibrate the data from the 6 different instruments used for the observations (see Fig. 4.9). A colour-correction was applied to the data from the Kanata observatory using the same stars to calculate the expected G-band magnitude from the V-band observations.

The X-ray, UVW1 and combined g-band light curves from 28 and 30 December 2014 are shown in Figs. 4.10 and 4.11 respectively.

4.4.3 X-ray / UV-Optical Correlations

I have calculated both the DCFs and ICCFs of the X-ray light curves with the UVW1 light curves on both nights of observation, and the G-band light curve on the second night of observation; as there was almost no G-band coverage during the *XMM-Newton* observations from the first night, the G-band data from this night was not cross-correlated.

Confidence intervals were calculated using X-ray light curves simulated with my 'DELCgen' Python code employing the Emmanoupolous et al. (2013) method, as described in Section 4.2.4. The light curves were simulated using PDF and PSD models fitted to

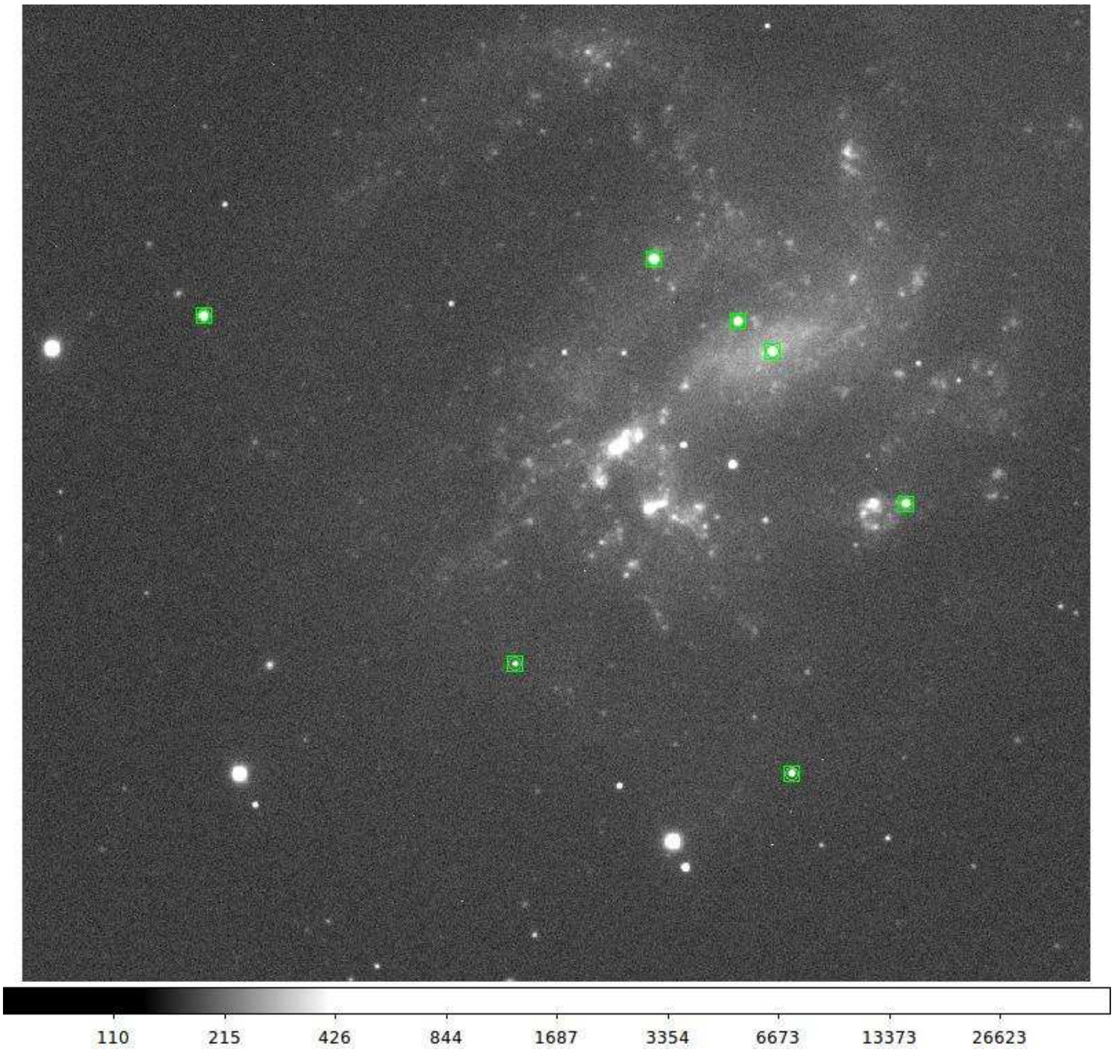

FIGURE 4.9: G-band image of NGC 4395 showing the locations of the standard stars used in aperture photometry.

the NGC 4395 X-ray data, using the methods also described in Section 4.2.4. The PDF was fitted with a log-normal distribution, given by

$$P(x) = \frac{1}{\sigma x\sqrt{2\pi}} e^{-\frac{(ln(x)/e^{\mu})^2}{2\sigma^2}} \tag{4.22}$$

where μ is the mean and σ is the standard deviation of the normally distributed logarithm of the variable. The best fit parameters of the model were $\sigma = 0.417$ and $\mu = -0.450$. A histogram of the 0.5-10 keV X-ray count rate of NGC 4395 overplotted with the best-fitting model is shown in Fig. 4.12. The histogram is well-fit by a lognormal distribution, as is typical of AGN light curves. The good fit to the data implies a low level of Poisson noise in the data relative to the intrinsic variability (the X-ray data used in this fit were

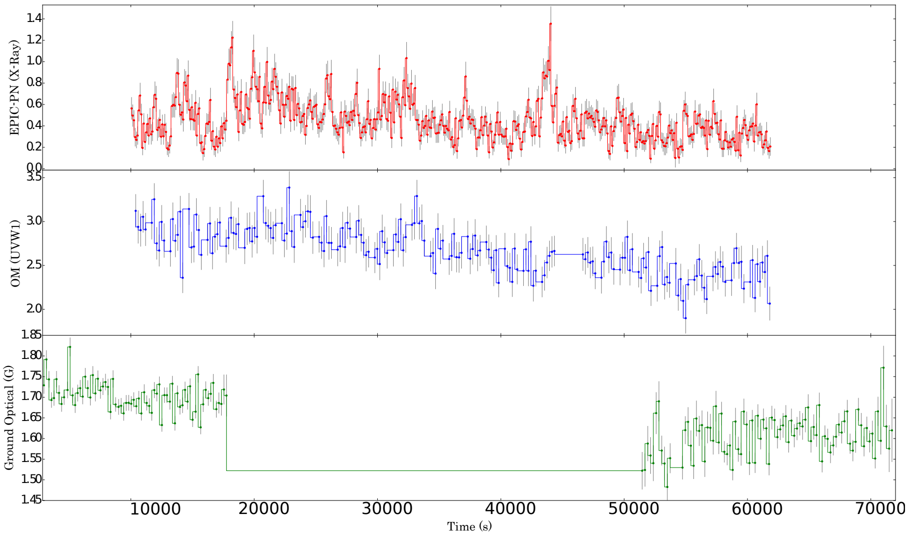

FIGURE 4.10: Light curves from the observations of NGC 4395 made on 28 December 2014: *(Top Panel) EPIC-PN* Long-term Swift 0.5-10 keV X-ray count rate. *(Middle Panel) OM* UVW1 flux. *(Bottom panel)* Ground-based g-band flux.

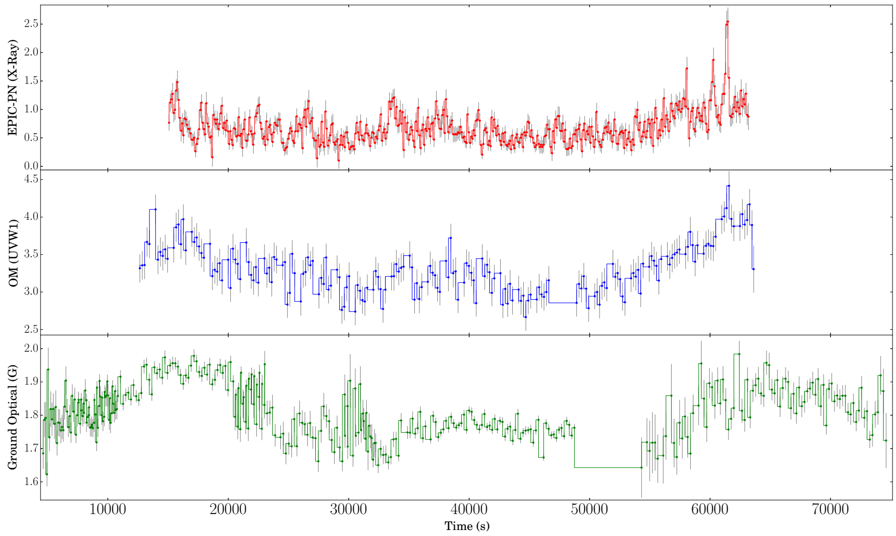

FIGURE 4.11: Light curves from the observations of NGC 4395 made on 30 December 2014: *(Top Panel) EPIC-PN* Long-term Swift 0.5-10 keV X-ray count rate. *(Middle Panel) OM* UVW1 flux. *(Bottom panel)* Ground-based g-band flux.

binned with the same interval as the optical data shown in Figs. 4.10 and 4.11, twice that of the X-ray light curves in those figures, meaning the error variance is also lower than shown in these X-ray light curves).

The PSD was fitted with both a bending power law of the form

$$P(\nu) = \frac{A\nu^{-\alpha_{low}}}{1 + (\nu/\nu_{bend})^{\alpha_{high}-\alpha_{low}}} + c \tag{4.23}$$

where A is the normalisation, ν_{bend} is the bending frequency, α_{high} is the high-frequency

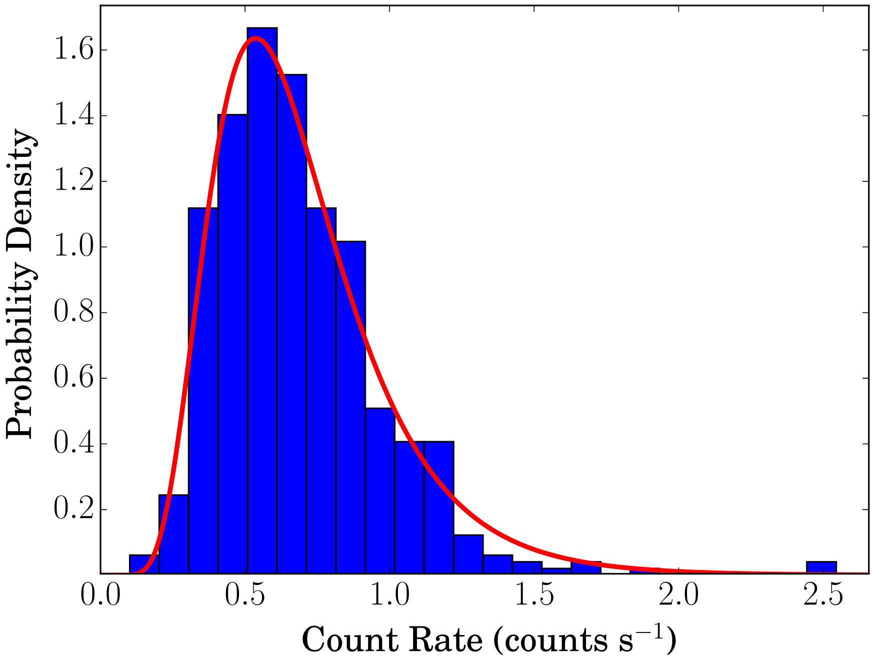

FIGURE 4.12: Histogram of the count rate of the *XMM-Newton EPIC-PN* data of NGC 4395, overplotted with the best fitting PDF model, consisting of a log-normal distribution.

slope, α_{low} is the low-frequency slope and c is a constant representing the Poisson noise level. The maximum-likelihood parameters for the NGC 4395 were $\nu_{bend} = 7.5 \times 10^{-2}$, $\alpha_{high} = 1.90$ and $\alpha_{low} = 0.90$. The low- and high-frequency slopes are both consistent with previous values for similar energy ranges (e.g. $\alpha_{low} = 1.20^{+0.40}_{-0.76}$, $\alpha_{high} = 1.92^{+0.24}_{-0.28}$ for 0.2-10.0 keV Vaughan, 2005), however the bend frequency is less consistent (e.g. $\nu_{bend} = 1.9^{+0.8}_{-1.5} \times 10^{-3}$ for 0.2-10.0 keV Vaughan, 2005); this is unsurprising, however, as Vaughan (2005) used 130 ks of data, compared to 2 sets of 50 ks here, meaning we had less low-frequency data. The difference will not cause great enough changes to the resultant simulated light curves to affect the confidence interval estimations. The periodogram of the data and the best-fitting model are shown in Fig. 4.13.

Both CCFs of the X-rays and UVW1 band from the first night show very weak correlations, with very broad peaks. The lack of a strong correlation is likely due to the low variability in both bands during this night of observations.

Conversely, both CCFs of the X-rays and UVW1 band on the second night show very strong correlations, with well-defined peaks at a few hundred seconds (see Figs. 4.16 and 4.17). In both cases, the peaks were very high confidence ($> 99\%$). The DCF between the X-rays and the G-band also shows a strong correlation, with a peak at

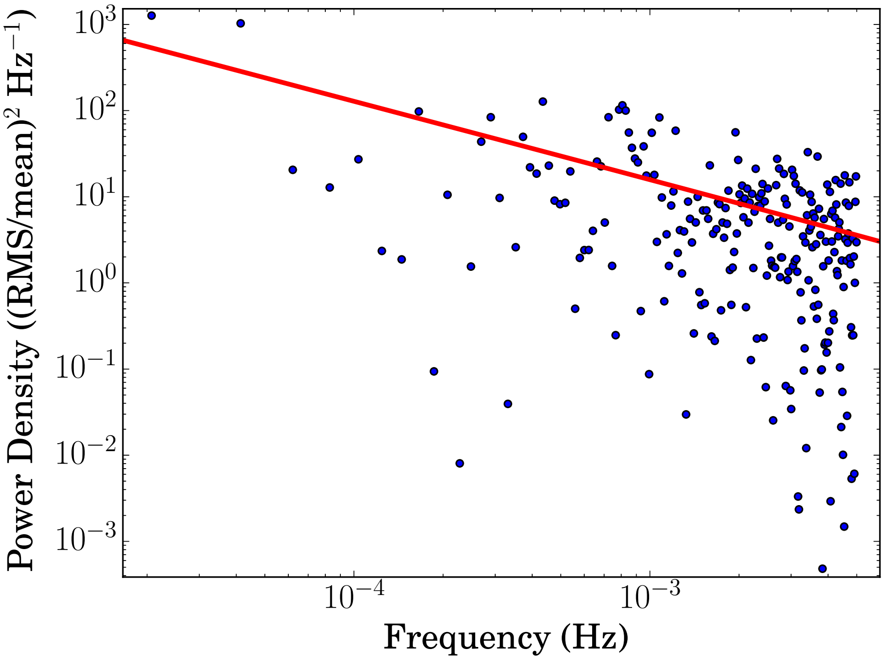

FIGURE 4.13: Periodogram of the NGC 4395 data, overplotted with the maximum-likelihood PSD model, consisting of a bending power law

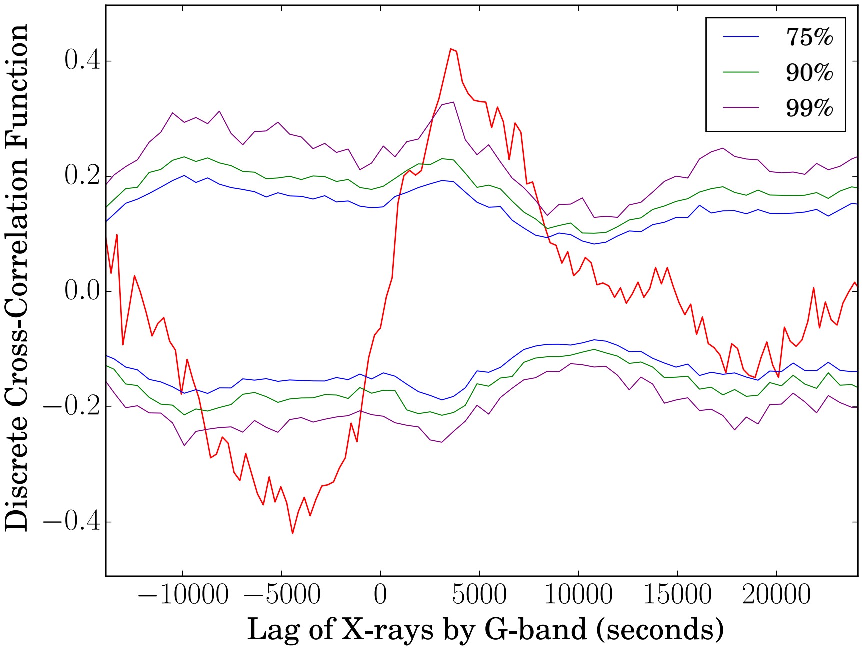

FIGURE 4.14: Discrete cross correlation function between the X-ray and g-band light curves from the first night of observations. The 95% (dashed red) and 99.99% (solid thin blue) confidence levels are also shown.

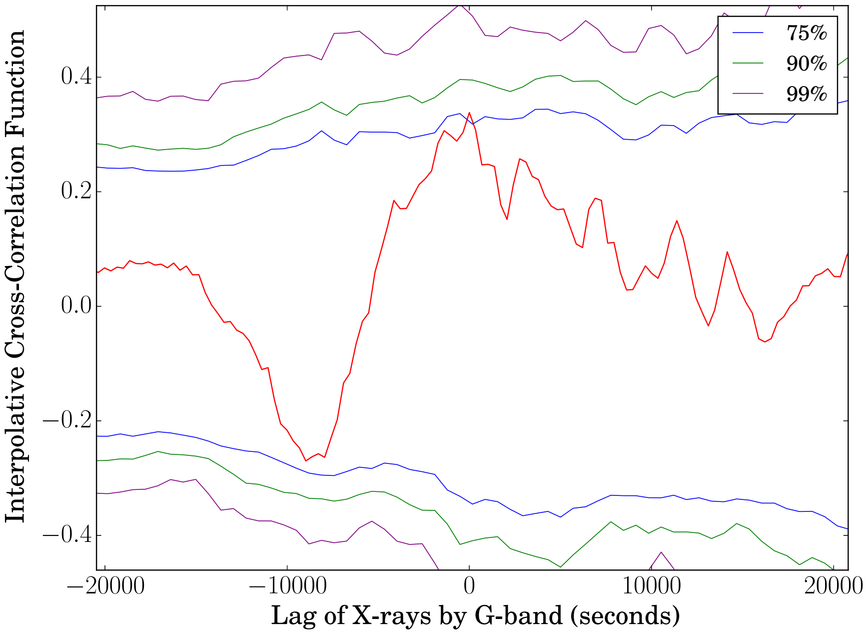

FIGURE 4.15: Discrete cross correlation function between the X-ray and g-band light curves from the second night of observations. The 95% (dashed red) and 99.99% (solid thin blue) confidence levels are also shown.

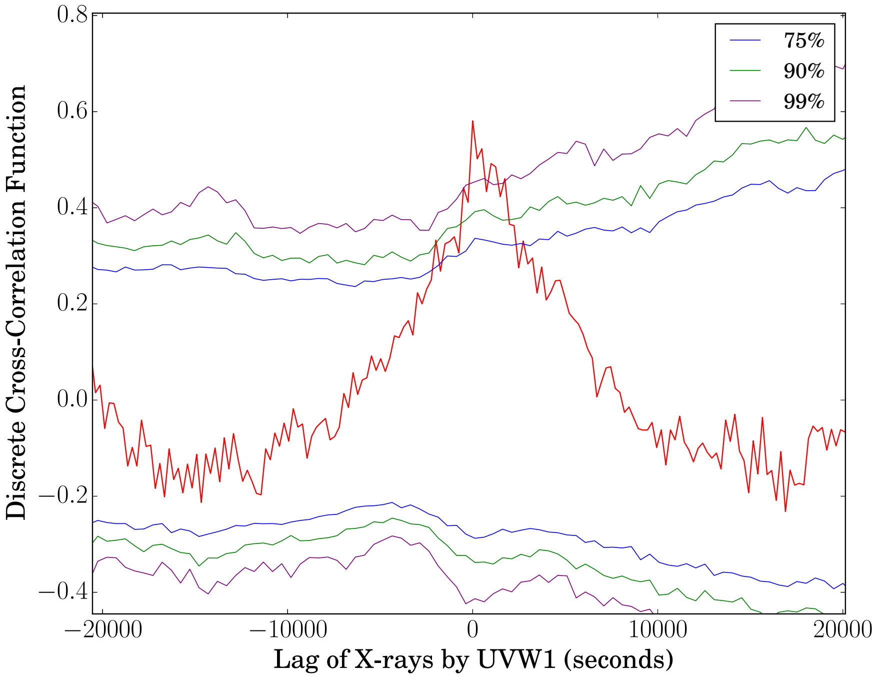

FIGURE 4.16: Discrete cross correlation function between the X-ray and uvw1-band light curves from the second night of observations. The 95% (dashed red) and 99.99% (solid thin blue) confidence levels are also shown.

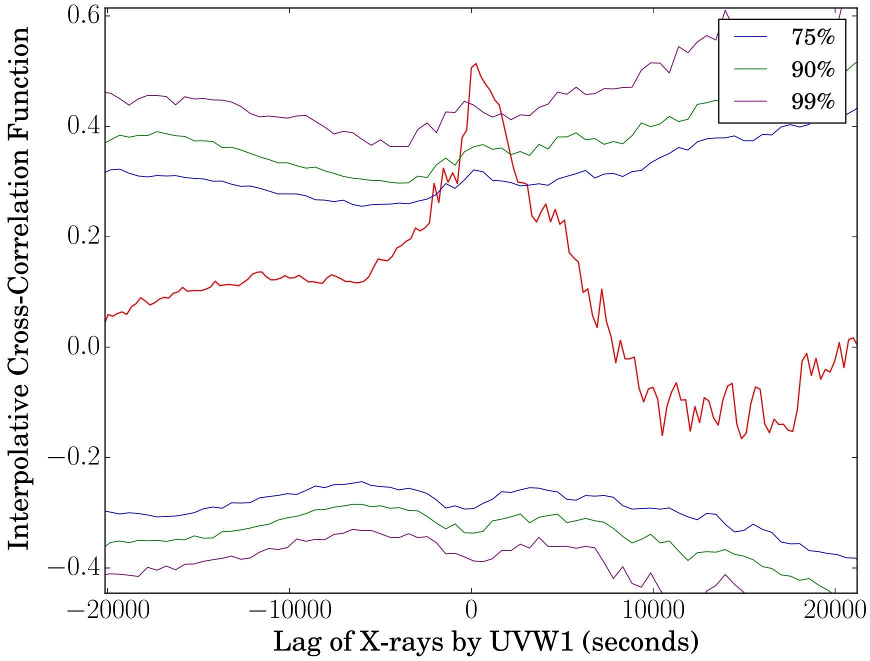

FIGURE 4.17: Discrete cross correlation function between the uvw2 band and uvw1-band light curves from the second night of observations. The 95% (dashed red) and 99.99% (solid thin blue) confidence levels are also shown.

several hundred seconds see Figs. 4.14. Interestingly, a negative peak (implying an anticorrelation) is also seen at a similar lag, but which leads the X-rays rather than lagging them. Both peaks are very high confidence ($> 99\%$). The ICF shows the same two peaks, though with considerably less confidence ($\sim 75\%$, see Fig. 4.15).

In order to refine the lags measurements of the UV/optical bands relative to the X-rays, I calculated lag probability distributions using JAVELIN (see Section 4.3.1) for both the UVW1 and g-bands (Fig. 4.18). The resultant lag estimates are 473^{+47}_{-98} s and 788^{+44}_{-54} s, taking the edge values of 90 % of the probability distribution as errors.

4.4.4 Modelling Lags in NGC 4395

In order to compare the observed lags in NGC 4395 to the expected lags from the standard Shakura-Sunyaev thin disc accretion model, lags were calculated using the reprocessing model described in Section 4.3.2. The lags were calculated using the previously measured parameters of the system: a mass of $M = 3.6 \pm 1.1 \times 10^5\ M_\odot$, accretion rate of $\dot{\text{m}}= 1 \times 10^{-3}$, X-ray luminosity of $L_X = 10^{40}$ erg s^{-1}, X-ray point source height of $H_X = 6\ R_G$ (Iwasawa et al., 2010, Peterson et al., 2005).

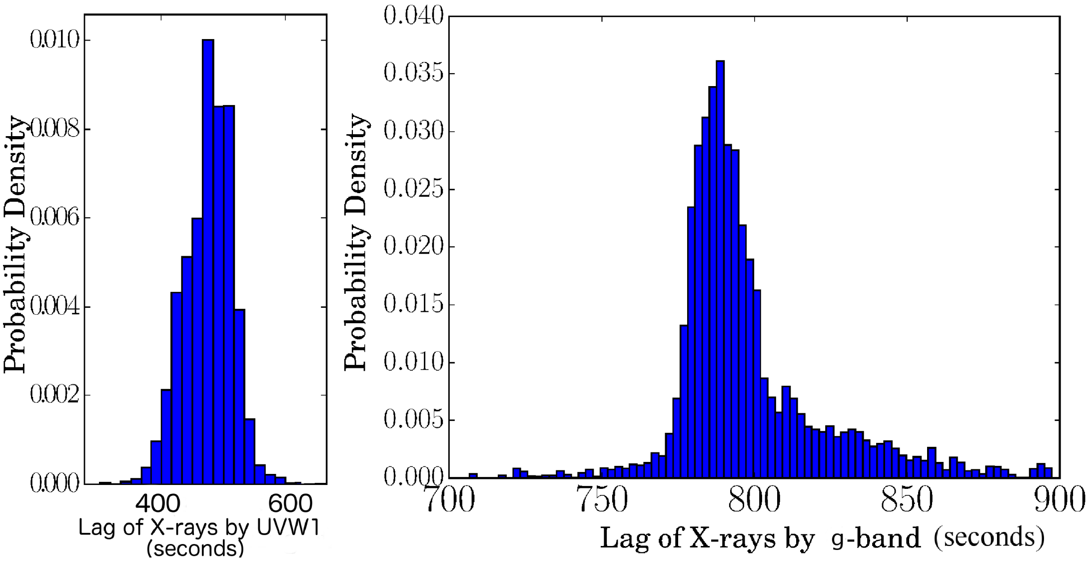

FIGURE 4.18: JAVELIN plots of the parameter distribution for the x-ray and g-band, using data from the 2nd night.

The lags were calculated using the *OM* UVW1 and Sloan Digital Sky Survey (SDSS) G-band transmission functions (see Fig. 4.8). Lags were taken as the time at between the arrival of the X-ray impulse and the arrival of 50% of the reprocessed flux. Lags were calculated for a range of inclinations, as the inclination of the system is unconstrained. The lags are shown, together with the lags measured from the data, in Fig. 4.19. The model lags agree with the measured lags very well, for an intermediate inclination of around $30-45°$; an inclination of 15° over-predicts the G-band lag, whilst a inclination of 75° under-predicts both the UVW1 and G-band lags.

4.5 Energetics

In addition to the lags, it is necessary to ensure that the energetics of reprocessing are consistent with the observed variability. The total blackbody flux from the accretion disc between two wavelengths, λ_1 and λ_2, is given by

$$F = \frac{2\pi hc^2}{D^2}\int_{\lambda_1}^{\lambda_2}\int_{R_{in}}^{R_{out}}\frac{R}{\lambda^4}\frac{1}{e^{\frac{hc}{\lambda k_B T(R)}}-1}d\lambda dR \tag{4.24}$$

where D is the distance to the objects, R_{in} and R_{out} are the inner and outer radii of the accretion disc, and $T(R)$ is the temperature profile of the illuminated disc, given by Eqn. 1.32. As $T(R)$ depends on the X-ray luminosity, as it changes the blackbody flux will

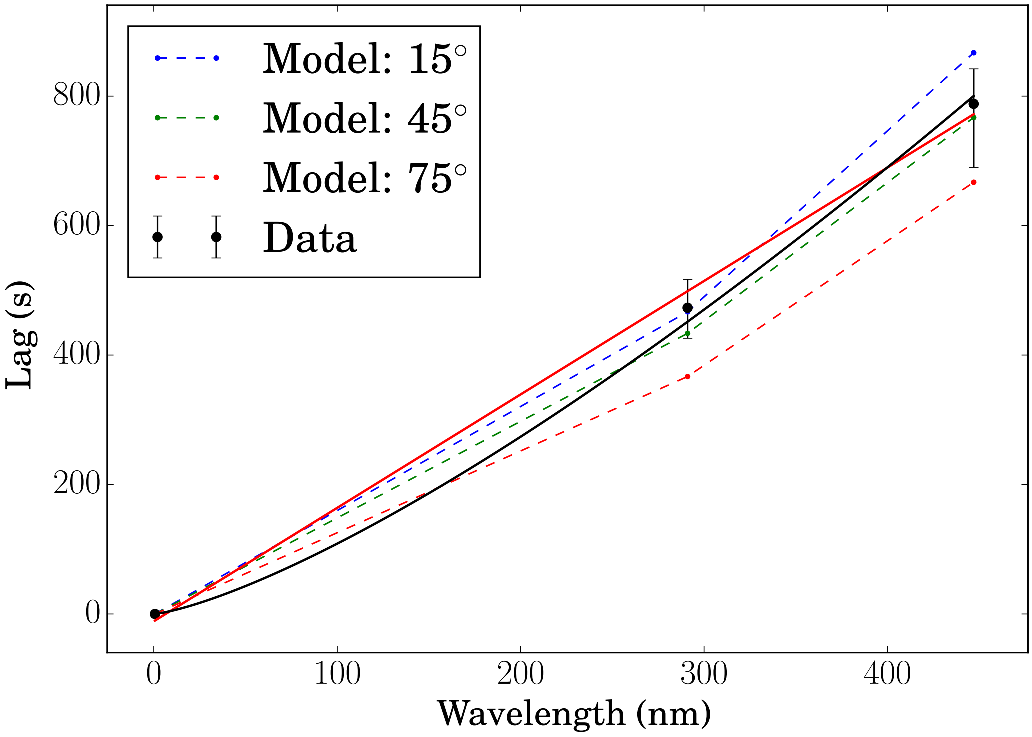

FIGURE 4.19: The time lags measured from the data of NGC 4395 (black points) plotted against wavelength and fitted with linear (red line) and $\lambda^{4/3}$ (black line) models. The lags modelled using the reprocessing code for an X-ray source height of 6 R_G are also shown for a range of inclinations (dashed lines).

also change, however the amount by which the flux at a given wavelength can change for a given change in the X-ray luminosity is limited by the solid angle subtended by the disc from the X-ray source, as well as the properties of the accretion disc (particularly the inner radius). By calculating the expected flux in a given UV/optical filter, we can therefore check which geometries are capable of producing the observed UV/optical variability from the observed X-ray variability.

The X-ray spectra of Seyfert AGN have been observed to have high-energy cut-offs at around 100 keV on average, largely between 50-150 keV (e.g. Molina et al., 2009). NGC 4395 has been observed at high energies by the *Suzaku Hard X-ray Detector(HXD)* at 15-35 keV and by the *International Gamma-Ray Astrophysics Laboratory Imager on-Board the INTEGRAL Satellite (INTEGRAL IBIS)* at 20-100 keV, with no cut-off observed at these energies. The 0.5-100 keV luminosity has been estimated to be $\sim 4 \times 10^{40}$ergss^{-1} using these observations (Iwasawa et al., 2010). As in our own observations, the spectrum is observed to have a photon index of ~ 1.4 below 10 keV, however above this energy it's spectrum is much softer, which a photon index of around 2 until 35 keV, and above this energy the INTEGRAL data imply a harder value again of ~ 1.5 (see Chapter 2 Iwasawa et al., 2010)).

Using the measured UVW1 flux range of $0.68 - 1.2 \times 10^{-12}$ergs^{-1}, I calculated the required X-ray illumination for a given X-ray source height. For an assumed height of $6R_G$, the X-ray luminosities required were $4 - 25 \times 10^{41}$ergs^{-1}, large compared to the estimated broad-band X-ray flux of $\sim 4 \times 10^{40}$ergss^{-1}, and to the observed 0.5-10 keV X-ray variability of ~ 10. However, for a higher X-ray height of $50R_G$, the values agree much better, requiring X-ray luminosities of $4 - 30 \times 10^{40}$ergs^{-1}, fairly consistent with both the estimated 0.5-100 keV luminosity and the observed 0.5-10 keV X-ray variability in our observations. Interestingly, X-ray reverberation mapping of NGC 4395 using full general relativistic modelling by Emmanoulopoulos et al. (2014) found an X-ray source height of $51.5^{+21.2}_{-36.8}$, entirely consistent with a high X-ray source. The errors on this measurement are large, however, and the estimates of the heights of most other AGN are much smaller ($\sim 3 - 6R_G$ Emmanoulopoulos et al., 2014). In the case that the X-ray source in NGC 4395 is at these lower heights, the energetics problem would still persist.

As the energetics imply a higher X-ray source height, the expected time lags from reprocessing in the thin disc model were recalculated using a height of $50R_G$. The resultant lags, for a range of inclinations, are shown in Fig. 4.20. The lags are still consistent with the data, for a similar inclination around of 45°.

4.6 Discussion

In Fig. 4.19 we plot both the UVW1 and G-band lags as a function of wavelength. Both a simple linear fit (i.e. $\beta = 1$, solid black line) and a curve of $\beta = 4/3$ (solid red line) fit the data well - as there are only two measured values and the models both go through the error bars of the data, the χ^2_R values are < 1 in both cases. These observations therefore indicate that reprocessing of X-rays is likely to be responsible for the UV/optical variability of NGC 4395, in agreement with the results of the work of McHardy et al. (2014) on NGC 5548.

The agreement between model values and the data also imply that reprocessing is responsible for the UV/optical variability. The agreement also shows that the predicted flux in the measured bands at a given radius is correctly predicted, unlike the lags

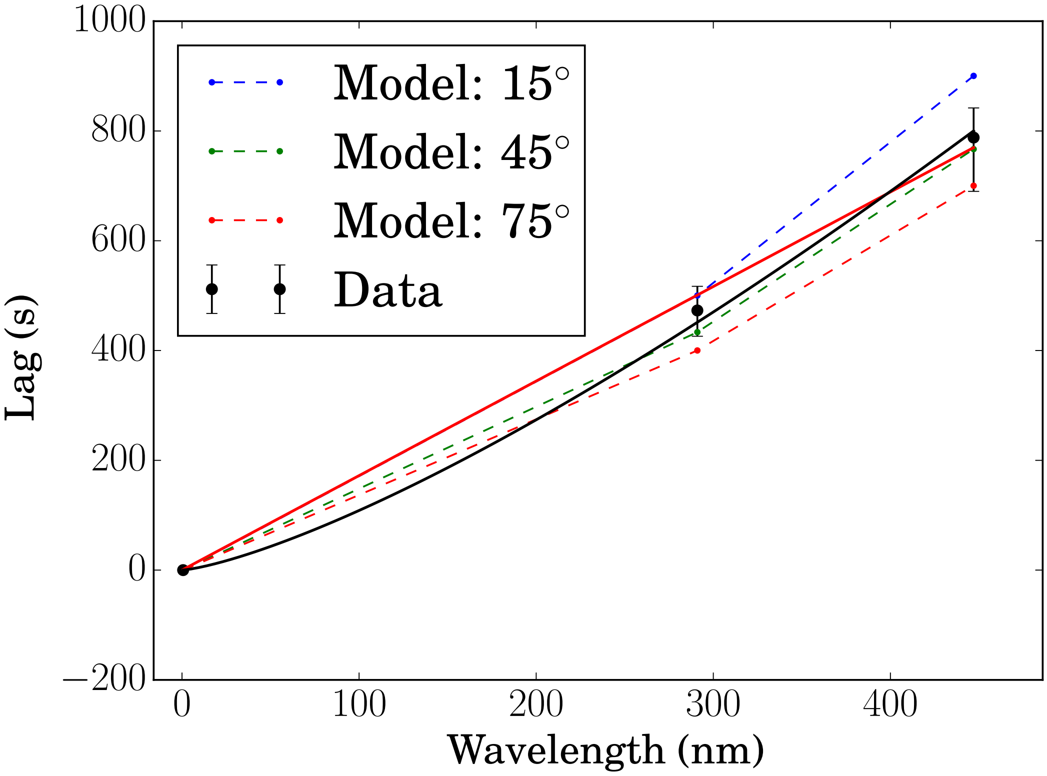

FIGURE 4.20: The time lags measured from the data of NGC 4395 (black points) plotted against wavelength and fitted with linear (red line) and $\lambda^{4/3}$ (black line) models. The lags modelled using the reprocessing code for an X-ray source height of 50 R_G are also shown for a range of inclinations (dashed lines).

measured in NGC 5548, which are longer than expected. The possible causes of these longer lags in NGC 5548, such as a clumpy outer disc or a lower radiative efficiency than expected, are therefore apparently not present in NGC 4395.

Due mainly to its lower black hole mass, the disc in NGC 4395 is expected to be $\sim 50\%$ hotter than that in NGC 5548. Increased disc temperature may lead to a more stable disc (Churazov et al., 2001), less sensitive to radiation-induced perturbations (Pringle, 1997) and therefore a lower likelihood of clumpiness. It is also possible that NGC 5548 is non-typical, and that measurements of further AGN will also point to reprocessing from a standard thin disc.

The expected wavelength dependence of the lags of $\lambda^{4/3}$ arises from the fact that the illumination of a disc, or any flat surface, per unit area decreases as R^{-3}. Any other source of reprocessing would therefore have to replicate this illumination dependence. If the reprocessing is occurring on the surface of optically thick 'clouds' for example, as proposed to explain the longer-than-expected lags in NGC 5548 by Gardner & Done (2016), their distribution would be significant in determining the wavelength dependence of the resultant lags. If the number of clouds is small enough that all or most of them are unobscured with respect to the central source, the illumination dependence will be R^{-2}, leading to a wavelength dependence of λ^2, inconsistent with the measurements of both NGC 5548 and NGC 4395. The number or size of the clouds would therefore have to decrease with radius linearly, or alternatively be arranged geometrically such as to essentially form a flat surface, such that the R^{-3} illumination is maintained. Whilst this is perhaps possible, it requires certain unknown conditions which are not required by the illuminated disc model, from which the wavelength dependence arises naturally, leaving the latter as the preferred model for the current data.

As these short-term NGC 4395 data point to reprocessing as the source of UV/optical variability on timescales of minutes-hours, it is worth noting that many AGN also show correlated variability on long timescales (weeks-months) throughout the UV/optical wavebands which does not appear in the X-ray variability (e.g. Cameron et al., 2012, McHardy et al., 2014). As the timescales for these correlations are still much shorter than the viscous timescale, this implies that the longer timescale variability is driven by the far UV or very soft X-rays from the inner edge of the disc, whose own variability is likely to be caused by accretion rate variations, as the X-ray variability does not appear to be important on these time scales. In order for this to be the case, however, the inner disc needs to have a greater scale height than the outer disc which it is irradiating, which could in turn lead to obscuration of the X-ray source, which would blur the correlation between the X-ray and the optical variability. Clumping of the inner disc could perhaps solve this problem, allowing some of the X-rays to hit the disc directly, but this in turn would reduce the X-ray illumination of the outer disc, potentially leading to problems with the energetics, for which the required X-ray luminosities are already potentially higher than those observed.

Chapter 5

Conclusions

"You win again, gravity!"

Zapp Brannigan

5.1 Main Results

In this thesis, I have presented the results of three AGN variability studies with the aim of shedding light on the physics of accretion and the resultant emission, and the geometry of the matter close to accreting supermassive black holes. I have examined the nature and causes of X-ray and UV/optical variability, and the effects of the geometry and behaviour of the matter surrounding the black hole on the spectrum and variability of this emission. The majority of this work has been published in 2 refereed journal papers and 3 refereed conference proceedings, the remainder will be published in a refereed paper imminently - see Connolly (2015a), Connolly et al. (2014, 2015, 2016b,a), McHardy et al. (2016).

In this chapter I will summarise the main results and implications of this work, followed by suggestions of future work which could expand on or complement these studies in order to move our understanding of AGN forward.

5.1.1 Intrinsic Variability of AGN X-Ray Spectra

In Chapter 2, I found that ‘harder-when-brighter’ X-ray spectral variability is common behaviour for individual LLAGN, caused by intrinsic variation of the photon index of the spectrum, as previously confirmed only in NGC 7213 (Emmanoulopoulos et al., 2012). The expected change in behaviour from harder- to softer-when-brighter at an accretion rate of $\sim 1\%$ of the Eddington rate, previously seen in other samples of AGN and in BHXRBs (e.g. Constantin et al., 2009, Hernández-García et al., 2014, Younes et al., 2011) is confirmed in the AGN in the Palomar sample which have been observed by *Swift*. These findings support the theory that a change in the seed photon source of the system occurs around this critical accretion rate, from a hot inner flow at lower accretion rates to the accretion disc at higher accretion rates. These results also add evidence to the idea that AGN are analogues of BHXRBs, LLAGN and Seyferts being equivalent to the ‘hard state’ in BHXRBs at lower and higher accretion rates, respectively.

5.1.2 Varying Accretion Disc Winds in AGN

In Chapter 3, I found evidence of long-term correlations between the degree of absorption in the X-ray spectra of AGN and their intrinsic X-ray luminosity. This correlation was particularly apparent in the Seyfert AGN NGC 1365, in which it is clear that this correlated change in absorption is due mainly to a decrease in the absorbing column along the line of sight with increasing luminosity. This was explained physically by a disc wind whose launching radius is linked to the luminosity of the system, such that an increase in luminosity shifts the wind too larger radii, meaning that, from certain viewing angles, the observer sees the intrinsic X-ray emission through a lower density portion of the wind. The long-term variability of the other two Seyfert AGN analysed in this chapter, NGC 5548 and Mkn 335, can also explained in the context of this model. The results highlight the importance of the inclusion of disc winds in spectral modelling of X-ray spectra, and the important part they play in X-ray variability.

5.1.3 Inter-Waveband Lags as Probes of Geometry in AGN

In Chapter 4, I found that the UV/optical variability of the Seyfert AGN NGC 4395 lags that X-ray variability on timescales of hundreds of seconds. This implies that the

UV/optical variability is due mainly to reprocessing of X-ray emission in the accretion disc. Modelling of the time lags expected from the standard Shakura & Sunyaev (1973) thin-disc accretion model showed that the magnitude of the lags is consistent with this model, in contrast to the lags measured in NGC 5548, which have been found to be longer than expected (McHardy et al., 2014). The results therefore demonstrate the importance of reprocessing in the variability of the UV/optical waveband in AGN and show evidence that this reprocessing occurs within the accretion disc.

5.2 Future Work

All three of these studies have implications which warrant further investigation. Further data and investigation would undoubtedly lead to stronger constraints on the variability of the photon index of the intrinsic emission of AGN at all accretion rates, long-term trends in the variability of X-ray absorbers in AGN, and the geometry of reprocessing material surrounding the black hole.

Data from hard X-ray instruments such as *NuSTAR* and the *Astrosat Large Area X-ray Proportional Counters (LAXPCs)* would allow the photon index of the intrinsic X-ray spectrum to be more accurately measured, particularly in systems which are highly absorbed or suffer from significant contamination by nearby hot gas emission. This in turn would allow the variability of the photon indices to be more precisely measured. Not only would this allow better constraint of how the photon index of systems in which it is known to vary, but also allow such variations to be detected in systems where the variation is very small, due to low-amplitude variability of the emission.

The wind model used to explain the absorption variability in NGC 1365, Mkn 335 and NGC 5548 is testable in a number of ways. More data of the kind used in this study, i.e. long-term soft X-ray data sensitive to absorption from instruments such as *Swift* and *XMM-Newton*, covering a larger sample of AGN, would help to find common trends in the long-term absorption variability present in these systems. Better measurement of the value and variability of the photon index of the intrinsic, unabsorbed spectrum by hard X-ray observatories, as described above, would also allow the degree of absorption in the spectrum to be constrained more precisely. The use of high-resolution X-ray spectroscopy data, from e.g. the *XMM-Newton Reflection Grating Spectrometer (RGS)* and the *Chandra Advanced CCD Imaging Spectrometer (ACIS)*, to measure absorption lines in the spectrum would allow measurement of both outflow velocities, giving the properties of the wind thought to be causing the observed long-term absorption. Measurement of absorption lines would also allow tighter constraints on the ionisation state of the absorber, and therefore constraints on how much changes in ionisation and changes in the absorbing column each contribute to absorption variability on long timescales. As both the observed properties and variability of the absorber can be predicted from the inclination in the variable wind model, these expected properties can be directly tested in order to verify the ability of this model to describe the absorption variability in AGN. X-ray polarimetry data from potential future missions, such as the *X-ray Imaging Polarimetry Explorer (XIPE)* and the *Black hole Evolution in Space-Time observatory (BEST)*, would provide invaluable information about the origin of separate components of the spectrum. As one of the two components in the spectra of NGC 1365 and Mkn 335 is thought to be scattered from the inner edge of the far side of the wind, it should be polarised; polarimetry measurements can therefore determine whether this is the case or not.

The lag measurement results from NGC 4395 can be built upon greatly simply by observing more systems and measuring the lags, where present, in these systems. The ability of *Astrosat* to measure three UV/optical bands simultaneously to both soft and hard X-ray measurements would allow time lags to be further constrained. As NGC 4395 seems to follow the predictions of the Shakura & Sunyaev (1973) model very well, whilst NGC 5548 does not, a larger sample with well-measured X-ray optical lags would help to determine whether either behaviour is more common, as well as shedding light on the reasons for the discrepancy between the NGC 5548 lags and the thin-disc model.

In addition to data, further development on the reprocessing code would allow the direct fitting of physical parameters to the UV data, by fitting the UV/optical data with a predicted light curve using the response of the disc to the X-ray data light curve. By using MCMC maximum likelihood methodology, likelihood distributions for the physical parameters of the model can be obtained. In this way parameters which are difficult to measure, such as the inclination of the system, can be constrained, as well as the usefulness of the model in describing accretion in AGN. The physical model itself could also be extended to include possible physical reasons for the long lags of NGC 5548, such as a flared disc and the effects of clumpiness at large radii.

5.3 Final Remarks

The results of this thesis highlight the importance of understanding all the factors leading to variability in the emission of AGN. Accurate measurement of the intrinsic spectrum of an AGN is not possible without knowledge of the physical properties and variability absorbers present between the central engine and the observer. In turn, measurement of the absorption in the X-ray spectra cannot be constrained without knowledge of the intrinsic spectrum, including the variability of the photon index. Finally, an understanding of the observed reprocessing of the X-ray spectrum into UV/optical emission requires knowledge of both the incident X-ray radiation and the geometry and composition of the material surrounding the black hole. It is therefore only with a complete view of the components of a unified model of AGN that we can fill in the gaps in our knowledge and explain the variability of AGN in their entirety.

"The pub? Ah, yes - a meeting place where people attempt to achieve advanced states of mental incompetence by the repeated consumption of fermented vegetable drinks."

Kryten

Appendix A

Notes on Spectral Fitting of Individual Palomar AGN

The following section contains details on the results of spectral fitting for each of the 24 AGN in our sample. Example spectra of each object, and the best-fitting spectral model, can be found in Figs. A.1 and A.2.

- **NGC 315**

  Only a single summed spectrum of NGC 315 could be produced from the available *Swift* data. Our best-fitting model consists of an absorbed power law, plus a hot gas component ($\chi^2_\mathrm{R} = 1.02$). Previous spectral modelling of NGC 315 has employed very similar models (e.g Matsumoto et al., 2001, Terashima et al., 2002, Younes et al., 2011). The photon index we measure is very similar to that found by Matsumoto et al. (2001) and Younes et al. (2011) ($\Gamma = 1.94$; slightly higher than that found by Terashima et al. (2002)).

- **NGC 1052**

  Three flux-binned spectra could be produced from the available *Swift* data of NGC 1052. We found that a single partial coverer provided a very good fit to the spectra. A fairly good fit is obtained when all the parameters are tied ($\chi^2_\mathrm{R} = 1.11$). However, allowing Γ, the absorbing column or the covering fraction to produces a fit which is statistically better in each case (f = 9.5 and p = 1.3×10^{-4}, f = 3.5 and p = 3.3×10^{-2}, f = 8.0 and p = 4.7×10^{-4} respectively). The best fit is obtained when only Γ is left free ($\chi^2_{\mathrm{R}} = 1.01$). Models in which both the absorbing and column and the covering fraction are free to vary but Γ is tied, or in which all three are free to vary, provided lower χ^2 values, but the added complexity is not required statistically when compared to the model in which only Γ is free to vary between flux-binned spectra ($\mathrm{f} = 1.7$ and $\mathrm{p} = 0.19, \mathrm{f} = 1.6$ and $\mathrm{p} = 0.186$ respectively). Previous studies by Weaver et al. (1999) and Hernández-García et al. (2013), using *ASCA* , *Chandra* and *XMM-Newton* data, also concluded that the spectrum was heavily absorbed by one or more partial-coverers.

For the best-fitting model, in which the absorber is constant and Γ is free to vary between flux-binned spectra, Γ is anticorrelated with the flux. Furthermore, the same anticorrelation is seen in our spectral fits when the absorbing column is allowed to vary as well as the photon index. The values of Γ found are between those found by Weaver et al. (1999) and by Hernández-García et al. (2013) $\Gamma = 1.37 - 1.70$ for similar models, though Hernández-García et al. (2013) attribute the primary cause of spectral changes in NGC 1052 to variations in the absorbing column, not the photon index. As the source displays harder-when-brighter behaviour, if the spectral variations are caused by absorption variation alone this absorption must be negatively correlated with the luminosity of the system, as in e.g. NGC 1365 (Connolly et al., 2014).

- **NGC 1068**

  Three flux-binned spectra could be produced from the available *Swift* data of NGC 1068. The components of our best-fitting model to the spectra required an absorbed power law, a hot gas component for contamination from the host. This is consistent with previous modelling of the source, which used similar models (e.g. Bauer et al., 2014, Brightman et al., 2015). However, the photon index we obtain is higher than that found with previous data from e.g. *NuStar* which included higher energies than those detected by *Swift*, though indices of > 2 have been found. NGC 1068 is widely thought to be a Compton-thick AGN, making the intrinsic emission difficult to model (Antonucci & Miller, 1985, Brightman et al., 2015, Ghisellini et al., 1994), as the degree of absorption could not be constrained with the energy range of *Swift*, the flux extracted from this spectrum was much lower than the true value. For these reasons, NGC 1068 was not included in the subsequent discussion of spectral variability behaviour.

- **NGC 2655**

  Insufficient *Swift* data was available to produce multiple flux-binned spectra for NGC 2655, so a single-summed spectrum was produced. We also find a partial covering model to be the best-fitting to the *Swift* data ($\chi^2_{\mathrm{R}} = 1.15$), when combined with an additional hot gas component. Previous work on NGC 2655 has also required a partial covering model, and a hot gas component in some cases (e.g. González-Martín et al., 2009, Terashima et al., 2002). The best-fitting model has a very hard photon index ($\Gamma = 1.35$), but this is consistent with what others have found previously (Terashima et al., 2002).

- **NGC 3147**

  Three flux-binned spectra of NGC 3147 were produced from the *Swift* data. We find the best-fitting model to the *Swift* data to be a simple power law for which Γ was allowed to vary ($\chi^2_{\mathrm{R}} = 0.73$), Previous modelling of the spectrum of NGC 3147 has also shown a lack of any strong absorption (e.g. Ptak et al., 1996). As the *Swift* data are already slightly over-fitted by this model ($\chi^2_{\mathrm{R}} < 1$), we assume that more complex models are incorrect, despite producing lower χ^2 values. We find similar values of the photon index to those found by (Ptak et al., 1996) ($\Gamma = 1.35 - 1.58$). This model show a a reduction in Γ with increasing intrinsic luminosity of the system.

- **NGC 3226**

  Only a single summed spectrum of NGC 3226 could be produced from the *Swift* data. We find that the spectrum is very well-fitted by a power law and a neutral absorber ($\chi^2_{\mathrm{R}} = 0.90$). Past studies disagree somewhat as to whether the best-fitting model for the spectrum of NGC 3226 is bremsstrahlung or a simple power law (e.g. Gondoin et al., 2004, González-Martín et al., 2009, Younes et al., 2011), but previous work agrees on the presence of a neutral absorber. We find a high value for the photon index, but with large uncertainties ($\Gamma = 2.57 \pm 0.42$); Gondoin et al. (2004) and Younes et al. (2011) find value which is lower, but which agree with ours within our errors.

- **NGC 3227**

  Sufficient *Swift* data of NGC 3227 was available to produce 10 flux-binned spectra. The best-fitting model to the *Swift* data consisted of a power law and an ionised absorber, with Γ free to vary but all parameters of the absorber tied ($\chi^2_{\rm R} = 1.07$), which is statistically superior to a neutral absorber ($\rm f = 16.3$ and $\rm p = 1.1 \times 10^{-7}$). Previous spectral modelling of NGC 3227 has also shown its spectrum to be absorbed by an ionised absorber (George et al., 1998, Ptak et al., 1994), though some more recent studies have used more complex models involving multiple ionised absorbers and a reflection component (e.g. Beuchert et al., 2015). The parameters of our best-fitting model show a positive correlation between the photon index and the intrinsic luminosity of the source, consistent with Sobolewska & Papadakis (2009), who also found the same correlation and range of photon indices ($\Gamma = 1.43 - 1.65$) in the $2 - 10$keV band.

- **NGC 3628**

  Only a single summed spectrum of NGC 3628 could be produced from the *Swift* data. We found a power law with a neutral absorber to be best-fitting to the *Swift* data. Previous studies have found the same spectral model to be best-fitting (Dahlem & Heckman, 1995, González-Martín et al., 2009), with a similarly low photon index ($\chi^2_{\rm R} = 1.36$) to that found in our best-fitting model.

- **NGC 3998**

  As there were few *Swift* data available for NGC 3998, we instead used the *RXTE* data from Skipper (2013), for which a large number of flux-binned spectra could be produced. The *RXTE* data are of quite low S/N, as NGC 3998 is a very faint source. The spectrum can be fitted reasonably well by a power law absorbed by the galactic absorbing column of $1.05 \times 10^{21}{\rm cm}^{-2}$, and shows no excesses which imply that this is not a good model. The fit is not improved by the addition of a further absorber, possibly because the *RXTE* does not extend below 3 keV, so is only sensitive to high absorbing columns. If it is assumed that the spectrum is absorbed and that the source of the spectral variability is changes in absorption instead of a changing Γ, a significantly worse fit is obtained. This is consistent with previous spectral studies of this source (Awaki et al., 1991, Ptak, 2004, Younes et al., 2011). The values obtained for the photon index in previous studies are all within the range found in this model ($\Gamma \sim 1.87 - 2.50$). In the best-fitting model, the photon index shows a clear anticorrelation with the intrinsic luminosity of the system. Younes et al. (2011) also found variations in Γ, but had only two observations so could not test for any correlation.

- **NGC 4051**

  There were sufficient *Swift* data to produce 10 flux-binned spectra of NGC 4051. We find that absorbed power law plus a hot gas component also fits the *Swift* data well ($\chi^2_{\mathrm{R}} = 1.10$). Previous spectral modelling of NGC 4051 with *XMM-Newton* data has also used an absorbed power law plus a hot gas component (e.g. Ponti et al., 2006). We find that the photon index is positively correlated with the flux, as found previously by Ponti et al. (2006), Sobolewska & Papadakis (2009) with *XMM-Newton* and *RXTE* in the $0.5 - 10$keV and $2 - 10$keV bands respectively, with the same range of values for the photon index ($\Gamma = 1.35 - 1.97$). This correlation is less clear in the $2 - 10$keV band, perhaps due to the absorption variations found by e.g. Lamer et al. (2003), Ponti et al. (2006) making our parameter measurements less accurate over the narrower band.

- **NGC 4151**

  There were sufficient *Swift* data to produce 7 flux-binned spectra of NGC 4151. We find a power law plus a neutral partially-covering absorber to be the best-fitting model to the *Swift* data ($\chi^2_{\mathrm{R}} = 1.02$). Previous work has also shown NGC 4151 to be best modelled with these components (e.g. Keck et al., 2015, Puccetti et al., 2007, with *ROSAT*, *NuSTAR* and *Sukaku* respectively). The values of the photon index we find are, however, very low. The large absorbing column and complex, variable absorption are likely to have limited accurate measurement of the underlying spectral index. We therefore exclude the results of the spectral fitting to NGC 4151 from the subsequent discussion.

- **NGC 4258**

  Only a single summed spectrum of NGC 4258 could be produced from the available *Swift* data. We find that a partial covering absorber and a hot gas component is required to obtain a good-fit ($\chi^2_{\mathrm{R}} = 1.03$), significantly better than a fully-covering absorber ($\chi^2_{\mathrm{R}} = 1.78$). Previous studies of NGC 4258 have, however, found the spectrum to be best modelled by a simple absorbed power law and a hot gas component (Terashima et al., 2002, Yamada et al., 2009). The value we find for the photon index ($\Gamma = 1.66$) is consistent with that of Terashima et al. (2002) and (Yamada et al., 2009).

- **NGC 4321**

Only a single spectrum of NGC 4321 could be produced from the *Swift* data. We find that an absorbed power law plus a hot gas component is best-fitting ($\chi^2_{\mathrm{R}} = 1.62$), consistent with previous spectral studies of NGC 4321 (González-Martín et al., 2009, Roberts et al., 2001). In our data, however, the hot gas component from the host is dominant, meaning the underlying spectral index is not well constrained. The results of this spectral fitting are therefore not included in subsequent analysis.

- **NGC 4388**

  Sufficient *Swift* data were available to produce 4 flux-binned spectra of NGC 4388. We also obtained a reasonable fit to the *Swift* data with a power law and a neutral absorber ($\chi^2_{\mathrm{R}} = 1.16$). This model did not require the photon index (or absorption) to vary between flux-binned spectra, though the spectra only cover a small range of fluxes and therefore may not be expected to change significantly. Previous studies have also fitted the spectrum with a model consisting of as absorbed power law (e.g. Elvis et al., 2004, Risaliti et al., 2002). However, we obtain a very low value for the photon index ($\Gamma = 1.10$), which does not agree with the value found in previous studies - together with the high level of absorption ($\mathrm{N_H} \sim 3 \times 10^{23}\mathrm{cm}^{-2}$), which is great enough to affect the majority of the *Swift XRT* energy range, were therefore conclude that the underlying spectrum, and therefore the intrinsic luminosity, of NGC 4388 are not well constrained. The results of the spectral fitting to NGC 4388 are therefore not included in subsequent analysis.

- **NGC 4395**

  The large quantity of *Swift* data of NGC 4395 allowed us to produce 22 flux-binned spectra. We find that a model consisting of a power law and an ionised absorber gives a good fit to the *Swift* data. The best-fitting model of the flux-binned spectra requires only the photon index to vary ($\chi^2_{\mathrm{R}} = 1.03$); although the model in which the ionisation state and absorbing column are free to vary does give a lower χ^2, the extra complexity is not statically required ($\mathrm{f} = 0.31, \mathrm{p} = 1.00$). The spectrum has previously been modelled with multiple absorbers with varying ionisation states and absorbing columns (e.g. Iwasawa et al., 2010, Nardini & Risaliti, 2011). The lack of a need for variability in the absorption, despite previous work showing absorption variability to be present, is perhaps due to the flux-binning averaging the absorption over the period covered by the data, but this is likely to add scatter to the parameter values. Some of the spectral indices obtained from this fit are very hard ($\Gamma = 0.91 - 1.60$), so absorption variability is not ruled out as the source of spectral variability, however the values are consistent with the values found by Iwasawa et al. (2010), who also found evidence of variations in Γ. Our spectral modelling therefore also implies that there is not any flux dependence in the degree of absorption.

- **NGC 4472**

  Spectral modelling of NGC 4472 has been limited due to its very low-luminosity. We find that an absorbed power law fits the spectrum of NGC 4472 very well in conjunction with a hot gas component ($\chi^2_{\mathrm{R}} = 1.03$) consistent with previous work, which has used a simple power law model (Loewenstein et al., 2001). However, the hot gas component dominates the spectrum in our data due to the low luminosity of the x-ray source, making constraints on the intrinsic spectrum less reliable; we find an unphysically high photon index of $\Gamma = 3.38$. We therefore conclude that the spectral fitting could not reliably find the parameters of the intrinsic spectrum and exclude the results from subsequent analysis.

- **NGC 4486**

  Four flux-binned spectra were produced from the available *Swift* data of NGC 4486. We find that a single power law plus a hot gas model gives a good fit to the spectra ($\chi^2_{\mathrm{R}} = 1.03$). The model in which Γ does not vary is best-fitting, as the model in which Γ varies is not statistically better ($\mathrm{f} = 0.1, \mathrm{p} = 0.96$), meaning we obtain only a single value for the whole range of luminosities. Previous spectral modelling of NGC 4486 has also mostly used a single, absorbed power law (e.g. Dudik et al., 2005, González-Martín et al., 2006), though some have used more complex, multi-component models (e.g. González-Martín et al., 2009). As the flux range is relatively small, it may be that in reality there are small variations which cannot be successfully resolved in the *Swift* data. The value for the photon index obtained ($\Gamma = 2.68$) is relatively high, but consistent with the value found by (González-Martín et al., 2009) within our errors.

- **NGC 4579**

Three flux-binned spectra were produced from the available *Swift* data of NGC 4486. We find an absorbed powerlaw and a hot gas component to be a good fit ($\chi^2_{\rm R} = 1.00$). Previous studies also required an absorbed powerlaw and a hot gas component (Dewangan et al., 2004, González-Martín et al., 2009). We find a range of photon indices very similar to those found by previous studies ($\Gamma = 1.7 - 2.0$). The photon index decreases with increasing luminosity in this model.

- **NGC 4736**

  Only a single summed spectrum of NGC 315 could be produced from the available *Swift* data. We find an absorbed power law plus a hot gas component to be the best-fitting to the *Swift* data. Previous studies successfully also model the spectrum of NGC 4736 with an absorbed power law and a hot gas component (e.g. Roberts et al., 2001, Terashima et al., 2002). We find a very similar value for the photon index to previous studies ($\Gamma = 1.45$).

- **NGC 5194**

  We find the spectrum of NGC 5194 a heavily absorbed power law with and a Gaussian to be the best fit to the *Swift* data. Previous spectral studies of NGC 5194 have also found it to be well fit by a heavily absorbed power law, with a strong Fe emission line (Ptak, 1999, Terashima et al., 2002). As the source is Compton thick, however, we cannot constrain the absorption well with the *Swift* data; we obtain an extremely low photon index ($\Gamma = 0.7$), significantly lower than that found in previous studies. We therefore conclude that both the value of Γ and the x-ray luminosity we obtain are unreliable and consequently do not include the results of the spectral fits to NGC 5194 in subsequent analysis.

- **NGC 5548**

  The large quantity of *Swift* data of NGC 5548 allowed us to produce 42 flux-binned spectra. We find that the flux-binned *Swift* data are well-fitted by a single, ionised absorber for which Γ, the absorbing column and the ionisation state are all free to vary ($\chi^2_{\rm R} = 0.94$). The data are also well fitted by changes in each of these parameters alone, but statistically the model in which they are all free to vary is superior ($\rm f = 3.3$ and $\rm p = 6.9 \times 10^{-21}$, $\rm f = 2.2$ and $\rm p = 5.4 \times 10^{-9}$, $\rm f = 662.7$ and $\rm p = 7.7 \times 10^{-141}$ compared to the models in which only Γ, the absorbing column or the ionisation state were free to vary, respectively). This is consistent with previous studies which hav found NGC 5548 possesses complex variable absorption (e.g. Kaastra et al., 2014, Steenbrugge et al., 2005).

In the best-fitting model, there does not appear to be any strong correlation between Γ and the intrinsic luminosity of the x-ray source, though there are hints of a negative correlation. The lack of any correlation being found may be due to the complex, variable absorption adding a large amount of scatter to the measure values, however a previous study by (Sobolewska & Papadakis, 2009) with *RXTE* (whose data is less affected by absorption at $3-20$keV) also did not find any significant correlation between Γ and luminosity in the $2-10$keV band, with the same scatter in Γ that we find. They also find a higher range of photon indices, further suggesting that the variable absorption in NGC 5548 is affecting the accuracy of our measurements of the photon index.

- **NGC 5806**

  Only a single summed spectrum of NGC 5806 could be produced from the available *Swift* data. We find that the *Swift* data for NGC 5806 are best-fitted by an absorbed power law ($\chi^2_{\rm R} = 1.16$), with a fairly typical photon index of $\Gamma = 1.65$. Although NGC 5806 has been classified as an AGN optically (Seth et al., 2008), there have been no X-ray spectral studies of this object to date; the X-ray data used in this study are taken from observations intended to look at the iPTF13bvn supernova which occurred in NGC 5806 in 2013 (the supernova occured near the edge of the galaxy and could therefore not have contaminated the spectrum of the nucleus) (Cao et al., 2013).

- **NGC 7331**

  Only a single summed spectrum of NGC 7331 could be produced from the available *Swift* data. We find an absorbed power law and a hot gas component to be best-fitting to the *Swift* data. Previous X-ray studies of NGC 7331 employed similar models (Gallo et al., 2006, González-Martín et al., 2006). We find a slightly lower photon index than previous studies, but the value obtained is the compatible within our errors ($\Gamma = 1.38 \pm 0.3$).

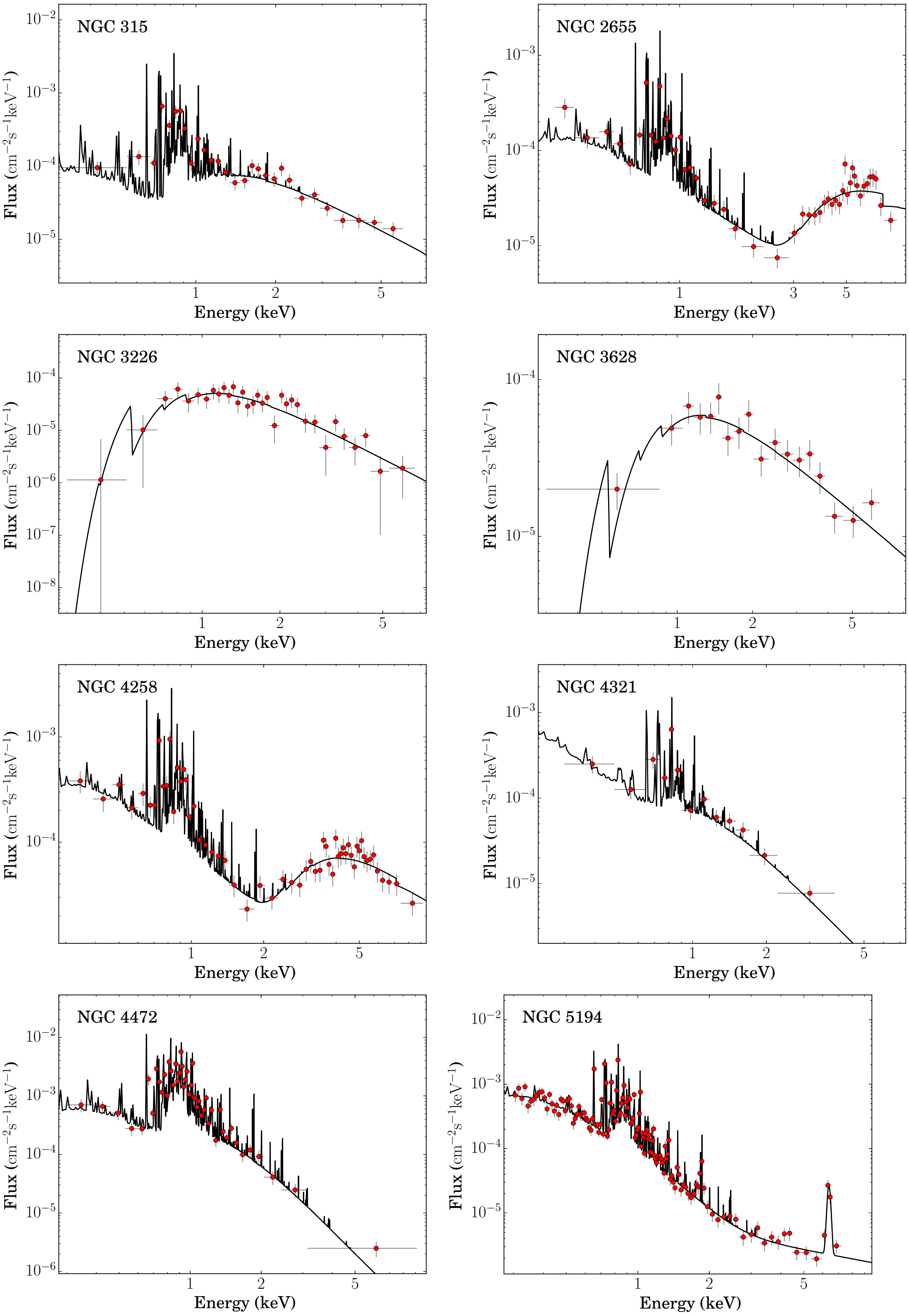

Figure A.1:]
The middle flux-binned spectrum (unfolded) of each of the AGN in the sample for which flux-binning was carried out (excluding M81 - see Fig. 2.6). The best-fitting spectral model for each object is also shown in black.

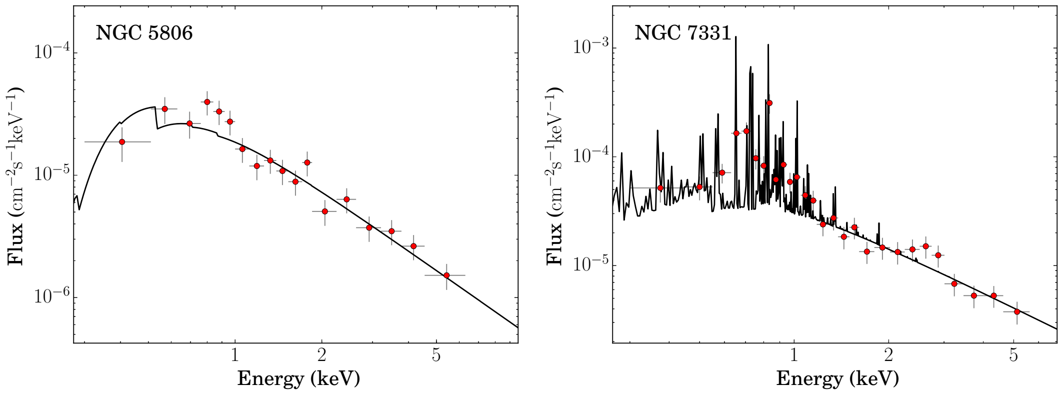

FIGURE A.1: (Continued)

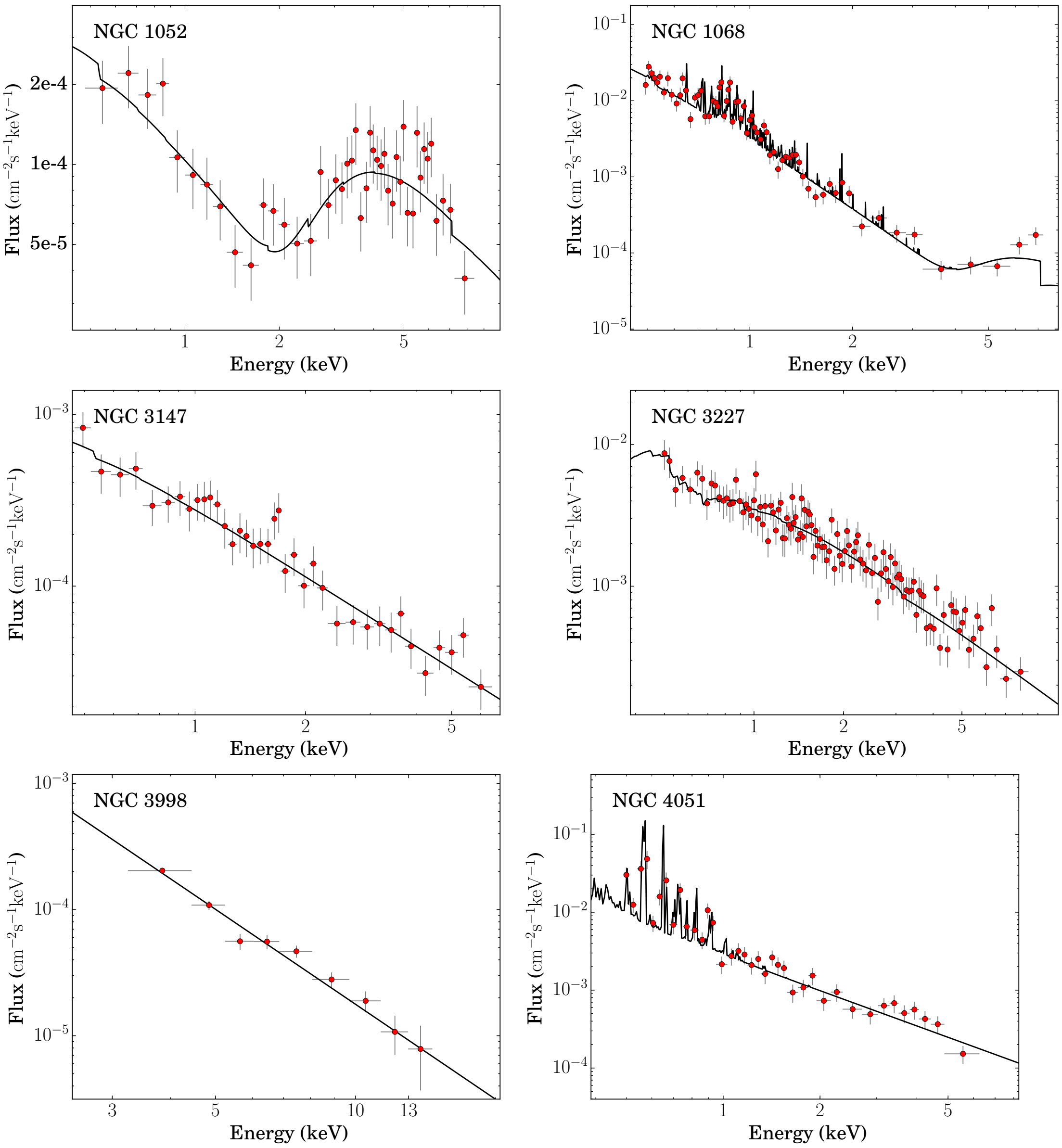

FIGURE A.2: The total spectrum (unfolded) for each of the AGN in the sample for which flux-binning could not be carried out. The best-fitting spectral model for each object is also shown in black.

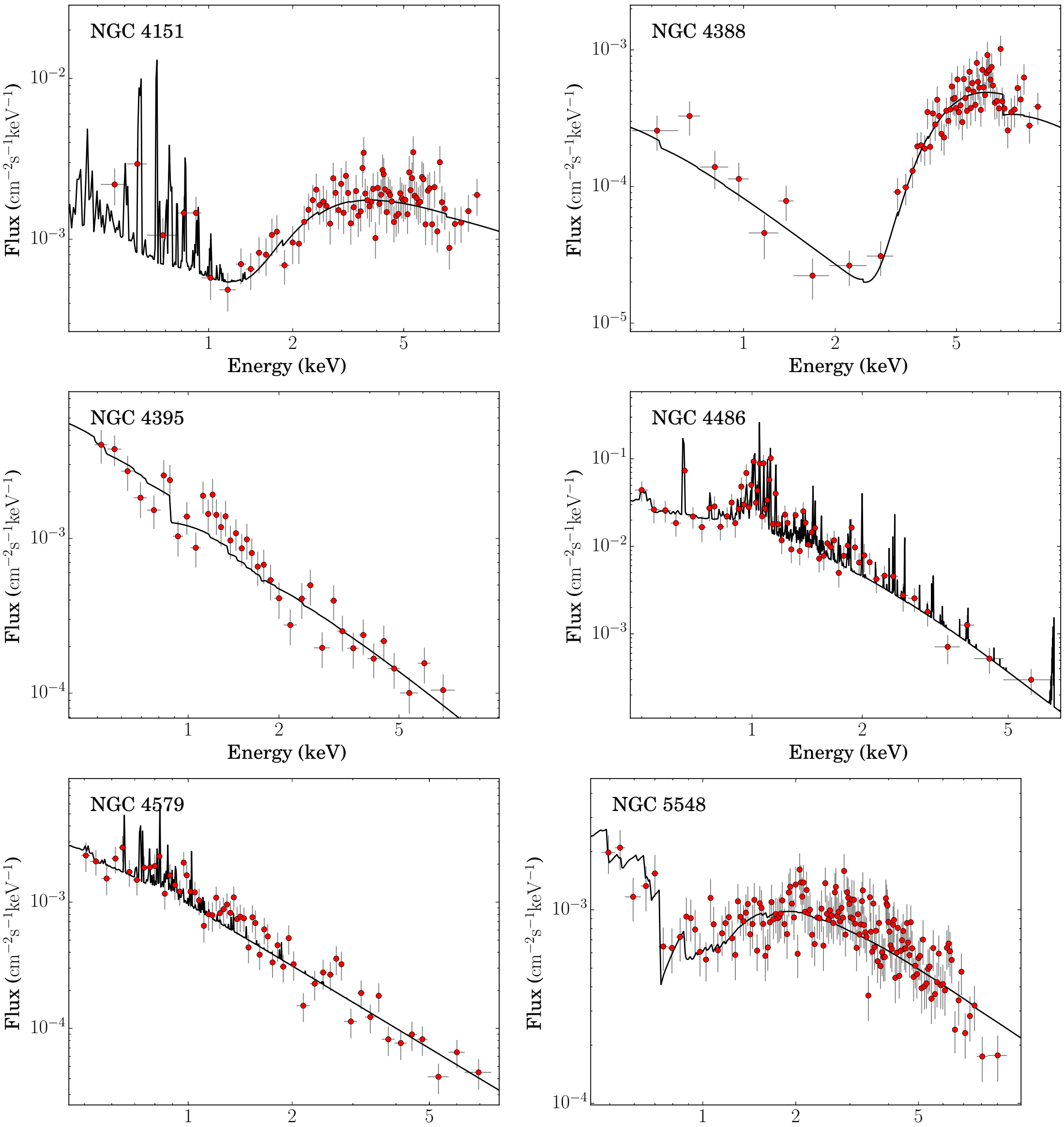

FIGURE A.2: (Continued)

Bibliography

Antonucci R. R. J., Miller J. S., 1985, ApJ, 297, 621

Arévalo P., Uttley P., Lira P., Breedt E., McHardy I. M., Churazov E., 2009, MNRAS, 397, 2004

Arnaud K., 1996, Astronomical Data Analysis Software Systems V, 101, 17

Awaki H., Koyama K., Kunieda H., Takano S., Tawara Y., 1991, ApJ, 366, 88

Axelsson M., Hjalmarsdotter L., Borgonovo L., Larsson S., 2008, A&A, 490, 253

Baganoff F. K., et al., 2003, ApJ, 591, 891

Ballantyne D., Ross R., Fabian A., 2001, MNRAS, 327, 10

Barret D., Vaughan S., 2012, ApJ, 746, 131

Bauer F. E., et al., 2014, ApJ, 812, 116

Bell M. E., et al., 2011, MNRAS, 411, 402

Beloborodov A. M., 1999a, ASPC, 161, 295

Beloborodov A. M., 1999b, ApJ, 510, 123

Bentz M. C., et al., 2006, ApJ, 651, 775

Bentz M. C., et al., 2007, ApJ, 662, 205

Berkley A. J., Kazanas D., Ozik J., 2000, ApJ, 535, 712

Beuchert T., et al., 2015, A&A, 584, 82

Blustin A. J., Page M. J., Fuerst S. V., Ashton C. E., 2005, A&A, 431, 111

Bondi H., 1952, MNRAS, 112, 195

Braito V., Ballo L., Reeves J. N., Risaliti G., Ptak A., Turner T. J., 2013, MNRAS, 428, 2516

Branduardi-Raymont G., 2005, in , The Physics of Accretion onto Compact Objects. Springer Berlin Heidelberg, Berlin, Heidelberg, pp 407–414

Breedt E., et al., 2009, MNRAS, 394, 427

Breedt E., et al., 2010, MNRAS, 403, 605

Brenneman L. W., et al., 2009, ApJ, 698, 528

Brenneman W., Risaliti G., Elvis M., Nardini E., 2012, MNRAS, 429, 1

Brightman M., et al., 2015, ApJ, 805, 41

Cackett E. M., Horne K., Winkler H., 2007, MNRAS, 380, 669

Cameron D. T., McHardy I., Dwelly T., Breedt E., Uttley P., Lira P., Arevalo P., 2012, MNRAS, 422, 902

Cannizzo J. K., Pudritz R. E., 1988, ApJ, 327, 840

Cao Y., et al., 2013, ApJ, 775, 7

Cappi M., et al., 2016, A&A, (accepted)

Castor J. I., Abbott D. C., Klein R. I., 1975, ApJ, 195, 157

Chelouche D., Netzer H., 2005, ApJ, 625, 95

Chidiac C., et al., 2016, A&A (accepted)

Childress M. J., et al., 2013, ApJ, 770, 29

Churazov E., Gilfanov M., Revnivtsev M., 2001, MNRAS, 321, 759

Connolly S. D., 2015a, PoS(SWIFT 10), 1, 131

Connolly S. D., 2015b, ASCL, 1602.012

Connolly S. D., McHardy I. M., Dwelly T., 2014, MNRAS, 440, 3503

Connolly S. D., et al., 2015, PoS(SWIFT 10), 1, 53

Connolly S. D., et al., 2016b, (in prep)

Connolly S. D., Mchardy I. M., Skipper C. J., Emmanoulopoulos D., 2016a, MNRAS

Constantin A., Green P., Aldcroft T., Kim D.-W., Haggard D., Barkhouse W., Anderson S. F., 2009, ApJ, 705, 1336

Coppi P. S., 1992, MNRAS, 258, 657

Coppi P. S., 1999, ASPC, 161, 375

Dahlem M., Heckman M., 1995, ApJ, 442, 49

Deeter J. E., 1984, ApJ, 281, 482

Denney K. D., et al., 2010, ApJ, 721, 715

Devereux N., Ford H., Tsvetanov Z., Jacoby G., 2003, AJ, 125, 1226

Dewangan G. C., Griffiths R. E., Di Matteo T., Schurch N. J., 2004, ApJ, 607, 788

Dexter J., Agol E., 2011, ApJL, 727, L24

Dickey J. M., Lockman F. J., 1990, ARA&A, 28, 215

Done C., Mulchaey J., Muchotzky R., Arnaud K., 1992, ApJ, 395

Done C., Pounds K. A., Nandra K., Fabian A. C., 1995, MNRAS, 275, 417

Done C., Madejski G., Smith D., 1996, ApJ, 463, 63

Dudik R. P., Satyapal S., Gliozzi M., Sambruna R. M., 2005, ApJ, 620, 113

Ebrero J., Kaastra J., Kriss J., Cappi M., 2014, A&A, 129, 68

Edelson R. A., Krolik J. H., 1988, ApJ, 333, 646

Edelson R. a., et al., 1996, ApJ, 470, 364

Edelson R., et al., 2015, ApJ, 806, 129

Elvis M., 2000, ApJ, 545, 63

Elvis M., Van Speybroeck L., 1982, ApJ, 257L, 51

Elvis M., Risaliti G., Nicastro F., Miller J. M., Fiore F., Puccetti S., 2004, ApJ, 615, 25

Emmanoulopoulos D., Papadakis I. E., McHardy I. M., Arévalo P., Calvelo D. E., Uttley P., 2012, MNRAS, 424, 1327

Emmanoulopoulos D., Papadakis I. E., Nicastro F., McHardy I. M., 2013, MNRAS, 429, 3439

Emmanoulopoulos D., Papadakis I. E., Dov iak M., McHardy I. M., 2014, MNRAS, 439, 3931

Emmanoupolous D., McHardy I. M., Papadakis I. E., 2013, MNRAS, 433, 907

Eracleous M., Hwang J. A., Flohic H. M. L. G., 2010, ApJS, 187, 135

Esin A. A., McClintock J. E., Narayan R., 1997, ApJ, 489, 865

Fabian A. C., Vaughan S., 2003, MNRAS, 340, L28

Fabian A. C., Miniutti G., Iwasawa K., Ross R. R., 2005, MNRAS, 361, 795

Fath E. A., 1909, Lick Observatory Bulletin, 5, 71

Filho M. E., Fraternali F., Markoff S., Nagar N. M., Barthel P. D., Ho L. C., Yuan F., 2004, A&A, 418, 429

Filho M. E., Barthel P. D., Ho L. C., 2006, A&A, 451, 71

Filippenko A. V., Sargent W. L. W., 1989, ApJ, 342, L11

Frank J., King A., Raine D., 2002, Accretion Power in Astrophysics, 3rd edn. Cambridge University Press, Cambridge

Gabriel C., et al., 2004, ADASS, 314, 759

Gallimore J. F., Baum S. a., O'Dea C. P., 2004, ApJ, p. 38

Gallo L. C., Lehmann I., Pietsch W., Boller T., Brinkmann W., Friedrich P., Grupe D., 2006, MNRAS, 365, 688

Gardner E., Done C., 2016, Arxiv, 16030.9564

Gaskell C. M., Sparke L. S., 1986, ApJ, 205

George I. M., Turner T. J., Netzer H., Nandra K., Mushotzky R. F., Yaqoob T., 1998, ApJS, 114, 73

Ghisellini G., Haardt F., Matt G., 1994, MNRAS, 267, 743

Ghisellini G., Maraschi L., Tavecchio F., 2009, MNRAS, 396, L105

Gillessen S., Eisenhauer F., Trippe S., Alexander T., Genzel R., Martins F., Ott T., 2009, ApJ, 692, 1075

Gliozzi M., Sambruna R. M., Jung I., Krawczynski H., Horan D., Tavecchio F., 2006, ApJ, 646, 61

Gondoin P., Orr A., Siddiqui H., 2004, A&A, 420, 905

González-Martín O., Masegosa J., Márquez I., Guerrero M. a., Dultzin-Hacyan D., 2006, A&A, 460, 45

González-Martín O., Masegosa J., Márquez I., Guainazzi M., Jiménez-Bailón E., 2009, A&A, 506, 1107

Grier C. J., et al., 2012, ApJ, 755, 60

Grupe D., Komossa S., Gallo L. C., Fabian A. C., Larsson J., Pradhan A. K., Xu D., Miniutti G., 2008, ApJ, 681, 982

Grupe D., Komossa S., Gallo L. C., Lia Longinotti A., Fabian A. C., Pradhan A. K., Gruberbauer M., Xu D., 2012, ApJS, 199, 28

Gu M., Cao X., 2009, MNRAS, 399, 349

Guainazzi M., Antonelli L. A., 1999, MNRAS, 304, 15

Harris D., Krawczynski H., 2006, ARA&A, 44, 463

Hernández-García L., González-Martín O., Márquez I., Masegosa J., 2013, A&A, 556, 47

Hernández-García L., González-Martín O., Masegosa J., Márquez I., 2014, A&A, 569, 26

Herrnstein J. R., Moran J. M., Greenhill L. J., Trotter A. S., 2005, ApJ, 629, 719

Higginbottom N., Knigge C., Long K. S., Sim S. A., Matthews J. H., 2013, MNRAS

Ho L. C., 1999, ApJ, 516, 672

Ho L. C., 2008, ARA&A, 46, 475

Ho L. C., Filippenko A. V., Sargent W. L. W., 1996, ApJ, 462, 183

Ho L. C., Filippenko A. V., Sargent W. L. W., 1997a, ApJS, 112, 315

Ho L. C., Filippenko A. V., Sargent W. L. W., 1997b, ApJ, 487, 568

Horiuchi S., et al., 2004, ApJ, 616, 110

Irwin J. a., Henriksen R. N., Krause M., Wang Q. D., Wiegert T., Murphy E. J., Heald G., Perlman E., 2015, ApJ, 809, 172

Ishisaki Y., et al., 1996, PASJ, 48, 237

Iwasawa K., Fabian a. C., Almaini O., Lira P., Lawrence A., Hayashida K., Inoue H., 2000, MNRAS, 318, 879

Iwasawa K., Tanaka Y., Gallo L. C., 2010, MNRAS, 514, 58

Iyomoto N., Makishima K., Fukazawa Y., Tashiro M., Ishisaki Y., 1997, PASJ, 49

Kaastra J. S., Mewe R., Liedahl D. A., Komossa S., Brinkman A. C., 2000, A&A, 354, 83

Kaastra J. S., et al., 2014, Science, 345, 64

Kalemci E., Tomsick J. a., Buxton M. M., Rothschild R. E., Pottschmidt K., Corbel S., Brocksopp C., Kaaret P., 2004, A&A, 622, 508

Keck M. L., et al., 2015, ApJ, 806, 149

Kelly B. C., Bechtold J., Siemiginowska A., 2009, ApJ, 698, 895

Khachikian E. Y., Weedman D. W., 1974, ApJ, 192, 581

Kirchner J. W., 2005, Phys. Rev. E, 71, 069902

Kishimoto M., et al., 2013, ApJL, 775, 36

Klotz A., Normand J., Conseil E., Parker S., Fabrega J., Maury A., 2012, CBET, 3276, 1

Knuth K. H., 2006, ArXiv, 0605197

Koerding E., Falcke H., Corbel S., 2006, A&A, 456, 439

Krawczynski H., et al., 2004, ApJ, 601, 151

Kuulkers E., Wijnands R., Belloni T., Mendez M., van Der Klis M., van Paradijs J., 1998, ApJ, 494, 753

Lamer G., Hardy I. M. M., Uttley P., Jahoda K., 2003, MNRAS, 338, 323

Larsson J., Miniutti G., Fabian A. C., Miller J. M., Reynolds C. S., Ponti G., 2008, MNRAS, 384, 1316

Laurent-Muehleisen S. A., Kollgaard R. I., Ryan P. J., Feigelson E. D., Brinkmann W., Siebert J., 2008, A&A, 122, 235

Lavaux G., Hudson M. J., 2011, MNRAS, 416, 2840

Leighly K. M. L., 1999, ApJ, 125, 317

Lewis K. T., Eracleous M., 2006, ApJ, 642, 711

Lightman A. P., Zdziarski A. A., 1987, ApJ, 319, 643

Lira P., Lawrence A., O'Brien P., Johnson R. A., Terlevich R., Bannister N., 1999, MNRAS, 305, 109

Lira P., Arévalo P., Uttley P., McHardy I., Breedt E., 2011, MNRAS, 415, 1290

Loewenstein M., Mushotzky R., Angelini L., Arnaud K., Quataert E., 2001, ApJ, 555, 21

Longinotti A. L., Sim S. A., Nandra K., Cappi M., 2007, MNRAS, 374, 237

Longinotti A. L., Nucita A., Santos-Lleo M., Guainazzi M., 2008, A&A, 484, 311

Lubiński P., Zdziarski a. a., Walter R., Paltani S., Beckmann V., Soldi S., Ferrigno C., Courvoisier T. J.-L., 2010, MNRAS, 408, 1851

Lyubarskii Y. E., 1997, MNRAS, 292, 679

Maccarone T. J., Gallo E., Fender R., 2003, MNRAS, 345, 19

Maiolino R., Rieke G. H., 1995, ApJ, 454, 95

Malizia A., Stephen J. B., Bassani L., Bird A. J., Panessa F., Ubertini P., 2009, MNRAS, 399, 944

Markoff S., et al., 2008, ApJ, 681, 905

Markowitz A. G., Krumpe M., Nikutta R., 2014, MNRAS, 439, 1403

Martí-Vidal I., Marcaide J. M., Alberdi A., Pérez-Torres M. A., Ros E., Guirado J. C., 2011, A&A, 533, A111

Matsumoto Y., Fukazawa Y., Nakazawa K., Iyomoto N., Makishima K., 2001, PASJ, 53, 475

Matt G., Guainazzi M., Maiolino R., 2003, MNRAS, 342

Matthews J. H., Knigge C., Long K. S., Sim S. A., Higginbottom N., Mangham S. W., 2016, MNRAS

McHardy I. M., Papadakis I. E., Uttley P., 1998, Nuclear Phys. B, 69, 509

McHardy I. M., et al., 2014, MNRAS, 444, 1469

McHardy I., et al., 2016, Astronomische Nachrichten

Merloni A., Heinz S., Di Matteo T., 2003, MNRAS, 345, 1057

Miller L., Turner T. J., Reeves J. N., 2008, A&A, 483, 437

Molina M., et al., 2009, MNRAS, 399, 1293

Morgan C. W., Kochanek C. S., Morgan N. D., Falco E. E., 2010, ApJ, 712, 1129

Morrison R., McCammon D., 1983, ApJ, 270, 119

Nagar N. M., Falcke H., Wilson a. S., 2005, A&A, 435, 521

Nandra K., Papadakis I. E., 2001, ApJ, 20, 41

Nandra K., Pounds K. A., 1994, MNRAS, 268, 405

Narayan R., 1994, ApJ, 428, L13

Narayan R., 1996, ApJ, 462, 136

Narayan R., 2005, Ap&SS, 300, 177

Nardini E., Risaliti G., 2011, MNRAS, 417, 3571

Nemmen R. S., StorchiBergmann T., Yuan F., Eracleous M., Terashima Y., Wilson A. S., 2006, ApJ, 643, 652

Nicastro F., 2000, ApJ, 530, L65

Nicastro F., et al., 2000, ApJ, 536, 718

Novikov I. D., Thorne K. S., 1973, in , Black holes (Les astres occlus). pp 343–450

Nowak M., Markoff S., Young A., 2010, MmSAI, 81, 414

O'Neill P. M., et al., 2006, ApJ, 645, 160

Osterbrock D. E., 1977, ApJ, 215, 733

Page D. N., Thorne K. S., 1974, ApJ, 191, 499

Page M. J., Breeveld A. A., Soria R., Wu K., Mason K. O., Starling R. L. C., Zane S., 2003, A&A, 400, 145

Page M. J., Soria R., Zane S., Wu K., Starling R. L. C., 2004, A&A, 422, 77

Pancoast A., Brewer B. J., Treu T., 2014a, MNRAS

Pancoast A., Brewer B. J., Treu T., Park D., Barth A. J., Bentz M. C., Woo J. H., 2014b, MNRAS, 445, 3073

Panessa F., Giroletti M., 2013, MNRAS, 432, 1138

Papadakis I. E., Lawrence A., 1993, MNRAS, 261, 612

Parker M. L., et al., 2014, MNRAS, 443, 1723

Pellegrini S., Cappi M., Bassani L., Malaguti G., Palumbo G. G. C., Persic M., 2000, A&A, 353, 447

Penna R. F., Sadowski A., McKinney J. C., 2011, MNRAS, 420, 684

Perez-Olea D. E., Colina L., 1996, ApJ, 468, 191

Peterson B. M., et al., 2004, ApJ, 613, 682

Peterson B. M., et al., 2005, pp 44–46

Ponti G., Miniutti G., Cappi M., Maraschi L., Fabian A. C., Iwasawa K., 2006, MNRAS, 368, 903

Pounds K., Stanger V. J., King A. R., Czerny B., 1986, MNRAS, 224, 443

Pounds K. A., Reeves J. N., Page K. L., Edelson R., Matt G., Perola G. C., 2003, MNRAS, 341, 953

Pounds K. A., Reeves J. N., Page K. L., O'Brien P. T., 2004, ApJ, 616, 696

Pringle J. E., 1997, MNRAS, 292, 136

Proga D., 2007, ASPC, 373, 267

Proga D., Stone J. M., Drew J. E., 1999, MNRAS, 310, 476

Proga D., Stone J. M., Kallman T. R., 2000, ApJ, 543, 686

Ptak A., 1999, ApJS, 120, 179

Ptak A., 2004, ApJ, 606, 173

Ptak A., Yaqoob T., Serlemitsos P. J., Mushotzky R., Otani C., 1994, ApJ, 436, 31

Ptak A., Yaqoob T., Serlemitsos P. J., Kunieda H., Terashima Y., 1996, ApJ, 459, 542

Puccetti S., Fiore F., Risaliti G., Capalbi M., Elvis M., Nicastro F., 2007, MNRAS, 377, 607

Reilman R. R., Manson S. T., 1979, ApJ1, 40

Risaliti G., 2007, ASPC, 373, 1

Risaliti G., Maiolino R., Salvati M., 1999, ApJ, 522, 157

Risaliti G., Maiolino R., Bassani L., 2000, A&A, 40, 33

Risaliti G., Elvis M., Nicastro F., 2002, ApJ, 571, 234

Risaliti G., Bianchi S., Matt G., Baldi A., Elvis M., Fabbiano G., Zezas A., 2005a, ApJ, 630, 1

Risaliti G., Bianchi S., Matt G., Baldi A., Elvis M., Fabbiano G., Zezas A., 2005b, ApJ, 630, 2

Risaliti G., Elvis M., Fabbiano G., Baldi A., Zezas A., Salvati M., 2007a, ApJ, 659, 1

Risaliti G., Elvis M., Fabbiano G., Baldi A., Zezas A., Salvati M., 2007b, ApJ, 659, 1

Risaliti G., et al., 2009, MNRAS, 393, 1

Risaliti G., et al., 2013, Nature, 494, 449

Roberts T. P., Schurch N. J., Warwick R. S., 2001, MNRAS, 324, 737

Russell D. M., Maitra D., Dunn R. J. H., Markoff S., 2010, MNRAS, 405, 1759

Schmidt M., 1963, Nature, 197, 1040

Sergeev S. G., et al., 2005, ApJ, 622, 129

Seth A., Agüeros M., Lee D., BasuZych A., 2008, ApJ, 678, 116

Seyfert C. K., 1943, ApJ, 97, 28

Shakura N. I., Sunyaev R. A., 1973, A&A, 24, 337

Shappee B. J., et al., 2014, ApJ, 788, 48

Shemmer O., Brandt W. N., Netzer H., Maiolino R., Kaspi S., 2006, ApJ, 646:, L29

Shemmer O., Brandt W. N., Netzer H., Maiolino R., Kaspi S., 2008, ApJ, 682, 13

Shields G. a., 1999, PASP, 111, 661

Skipper C. J., 2013, PhD Thesis

Skipper C. J., McHardy I. M., 2016, MNRAS, 458, 1696

Skipper C. J., Mc Hardy I. M., Maccarone T. J., 2013, MNRAS, 434, 574

Slipher V. M., 1909, Lowell Observatory Bulletin, 3, 59

Sobolewska A., Papadakis I. E., 2009, MNRAS, 399, 1597

Sobolewska M. a., Papadakis I. E., Done C., Malzac J., 2011, MNRAS, 417, 280

Sramek R., 1975, ApJ, 80, 771

Starling R. L. C., Page M. J., Branduardi-Raymont G., Breeveld A. A., Soria R., Wu K., 2005, MNRAS, 356, 727

Steenbrugge K. C., et al., 2005, A&A, 434, 569

Swartz D. A., Ghosh K. K., Mccollough M. L., Pannuti T. G., Tennant A. F., Wu K., 2003, ApJ, 144, 213

Taylor R. D., Uttley P., Hardy I. M. M., Hardy M., 2003, MNRAS, 342, 31

Terashima Y., Iyomoto N., Ho L. C., Ptak A., 2002, ApJ, 139, 1

Thim F., Hoessel J. G., Saha A., Claver J., Dolphin A., Tammann G. A., 2004, ApJ, 127, 2322

Timmer J., Konig M., 1995, A&A, 300, 707

Tombesi F., Cappi M., Reeves J., Nemmen R., Braito V., Gaspari M., Reynolds C. S., 2013, MNRAS, 430, 1102

Turner T. J., Miller L., 2009, A&AR, 17, 47

Turner T., Nandra K., George I., Fabian A. C., Pounds K., 1993, ApJ, 419

Turner T. J., Miller L., Reeves J. N., Kraemer S. B., 2007, A&A, 475, 121

Urry C. M., Padovani P., Fisica D., Universit I. I., 1995, PASP, 107

Uttley P., Hardy I. M. M., Papadakis I. E., Guainazzi M., Fruscione A., 1999, 307, 6

Uttley P., McHardy I. M., Papadakis I. E., 2002, MNRAS, 332, 231

Uttley P., Edelson R., McHardy I. M., Peterson B. M., Markowitz A., 2003, ApJ, 584, 53

Uttley P., McHardy I. M., Vaughan S., 2005, MNRAS, 359, 345

Uttley P., Hardy I. M. M., Papadakis I. E., 2008, MNRAS, 000

Vasudevan R. V., Fabian a. C., 2007, MNRAS, 381, 1235

Vasudevan R. V., Fabian a. C., 2009, MNRAS, 392, 1124

Vaughan S., 2005, A&A, 431

Wales D., Doye J. P. K., 1997, J. Phys. Chem. A, 101, 5111

Walsh J. L., van den Bosch R. C. E., Barth A. J., Sarzi M., 2012, ApJ, 753, 79

Wang J., Fabbiano G., Elvis M., Risaliti G., Mazzarella J. M., Howell J. H., Lord S., 2009, ApJ, 694, 718

Weaver K. A., Wilson A. S., Henkel C., Braatz J. A., 1999, ApJ, 520, 130

White R. J., 1994, PASP, 106, 879

Wilkins D. R., Gallo L. C., Grupe D., Bonson K., Komossa S., Fabian A. C., 2015, MNRAS, 454, 4440

Woltjer L., 1959, ApJ, 130, 38

Woo J., Urry C. M., 2002, ApJ, 579, 530

Wu Q., Gu M., 2008, ApJ, 682, 212

Yamada S., Itoh T., Makishima K., Nakazawa K., 2009, PASJ, 61, 309

Yamaoka K., Uzawa M., Arai M., Yamazaki T., Yoshida A., 2005, ChJAS, 5, 273

Yang Q.-x., Xie F.-g., Yuan F., Zdziarski A. a., Gierli M., Ho L. C., Yu Z., 2015, MNRAS, 447, 1692

Younes G., Porquet D., Sabra B., Reeves J. N., 2011, A&A, 530, 149

Young A. J., Nowak M. A., 2007, ApJ, 669, 830

Yuan F., Taam R. E., Misra R., Wu X., Xue Y., 2007, ApJ, 658, 282

Zdziarski A. A., Lubi P., Smith D. A., 1999, MNRAS, 303, 11

Zhang Y. H., Treves A., Maraschi L., Bai J. M., Liu F. K., 2006, ApJ, 637, 699

Zhao J.-H., Bower G. C., Goss W. M., 2001, ApJ, 547, L29

Zu Y., Kochanek C. S., Peterson B. M., 2011, ApJ, 735, 80

Zu Y., Kochanek C. S., Kozłowski S., Udalski A., 2013, ApJ, 765, 106

van Groningen E., 1987, A&A, 186, 103